AD-A258 266

UMENTATION PAGE

Form Approved
OMB No. 0704-0188

1. AGENCY USE ONLY (Leave blank)	2. REPORT DATE	3. REPORT TYPE AND DATES COVERED
		XXXXXXXDISSERTATION

4. TITLE AND SUBTITLE
Finite Element Analysis of Concrete Subjected to Ordnance Velocity Impact

5. FUNDING NUMBERS

6. AUTHOR(S)
Darren L. Rice, Captain

7. PERFORMING ORGANIZATION NAME(S) AND ADDRESS(ES)
AFIT Student Attending: Purdue University

8. PERFORMING ORGANIZATION REPORT NUMBER
AFIT/CI/CIA- 92-023D

9. SPONSORING/MONITORING AGENCY NAME(S) AND ADDRESS(ES)
AFIT/CI
Wright-Patterson AFB OH 45433-6583

10. SPONSORING/MONITORING AGENCY REPORT NUMBER

11. SUPPLEMENTARY NOTES

12a. DISTRIBUTION/AVAILABILITY STATEMENT
Approved for Public Release IAW 190-1
Distributed Unlimited
ERNEST A. HAYGOOD, Captain, USAF
Executive Officer

12b. DISTRIBUTION CODE

13. ABSTRACT (Maximum 200 words)

14. SUBJECT TERMS	15. NUMBER OF PAGES 206
	16. PRICE CODE

17. SECURITY CLASSIFICATION OF REPORT	18. SECURITY CLASSIFICATION OF THIS PAGE	19. SECURITY CLASSIFICATION OF ABSTRACT	20. LIMITATION OF ABSTRACT

Graduate School Form 9
(Revised 8/89)

PURDUE UNIVERSITY
GRADUATE SCHOOL
Thesis Acceptance

This is to certify that the thesis prepared

By Darren L. Rice

Entitled

Finite Element Analysis of Concrete Subjected to Ordnance Velocity Impact

Complies with University regulations and meets the standards of the Graduate School for originality and quality

For the degree of Doctor of Philosophy

Signed by the final examining committee:

H. C. Rice, chair

C. Douglas Sutton

Harriett H. Jones

John N. Fox

Approved by:

Vincent P. Drnevich — Department Head

April 22, 1992 — Date

☐ is
This thesis ☒ is not to be regarded as confidential

H. C. Rice
Major Professor

FINITE ELEMENT ANALYSIS OF CONCRETE SUBJECTED TO ORDNANCE VELOCITY IMPACT

A Thesis

Submitted to the Faculty

of

Purdue University

by

Darren L. Rice

In Partial Fulfillment of the

Requirements for the Degree

of

Doctor of Philosophy

May 1992

This thesis is dedicated to Hope for her love and patience

and to my parents for instilling in me the desire to learn.

(There are matrices, Dad.)

ACKNOWLEDGEMENTS

The author is greatly indebted to his major professor, Professor Edward C. Ting, for teaching him so much about engineering and life... not necessarily in that order. Without the privilege of having Dr. Ting as his major professor, the author would not have started, much less completed, this work. The author would like to thank Professors C.D. Sutton, G.D. Jeong, J.F. Doyle, and T.N. Farris for consenting to sit on his examining committee and for their greatly appreciated advice. The author would also like to express his deep appreciation for the knowledge he gained from his many conversations with Mr. Nicholas Coburn.

The author would also like to thank Douglas B. Cleary for his friendship, help, and suggestions and Ed, Paul, and Christine for making Wednesdays an official holiday. In order to thank all the professors and fellow graduate students who helped the author, this thesis would be a two volume set. The author would be remiss if he didn't specifically thank his office-mates, Maheeb Abdel-Ghaffar, Tim Philpot, and Kyle Honeycutt for putting up with him and the computer desk.

Finally, the author thanks the Air Force Institute of Technology and the United States Air Force for giving him one of the best assignments for which an officer could hope.

TABLE OF CONTENTS

Page

Page

LIST OF TABLES

LIST OF FIGURES

Figure Page

Figure Page

Figure Page

Figure Page

Figure Page

ABSTRACT

Rice, Darren L. Ph.D., Purdue University, May 1992. Finite Element Analysis of Concrete Subjected to Ordnance Velocity Impact. Major Professor: Dr. Edward C. Ting.

Ordnance velocity impact of materials such as concrete results in complex reaction phenomena. Attempts to analyse the problem have taken the form of empirical solutions, analytical models, and numerical methods. The form which currently shows the greatest ability to predict the solution to the impact problem is numerical methodology. One such form of solution is the finite element method.

The finite element method traditionally relies on inter-element continuity and, thus, cannot represent fragmentation failure modes found in concrete impact. To more accurately model the physical phenomena present, a fragmentation algorithm is incorporated into the finite element method. As fragmentation results in large displacements, a large deformation formulation based on updated material geometry is also developed.

Example problems using frame, plane-stress/strain, and axisymmetric elements are presented to demonstrate the fragmentation and large deformation capabilities. A final series of problems is also shown which uses the resulting modified finite element method in solving low-velocity and ordnance velocity impact of unreinforced concrete.

CHAPTER 1 BACKGROUND AND RESEARCH OBJECTIVES

1.1 Introduction

A majority of the early effort in the study of ballistic impact is due to its applications in military technology. The need for information in the development of weapons and in the defense of weapons has led to extensive research into the impact response of many materials such as metals, composites, ceramics, and concrete. Non-military applications have more recently become equally important. Some of these include particle impact on space vehicles, impact on nuclear reactor containment facilities, and projectile impact used in the rock mining industry. Of particular interest to this study are those applications, both military and civilian, where the target is composed of concrete as the unique properties of concrete can create complex response mechanisms.

Regardless of the application, Wright and Frank [90] state the basic problem of ballistic penetration as:

> "Given a projectile, target, and details of the initial geometry, kinematics, and materials; determine whether or not the target will be perforated upon impact. If perforated, determine what the residual characteristics of projectile and target will be, and if not, determine how deep a hole will be made."

This seemingly simple statement is the cover for a diverse multitude of response and failure mechanisms which, to this day, are not fully understood to the point where they

may be accurately and completely predicted.

The objective of this review is to summarize the problem development of ordnance velocity impact of general targets, with special focus on the projectile impact of concrete targets. This problem is important in both military applications for the analysis of protective shelters and in the nuclear energy industry in reactor containment facility design. The ordnance velocity range of concrete impact possess response mechanisms which makes its study particularly interesting. These mechanisms include stress wave and contact induced failures and the resulting fragmentation of the material.

1.2 Behavior and phenomena

State-of-the-art surveys pertaining to projectile impact have been reported in the literature. One of these surveys which deserves special mention is the paper, "The mechanics of penetration of projectiles into targets" (Backman and Goldsmith [8]) which presents an overview of the subject detailing impact mechanics and various solution techniques. One important aspect of the paper is the reference list which contains 278 books and papers spanning over 100 years. Another paper, "Ballistic impact: the status of analytical and numerical modeling" (Anderson and Bodner [4]) is the follow-on to Backman and Goldsmith treating the 10 years of progress occurring between the two papers. These papers treat impact in general discussing most types of projectiles and targets.

The specific topic of concrete impact is not covered extensively in the literature. One of the papers dealing with the impact of concrete structures is "A review of

procedures for the analysis and design of concrete structures to resist missile impact effects" (Kennedy [45]). A later survey of impact/penetration of concrete is, "Energy release protection for pressurized systems. Part II. Review of studies into impact/terminal ballistics" (Brown [19]).

The material contained in these reviews and other papers will be examined in order to give a better understanding of impact mechanics in general, and also the phenomena directly related to the impact of concrete and like materials.

1.2.1 Problem classification

The phrase "ballistic impact" can take on very different connotations depending on the individual's base of reference. A 16 inch naval gun shell striking armor plate, a tornado-borne tree trunk striking a concrete containment facility, and a meteorite striking a space vehicle at many times the speed of sound all fall into this very general area of study. As could be expected, the responses of the targets and projectiles are as different as the situations themselves. These differences dictate the need for special analysis techniques or may allow the use assumptions which do not apply to all forms of impact. Therefore, the problems are commonly divided into sub-areas by three parameters: a) Impact velocity, b) Projectile type, and c) Target type which will be defined in this section.

1.2.1.1 Impact velocity

In many engineering applications, the loading on a structure acts relatively independent of time and may be treated using static solutions. When the structure is loaded in a manner which is not independent of time, a dynamic analysis must be considered.

Seely [77], states there are two ways to treat the dynamic responses. The first method deals with relatively low rates of loading which impart a structural response qualitatively very similar to the static response. The main difference between the static and dynamic loadings is the magnitude of response. The dynamic problem may be solved using a static loading method including a magnification factor. This is the primary method of analysis found in standard design codes like the LRFD and AASHTO manuals. The second method of *analyzing* the dynamic loadings is intended for applications where the rate of loading is increased such that the induced response no longer resembles an amplified static response. This type of problem requires a more accurate analysis as the dynamic effects can change material properties, effective boundary conditions, and failure modes. The broad range of loading rates can also create unique response mechanisms which require specific means of analysis. One common method of classifying the loading rate in impact problems is by the velocity of the impacting projectile.

Backman and Goldsmith [8] give a rough outline of impact velocity ranges as: a) Sub-ordnance range of 25-100 m/sec, b) Ordnance range of 500-1300 m/sec (so-named as this is the usual velocity range of conventional firearms), c) Ultra-ordnance range of

1300-3000 m/sec, and d) Hypervelocity range of above 3000 m/sec. Seely [77] states the ranges depend on changes in material and structural behavior and, thus, implies different interacting material properties may give a different class of reaction. This can be seen in another definition set given by Backman and Goldsmith [8] which uses target and projectile properties to define velocity ranges. The first range defined is that where only elastic response occurs in both the target and projectile. The second range is one in which plastic deformations occur. The third range is where the predominant response is produced through the propagation of elastic, plastic, and hydrodynamic stress waves. The region beyond the hydrodynamic range includes shock wave response. The highest velocity regime considered is termed hypervelocity and is characterized by comminution, phase changes, etc.

Zukas [98] gives a very general classification of impact velocities in terms of response mechanisms. In the low-velocity range (<250 m/sec), there is a combination of both a local response at the point of impact and an overall structural response away from the impact area. In these velocities the response time can be described in the milli-seconds range. In the next class of velocities (0.5-2.0 km/sec), wave effects predominate and the overall structural response becomes subordinate to the much greater localized response at the point of impact. This localized deformation is usually confined to 2-3 times the diameter of the projectile according to Zukas [98]; but, as shown later, can be larger for concrete targets. The reaction occurs in the micro-second time domain. Higher speeds (2-3 km/sec) create large localized pressures greatly exceeding the impact strength of the materials strengths. Speeds above this are

classified, similar to Backman and Goldsmith [8], by explosive vaporization effects. A chart showing these ranges along with their corresponding strain rates, effects, etc. is extracted from Zukas [98] and presented as Table 1.1. Zukas [98] noted divisions of these ranges are only a guideline and depend on the particular problem.

Kimsey [48] classifies the kinetic energy penetration regime as that in the 0.5 to 2 km/sec range which is the same as the ordnance velocity range of Zukas [98]. It is stated the important characteristics involved in this regime are inertial forces and material failure strengths. The equations needed to be solved for such a velocity range are the equations of motion and the constitutive equations which need to include the ability to handle large localized plastic flow.

1.2.1.2 Projectile type

Also important in classification of impact problems are the characteristics of the projectile. The geometry, material composition, and trajectory of the projectile are a great influence on the final condition of a target.

Table 1.2 is a compilation of projectile characteristics listed in Zukas [98]. Seven separate means of classifying the projectile are given, where the first five (basic shape, nose configuration, density, trajectory, and impact condition) can be considered input parameters and the last two projectile characteristics (final condition shape and location) being the output.

Backman and Goldsmith [8] state the minimum parameters needed to determine the "ballistic limit" for a projectile to remain intact are mass, total projectile length, nose

shape and length, diameter, and density. The ballistic limit is defined in [8] and [3] as:

> "Ballistic Limit - The average of two striking velocities, one of which is the highest velocity giving a partial penetration and the other of which is the lowest velocity giving a complete penetration..."

Figure 1.1, though, shows the ambiguity between partial and complete penetration which are defined somewhat different by different agencies (Backman and Goldsmith [8]).

Backman and Goldsmith, [8] and [35], define the penetrator shape as various degrees of "sharp" and "blunt." This shape can play a major role in particular deformation modes discussed later. Sharp noses are defined as having a nose half-angle of 14° with blunt noses having the half-angle measuring 90°. "Pseudo-sharp" noses and "Pseudo-blunt" noses are between these two limits and vary from 30° to 50°. They then go on to a simpler definition of nose shape from [52] where the nose length is greater than its diameter for sharp noses and less than the diameter for blunt noses. The effectiveness of the nose shape in penetrating must be qualified by its deformability. A sharp but deformable projectile can behave like a blunt projectile due to the relative hardness of the target.

The projectile's deformation upon impact will be shown to be an important consideration when determining modes of target failure. Backman and Goldsmith [8] point out the projectile deformation is affected by target deformation. This is seen in tests of steel projectiles impacting sandstone and concrete targets where the projectile acts as a rigid penetrator for one type of target material but as a deformable penetrator for the other. Of course, the converse is also assumed to be true with a rigid projectile

imparting more energy to target deformation than the projectile which dissipates some of the initial kinetic energy in its own deformation.

The flight of the projectile is defined [8] by its obliquity upon impact (angle between the velocity vector and the normal vector into the target) and its orientation (angle between the projectile's axis of symmetry and velocity vector) as shown in Figure 1.2. These two characteristics are important parameters in determining the amount of energy the target will be required to absorb.

1.2.1.3 Target type

With the initial striking velocity defined and the projectile's characteristics known, the remaining portion of the impact problem is the type of target being impacted. The two major characteristics of the target are its geometry and its material composition. Backman and Goldsmith [8] give a qualitative description of target classification related to thickness as:

> "(a) semi-infinite, if there is no influence of the distal boundary on the penetration process.
> (b) thick, if there is influence of the distal boundary on the penetration process only after substantial travel into the target element.
> (c) intermediate, if the rear surface exerts considerable influence on the deformation process during all (or nearly all) of the penetrator motion, and
> (d) thin, if stress and deformation gradients throughout its thickness do not exist."

In this same article, quantitative values are also given to these definitions by relating the target thickness, h, projectile length, L, and the elastic wave speeds of the target, C_t, and projectile, C_p. This is done by using the number of wave traversals in the plate

during a single traversal of the elastic wave in the projectile. Thin targets have more than five traversals, intermediate targets have between one and five, and thick targets have less than one.

Bodner [18] defines the target thickness as:

(a) Thin: no stress or deformation gradient through the target thickness

(b) Moderately Thick: target thickness approximately projectile diameter

and also includes using the number of deformation modes occurring during the penetration to define the target thickness. A thin target will exhibit only one deformation mode while a thick target will undergo multiple modes of failure.

The other significant target property is the material composition of the target. Backman and Goldsmith [8] divide target materials into naturally occurring (eg. soil, rock, etc.) and those which are man-made (eg. metals, composites, concrete). One problem with this method is the man-made material concrete behaves much more like natural rock than other man-made materials such as metals. They also give a division by weight with lightweight being up to a specific gravity of 3, intermediate ranging up to 8, and heavy materials above 8.

A different means of classification which has a more direct meaning in the problem is termed penetrability and is done by measuring relative depth of penetration in various target materials using constant velocity and projectile parameters. Some non-dimensional examples of this style of classification are taken from [8] and shown in Table 1.3. Low resistant materials are mainly soils resulting from their porosity,

anisotropy, and inhomogeneities. The moderately resistant materials are those such as wood, concrete, and reinforced concrete. They state such materials may be represented with the same types of models as used for the homogeneous metals which compromise the highly resistant materials.

Backman and Goldsmith [8] give a list of the main assumptions which are valid for most applications of ordnance velocity target modeling. The first is one of the most important and useful of the assumptions. This assumption is that due to the velocity of impact, the response of the structure is localized to the area of impact within a multiple of the projectile diameter (discussed earlier). This allows the disregarding of sometimes complicated boundary conditions away from the point of impact. The second assumption is to neglect all substructure (defined as "any single functional or operational unit of the target...") rigid body motion. The third is the neglecting of all thermal effects including friction. Thermal effects, though, do play an important part in one of the deformation modes in metals mentioned later. The neglecting of friction has been justified in concrete impact in Yuan [94]. The fourth assumption is related to the first by stating all targets have planar surfaces. The last states all target elements are initially stress free.

1.2.1.4 Summary

The ballistic impact/penetration problem covers a wide range of input parameters and, thus, is usually categorized by the three main areas of the impact velocity, projectile type, and target type These three divisions, though, cannot be considered

independent of the other two. For example, the term thin or thick target is highly dependent on the projectile, and the sharpness or bluntness of the projectile is highly dependent on the relative hardness of the target. Therefore, even though impact problems are commonly categorized using these divisions, the entire problem must be studied for an accurate assessment to be made.

1.2.2 Impact response and failure modes

Once input parameters are defined, the target's reaction upon impact must be understood. As was shown in the section on impact velocity, in order to perform a comprehensive summary of all possible response mechanisms, quasi-static to explosive vaporization phenomena would need to be examined. The ordnance velocity regime of impact is that range being emphasised in this report. Therefore, the discussion of failure and penetration modes will be restricted those common to these velocities. Particular emphasis will be given to those modes most frequently observed during impact of reinforced and plain concrete targets.

The response and failure modes can be divided into two groups. The first group is that which is caused by direct contact with the projectile. The second group contains those which are stress wave induced [4].

1.2.2.1 Contact induced response

When the projectile strikes the target, the target material must find a means of moving out of the path of the projectile. In doing this, the target may experience modes

of failure called contact modes.

At relatively low velocities in the sub-ordnance range, the predominant mode of failure in materials such as concrete is closely related to a punching shear failure found in static tests. A cross-section of a low velocity impact failure is shown in Figure 1.3(a).

As the velocity increases, the inertial properties of the target cause an increase in damage away from the projectile at the impact surface. This mode, called cratering and shown in Figure 1.3(b), is caused by large shear stresses being caused directly ahead of the projectile. The tunneling mode can be a result of plugging in moderately thick targets, Figure 1.3(c), or radial movement in thicker targets, Figure 1.3(d). Figures 1.3(e), ductile hole growth, and 1.3(f), petaling, are found in the impact of ductile materials and will not be discussed.

Maurer and Rinehart [63] explained the mechanisms involved in the cratering and tunneling modes of target response. The report was based on tests of steel projectiles fired into rock (sandstone and granite) at 300 ft/sec to 6000 ft/sec but can be applied to concrete due to their similar properties. The impact created a cross section (Figure 1.4) similar to Nash, Zabel, and Wenzel [66], but the main emphasis was on the fractures which occurred at relatively constant intervals between the bottom of the crater (cup) and bottom of the tunnel (burrow). The cracks propagated along spiral paths represented by an equation:

$$r = r_o \, e^{\pm(\theta \tan(45^\circ + \frac{1}{2}\phi))}$$

where r = Radius vector of the spiral, r_o = Distance from impact to intersection of spiral

and free surface, θ= Polar angle from upper surface, and ϕ = Internal angle of friction for target material. A set of these spirals is seen superimposed on a typical target (sandstone) in Figure 1.5. Maurer and Rinehart [63] state these lines coincide with the paths of maximum shear generated by the impact. Bauer and Calder [11] also report the same logarithmic spiral behavior in rock targets with non-deformable projectiles. A trace of a photograph from this test is shown in Figure 1.6 which shows these spirals. Maurer and Rinehart [63] form an empirical relationship between the penetration depth of the projectile and the target's shear strength. Close correlation is reported supporting the reasoning. Therefore, it is assumed the impact crater is formed by the uppermost of these spirals reaching the target surface and fragmenting the material.

The fragments from the impact crater are ejected from the target at a considerable velocity. Kumano and Goldsmith [54] reported tests where the ejecta from the crater traveled at or near the velocity of the projectile. Experiments (Forrestal [25]) have shown this phase of the penetration to induce a monotonic rise in the deceleration of the projectile.

When the projectile has proceeded deep enough into the target, the shear spirals do not reach the surface and a new mode of creating a path for the projectile to pass must occur. This new mode is tunneling which occurs due to a crushing of the material in front of the projectile and due to radial movement of the material away from the projectile. The relative magnitudes of the crushing and radial movement depend on the nose shape of the projectile. The tunneling mode is highly dependent on whether the projectile is relatively non-deformable as shown in tests on concrete, sandstone, and

granite (Maurer and Rinehart [63] and Nash, et. al. [66]). When a steel projectile impacted the relatively soft concrete and sandstone, the projectile retained its original shape and a tunnel formed. When the granite was impacted by the same type of projectile, the projectile deformed due to the granite being stronger and only a crater was formed. Experimental data from [25] show the peak deceleration of a projectile to occur as the tunnel develops. Therefore if a projectile is going to experience stresses above its yield point, it would experience them before developing the tunnel. This yielding of the projectile would consume a great deal of its impact kinetic energy and thus greatly reduce the chances of a tunnel forming.

1.2.2.2 Wave induced response

When a target is impacted at an ordnance velocity, the entire structure does not participate in the energy dissipation as only a local area around the point of impact deforms to any great extent. Even this local area does not all react at the same time: it takes time for material through the thickness of the structure to "realize" it has been hit. Some stresses are propagated through the structure by waves which travel at material property dependent velocities. The type of wave most important to, and thus most treated in, target deformation is the dilatational wave in which the particle velocity and wave propagation velocity vectors are along the same line. Zukas [98] uses a standard wave equation for the dilatational waves.

These stress waves cause three modes of target failure. The first two are radial cracking and fracture. Radial cracking occurs in materials which have compressive

strengths greater than the tensile strength and is due to the relief wave following the initial compressive wave. Fracture occurs in targets composed of weak, low density targets where the initial compressive wave is greater than the compressive strength.

The third mode of wave induced failure is the result of a compressive result of an incident compressive wave reflecting off a free surface. Due to the requirement of stress free conditions at the surface, the wave is reflected from the boundary opposite in sign to the incident wave but equal in magnitude. Therefore, the incident compressive wave will be reflected as a tensile wave. In materials such as concrete with lower tensile strength than compressive strength, the compressive wave magnitude may be lower than this strength, but the reflected tensile wave might exceed the failure strength. As the static tensile strength of concrete is 1/10th to 1/20th of its compressive strength (this ratio is not the same in high strain-rate applications), the tensile wave can cause fracture and fragmentation as shown in Figure 1.3(g). Zukas [98] explains the large tensile stress can cause multiple layers of fracture. As in the impact crater ejecta, these fragments can fly off the target at relatively high velocities and, in some cases, are as much of a danger as the penetrating projectile itself.

1.2.2.3 Summary

Figure 1.7 shows a breakdown of the three modes of failure which are prevalent in the penetration process of concrete targets. These modes are cratering, tunneling, and scabbing. The cratering due to the shear trajectories and the scabbing due to the reflected wave will occur with both deformable and non-deformable projectiles at

ordnance velocity. The tunneling due to the crushing and radial movement will occur only in the rigid projectile case (Figure 1.8). Therefore, complete perforation of a plate in deformable projectile impact will only occur if the target thickness is such the crater and spall depths meet.

1.2.3 Remarks

Earlier in the chapter, it was stated ordnance velocity impact caused a localized zone of damage which was approximately two to three times the diameter of the projectile. As much of the interest in earlier works on projectile penetration lay in the area of homogeneous, isotropic, ductile materials such as steel and aluminum, this assumption was realistic. When targets such as concrete or rock enter the problem, the region of deformation grows considerably. Bauer and Calder [11] have results showing crater to projectile diameter ratios in excess of 11 to 1, Nash, Zabel, and Wenzel [66] have shown approximately the same for semi-infinite concrete, and tests of concrete plates at Purdue University have shown crater ratios of approximately 12 to 1 and distal face scabbing diameter ratios in excess of 20 to 1. Even though this shows the increased damage zone of rock and concrete targets, these effects can still be classified as local. Halder [29] showed analytically energy absorbed by local deformations was approximately 98% of the energy absorbed in the impact with the other 2% being due to the overall structural response.

As can be seen, the impact/penetration phenomenon is complicated in general and made even more complex with the introduction of concrete as the target material. The

interaction of various modes of penetration (cratering, tunneling, scabbing) creates a highly complex problem.

1.3 Modeling and analysis

The study of ballistic impact and penetration phenomena has been active for centuries, but a full understanding and accurate prediction of the problem is still well beyond current capabilities. Various solution techniques for modeling and analysing impact can be grouped into three categories: a) Empirical approaches based on experimental data, b) Analytical models based on simplifications, and c) Numerical solutions.

1.3.1 Empirical approaches

Based on known input, measured output, and a large number of tests, a correlation between changes in the output data and the input parameters can be determined. This is known as an empirical approach and is widely used in design for impact and penetration. It has been the chosen method of solution mainly due to the fact only a rudimentary knowledge of the phenomena is needed to produce a satisfactory relation which need not be based on a rational modeling of the processes. These relations can give accurate, useful results as long as they are used within the parameters of the tests.

Some of the early relations for the use in impact problems have been summarized in Backman and Goldsmith [8]:

Morin (1833)	$\frac{P}{D} = 2\,m\,v_o^2 / a_1 \pi D^3$
Dideon	$\frac{P}{D} = a_2\,\rho_t \ln(1 + a_3 v_o^2)$
de Marre (1886)	$E_o = a_6\,D^{1.5}\,h_o^{1.4}$

where P = Penetration depth, D = Diameter of projectile, E_o = Required initial kinetic energy for perforation, ρ_t = Target density, m = Projectile mass, v_o = Initial projectile velocity, h_o = Target thickness, and a_i = Empirically derived constants. The above relations exhibit important aspects of empirical formulae. First, as shown in Morin's equation, the lack of specific target information allows one to deduce (as pointed out in [8]) this equation is only meant for one specific target material. Also, as these equations were all formulated using SI units, a change of systems would alter the constants. The limited number of variables in de Marre's equation shows the importance of the constant a_6. Backman and Goldsmith [8] also reviewed common empirical relations for each of the following categories of problems: a) Semi-infinite target, b) Thin plate penetration and perforation, and c) Intermediate and thick targets. The restrictions on the application of these equations mark the primary shortfall of empirical approaches. One example is the limit placed on target thickness which reduces the usefulness of the formulae.

Reviews of the empirical relations used in concrete for concrete penetration/perforation problems can be found in Kennedy [45], Sliter [80], and Brown [19]. A commonly used relation when dealing with a non-deformable projectile on a semi-infinite concrete target is the modified Petry formula [45]:

$$x = 12\,K_p\,A_p \log_{10}\left(1 + \frac{V^2}{215000}\right) \qquad (1.1)$$

where x = Penetration depth, K_p = Coefficient depending on concrete (0.00799 for

massive concrete, 0.00426 for "normally" reinforced concrete, and 0.00284 for "specially" reinforced concrete), A_p = Weight of projectile per unit projected area (lb/ft^2), and V = Projectile velocity. Amirikan, from [45], extended this formula to the perforation of concrete slabs where the maximum thickness of slab which would be perforated would be twice the calculated penetration depth, and the maximum thickness of a slab which will experience scabbing is approximately 2.2 times the penetration depth.

The Army Corps of Engineer (ACE) formula established in 1946 is:

$$\left[\frac{x}{d}\right] = \frac{282\, D\, d^{0.215}}{f_c'^{0.5}} \left[\frac{V}{1000}\right]^{1.5} + 0.5 \qquad (1.2)$$

where x,V = Defined previously, d = Projectile diameter, D = Projectile weight / d^3, and f_c' = Concrete compressive strength. The perforation thickness, e, and scabbing thickness, s, based on Equation 1.2 are:

$$\frac{e}{d} = 1.32 + 1.24\left[\frac{x}{d}\right] \qquad \left(3 \le \frac{e}{d} \le 18\right) \qquad (1.3)$$

$$\frac{s}{d} = 2.12 + 1.36\left[\frac{x}{d}\right] \qquad \left(3 \le \frac{s}{d} \le 18\right) \qquad (1.4)$$

Notice the limits on e/d and s/d in Equations 1.3 and 1.4.

The National Defense Research Committee (NDRC) proposed its own formula in 1946 using:

$$G_{(x/d)} = K\, N\, d^{0.20}\, D \left[\frac{V}{1000}\right]^{1.80}$$

where

$$G_{(x/d)} = \left[\frac{x}{2d}\right]^2 \qquad \left[\frac{x}{d}\right] \le 2.0 \tag{1.5a}$$

$$G_{(x/d)} = \left[\frac{x}{d}\right] - 1 \qquad \left[\frac{x}{d}\right] \ge 2.0 \tag{1.5b}$$

N = Missile shape factor (0.72 for flat nosed, 0.84 for blunt nosed, 1.00 for spherical nosed, and 1.14 for sharp nosed) and K = Concrete penetrability factor (Defined later in 1966 as $K = 180/\sqrt{f'_c}$). For the previously stated range of $x/d \ge 3$, Equations 1.5a and 1.5b can be used with Equations 1.3 and 1.4 for the perforation and scabbing thicknesses. One of the NDRC formula's strengths was its ability to be used to also calculate time histories of the impact force and penetration depth. Brown [19] gave a comprehensive listing of most of the known empirical impact formulae used in calculation of concrete penetration. Table 1.4 shows some formulae from Brown [19] which were not covered above. As these relationships are trying to describe the same phenomena, the results do not differ greatly from one equation to the other. Figure 1.9 (Kennedy [45]) shows computed penetration using the NDRC formula versus experimental penetration data for a semi-infinite target at various x/d values. It shows the empirical relations can be accurate within stated parameters but error grows quickly as x/d falls below 0.5.

Another set of empirical relations can be found in Maurer and Rinehart [63]. The main reason to mention their results is, even though the equation is based on the impact of rock targets, the research showed an important point in the mechanics of the penetration. The equation has the form

$$P = K_1 (M/A) (v_o - v_c)$$

where K_1 = Constant related to target material properties, M = Projectile mass, a =

Projectile cross-sectional area, v_o = Initial projectile velocity, and v_c = Minimum velocity at which cratering will occur. This equation is shown to apply to both sandstone and granite (materials shown to be weaker and stronger than concrete). They also showed the inverse of the experimentally determined K_1 for various materials is linearly related to the material's shear strength. The relationship shows the importance of the shear strength of the target material in impact problems. However, it should be noted the relationship was based on the static shear strengths and not the dynamic strengths.

Empirical relations are useful tools in the analysis of impact problems. As long as they are used in applications where the actual conditions are within the test parameters, they can give accurate results. For new design considerations not within the given limits, a new set of tests has to be performed. The time and cost to develop accurate formulas can be prohibitive. Thus, it would be preferable to study the actual physical processes and propose rational analytical models. Such analyses are more easily adaptable to various ranges of parameters and thus reduce the total number of test required.

1.3.2 Analytical modeling

Analytical models are designed such that the physical problem is formulated by a set of simplified equations which are more easily solved. The simplification is done by using assumptions to reduce the number of unknowns or to simplify a complex process to a more solvable one. The solution usually centers on one predominant failure mode

and, according to Anderson and Bodner [4], mainly solves for the contact modes (i.e. plugging or tunneling) as opposed to the wave induced modes.

An example of the derivation of equations used in an analytic model for ductile hole enlargement in a thin plate metal target is given in Backman and Goldsmith [8]. Even though this is a relatively simple problem with only one mode of penetration present, the final equation can be complicated. For a more complicated failure series such as those shown in Figure 1.10 (Ravid and Bodner [73]), the equations become considerably more involved.

Most of the analytical models [2,57,71,89,94] considered the impact of projectiles on metal targets using ductile type failure modes. Only a few solutions considered concrete impact. A model was developed by Luk and Forrestal [59] for the penetration of a rigid projectile into a semi-infinite reinforced concrete target. The reinforcing was assumed only to control radial cracking and did not have a significant effect on the overall behavior. The failure mode assumed in this model was tunneling approximated by a spherical cavity expansion model which had been used successfully in the representation of rigid projectiles penetrating metal targets by Goodier, from [59]. The equations are formulated by first neglecting friction between the projectile and target. Therefore the incremental forces on the spherical projectile nose in the axial direction can be calculated as:

$$dF_z = 2\,\pi\,R\,a\cos\theta\;\sigma_n(V_z,\theta)\,d\theta$$

where $\sigma_n(V_z,\theta)$ is the normal stress on the nose which is a function of projectile velocity, and the other variables are shown in Figure 1.11. Therefore the total force on

the projectile is:

$$F_z = \pi a^2 \int_0^{\pi/2} \sigma_n(V_z,\theta) \sin 2\theta \, d\theta$$

In order to derive an expression for $\sigma_n(V_z,\theta)$ the response is approximated by the elastic-plastic cavity expansion of a sphere. The final form of the penetration equation takes on two parts as a locked hydrostat response is more accurate for the high initial velocities during the early stages of penetration but at a certain velocity, V_t which occurs after a penetration to a depth P_t, a linear hydrostat model is more accurate. Theses two parts are:

$$P_t = \frac{m}{2\beta} \ln\left[\frac{\alpha+\beta v_o^2}{\alpha+\beta v_t^2}\right] \quad \text{and} \quad P = P_t + \frac{m}{2\beta} \ln\left[1 + \frac{\beta v_t^2}{\alpha}\right]$$

where only α and β are constants which depend on the shape of the projectile nose and are solved for with the linear and locked hydrostat models. The analysis gives penetration values close to the tests but the values are consistently overestimated. One possible reason is the model treats the process as a steady state expansion of a sphere neglecting the transfer of energy needed to start the expansion and to propagate the axial fracture to allow the forward progress of the projectile. Also, no triaxial data were available from the original tests and the triaxial data were extrapolated from uniaxial data which were available. Other models for the penetration of concrete [24] and geomaterials [54,58,91] assume a semi-infinite target and limit the mode of failure. These models are not sufficiently general for the prediction of overall behaviors.

The analytical models are important tools for the understanding of impact mechanics. They permit one to study the predominant mode of penetration by

comparing the results to experimental data. This also leads a primary drawback of the method as it is most useful in problems where one mode is the dominant failure process such as thin plate perforation. As shown previously, Ravid and Bodner [73] have derived an analytical model capable of treating multiple failure modes present in the penetration of intermediate and thick targets. The complexity of the problem dictates some simplifications be made in the deformation processes.

The limitations of the empirical and analytical approaches have shown a need for an alternate technique. Desirable attributes of this technique would be the ability to predict response as opposed to merely repeating it and to incorporate all phenomena involved instead of requiring simplifications to reduce the complexity. It is then natural to consider numerical modelings.

1.3.3 Numerical approaches

The desired result in the solution of impact/penetration problems is to input projectile velocity, projectile characteristics, and target characteristics and receive as output the complete time histories of target deformation, failure, and residual projectile characteristics without altering the problem geometry and loading conditions or introducing material simplifications. Numerical study of impact, reported since 1958 [4], is thus becoming more prevalent as computing facilities become increasingly powerful and accessible.

There are two major divisions of numerical methods used in the study of impact problems. The finite block method, distinct element method, etc. constitute the first of

these groups and are mainly used in the qualitative simulation of impact. The other group consists of such methods as the finite element method, finite difference method, etc. and is termed numerical analysis. The objective is to obtain qualitative predictions of the failure mode and accurate evaluations of stress and deformation for design.

The numerical simulation techniques such as the finite block method and distinct element method are usually applied to discontinuous media such as soils or jointed rock to obtain the motion history of the penetrator and target. This is done by modeling the system as a grouping of separate blocks. The block interaction consists of contact forces which are determined by restricting block inter-penetration. These systems are then put into equilibrium using iterative techniques, or time integration can be used to solve for the resulting displacements.

One example of a numerical simulation technique applied to an impact problem is by Gelman, Nelson, and Ito [27]. A distinct element method is applied to ordnance velocity impact (2500, 2000, and 1500 ft/sec) of a steel penetrator into boulders. Target and penetrator configurations at various times are shown for the 2000 ft/sec impact in Figure 1.12. An observation of the results is no boulder elements are fractured which do not come into direct contact with the penetrator. This result is interesting if experimental data is able to confirm this. It is possible the joints between the boulders do dissipate enough energy to localize the damage to these elements and not create the greater fragmentation found in a more continuous system such as concrete.

A possible limitation in the application of numerical simulation techniques to concrete targets can be observed in the results of Figure 1.12. The path of the

penetrator and the resulting target damage can be highly dependent on the initial mesh used. This is acceptable in the study of discontinuous media where joints and element boundaries can be clearly defined. In continuous media such as concrete, the use of direction oriented finite blocks or distinct elements can lead to unreliable predictions.

The numerical analysis used in impact and penetration problems consist mainly of finite difference and finite element methods. The finite difference method discretizes a continuum into points whose differences replace the derivatives in governing equations [98]. The finite element method divides the continuum into small regions where all the field variables within the element are interpreted by the value of the variable at the nodes of the element. All of the elements together are put into equilibrium defined by a force balance or a variational principle.

These two methods of discretization commonly use one of two ways of describing the field variables. A Lagrangian formulation tracks the difference points or the element nodes, whereas an Eulerian formulation tracks the material passing through fixed control volumes. The Lagrangian formulation is commonly used in solid problems and has the advantages:

1) Relatively complex convected equations of mass flow are not required.

2) The tracking of specific material points allows distinct definition of structural boundaries and material layers.

3) Specific material properties (e.g. inelastic or anisotropic) are more easily handled.

One problem with a Lagrangian formulation, though, is large local distortions of the mesh can occur in impact problems. These distortions can lead to elements folding and negative element areas if other than three-node elements are used. Also, if element size controls the time step in the time integration scheme, uneconomical requirements in the step can result. This problem can be treated by re-meshing the structure during the computer run by hand or with an automatic mesh processor within the program. This has been proven successful in the TOODY and DYNA codes [98]. The Eulerian formulation handles the large deformations much more easily but at the cost of creating non-distinct material interfaces and structure boundaries. Some success has been achieved by combining the strengths of both of these in mixed formulations [98].

The previous discussion treats spatial variables. Equally important is the method of representing the dimension of time. The two general classifications of time integration schemes are implicit and explicit both of which use finite difference discretization of time. Without going into details, it is generally accepted the explicit scheme is more appropriate for wave propagation found in ordnance velocity impact [98]. This scheme requires a relatively small time step as it is conditionally stable. This can be uneconomical in penetration problems as only a limited portion of the mesh is actually undergoing the large deformation requiring a small time step. Belytschko and Liu [16] considered one remedy by introducing a method of applying different time increments to different parts of the mesh. The small time step, though, is not necessarily a hindrance as the large deformations and strain rates of impact may require a small time step for reasonable accuracy thus negating the benefits of using an implicit algorithm

with unlimited time step size.

The choice of which type of code is more appropriate for a specific problem is important in the numerical analysis of impact. Reviews of current codes and their capabilities can be found in Zukas, et. al. [98] and Belytschko [13].

As the code should have the proper choice of time and space discretization, it should also contain the proper material models for the penetration process. Without this ability the numerical analysis often degenerates to a qualitative measure and leads to empirical curve fitting and matching known test data and lose the ability to predict response.

For the impact and penetration study, local failure behavior of the structure is very important and must be properly modeled in order to achieve an accurate prediction. The failure process may be considered as a two step sequence. The first step is defining what constitutes a local failure, or a failure criterion. The second step is defining how a particular failure will affect future response, or a material model for post-failure concrete medium.

A complete failure model for concrete impact must be capable of detecting various modes of failure. Tensile strength is important in the distal face spalling. Shear strength can be used to determine the cratering caused by the shear spirals. Compressive strength is crucial in the crushing and radial expansion present in the tunneling. As the failure is localized in impact, the surrounding concrete acts as confinement. Thus, the important effect of three-dimensional hydrostatic pressure upon the failure criterion and the failure mode must be included in the concrete modeling.

The main underlying principle involved with the correct representation of the failure involves the ability to correctly describe the material stress-strain response and its failure criteria at the high strain-rates. Experiments and theories proposed in the area of concrete behavior, fracture, and failure [2, 12, 17, 20, 28, 39, 40, 43, 49, 50, 64, 65, 70, 74, 78, 81-83, 85] have not provided definitive answers. The one agreed upon fact is the material properties such as ultimate compressive, tensile, and shear strengths are strain-rate dependent and need to be accounted for in the numerical modeling.

The manner in which the failure is treated once it has been detected can be extremely important. Tensile failure has been assumed which includes restricting failed elements to sustaining hydrostatic compressive stresses only and accumulative damage models to redistribute post-failure stresses. Elements failed in compression are often assumed to lose the ability to sustain any stress and only retaining mass. Considerably more research is needed in this area.

An important part of the impact response analysis is to predict the path of the projectile through the target. To model this, phenomenon requires the ability to create and relocate a sliding surface which does not allow penetration of projectile nodes/elements into target nodes/elements. The handling of sliding surfaces has been extensively discussed in the literature [4, 16, 48, 53, 98] and can be treated with impenetrability conditions using a master-slave nodes concept [16]. Failed elements along the sliding path may be redefined to have mass but no stress sustaining capability thus allowing the projectile to follow any newly created paths [4].

A prevalent result of ordnance velocity impact in concrete targets is the creation of fragments due to the cratering and spalling failure modes. These fragments may be ejected at considerable velocity. They may be of great importance in the analysis for two reasons. They may cause damage themselves to surrounding structures which may be significant. The fragmentation due to spallation may also be crucial as the loss of material off the distal face of the target can influence the ability if the projectile to completely perforate the target. Finite element solutions of concrete impact have largely ignored this question of fragmentation.

There are examples of attempts to numerically solve concrete impact problems found in the literature. One of these analyses was conducted by Johnson, Stryk, and Nixon [42]. In this problem, the penetration of a semi-infinite concrete target by a non-deformable steel projectile is solved in 2 and 3-Dimensions using 3-node triangular planar and axisymmetric finite elements shown in Figure 1.13. The only failure mode considered is termed "erosion" which creates a tunnel for the projectile by treating elements stressed beyond a limit to be non-stress sustaining lumped nodal masses. A finite element solution which uses a different method of creating a path for the projectile is used as the baseline. The baseline program uses a simple radial expansion of the material around the projectile to model the "tunneling" type of penetration. This second method is similar to the approach considered in Luk and Forrestal [59] which used an analytical method.

The two finite element processes give close results. Part of the final target configuration results are reproduced in Figure 1.13. Quantitatively, an 11% greater

depth of penetration was found for the "eroding" target. The main advantage cited for the "eroding" model of penetration is the use of only 18% of the CPU time of the "tunneling" model. This is due to the fact the eroding process removes highly deformed elements from controlling the time integration step size whereas the tunneling leaves these greatly compressed elements in the calculations.

Another finite element solution for concrete impact was reported by Heider [31]. This work used a 3-D finite element model to simulate the impact of a kinetic energy projectile into a target with the desired results being a failure analysis (maximum allowable strain) of the penetrator. The penetrators were in the lower limits of the ordnance velocity range (500-600 m/s). The concrete model used does not allow failure of the concrete but creates a path for the penetrator by releasing target nodes at the axis of symmetry if the target node enters a defined "impact zone." It did not allow for cratering or spalling and could, thus, be considered a conservative model for determination of penetrator failure.

Several of the finite element solutions for concrete impact deal with sub-ordnance velocities [23, 62] and do not represent the wave effects critical to the ordnance velocity problem. Examples which involve the ordnance velocity impact of metal targets are also shown. Although metal targets are much simpler to analyse, they are included to show capabilities in finite element codes which would be desirable to implement in concrete impact applications.

One such example is found in Zukas [98] involving the hypervelocity impact (5.182 km/sec) of a nylon sphere (9.53 mm diameter) against an armor-steel target (12.7 mm

thick). The results, shown schematically in Figure 1.14, show the ability of finite elements to accurately represent the actual processes involved (cratering and spalling) with the dimensions of the crater diameter and depth, spall thickness and length, and other dimensions nearly duplicating the experimental results. The CDC 6600 time used for such a problem is around 12 hours with the Lagrangian code also requiring user input during the run to rezone the deformed mesh.

Another example of metal plate perforation was given by Kimsey [48]. The interesting aspects of this model are the ability to replicate complete perforation of the plate and terminal ballistics of the projectile as shown in Figure 1.15.

As shown above, the numerical studies of impact/penetration problems for metal targets have the ability to model the detailed processes in the impact. Research is needed to extend similar solution capability to concrete impact.

1.4 Conclusions

Ballistic impact analysis, though studied for centuries, remains in its infancy. The processes involved during the impact/penetration of targets at ordnance velocities are complex and involve both wave induced and contact induced mechanisms. The impact/penetration of concrete has received much attention but mainly through the use of empirical studies. These studies are useful in practice as long as they are applied within the narrow ranges for which the experiments are performed. The simplified analytical studies have the ability to handle a greater range of problems. However, this advantage is offset by the simplifications required in the processes in order to constrain

the equations to manageable proportions.

Numerical methods such as the finite element method are the most likely to be able to predict response in ordnance velocity impact. The use of general continuum mechanics formulations allows a broader range of application. The discretization of the continuum and the use of efficient solution algorithms should allow more realistic processes to be modeled.

Of the three general classifications of concrete target response (cratering, tunneling, and spalling), cratering and spalling involve fragmenting with tunneling involving it to a lesser degree. Thus, a truly accurate finite element solution to the concrete impact problem is not possible until these phenomena can be properly modeled.

The finite element method assumes continuity between elements. The finite block method and distinct element method primarily treat contacts between blocks and no initial tension between blocks. Thus, the present finite element method is suited for the stress analysis at the earlier stages of the impact before fragmentation and the discrete block methods show more capability in the later stages after the fragmenting has occurred. What is required is a hybrid technique which utilizes finite element mesh continuity until fracture with the trajectory of each individual fragmented element being traced after failure by a discrete approach.

1.5 Research objectives

The goal for this research is to develop and implement finite element algorithms capable of modeling the impact response of concrete targets to ordnance velocity

impact.

A primary objective in modeling impact response is the ability to allow fragmentation of finite elements which is a predominant phenomenon in impact. Fragmentation is first developed for frame and rod elements due to the single-dimensionality of the problem. It is then extended to plane-stress, plane-strain, and axisymmetric elements which are used to model thin and moderately thick concrete targets.

Also involved in the research is the development of an updated geometry finite element formulation to treat the extremely large displacements found in fragmentation. As in the previous algorithm, the updated geometry is first developed for frame elements and then extended to the planar and axisymmetric elements.

Since this research is oriented to the analysis of problems for which little quantitative data is available, it is hoped these newly developed algorithms will reproduce the qualitative results of concrete impact. In order to compare the results to experimental tests and mechanics of behavior, several algorithms developed by other researchers are also incorporated into the code. These include non-linear concrete modeling, projectile penetration, and inter-element penetration. These are intended to more completely simulate the actual phenomena.

Table 1.1 Range of impact response from Zukas (1982)

Velocity	Strain Rate Range	Response
< 50 m/sec	10^0/sec	Mostly Elastic, Some Plastic
50-500 m/sec	10^2/sec	Mostly Plastic
500-1000 m/sec	10^4/sec	Transition to Fluid Behavior
1-3 km/sec	10^5/sec	Mainly Fluid Behavior
3-12 km/sec	10^7/sec	Compressibility Significant
>12 km/sec	10^8/sec	Vaporization of Solids

Table 1.2 Projectile characteristics from Zukas (1982)

Geometry			
Basic shape	Solid rod Sphere Hollow shell Irregular solid	Nose configuration	Cone Ogive Hemisphere Right cirular cylinder
Material			
Density	Lightweight wood, plastics ceramics, aluminum Intermediate steel, copper Heavy lead, tungsten		
Flight characteristics			
Trajectory	Straight (stable) Curved (stable) Tumbling (unstable)	Impact condition	Normal Oblique
Final condition			
Shape	Undeformed Plastically deformed Fractured Shattered	Location	Rebound Partial penetration Perforation

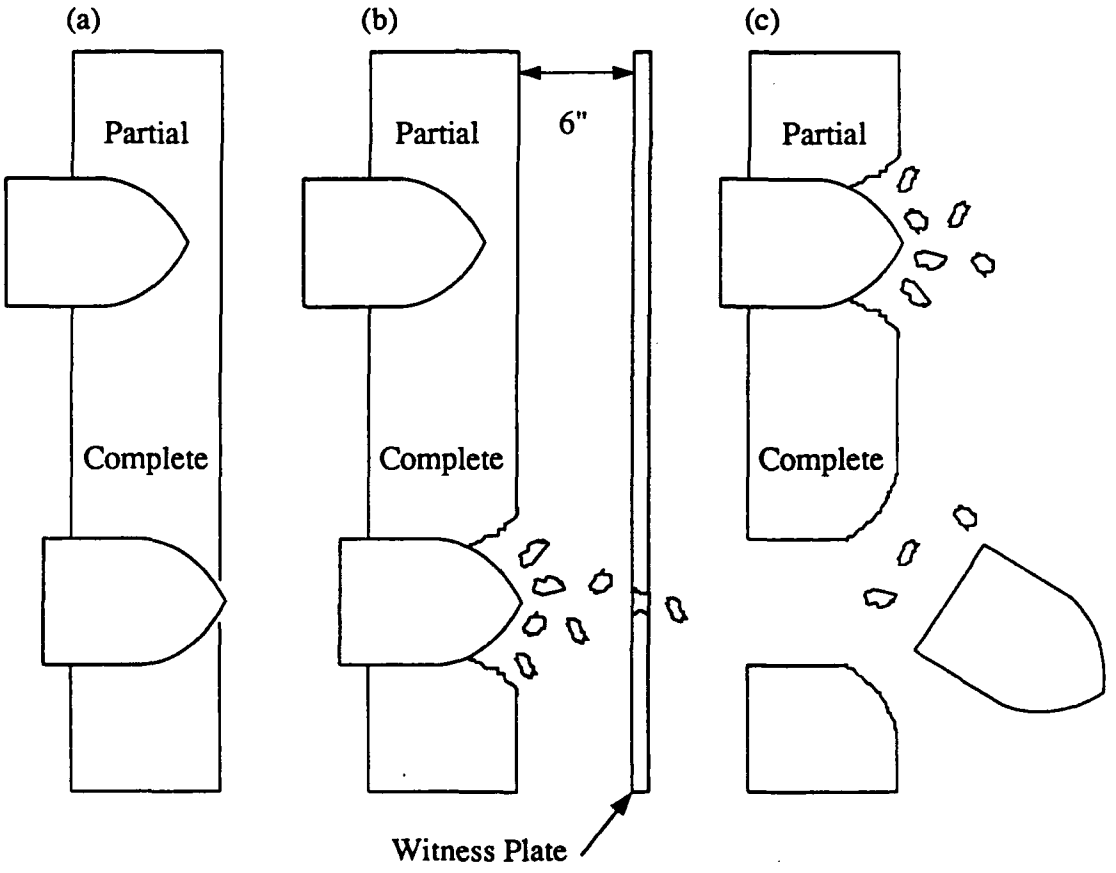

Figure 1.1 Definitions of partial and complete penetration for (a) Army Ballistic Limit, (b) Protection Ballistic Limit, and (c) Navy Ballistic Limit from Backman and Goldsmith (1978)

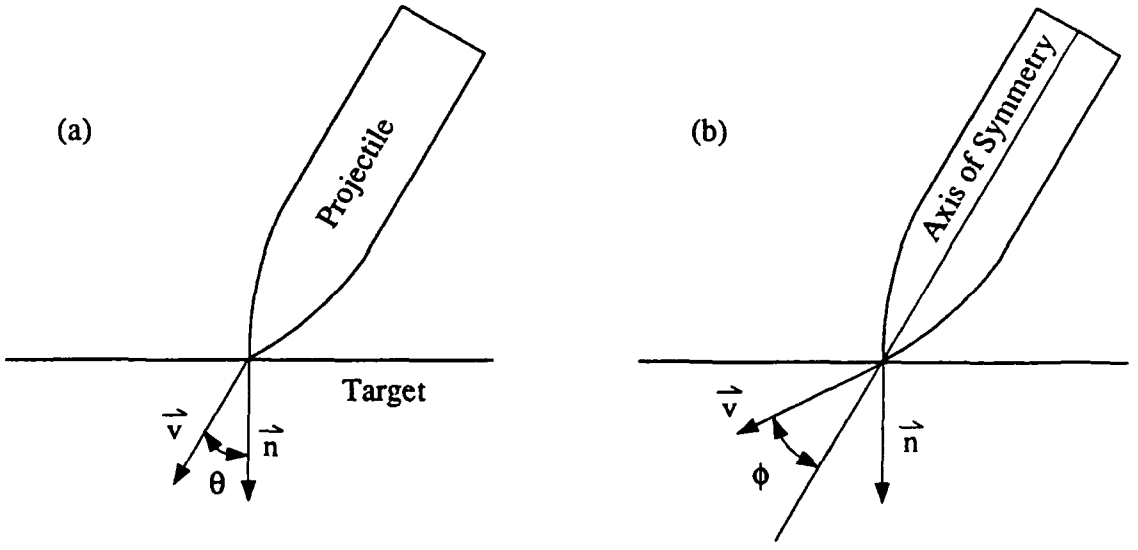

Figure 1.2 (a) Obliquity angleθ and (b) orientation angleϕ

Table 1.3 Relative target penetrability from Backman and Goldsmith (1978)

Target Material	Relative Penetration
Wet Mud	3700
Sand	580
Concrete (2500 psi)	60
Concrete (5000 psi)	42
Aluminum Alloy 2024-T3	2.5
Steel (BHN) 100	1.0

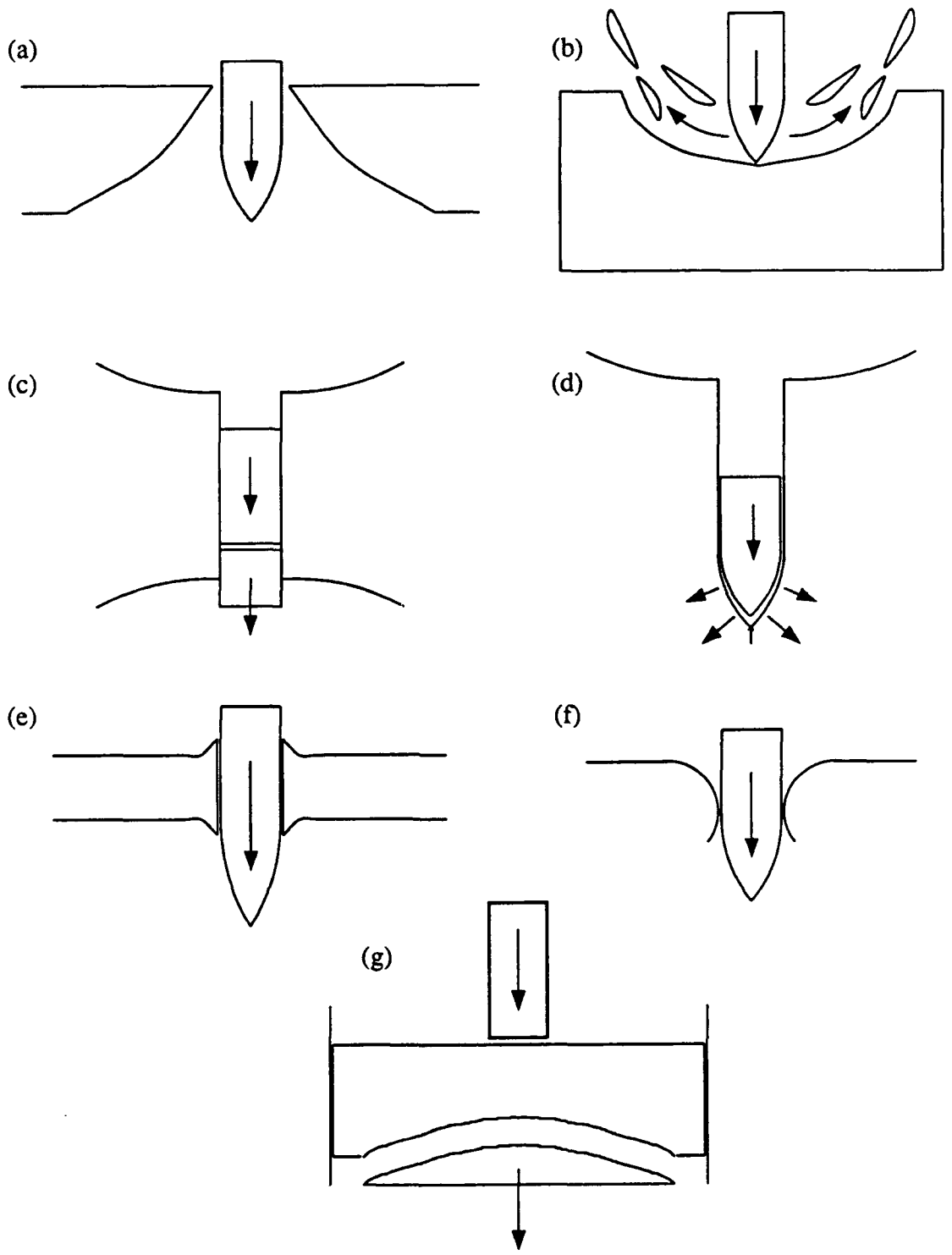

Figure 1.3 Failure modes of (a) punching, (b) cratering, (c) plugging, (d) radial expansion, (e) ductile hole growth, (f) petaling, and (g) spalling

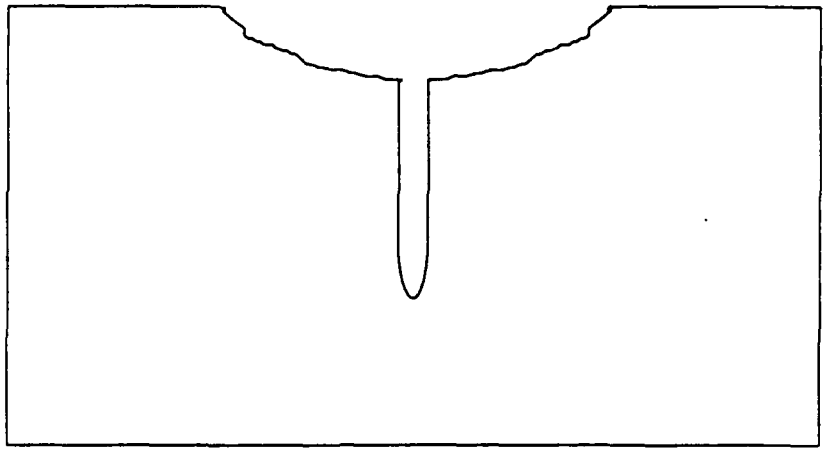

Figure 1.4 Target cross-section with cratering and tunneling from Nash, Zabel, and Wenzel (1985)

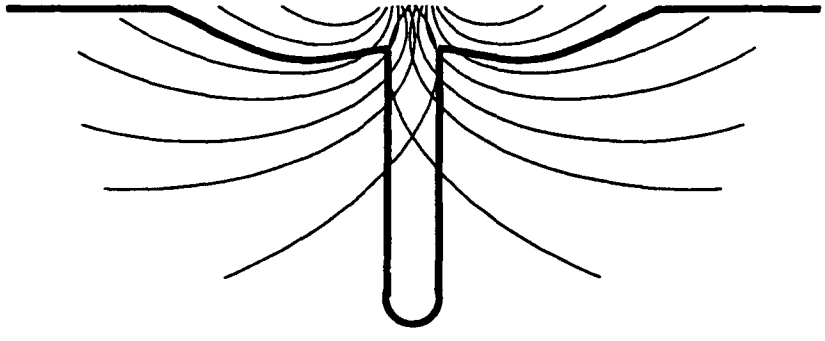

Figure 1.5 Shear spirals on target cross-section from Maurer and Rinehart (1960)

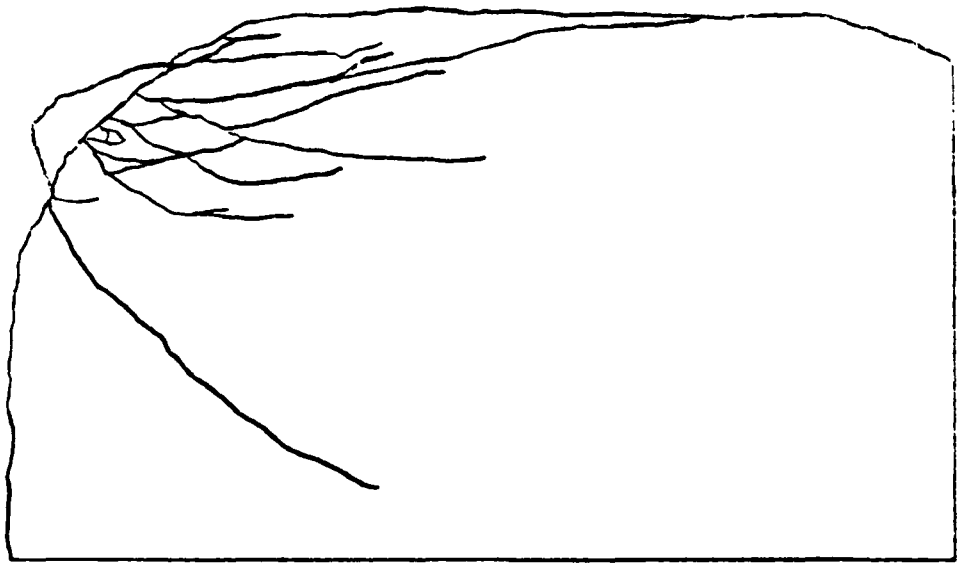

Figure 1.6 Trace of shear spirals from photograph of target cross-section from Bauer and Calder (1969)

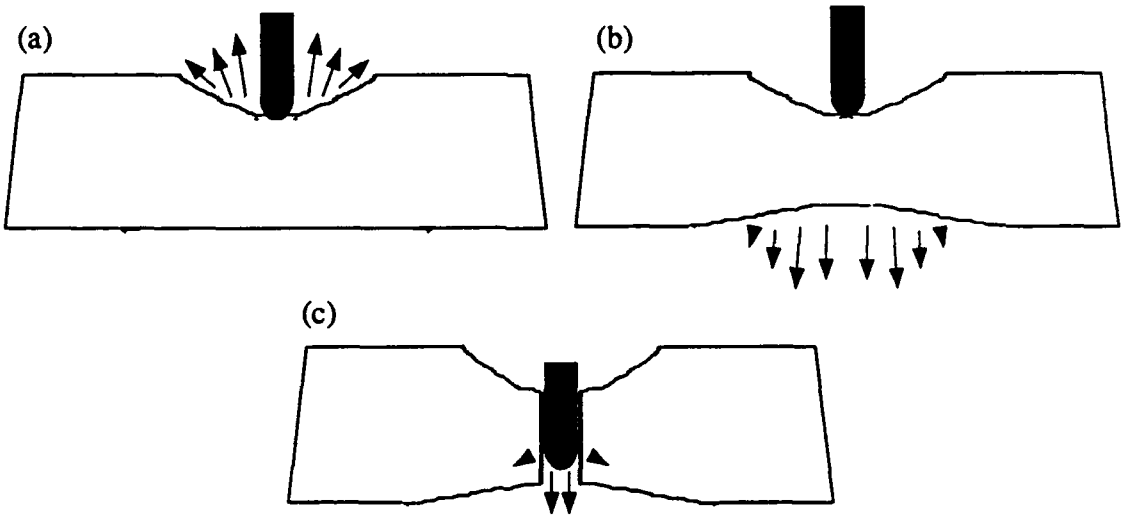

Figure 1.7 Concrete failure modes of (a) cratering, (b) spalling or scabbing, and (c) tunneling

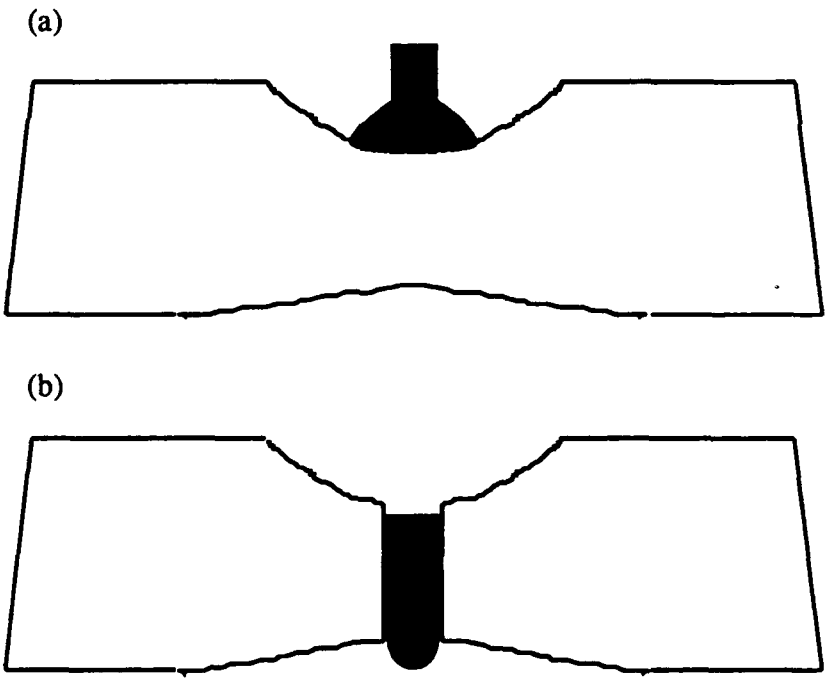

Figure 1.8 Concrete impact by (a) deformable projectile and (b) non-deformable projectile

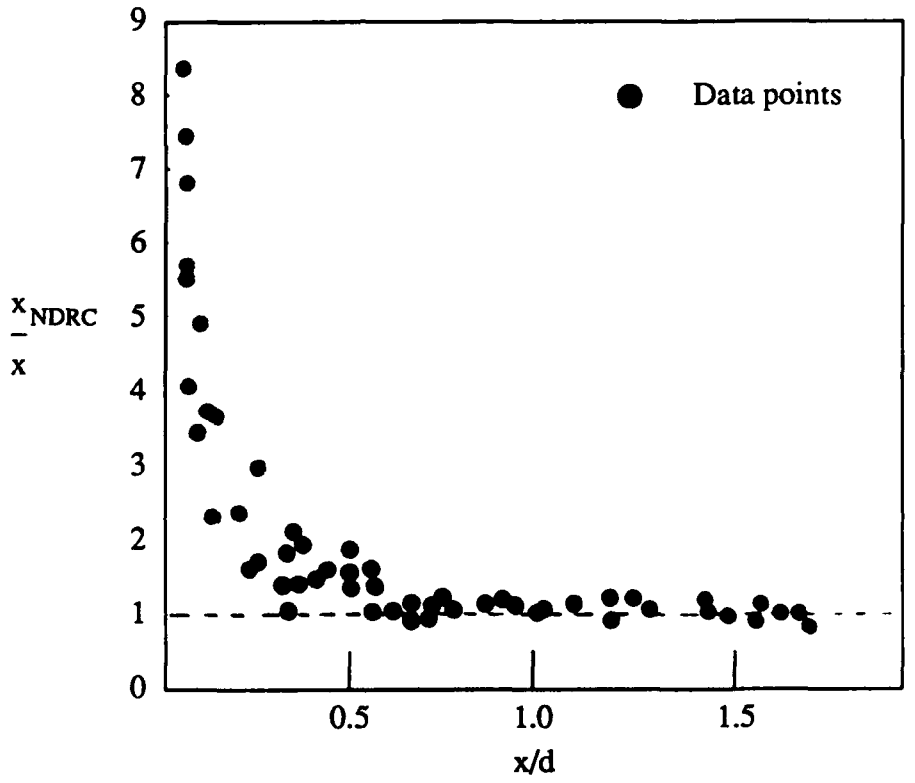

Figure 1.9 NDRC empirical formula compared to experimental data at various x/d ratios from Kennedy (1976)

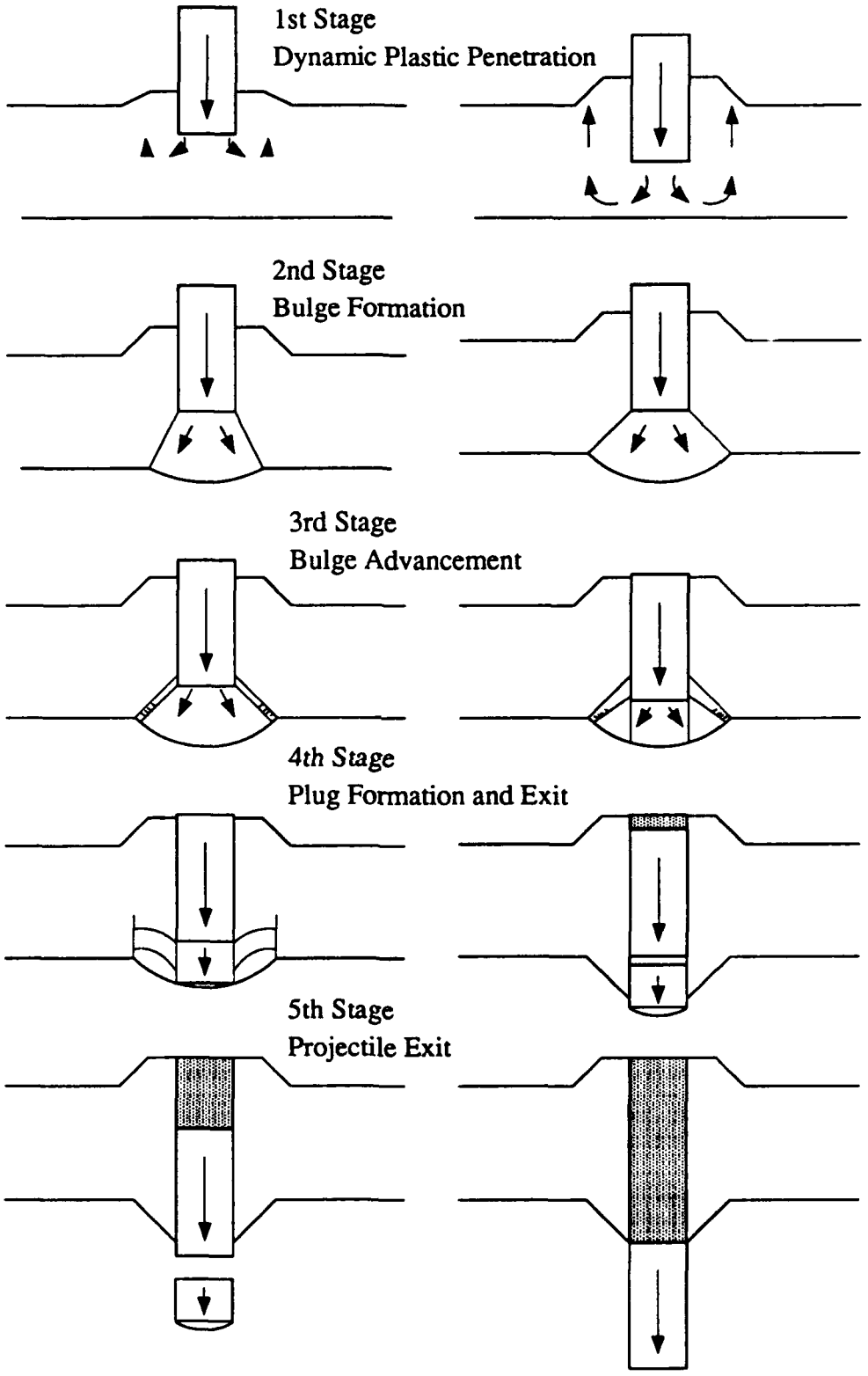

Figure 1.10 5-stage failure process from Ravid and Bodner (1983)

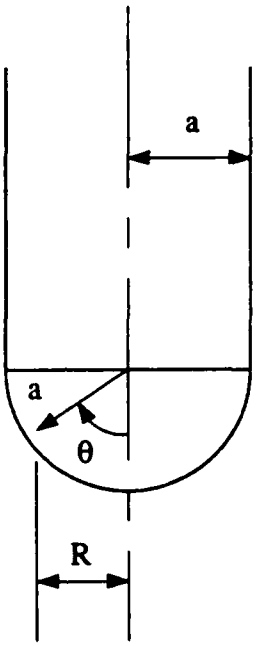

Figure 1.11 Projectile parameters from Luk and Forrestal (1987)
for analytical solution of concrete impact

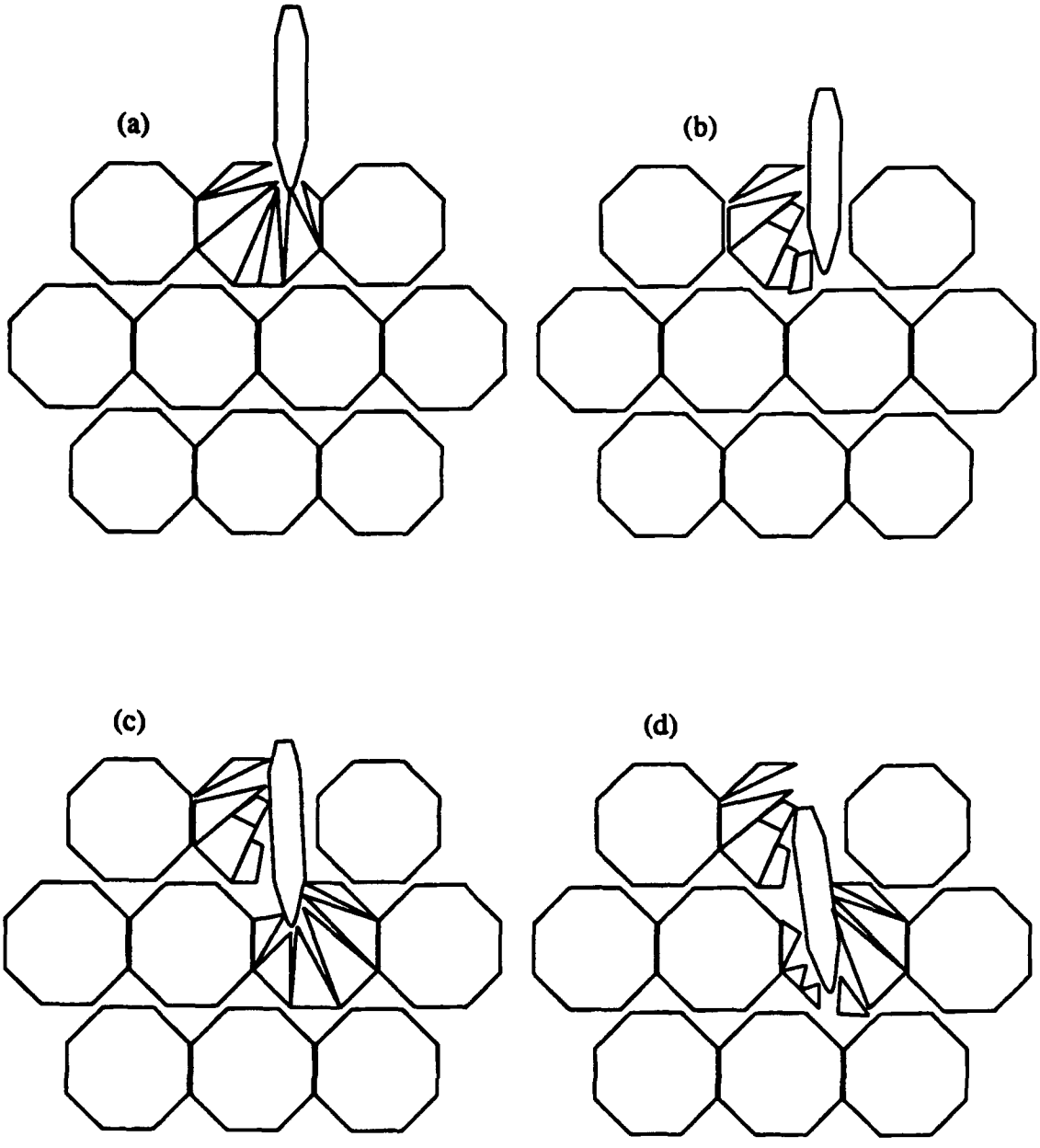

Figure 1.12 Distinct element simulation of 2,000 ft/sec penetrator impact into boulder mesh at (a) 0.5 sec, (b) 1.5 sec, (c) 2.5 sec, and (d) 3.5 sec from Gelman, Nelson, and Ito (1987)

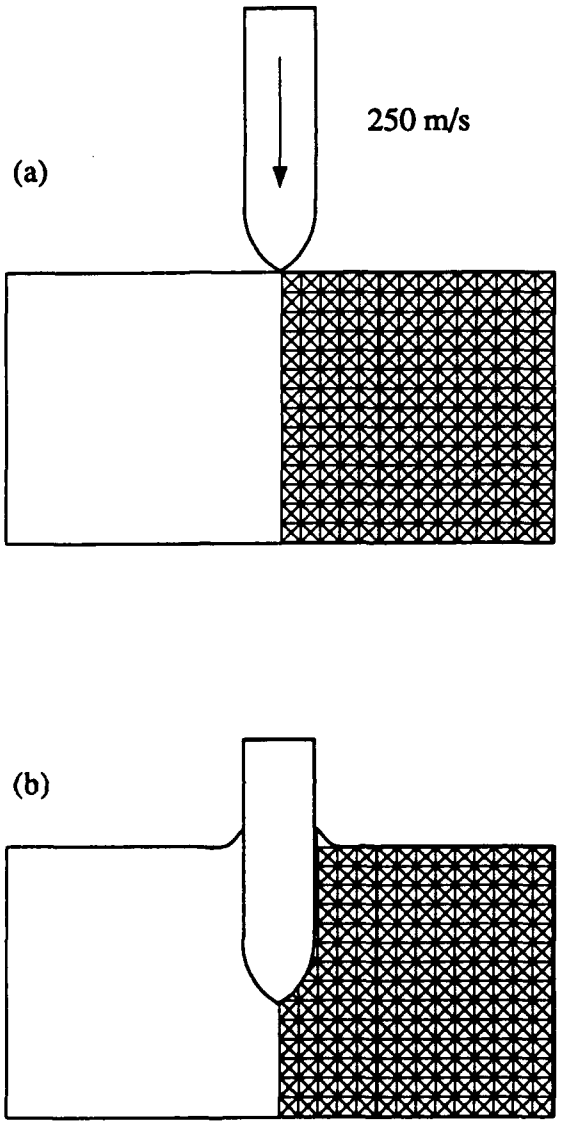

Figure 1.13 Finite element analysis of concrete impact from Johnson, Stryk, and Nixon (1988) showing (a) initial and (b) final configurations

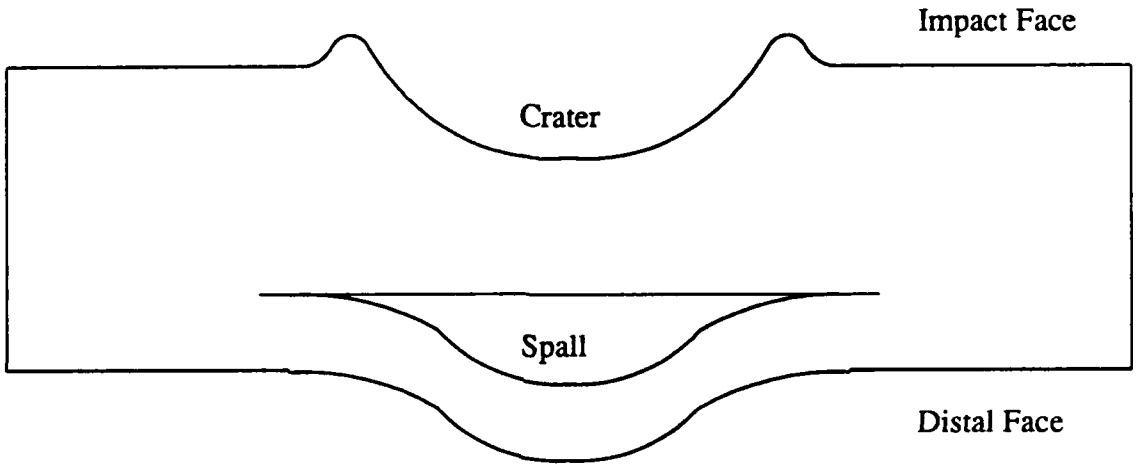

Figure 1.14 Finite element analysis of hypervelocity impact from Zukas (1982)

(a)

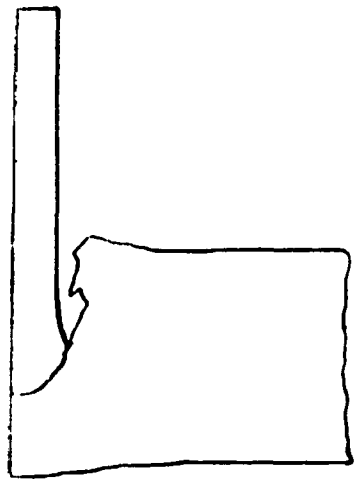

(b)

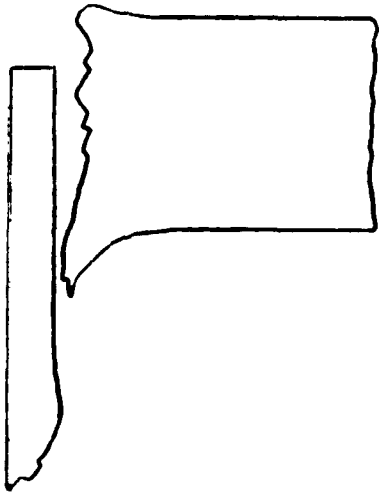

Figure 1.15 Finite element analysis of imapct on a metal plate at (a) 50 μ s and (b) 120 μ s from Kimsey (1983)

Table 1.4 Empirical formulae for use in concrete impact from Brown (1986)

Karr formula for perforation	$(e-a)/d=3.19x/d-0.718(x/d)^2$ $(e-a)/d=1.32+1.24(x/d)$	$x/d<1.35$ $x/d>1.35$ and $3\leq(e/d)\leq18$ a = minium aggregate size of concrete
Ballistic Research Laboratory (BRL) formula	$e/d=7.8Dd^{0.2}(V_s/1000)^{1.33}$ $e/d=[(427Dd^{0.2})/(f'c)^{1/2}](V_s/1000)^{1.33}$	
Modified BRL formula for perforation and the scabbing thickness	$s=2e$	
Ammann and Whitney formula	$x/d=[(282NDd^{0.2})/(f'c)^{1/2}](V_s/1000)^{1.8}$	fragments traveling over 1000 ft/s
CEA-EDF formula for perforation	$V_s=1.43lf'c(e^2/Dd^2)l^{1/2}$	
Bechtel scabbing formula	$S=(15.5/f'c^{1/2})(W^{0.4}V_s^{0.5}/d^{0.2})$	

CHAPTER 2 DISCRETIZATION OF CONTINUA

2.1 Introduction

The basis of numerical analyses is the discretization of a continuum into a finite number of volumes, points, etc. The method used in this discretizing depends largely on the continuum, the type of problem being solved, and, to some extent, the preference of the user. The problem of solid impact requires the discretization of both time and space due to the inherent dynamic nature of the analysis.

As shown in Chapter 1, there is extensive research into which numerical techniques are best suited for the study of solid impact. In this research, the finite difference method is used for discretization of time and the finite element method is used for discretization of space.

2.2 Explicit time integration

There are two broad categories of methods used in direct time integration of structural problems. The explicit methods are conditionally stable depending on the chosen time step but do not require the solution of a system of equations when used with lumped nodal mass matrices. The implicit methods do not, in general, have these stability problems but are computationally more complex as they do form a system of

equations and may also require iterative techniques. There is extensive literature on the strengths and weaknesses of both methods with explicit time integration using lumped nodal masses being favored in transient dynamic problems such as impact [14, 16, 26, 46, 47, 60, 72, 98].

The time integration technique used in the current research is the central-difference explicit method which extrapolates the displacement at the time step $t_{t+\Delta t}$ by using displacements, velocities, etc., from previous time steps [88]. Using the variables defined in Figure 2.1, the acceleration of a point at time i, $\ddot{u}_i$, is given by

$$\ddot{u}_i = \frac{1}{\Delta t^2}[u_{i-\Delta t} - 2u_i + u_{i+\Delta t}] \tag{2.1}$$

and the velocity at the same time, $\dot{u}_i$, by

$$\dot{u}_i = \frac{1}{2\Delta t}[u_{i+\Delta t} - u_{i-\Delta t}] \tag{2.2}$$

Assume a multi-degree of freedom system is expressed by the equation

$$\underline{M}\,\ddot{\underline{U}} + \underline{C}\,\dot{\underline{U}} + \underline{K}\,\underline{U} = \underline{F}^{ext} \tag{2.3}$$

where $\underline{M}$, $\underline{C}$, $\underline{K}$, and $\underline{U}$ are the mass, damping, stiffness, and displacement matrices for the system, respectively. Equation 2.3 can be rearranged to give

$$\ddot{\underline{U}} = \underline{M}^{-1}(\underline{F}^{ext} - \underline{C}\,\dot{\underline{U}} - \underline{K}\,\underline{U}) \tag{2.4}$$

The use of a diagonal lumped nodal mass matrix allows $\underline{M}^{-1}$ to be the reciprocal of the diagonal term. By solving an undamped system and denoting the stiffness term, $\underline{K}\,\underline{U}$, as the internal force at the node, $\underline{f}^{int}$, Equation 2.4 is effectively decoupled becoming

$$\ddot{u}_j = \frac{1}{m_j}(f_j^{ext} - f_j^{int}) \tag{2.5}$$

where m, u, f^{ext}, and f^{int} are the mass, displacement, external force, and internal force

of node j. Dropping the subscript "j" and substituting Equation 2.1 into Equation 2.5 give

$$\frac{1}{\Delta t^2}[u_{i-\Delta t} - 2u_i + u_{i+\Delta t}] = \frac{1}{m}(f^{ext} - f^{int}) \tag{2.6}$$

which, when rearranged, gives the displacement at time i+Δt as

$$u_{i+\Delta t} = \frac{2\,\Delta t^2}{m}(f^{ext} - f^{int}) + 2u_i - u_{i-\Delta t} \tag{2.7}$$

Therefore, the displacements from the current time step and previous time step along with the internal and external forces at the current time step are used to extrapolate the displacement at the next time step. This procedure is performed for each node and then used throughout the time interval of the problem. The time algorithm is started by first calculating a pseudo-displacement at time 0–Δt. This is done using the initial displacement, u_0, velocity, $\dot{u}_0$, and acceleration, $\ddot{u}_0$, of the problem in the equation

$$u_{-\Delta t} = u_0 - \Delta t\dot{u}_0 + \frac{\Delta t^2}{2}\ddot{u}_0 \tag{2.8}$$

As previously discussed, the explicit time integration techniques are conditionally stable. The critical time step, Δt_{cr}, is defined by the equation

$$\Delta t_{cr} = \frac{2}{\omega_n} = \frac{T_n}{\pi} \tag{2.9}$$

with ω_n the highest frequency present in the mesh and T_n the lowest period found in the mesh [88].

2.3 Finite element formulation

The discretization of the space continuum is accomplished using the finite element method. This method divides the structure being analysed into areas called elements.

Each element has a discrete number of points called nodes. The values of the field variables (e.g. displacement, velocity, etc.) at these nodes are used to interpolate the values throughout the element to which the nodes are connected. The elements form a continuous structure, or mesh, by sharing nodes with other elements.

In a "conventional" finite element analysis, the stiffness and mass matrices for each element are calculated and then combined, or assembled, into the structure stiffness and mass matrices which are the same as those found in Equation 2.3. With the use of the explicit time integration discussed above and lumped nodal masses, the assemblage of stiffness matrices is not necessary which eliminates the need to solve a system of equations. Instead, the nodal masses and the internal nodal forces are calculated at the element level and then assembled in a vector form for the terms found in Equation 2.5.

2.3.1 Nodal masses

There are various techniques of modeling the inertial resistance of a structure in dynamic analyses. One method is to use the same shape functions used in interpolating the field variables through the element to calculate the element mass matrix. This type of matrix is called a consistent mass matrix and is given by

$$\underset{\sim}{M}_e = \int_V \underset{\sim}{N}^t \underset{\sim}{N} \rho \, dV \tag{2.10}$$

The consistent mass matrix is not generally diagonal and therefore does not lend itself well to explicit time integration.

The type of mass matrix commonly used in conjunction with explicit time integration is the lumped nodal mass matrix. There are various means of lumping the

masses to the nodes. The method used in the present study is given by the equation

$$m_j^e = \int_{V_e} N_j \, \rho \, dV_e \tag{2.11}$$

where m_j^e is the mass of the jth node of element e, ρ is the mass density of the material, and N_j is the j^{th} shape function (Zienkiewicz and Taylor [96]). The total mass of node j is then found by traditional assemblage techniques of the elements. As the present study uses three element types (2-D frame, plane-stress/strain, and axisymmetric) the equations used in the three different mass matrices will be discussed.

The frame element in the study is developed in two dimensions with the translational masses calculated in the X-Y plane. The masses, m_{xt} and m_{yt}, are lumped at each end of the element and are given by

$$m_{xt} = m_{yt} = \frac{\rho A l}{2} \tag{2.12}$$

with A being the element cross-sectional area and l being the element length. The rotational inertia, m_{zr}, is only needed about the Z axis and is given by (Saha and Ting [75])

$$m_{zr} = \frac{\rho A l^3}{24} + \frac{\rho l I_{zz}}{2} \tag{2.13}$$

The restricting of the frame element to two dimensions simplifies the treatment of the rotational equations of motion as there is no need to calculate the directions and values of the principal rotational inertias. As the translational masses are the same in both directions, this added step is not necessary.

As the plane-stress/strain element and the axisymmetric element do not include rotational degrees-of-freedom, only the translational masses are calculated. Both types

of elements have four nodes per element and are formulated using isoparametric transformations. The mass for the j^{th} (j=1,2,3,4) node of element e in a plane-stress/strain element is

$$m_j^e = b\,\rho \int_{-1}^{+1}\int_{-1}^{+1} \underset{\sim}{N}_j(s,t)\,|J|\,dsdt \tag{2.14}$$

with b being the element thickness, $\underset{\sim}{N}_j(s,t)$ the j^{th} isoparametric shape function, |J| the determinant of the jacobian, and s and t the isoparametric coordinates. The mass of the same node in an axisymmetric element is given by

$$m_j^e = 2\pi\,\rho \int_{-1}^{+1}\int_{-1}^{+1} \underset{\sim}{N}_j(s,t)\,r(s,t)\,|J|\,dsdt \tag{2.15}$$

with r(s,t) being the radius of the integration point in the isoparametric coordinates. The integration is done using Guassian four-point numerical integration.

2.3.2 Internal nodal forces

The second purpose of the finite element discretization is to calculate the internal nodal forces, f_j^{int}, found in Equation 2.5. The current study calculates the internal forces in the frame elements assuming linear-elastic, small deformation beam theory to calculate the internal moments and an uncoupled linear force-displacement relationship for the axial forces. The frame element may undergo large displacements causing a non-linear displacement-deformation relationship (sometimes referred to as geometrically non-linear) which is treated with a co-rotational formulation. The plane-stress/strain element also assumes a linear elastic material and incorporates the co-rotational formulation. The axisymmetric element includes a non-linear material model

but does not use co-rotational coordinates in its formulation.

2.3.2.1 Co-rotational formulation

Formulations for the finite element analysis of structures undergoing large deflection have been proposed for both static and dynamic loadings [9, 10, 38, 46, 47]. One which is widely used is the co-rotational formulation. This method uses the approach that it is easier to treat large deflection of structures by separating the rigid-body (or approximate rigid-body) displacements of the i^{th} element, $\underline{d}_i^r$, from the total displacements, $\underline{d}_i$, of the element leaving only the deformation displacements , $\underline{d}_i^d$, as

$$\underline{d}_i^d = \underline{d}_i - \underline{d}_i^r \tag{2.16}$$

allowing the application of infinitesimal strain-deformation relations to the material properties. The separation is accomplished by using convected, or co-rotational, coordinate systems [61, 68].

Earlier formulations based on convected coordinates were introduced by Argyris, et. al. [5] for the static analysis of large displacement but small deformation problems using an incremental approach. Transient dynamic analyses were proposed by Belytschko and Hsieh [14] using a total formulation. This latter formulation has been proven effective in dynamic analyses with moderate rotations. A number of references [15, 60] and general purpose computer codes, such as DYPLAS and WHAM [13], STRAW [44], and DYNA3D [30] have been reported in recent years.

The co-rotational approach uses three stages of displacement history, shown in Figure 2.2, which are: 1) The original geometry, $\underline{X}$, at time=0, 2) The current deformed

geometry, $\underset{\sim}{x}$, at time=t, and 3) The convected geometry, $\hat{\underset{\sim}{x}}$, at the same time as in stage 2. The approach is based on the premise that each element has its own local, or convected, coordinate system, $\hat{\underset{\sim}{x}}$, which rotates and translates with the element throughout its load-displacement history [61]. This rigid-body motion is represented by the Q matrix shown in Figure 2.2. Therefore, the transformation of the global displacements of the element into these convected coordinates creates a "pure deformation" displacement field

$$\hat{\underset{\sim}{d}}_i^d = \underset{\sim}{Q}_i^T \underset{\sim}{d}_i \tag{2.17}$$

Separating the rigid body motion from the displacement terms allows the elimination of higher order terms in the element kinematic functions which account for geometry induced non-linearity which is now treated by the previously mentioned transformation.

The element displacement vector, $\underset{\sim}{u}$, may be represented by using the nodal displacement vector, $\underset{\sim}{d}_i$, and the element displacement shape function, $\underset{\sim}{N}$, allowing:

$$\underset{\sim}{u} = \underset{\sim}{N}\, \underset{\sim}{d}_i \tag{2.18}$$

As only the deformation displacement contributes to internal force and using Equation 2.18, the shape function may be simplified to $\underset{\sim}{N}'$ giving

$$\hat{\underset{\sim}{u}}^d = \underset{\sim}{N}' \hat{\underset{\sim}{d}}_i^d \tag{2.19}$$

where $\hat{\underset{\sim}{u}}^d$ is the vector of element deformation displacements. As the rigid body displacement has effectively been removed from the finite element formulation and assuming small deformation, the strain in the element, $\hat{\underset{\sim}{\varepsilon}}$, is given by

$$\hat{\underset{\sim}{\varepsilon}} = \hat{\underset{\sim}{D}}_f \hat{\underset{\sim}{u}} \tag{2.20}$$

with $\hat{\underset{\sim}{D}}_f$ defined for a plane stress or plane strain problem by

$$\hat{\underline{D}}_f = \begin{bmatrix} \frac{\partial(\,)}{\partial \hat{x}} & 0 \\ 0 & \frac{\partial(\,)}{\partial \hat{y}} \\ \frac{\partial(\,)}{\partial \hat{y}} & \frac{\partial(\,)}{\partial \hat{x}} \end{bmatrix} \tag{2.21}$$

Using Equation 2.19, Equation 2.20 becomes

$$\hat{\underline{\varepsilon}} = \hat{\underline{B}}\ \hat{\underline{d}}_i^d \tag{2.22}$$

where $\hat{\underline{B}}$ is the matrix of shape function derivatives given by

$$\hat{\underline{B}} = \hat{\underline{D}}_f\ \underline{N}'$$

The system can be put into equilibrium using a virtual work formulation where

$$\delta W^{int} = \delta W^{ext} \tag{2.23}$$

The term on the left of Equation 2.23 is the internal virtual work and can be represented by

$$\delta W^{int} = \sum_{i=1}^{\#el} \int_{V_i} \delta\hat{\underline{\varepsilon}}^T \hat{\underline{\sigma}}\ dV \tag{2.24}$$

where $\hat{\underline{\sigma}}$ is the stress in the element. Using Equations 2.18, 2.19, and 2.22 in Equation 2.24 gives

$$\delta W^{int} = \sum_{i=1}^{\#el} (\delta\underline{d}_i^d)^T\ (\underline{Q}_i) \int_{V_i} \hat{\underline{B}}^T \hat{\underline{\sigma}}\ dV \tag{2.25}$$

The term on the right of Equation 2.23 is a combination of external virtual work. Using d'Alembert's principle to account for inertial forces gives

$$\delta W^{ext} = \sum_{i=1}^{\#el} \left[\delta\underline{d}_i^T \underline{f}_i^{ext} - \delta\underline{d}_i^T \int_{V_i} \rho_i \underline{N}^T \underline{N}' \ddot{\underline{d}}_i\ dV \right] \tag{2.26}$$

where $\underline{f}_i^{ext}$ is the vector of external forces in global coordinates, ρ is the mass density, and $\ddot{\underline{d}}_i$ is the acceleration vector. Define

$$\underline{f}_i^{int} = Q_i \int_{V_i} \hat{\underline{B}}^T \hat{\underline{\sigma}} \, dV \tag{2.27}$$

and

$$\underline{m}_i = \int_{V_i} \rho_i \underline{N}^T \underline{N}' \, dV \tag{2.28}$$

Combining Equations 2.24-2.28 results in

$$\delta \underline{d}^T \sum_{i=1}^{\#el} \left[\underline{m}_i \ddot{\underline{d}} + (\underline{f}_i^{int} - \underline{f}_i^{ext}) \right] = 0 \tag{2.29}$$

where $\underline{d}$ is the global displacement matrix. As $\delta \underline{d}_i^T$ are arbitrary,

$$\sum_{i=1}^{\#el} \left[\underline{m}_i \ddot{\underline{d}} + (\underline{f}_i^{int} - \underline{f}_i^{ext}) \right] = \underline{0} \tag{2.30}$$

or in an assembled global form

$$\underline{M} \ddot{\underline{d}} + \underline{F}^{int} = \underline{F}^{ext} \tag{2.31}$$

If a lumped nodal mass matrix is used, the acceleration vector, $\ddot{\underline{d}}$, is given by

$$\ddot{d}_j = \frac{1}{M_j} (F_j^{ext} - F_j^{int}) \, , \; j=1,2,3,...,n \tag{2.32}$$

where $\frac{1}{M_j}$ are the reciprocals of the diagonal terms of $\underline{M}$ and "n" the total number of degrees of freedom.

The co-rotational formulation in combination with explicit time integration has been proven very effective in applications involving transient dynamic problems. The formulation, however, becomes ineffective when (see Equation 2.16) $\underline{d}_i^r$ dominates $\underline{d}_i^d$ by such a magnitude $\underline{d}_i^d$ becomes numerically insignificant.

2.3.2.2 Planar-frame element forces

The co-rotational approach in calculating internal forces for a planar-frame element uses the geometries shown in Figure 2.3. The deformation displacements necessary for the calculation are the rotations at the nodes, $\hat{\theta}_{1z}$ and $\hat{\theta}_{2z}$, and the change in length of the element, $l - l_o$. These internal force calculations are based on small deformation assumptions.

To calculate the two angles of rotational deformation, the rigid body rotation of the element, ψ_z, must be calculated. One method of doing this is to assign the unit directional vector $\underline{e}_o$ to the initial geometry and $\underline{e}$ to the current geometry. These vectors are defined by nodes 1 and 2 of the respective geometries. Using the cross product of these vectors gives the rigid body rotation as

$$\psi_z = \sin^{-1}\left[\left| \underline{e}_o \times \underline{e} \right| \right] \tag{2.33}$$

Subtracting ψ_z from the total local end rotations θ_{1z} and θ_{2z}, gives the frame end slopes in the convected coordinates, $\hat{\underline{x}}$

$$\hat{\theta}_{1z} = \theta_{1z} - \psi_z \tag{2.34a}$$

$$\hat{\theta}_{2z} = \theta_{2z} - \psi_z \tag{2.34b}$$

shown in Figure 2.3.

The internal nodal forces can be calculated by using the direct-stiffness equations based on small deformation assumptions thus allowing superposition of simple beam theory and axial force-displacement relationship. The end moments are :

$$m_{1z} = \frac{2EI_z}{l}(2\hat{\theta}_{1z} + \hat{\theta}_{2z}) \tag{2.35a}$$

$$m_{2z} = \frac{2EI_z}{l}(\hat{\theta}_{1z} + 2\hat{\theta}_{2z}) \tag{2.35b}$$

where E = Young's Modulus of Elasticity, I_z = Second Moment of Inertia of the Section about z-axis, and l = Element Length The end moments are then used to calculate the end shear forces, f_{1y} and f_{2y}, by enforcing element static equilibrium giving:

$$f_{1y} = \frac{(m_{1z}+m_{2z})}{l} \tag{2.36a}$$

$$f_{2y} = -f_{1y} \tag{2.36b}$$

The axial forces, f_{1x} and f_{2x}, can be calculated by using the current element length and the initial element length in a force displacement relation and element equilibrium giving:

$$f_{1x} = \frac{-EA}{l}(l-l_o) \tag{2.37a}$$

$$f_{2x} = -f_{1x} \tag{2.37b}$$

where A is the element cross-sectional area.

These local forces, $\underset{\sim}{f}^{int}$, (shown in Figure 2.4) can then be transformed and the global forces, $\underset{\sim}{F}^{int}$, are given by:

$$\underset{\sim}{F}^{int} = \underset{\sim}{T}_d^T \underset{\sim}{f}^{int} \tag{2.38}$$

where $\underset{\sim}{T}_d$ is the transformation matrix between the current convected coordinates to the global coordinates.

2.3.2.3 Plane-stress/strain element forces

The plane-stress/strain element used in the current study is a four-node isoparametric as shown in Figure 2.5. The co-rotational formulation uses the global nodal coordinates and displacements shown in Figure 2.6 to calculate the deformation displacements using the same basis as found in the frame element.

The co-rotational approach for the four-node isoparametric element is an extension of the approach used on the three-node triangular element developed by Belytschko and Hsieh [14]. The (approximate) rigid body rotation, θ, shown in Figure 2.7 is calculated by using the nodal coordinates, x and y, and displacements, u and v, of nodes 1, 2, and 4 giving

$$\theta = \arctan\left[\frac{y_4 v_2 - y_2 v_4 + x_4 u_2 - x_2 u_4}{4A + y_4 u_2 - y_2 u_4 - x_4 v_2 + x_2 v_4}\right] \tag{2.39}$$

where the nodal coordinates and displacements of nodes 2 and 4 are relative to the coordinates and displacements of node 1 and A is the area of the "pseudo-triangle" formed by nodes 1, 2, and 4. The deformation displacements, u^{def} and v^{def}, are then given by using θ giving

$$\begin{Bmatrix} u_i^{def} \\ v_i^{def} \end{Bmatrix} = \underset{\sim}{a} \begin{Bmatrix} u_i \\ v_i \end{Bmatrix} + (\underset{\sim}{a} - \underset{\sim}{I}) \begin{Bmatrix} x_i \\ y_i \end{Bmatrix} \quad (i=2,3,4) \tag{2.40}$$

with all displacements and coordinates being relative to node 1, $\underset{\sim}{I}$ being the identity matrix, and $\underset{\sim}{a}$ given by

$$\underset{\sim}{a} = \begin{bmatrix} \cos\theta & \sin\theta \\ -\sin\theta & \cos\theta \end{bmatrix} \tag{2.41}$$

The deformation displacements are used to find the internal nodal forces for the element by using a finite element relationship at the element level which gives

$$\underline{f}_e^{int} = \underline{k}_e \, \underline{d}_e^{def} \tag{2.42}$$

where $\underline{d}_e^{def}$ are the deformation displacements given by Equation 2.40 and $\underline{k}_e$ is the element stiffness matrix for a standard 4-node isoparametric planar element. This matrix is defined as

$$\underline{k}_e = b \int_{-1}^{1} \int_{-1}^{1} \underline{B}^T \, \underline{D} \, \underline{B} \, |\underline{J}| \, ds dt \tag{2.43}$$

with b the element thickness, $\underline{B}$ defined earlier by Equation 2.22 and given by

$$\underline{B} = \frac{1}{|\underline{J}|} [\underline{B}_1 \; \underline{B}_2 \; \underline{B}_3 \; \underline{B}_4 \,] \tag{2.44}$$

with $\underline{J}$ being

$$\underline{J} = \begin{bmatrix} x_s & y_s \\ x_t & y_t \end{bmatrix}$$

and $\underline{B}_i$ being

$$\underline{B}_i = \begin{bmatrix} y_t N_{i,s} - y_s N_{i,t} & 0 \\ 0 & x_s N_{i,t} - x_t N_{i,s} \\ x_s N_{i,t} - x_t N_{i,s} & y_t N_{i,s} - y_s N_{i,t} \end{bmatrix}$$

The components of these matrices are defined by

$$N_{i,t} = \frac{\partial N_i}{\partial t} \qquad N_{i,s} = \frac{\partial N_i}{\partial s}$$

$$y_t = \sum_{i=1}^{4} \frac{\partial N_i}{\partial t} y_i \qquad y_s = \sum_{i=1}^{4} \frac{\partial N_i}{\partial s} y_i$$

$$x_t = \sum_{i=1}^{4} \frac{\partial N_i}{\partial t} x_i \qquad x_s = \sum_{i=1}^{4} \frac{\partial N_i}{\partial s} x_i$$

The elastic material properties matrix, $\underline{D}$, is formed to reflect either plane-stress or

plain-strain conditions. The stiffness matrix is calculated using four-point Gaussian numerical integration.

The element forces given in Equation 2.27 are in the convected coordinates. The transformation to global coordinate forces, $\underset{\sim}{f}_e^{gl}$, is accomplished using the $\underset{\sim}{a}$ matrix defined in Equation 2.41 giving

$$\underset{\sim}{f}_e^{int} = \underset{\sim}{A}^T \hat{\underset{\sim}{f}}_e \tag{2.45}$$

with $\underset{\sim}{A}^T$ defined by

$$\underset{\sim}{A}^T = \begin{bmatrix} \underset{\sim}{a}^T & 0 & 0 & 0 \\ 0 & \underset{\sim}{a}^T & 0 & 0 \\ 0 & 0 & \underset{\sim}{a}^T & 0 \\ 0 & 0 & 0 & \underset{\sim}{a}^T \end{bmatrix}$$

2.3.2.4 Axisymmetric element forces

The axisymmetric element used in the study is also a four-node isoparametric element which allows the same approximate development of the internal forces as detailed for the plane-stress/strain element. The use of a non-linear material model dictates some changes as does not including the co-rotational approach in the element formulation.

The element uses the same coordinate system as shown for the planar-element. The internal nodal forces are calculated at the element level as with the planar-frame and planar-membrane elements. The element stiffness matrix, $\underset{\sim}{k}_e$, is not formed as the element forces, f_e^{int}, are calculated using the standard (not co-rotational) form of Equation 2.27 giving

$$\underset{\sim}{f}_e^{int} = \int_{V_i} \underset{\sim}{B}^T \underset{\sim}{\sigma}\, dV \tag{2.46}$$

The $\underset{\sim}{B}$ matrix is of the same general form as shown in Equation 2.44 but with the $\underset{\sim}{B}_i$ sub-matrix now defined for axisymmetric conditions as

$$\underset{\sim}{B}_i = \begin{bmatrix} y_t N_{i,s} - y_s N_{i,t} & 0 \\ 0 & x_s N_{i,t} - x_t N_{i,s} \\ \dfrac{|\underset{\sim}{J}|}{x} & 0 \\ x_s N_{i,t} - x_t N_{i,s} & y_t N_{i,s} - y_s N_{i,t} \end{bmatrix} \tag{2.47}$$

The vector of strains, given by

$$\underset{\sim}{\varepsilon} = \begin{Bmatrix} \varepsilon_x \\ \varepsilon_y \\ \varepsilon_t \\ \varepsilon_{xy} \end{Bmatrix} \tag{2.48}$$

(ε_t is the tangential strain) is calculated by the relationship

$$\underset{\sim}{\varepsilon} = \underset{\sim}{B}\, \underset{\sim}{d}_e \tag{2.49}$$

Determining the stress vector, $\underset{\sim}{\sigma}$, using the strains will be discussed in Chapter 4 which describes the concrete material model.

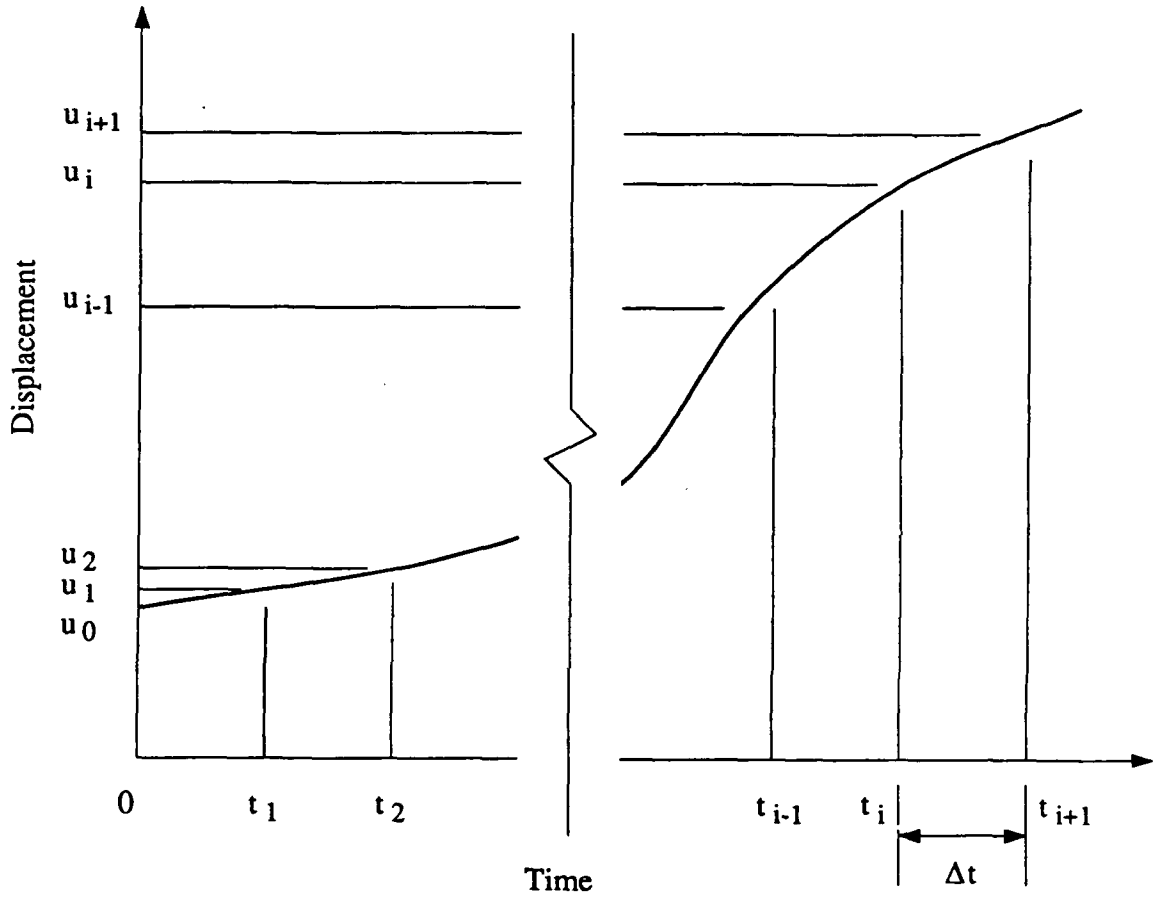

Figure 2.1 Time-displacement curve for use in central-difference time integration from Weaver and Johnston (1987)

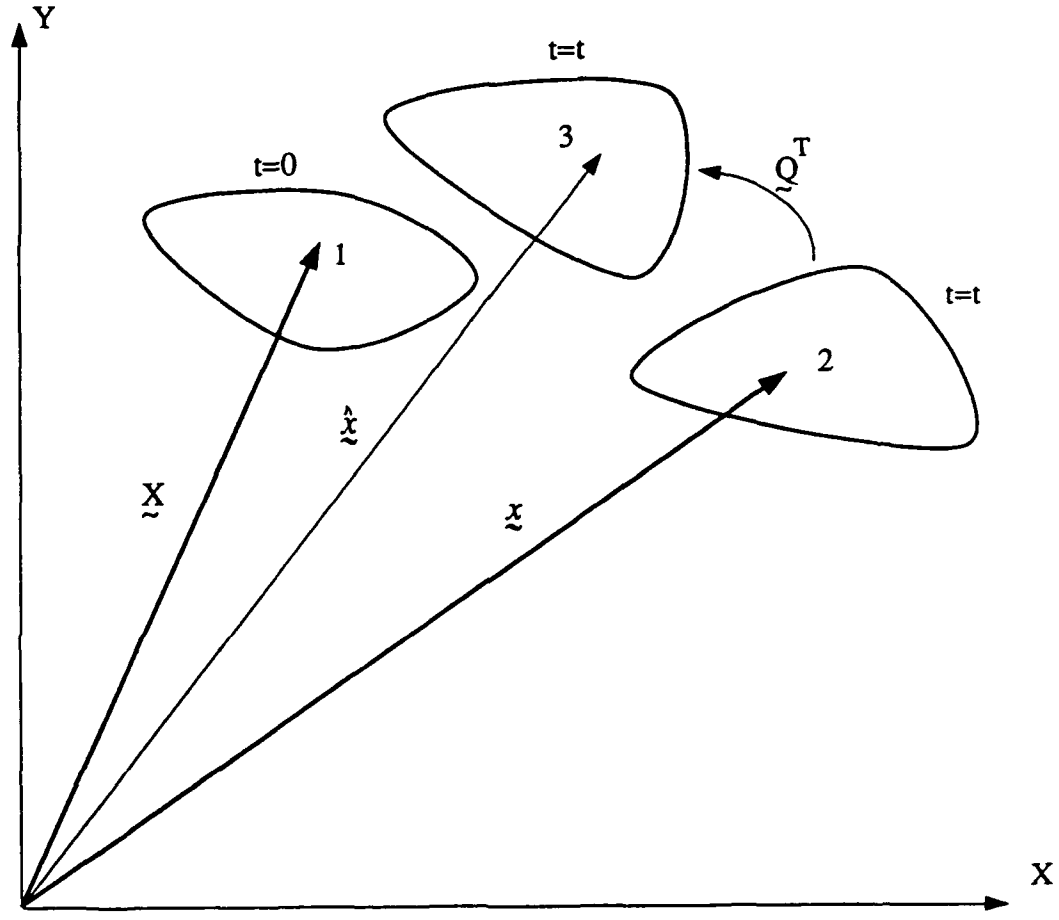

Figure 2.2 Stages of deformation in co-rotational formulation

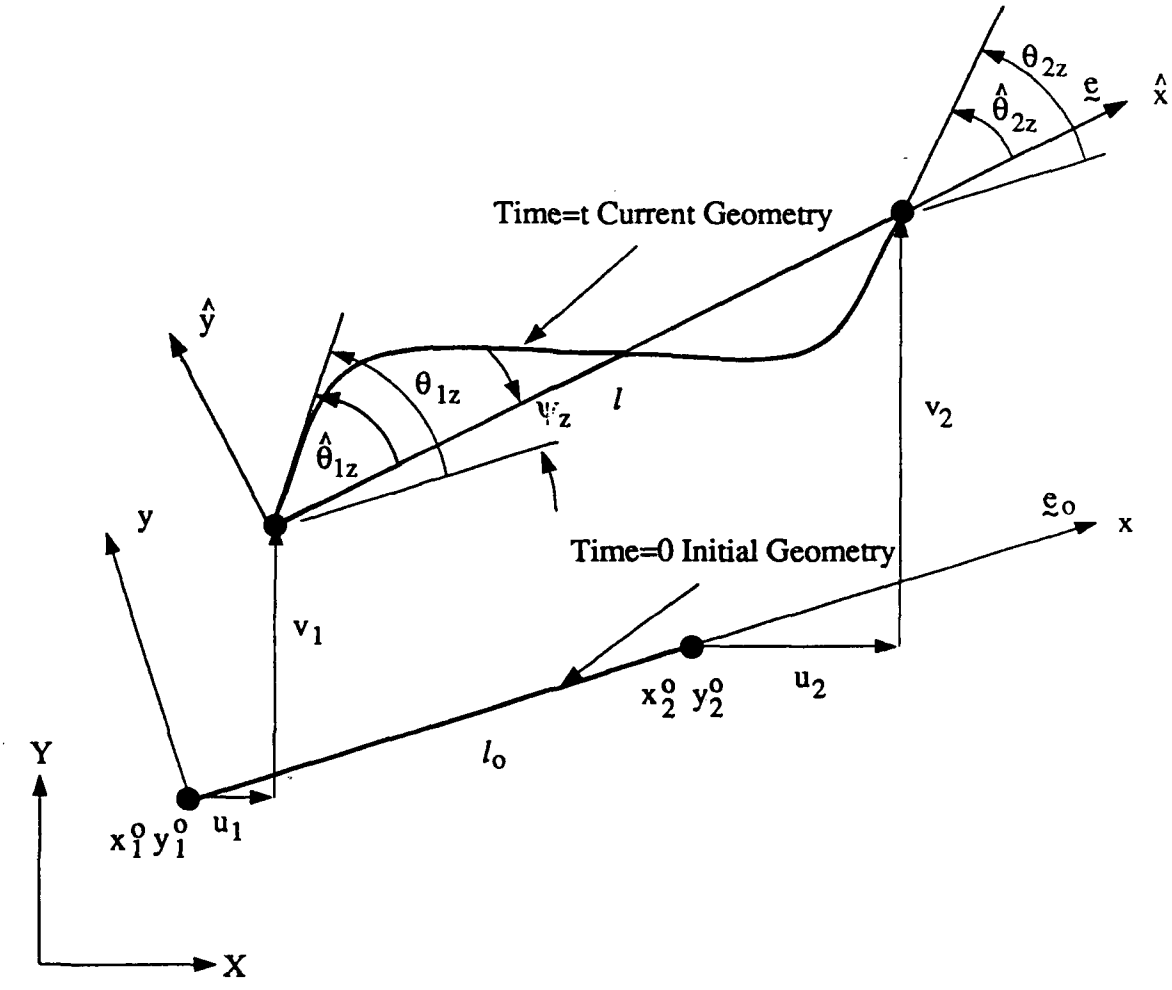

Figure 2.3 Initial and current geometries used for planar frame element in co-rotational approach

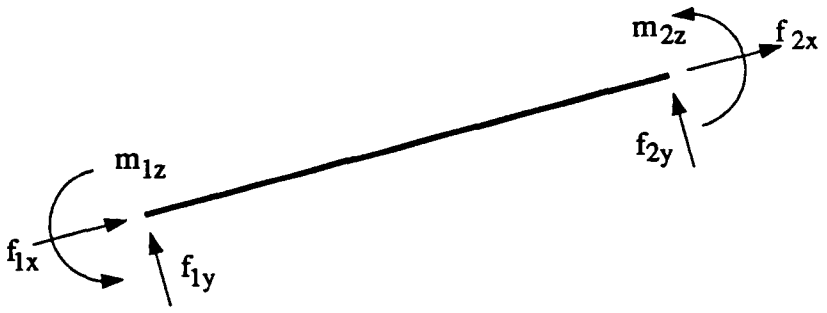

Figure 2.4 Internal element forces in local coordinates for planar frame

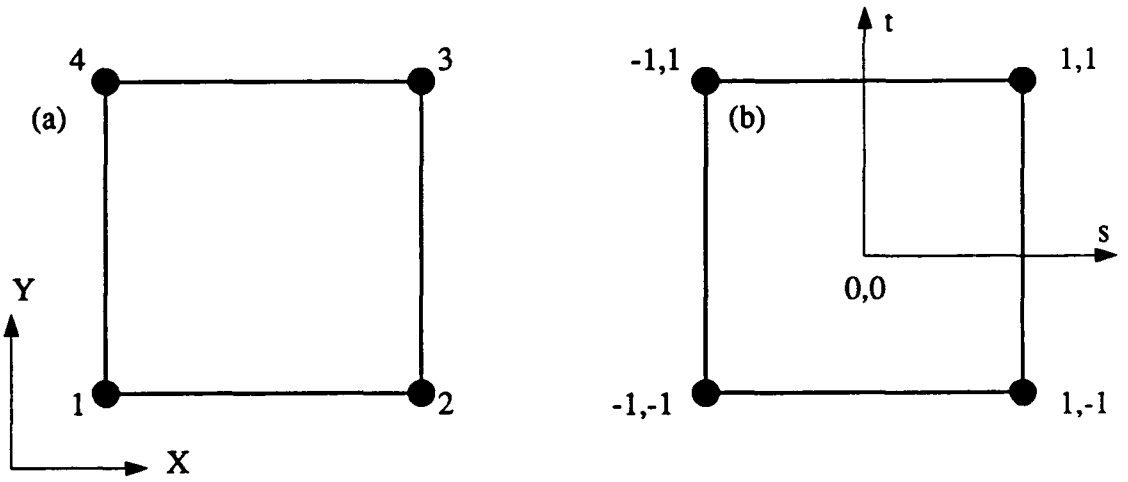

Figure 2.5 4-node isoparametric plane-stress/strain element in (a) global and (b) natural coordinates

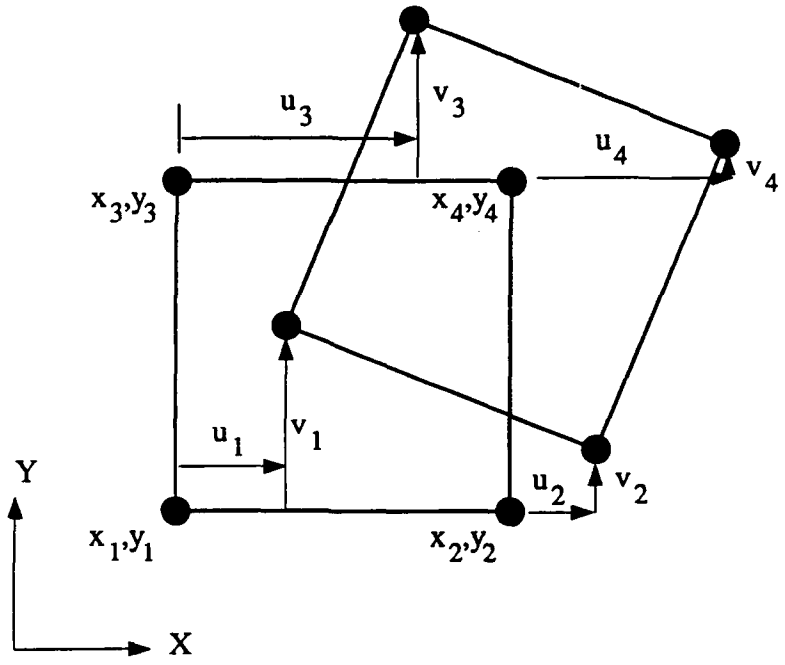

Figure 2.6 Element nodal coordinates and displacements

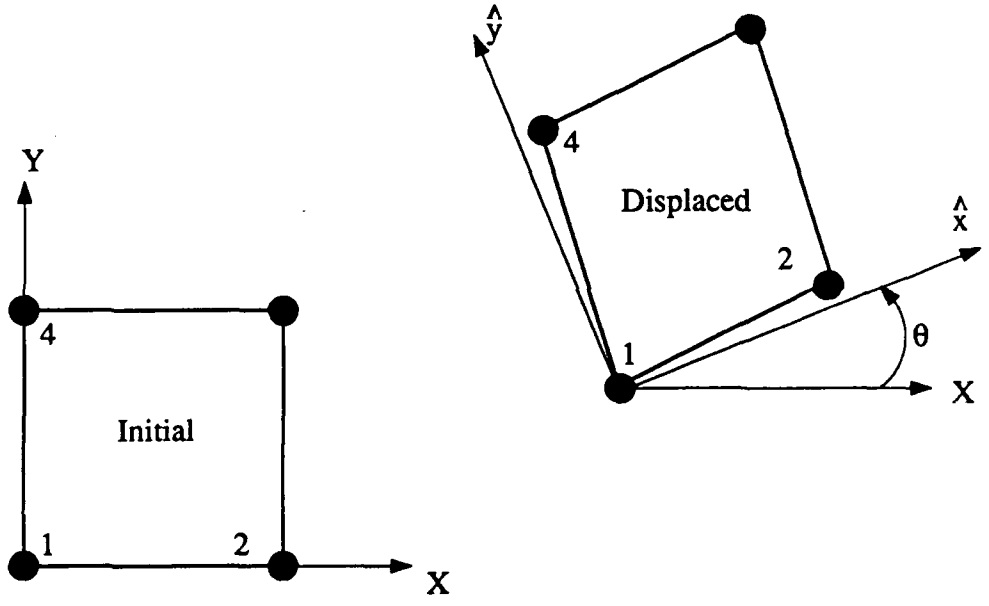

Figure 2.7 Initial configuration of 4-node isoparametric planar element and displaced configuration showing co-rotational coordinate system

CHAPTER 3 FINITE ELEMENT FRAGMENTATION ALGORITHM

3.1 Introduction

There are two common groupings of numerical methods used in the study of structural response. One of these groups can be classified as numerical analysis and consists of the finite element method, finite difference method, etc. These techniques are intended mainly for the pre-failure and failure analysis of a continuous medium by giving quantitative predictions of stress, strain, and displacement values. The second group can be termed numerical simulation and consists of the finite block method, distinct element method, etc. This group is utilized chiefly in modeling discontinuous media to qualitatively recreate the behavior of granular or jointed materials through motion histories using the contact forces acting on the discrete bodies (Babosa and Ghaboussi [7], Heuze, et. al. [32], Shi [79]).

The study of structures subjected to high-rate transient loads known as impacts and shocks can necessitate the ability to analyze a continuous medium which transitions to multiple distinct bodies due to fragmentation. Currently, neither one of these two groups of numerical methods can accurately predict this entire spectrum of behavior. To develop such a capability, the numerical technique is required to be able to calculate pre-failure displacements, stresses, and displacements in the continuous medium and then transition to a discontinuous structure due to the fragmentation, track these

fragments, and still be able to calculate stresses and displacement histories in the fragments as well as the remaining structure. As a step in this direction, a finite element based fragmentation algorithm is proposed. This algorithm uses the finite element method and explicit time integration coupled with the ability to allow fragmentation of elements if a failure criterion is violated. Through the use of an updated geometry formulation, the algorithm is capable of creating new surfaces due to fragmentations, tracking these fragments, providing good prediction of further fragment development, and calculating stresses and displacements in all the fragmented structural components.

3.2 The algorithm

The objective of developing an element fragmentation algorithm is straightforward: to create two nodes where only one previously existed if a fracture criterion is violated, as shown in Figure 3.1. To simplify the process, a new node is created in the element where the violation is detected, and the original node stays with the other adjacent elements at the point of fracture. As these two nodes are not connected, the elements, originally connected, are moved apart and new free surfaces are formed.

In this study, the algorithm is applied to the study of impact response of structures and thus, its implementation is illustrated by a code designed for dynamic analysis. The specific code selected for implementation adopts an explicit time integration technique with lumped nodal masses which has been proven effective in transient dynamic problems (Fu [26] and Park [72]). This combination of solution procedure seems to be very convenient for fragmentation analysis since there is no need to renumber the entire

mesh when a node is added, and the memory management is straightforward.

An algorithm flowchart, shown in Figure 3.2, gives a schematic representation of the operations. The bold boxes are those steps unique to the fragmentation technique with the non-bold boxes being steps used in a typical explicit time integration scheme. The reader is referred to Belytschko and Liu [16] for a list of references on explicit algorithms for impact problems.

In the following, the basic modifications of the explicit co-rotational approach to include element fragmentation are briefly outlined. The steps can be categorized as:

- Stress/strain calculations and fracture criterion
- Nodal connectivity check
- Dynamic allocation and storage expansion
- Force calculations
- Time increment considerations

3.2.1 Fracture Criterion

To determine the location of a surface formation, the elements' internal stresses (or strains depending on the criterion used) are first calculated for each time step. The use of a finite element formulation, based on the co-rotational approach seem to compliment the explicit time integration quite well. Adopting these formulations greatly simplifies the modifications necessary for the implementation of failure criteria and the fragmentation. For details of the application of the co-rotational approach, the reader is referenced to Belytschko and Hsieh [14], Belytschko and Schwer [15],

Marchertas and Belytschko [60], and Mattiasson [61], for example.

Briefly, the equations of motion can be written in the form

$$\ddot{d}_j = \frac{1}{M_j} (F_j^{ext} - F_j^{int}), \; j=1,2,...,n \tag{3.1}$$

where $\ddot{d}$ is the acceleration, M is the nodal mass, F^{ext} is the external nodal force, and F^{int} is the internal nodal force for the j^{th} degree of freedom. The element forces, $\underset{\sim}{f}_e^{int}$, which make up the vector of internal nodal forces, $\underset{\sim}{F}^{int}$, are calculated at the element level where $\underset{\sim}{f}_e^{int}$ can be given by

$$\underset{\sim}{f}_e^{int} = \int_{V_e} \underset{\sim}{B}^T \underset{\sim}{\sigma} \, dV_e \tag{3.2}$$

where $\underset{\sim}{B}^T$ is the matrix of shape function derivatives and $\underset{\sim}{\sigma}$ is the element internal stress vector. For the explicit approach, stresses are computed using the nodal displacements and material parameters calculated during the previous time step.

After the current state of stress is calculated, the fracture criterion is examined. The criterion may be implemented in terms of stresses, strains, displacements, or a hybrid form. Empirical formulations may also be considered. If the state of stress and deformation in a particular element exceeds the failure criterion, the fragmentation algorithm starts by first storing the element and nodal numbers. The program sequence is then redirected to determine whether a new surface is allowed to form at this node for the current state of stress and deformation.

3.2.2 Nodal connectivity check

The relatively small time step required in the conditionally stable explicit time

integration procedure and the lumped nodal masses used for ease of calculation can result in non-zero stresses being calculated at what should be stress free surfaces. For this reason, the node where the state of stress has exceeded the failure criterion must first be checked to ensure there is some type of restraint currently existing at the node. This restraint may be in the form of a support or another element being attached. If the node where the criterion is exceeded is found to be an unrestrained node, the program returns to the normal looping as if no failure had been detected. If the node does have some existing restraints, fracture is allowed to occur and the program drops out of the normal looping and redirected to create the new surfaces.

The type of element used in the algorithm determines the type of fracture allowed. For example, a frame element containing a nodal stress exceeding the criterion would create the fracture by releasing that node from all other elements connected to it. This non-directionality of the fracture means the nodal connectivity search requires only finding one other element in any direction sharing the fracture node for fracture to be allowed as shown in Figure 3.3. A plane or three-dimensional solid element, though, raises an additional consideration of direction of fracture. If, for example, a 4-node plane-stress element is used; fracture may occur in any one of three directions for each node of the element as shown in Figure 3.4(a-d). The direction of fragmentation is first determined by using the state of stress (or strain) calculated for the node of the element to find the direction of maximum tensile stress relative to the element's current orientation. The face to be released is chosen by comparing this direction to the stress rosette shown in Figure 3.5. If the maximum tensile stress direction falls within the

range of face 1 on the rosette, the node is released in the vertical direction as in part (b) of Figure 3.4. If the direction is within the face 2 range of the rosette, the release is in the horizontal direction (Figure 3.4(c)). The diagonal release is dictated by the geometry of the element and the particular node where the fracture occurs. Nodes 1 and 3 can only sustain a release in the face 4 region and nodes 2 and 4 can only release in the face 3 region. This directionality of the release requires a layer connectivity check.

An example of a layer connectivity check is shown in Figure 3.6. Node "n" of element "e" in horizontal layer "i" is found to exceed the failure criterion with the principal tensile stress, σ_1, shown. Thus, the crack will form in the horizontal direction between layers "i" and "i-1". Layer "i-1" is searched to determine if any element in the layer also contains node "n." If this layer does not contain "n", no fracture is allowed and the program is continued. If "n" is found, fracture is allowed at this interface and node "n" remains the same in layer "i-1" and becomes "N+1" in layer "i" as seen in Figure 3.6(b) where "N" is the total of nodes in the mesh prior to fracture.

In the present algorithm, the maximum tensile stress is used to determine the fracture surface direction. Other criteria can be introduced based on a similar consideration. Except for the connectivity check, other aspects of the fragmentation algorithm are essentially the same for all types of elements. Hence, the rest of this chapter will only treat nodal fracture of a frame element for simplicity of explanation.

3.2.3 Update dynamic allocation

Once it is confirmed a new surface needs to be created, the next step in the algorithm is to create an expanded dynamic storage array. The objective of this subroutine is to reposition the existing memory locations in the dynamic allocation array and add new values appropriate for the new mesh. For example, a mesh with "N" nodes with "D" degrees of freedom per node stores "N x D" displacements before fracture. After the fracture of node "n" ($1 \leq n \leq N$) occurs, there are "N+1" nodes and, therefore, "(N+1) x D" displacements. The displacements of the newly created node, "N+1", are the same as node "n" and are stored in the last "D" spaces of the displacement sub-array which is now dimensioned to "(N+1) x D."

The reallocation may also reflect options of the computer code. For example, selected output values may be stored. If a fractured node is the one for which output is requested, storage for both the original node and the newly created node are allocated.

Additional modifications needed for the new dynamic allocation array include the new mesh characteristics. The external nodal force array must be changed and expanded for the fracture node and the new node. In the present algorithm, any pre-existing external forces are arbitrarily zeroed at both of the nodes after fracture occurs. Similarly, the lumped mass matrix requires recalculation and reallocation based on the updated element connectivity.

To simplify coding the reallocation/expansion, a "dummy array" may be used where the values of the original array are temporarily stored in their new positions without writing over other array values. After this relocation and addition of values is

accomplished, the dummy array values are passed back to the original array for use in the main program.

3.2.4 Internal force calculation

After the storage re-allocation is completed, the algorithm returns to the internal force calculation within the same time increment. The force calculation starts from calculating stresses in the same element where the fracture occurs, thus allowing more than one fracture to occur in the same element. The process repeats until all elements in the mesh are fracture checked and modified. For the coding, when the program returns to the internal force sub-routine after creating a new surface, the algorithm is back to the original looping until the next fracture is detected. Thus, no new coding is necessary for the force calculations.

3.2.5 Time increment considerations

The time increment used in the current study is constant throughout the time history and is based on the highest frequency found within the elements in the mesh. If the time step chosen is close to the maximum stable time increment, the sudden change in displacements and velocities caused by fragmentation of the mesh can cause problems in the time integration stability. However, throughout the numerical examples, this has not been a major hindrance as the time step necessary for the higher velocity impact response is usually small enough this instability did not occur. Hence, modifications were not necessary. For slower loading conditions, time increment considerations may

need more careful evaluation when element fragmentation occurs.

3.3 Numerical results

To illustrate the algorithm, the fragmentation of plane frames is first considered. In the experience of this research, the fragmentation of frame elements due to bending seems to create the most severe numerical problems. Plane solids appear to be much more stable.

The code selected for modification is a code called LADDAS (Large Displacement Dynamic Analysis of Space Frames). LADDAS is designed for space frame analysis using the traditional co-rotational approach and explicit time integration. The present modifications include both the fragmentation algorithm and updated co-rotational approach for large displacements.

Examples presented are designed to illustrate special features of the technique. The first two examples show the ability of the algorithm to create a surface if a criterion is violated and to numerically follow the trajectory of each fragmented component. The third shows the capability to quantitatively predict stresses and fracture sequence. The last problem shows the application of the algorithm using axisymmetric solid elements.

Problem 3.1 is a fixed base three story, one bay frame subjected to seismic excitation in the form of ground acceleration data. The base acceleration values used are ten times the values recorded from the 1940 El-Centro earthquake in the north-south direction with the acceleration history shown in Figure 3.7(a). The frame is made up of three different frame element properties and a weakened element to simulate a

structural flaw with the frame's geometry and member properties shown in Figure 3.7(b). The mesh is composed of 37 nodes and 38 elements with each element being 36 inches in length. There are 5 elements in each bottom story column and 4 elements in each column in the top two stories. The two cross members consist of 4 elements each.

The weakened member is located in the right second story column at the upper joint and causes the stress at node 14 to exceed the fracture criterion of 3,600 psi in tension. This causes a discontinuity to form between element 14 and the two other elements previously connected by node 14 as shown in Figure 3.8. The parting of element 14 and the other two elements causes a severe change in the structure's frequency as shown by the displacement histories of nodes 14a, 14b, and 34 in Figures 3.9(a-c) and 3.10(a-c). The ability to fragment elements thus allows the study of a rapid change in structural frequency during the middle of loading. The time step size used is 1×10^{-4} seconds and the 10,000 time steps used take approximately 4 CPU minutes on a Gould NP-1 computer.

Problem 3.2 is a fixed-fixed beam subjected to impact forces at nodes 7, 8, and 9 which are located in the middle of the beam. This example is intended to show the algorithm's ability to create multiple fragments which are completely separate of the original mesh.

The problem geometry, material properties, section properties, and load history are shown in Figure 3.11. The mesh is made up of 14 elements with each element being 5 inches in length. The external forces at a node are set to zero once the maximum tensile stress of 1,200 psi is exceeded. The 200,000 time steps of 0.5×10^{-6} seconds are

used to show the structure through one second of real time. The entire event takes approximately 25 minutes of CPU time on a Gould NP-1 computer in the Purdue University Engineering Computer Network.

After the load is applied, two elements between the forces and two elements immediately adjacent to the forces show fracture. Thus, the structure is broken into six components as shown in Figure 3.11(c). Figures 3.12 and 3.13 are traces of the end nodes of each of the six separate structural components. Figure 3.13 is an enlarged views of the middle portion of the mesh where extremely large translations and rotations are encountered. The numbers shown are the node numbers traced with the subscript being the element with which the nodes remain after fragmentation occurs. It is apparent the traditional co-rotational approach is not capable of tracking the large rotations of the middle four fragments which leads to errors and instability. As a result, the fragmented elements experience unreasonably large changes of length. Figure 3.14 shows the deformed configurations of the structure at 0.1 second intervals.

Problem 3.3 considers a longitudinal stress wave which induces fracture in a rod with free-free end conditions. The rod is composed of 51 nodes and 50 elements 0.1 inches long. A compressive force history, shown in Figure 3.15(a), creating a maximum stress of 310 psi is applied at the right end of the rod which imparts a compressive stress wave traveling to the left. The incident wave is reflected by the left end as a tensile wave due to the requirement of stress free conditions at the free end. The tensile failure strength of the material is arbitrarily set at 300 psi.

Based on uniaxial elastic stress wave theory, the wave velocity is calculated as c = 135,000 in/sec. The wave should take 3.7×10^{-5} sec to reach the left end of the 5" rod. The incident wave will reduce the reflected wave until 3/4 of the wave has been reflected resulting in a net tensile stress of over 300 psi (assumed material tensile strength) at 4.6×10^{-5} secs which agrees with the numerical prediction of 4.7×10^{-5} secs. The fragmenting should occur at 1/4 of the wave's length from the left end which is 0.404 inches which also agrees with the numerical prediction of fragmenting occurring within element 46. After the first failure occurs in the rod, no failure was predicted in the right portion of the rod which agrees with the expected physical phenomenon. The initial structure and the final geometry after fracture are shown in Figure 3.15(b-c). Stress histories of element 10 with and without the fragmenting are shown in Figure 3.16(a-b).

Problem 3.4 is an application of the fragmentation algorithm to an axisymmetric problem using 4-node isoparametric elements. The geometry of the problem is shown in Figure 3.17(b) with the initial structure being a cylinder with a cylindrical interior void subjected to the pressure history shown in Figure 3.17(a). The mesh is composed of 600 elements with dimensions of 0.2 x 0.2 inches in the plane of symmetry. The time step was taken as 1×10^{-6} seconds. For 2000 time steps, the computation required approximately 100 minutes of CPU time on the Gould NP-1 computer.

The Hsieh-Ting-Chen 4-Parameter failure criterion (Hsieh, Ting, and Chen [33]) for concrete material was used for fragmentation. Figure 3.18 shows the mesh for the elastic-fragment case at various times throughout the displacement history.

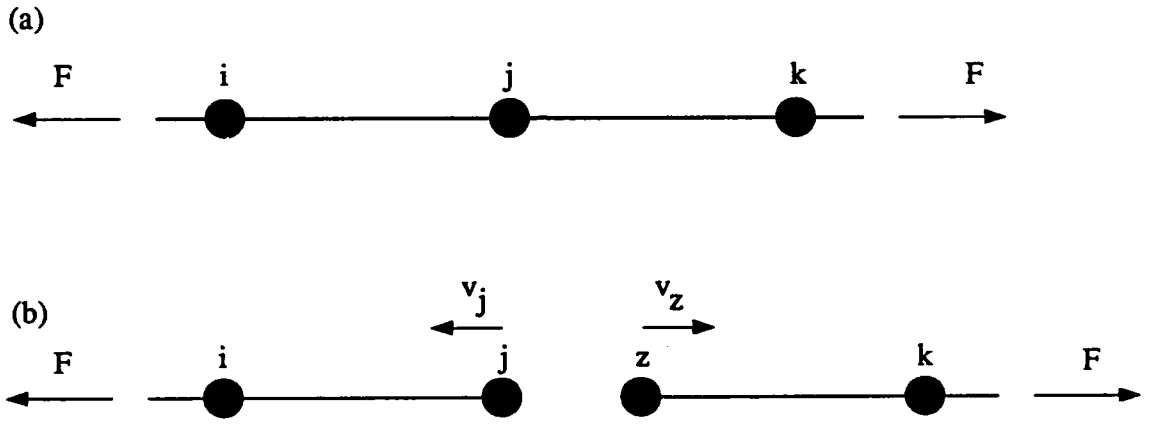

Figure 3.1 (a) Pre-release and (b) post-release of node

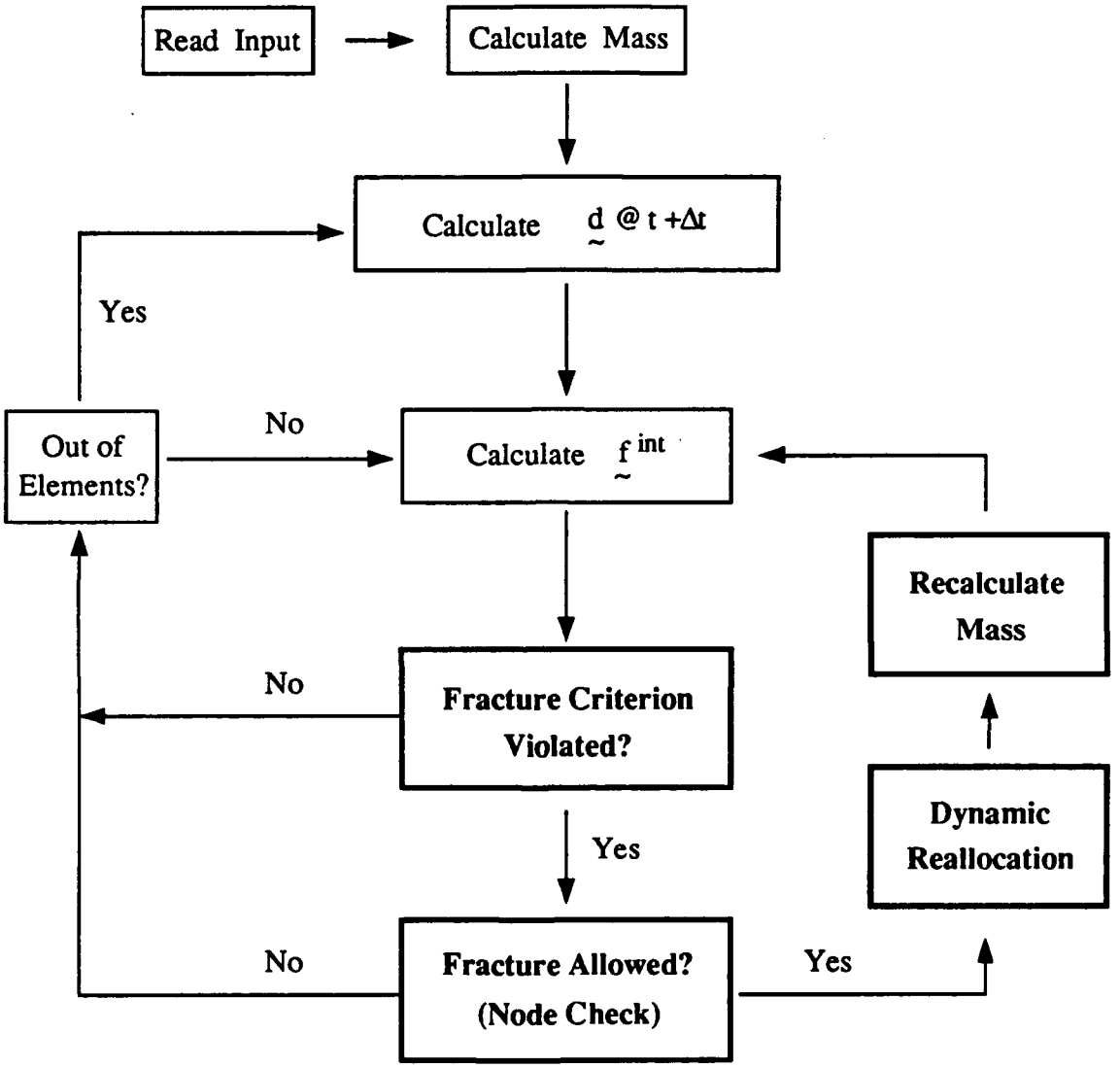

Figure 3.2 Flowchart of fragmentation algorithm

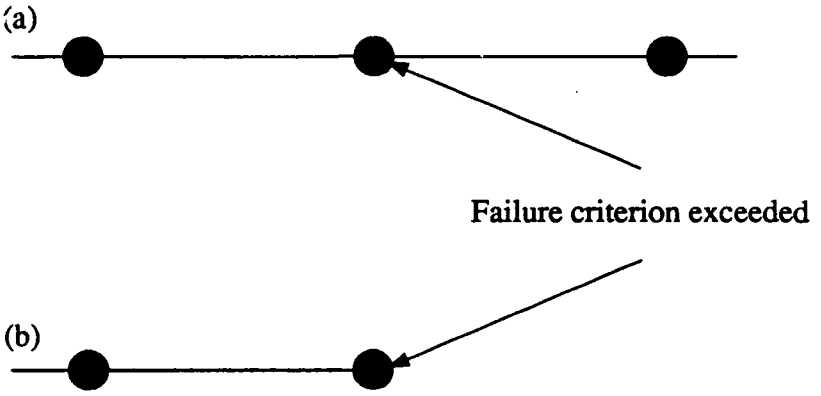

Figure 3.3 1-dimensional release (a) allowed and (b) not allowed

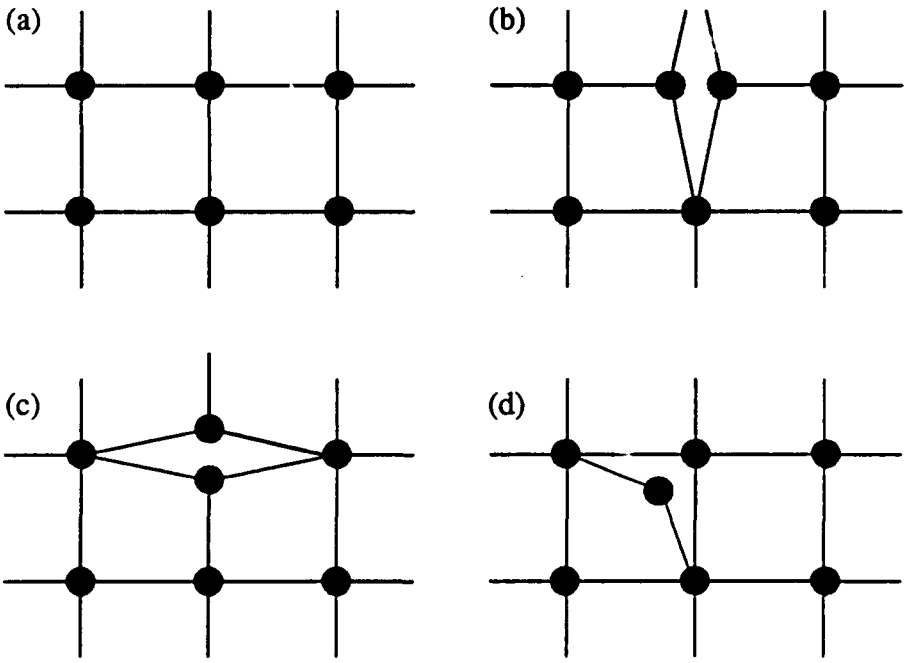

Figure 3.4 2-dimensional release showing (a) initial mesh, (b) vertical crack, (c) horizontal crack, and (d) diagonal crack

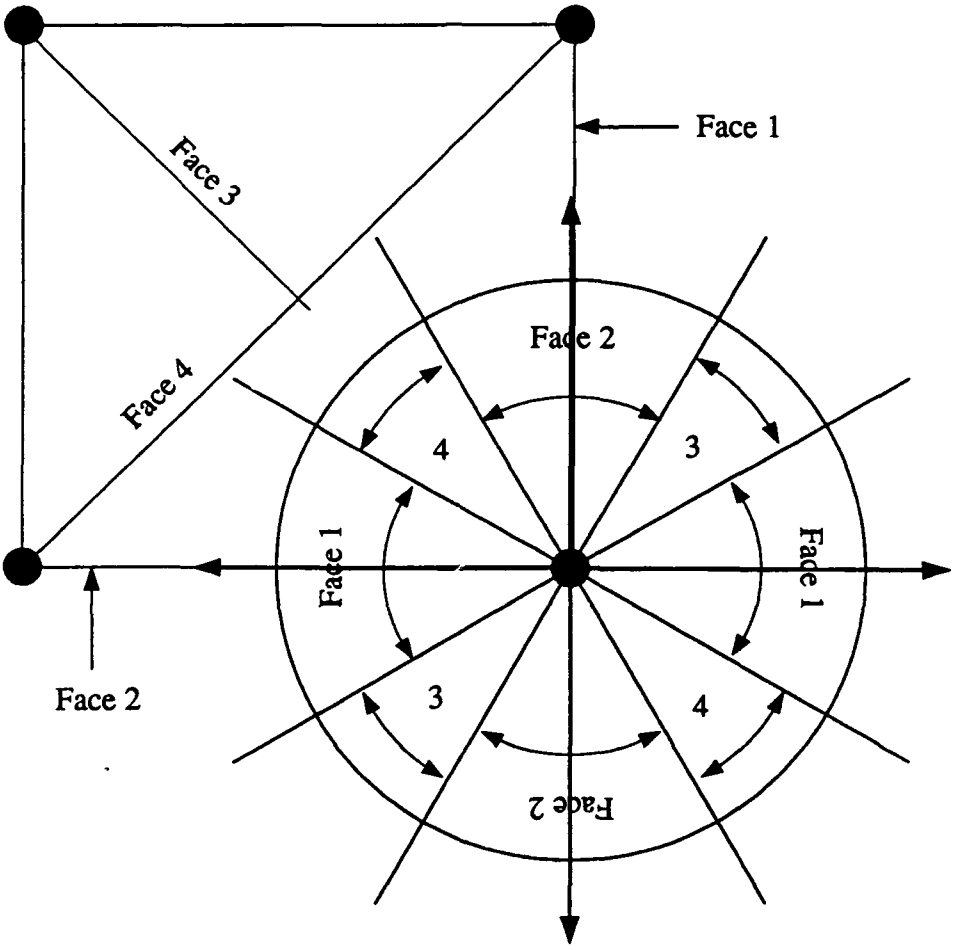

Figure 3.5 Stress rosette for fracture direction calculation

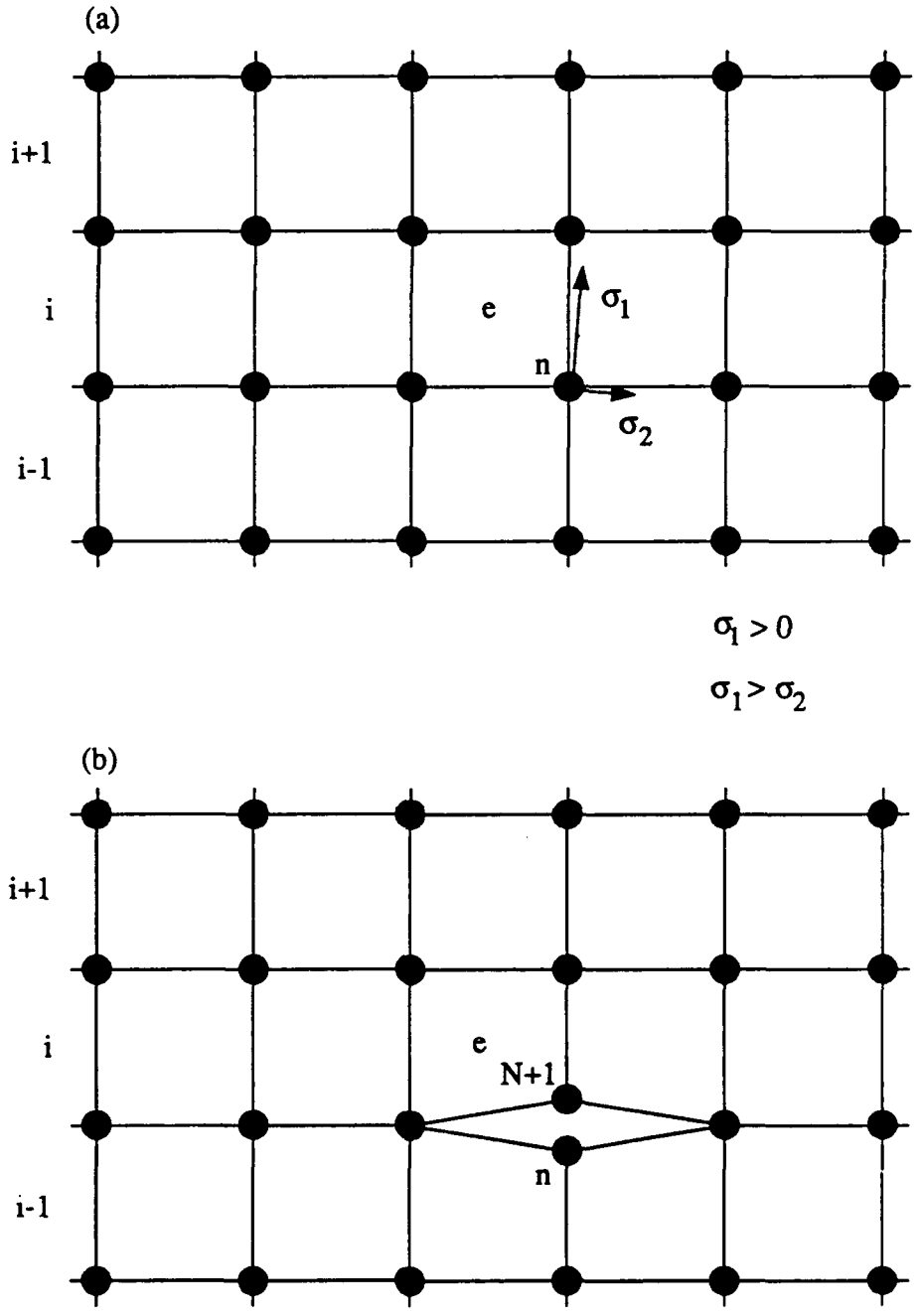

Figure 3.6 (a) Pre-release and (b) post-release of layer

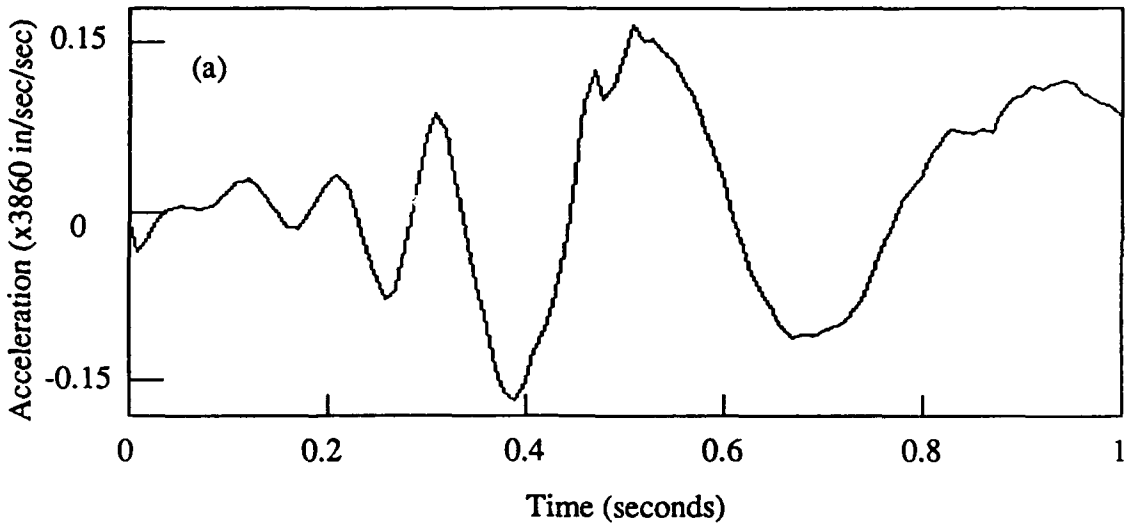

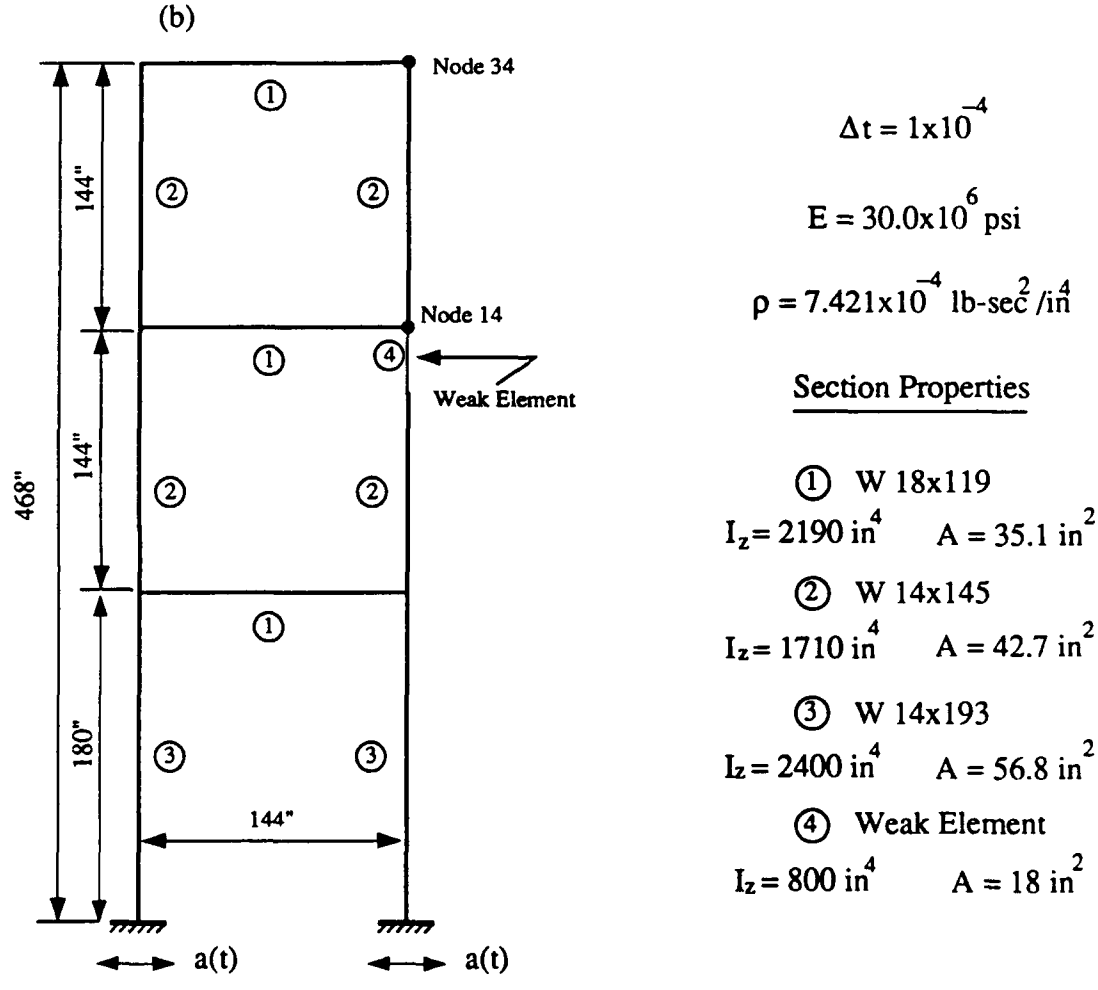

Figure 3.7 Problem 3.1 (a) ground acceleration history and (b) frame geometry, section properties, and material properties

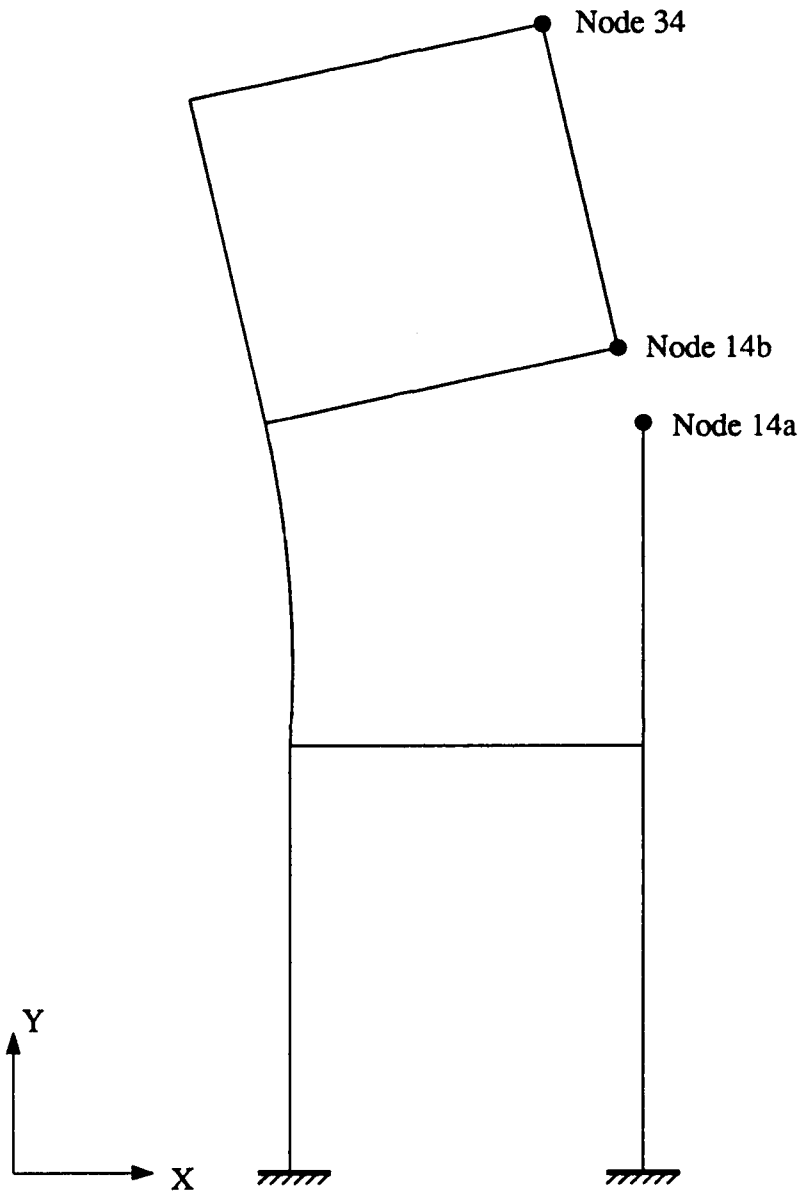

Figure 3.8 Problem 3.1 fragmented structure configuration

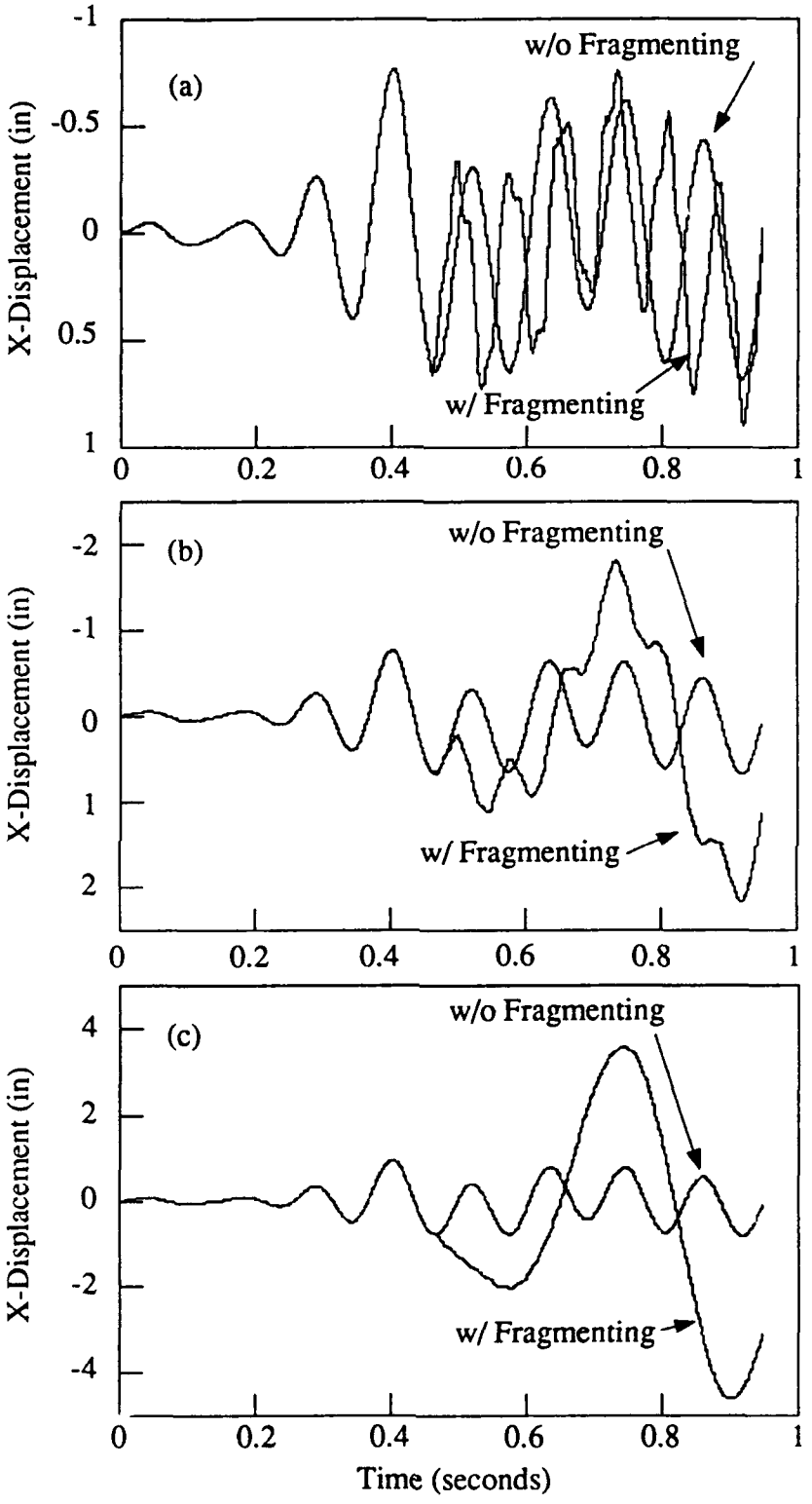

Figure 3.9 Problem 3.1 x-displacement history of (a) node 14a, (b) node 14b, and (c) node 34 without and with fragmenting permitted

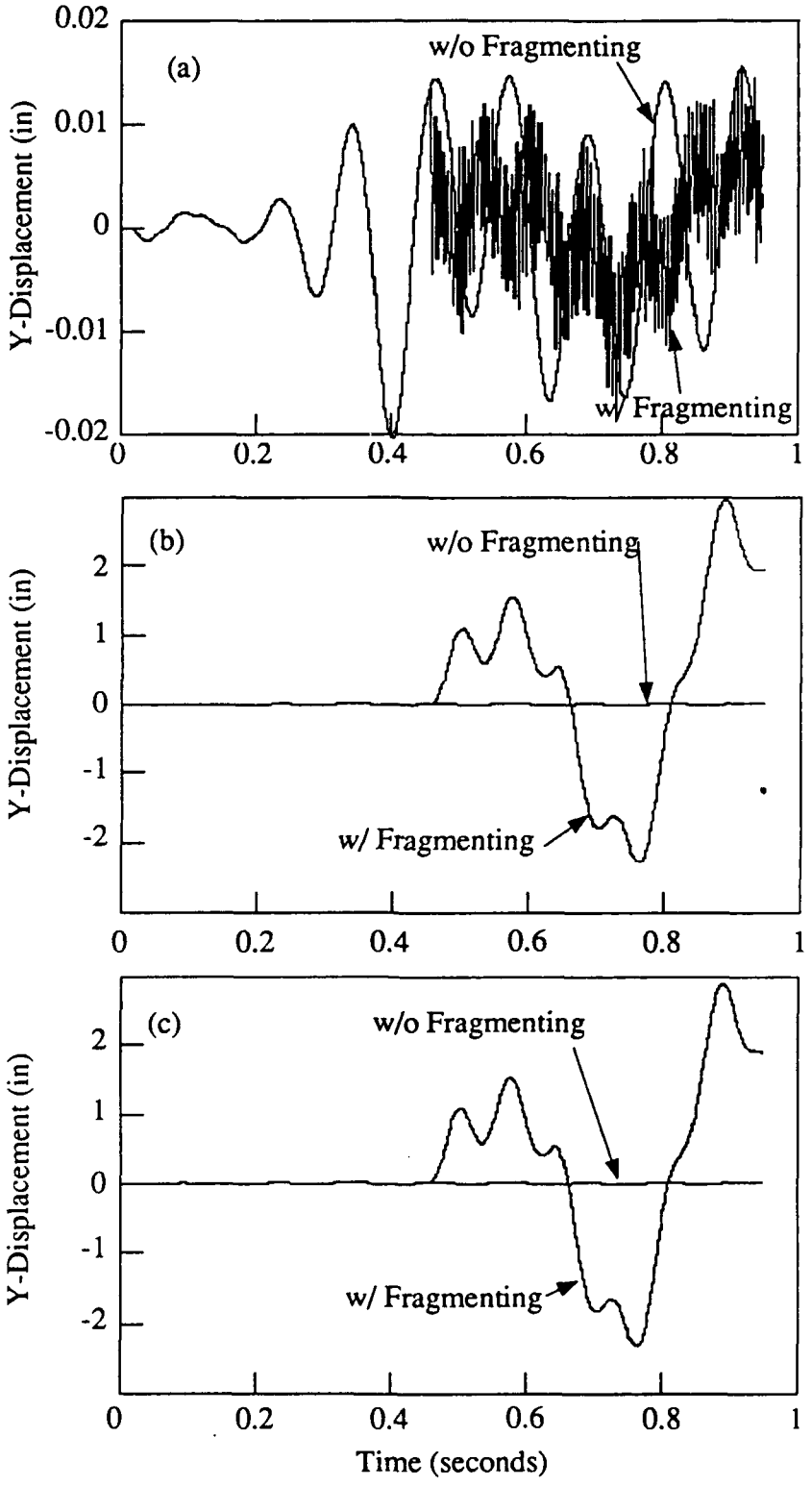

Figure 3.10 Problem 3.1 y-displacement history of (a) node 14a, (b) node 14b, and (c) node 34 without and with fragmenting permitted

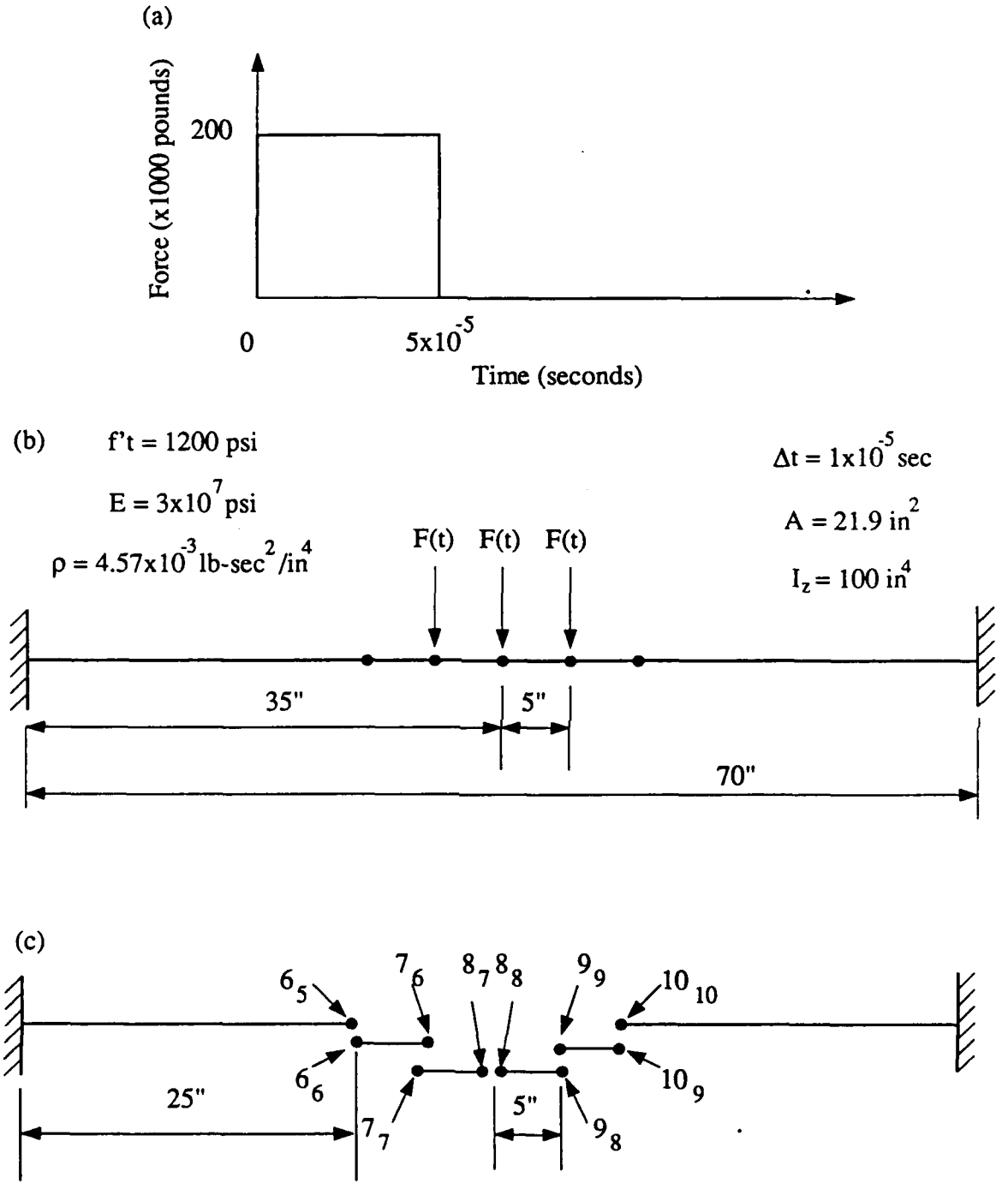

Figure 3.11 Problem 3.2 (a) load history, (b) beam geometry, section properties, and material properties, and (c) fragmented geometry

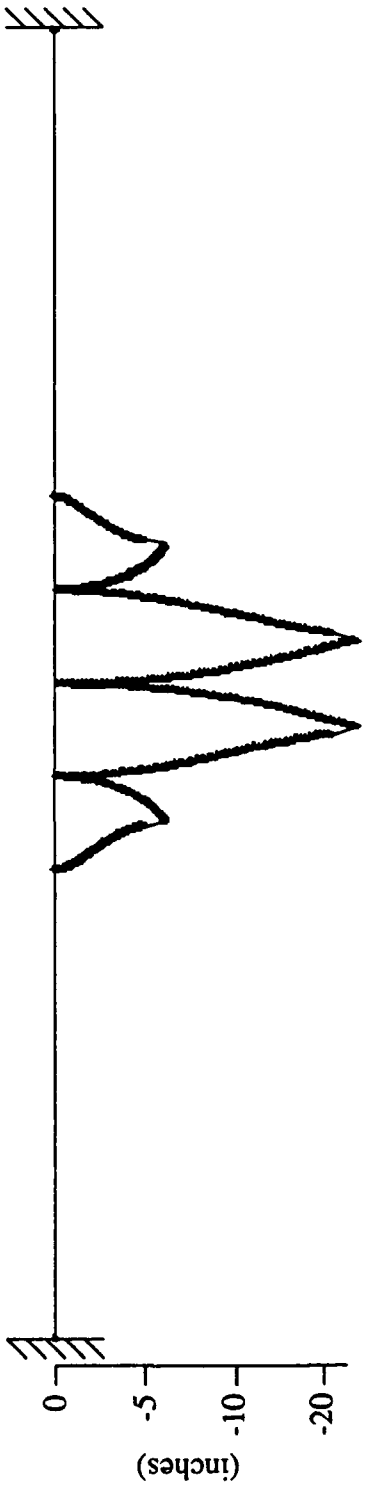

Figure 3.12 Problem 3.2 displacement history trace of fragment end nodes

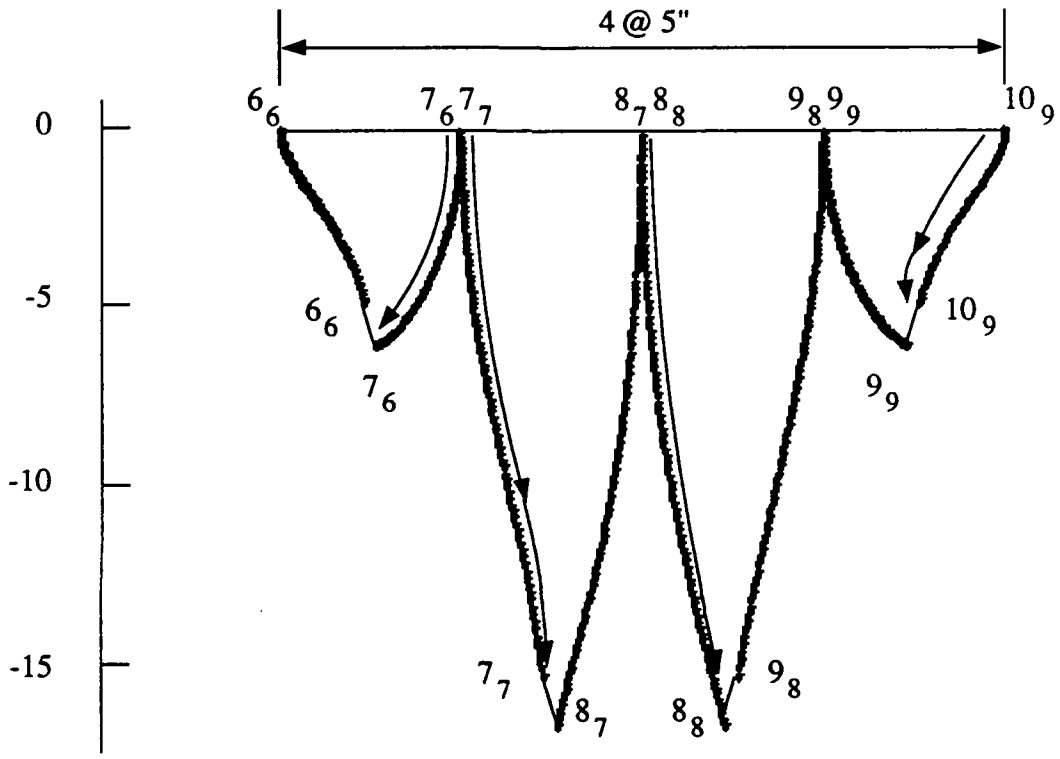

Figure 3.13 Enlargement of Figure 3.12 middle section showing displacement trace of fragments

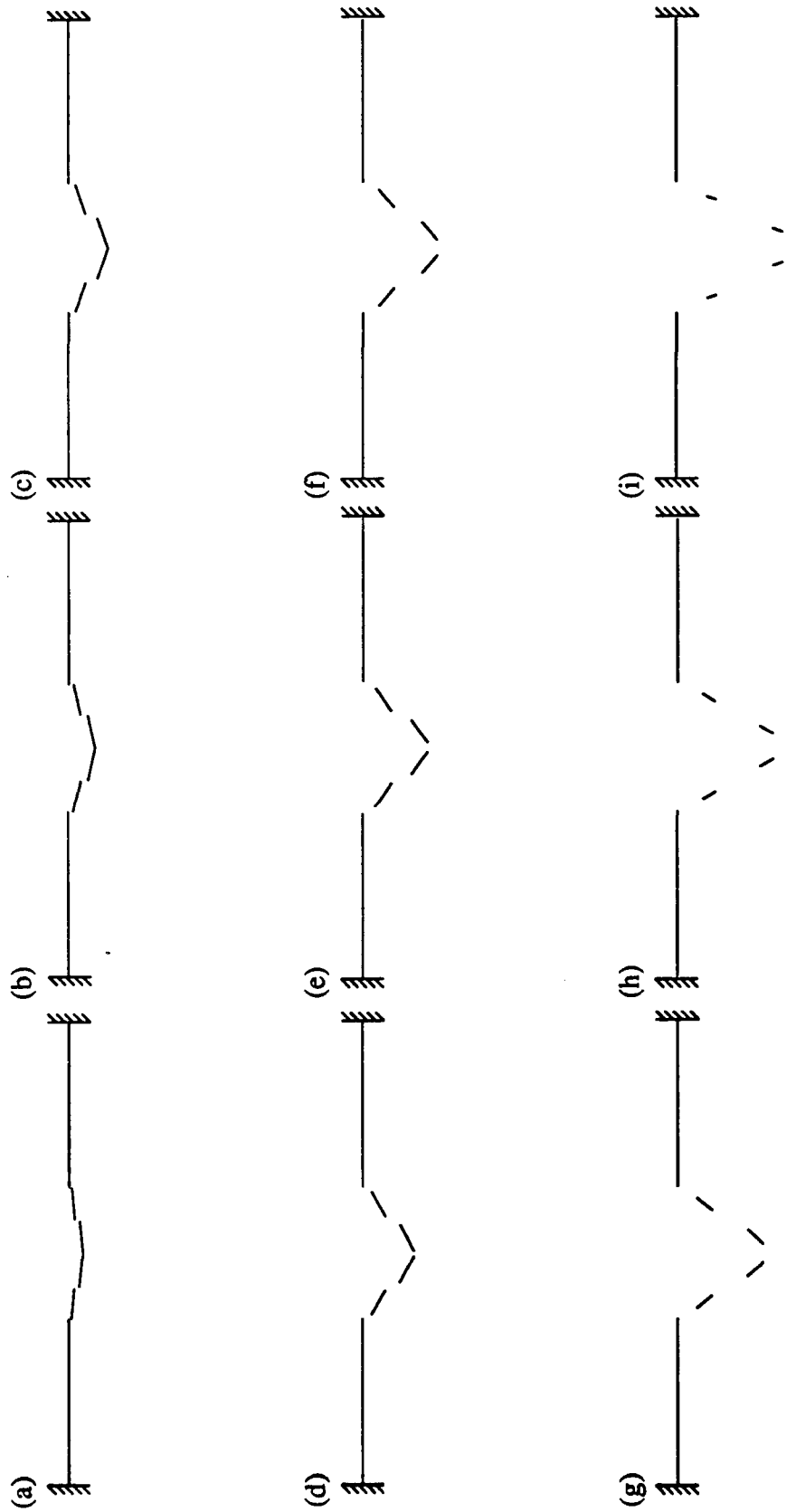

Figure 3.14 Displaced configuration of Problem 3.2 at (a) 0.1, (b) 0.2, (c) 0.3, (d) 0.4, (e) 0.5, (f) 0.6, (g) 0.7, (h) 0.8, and (i) 0.9 seconds

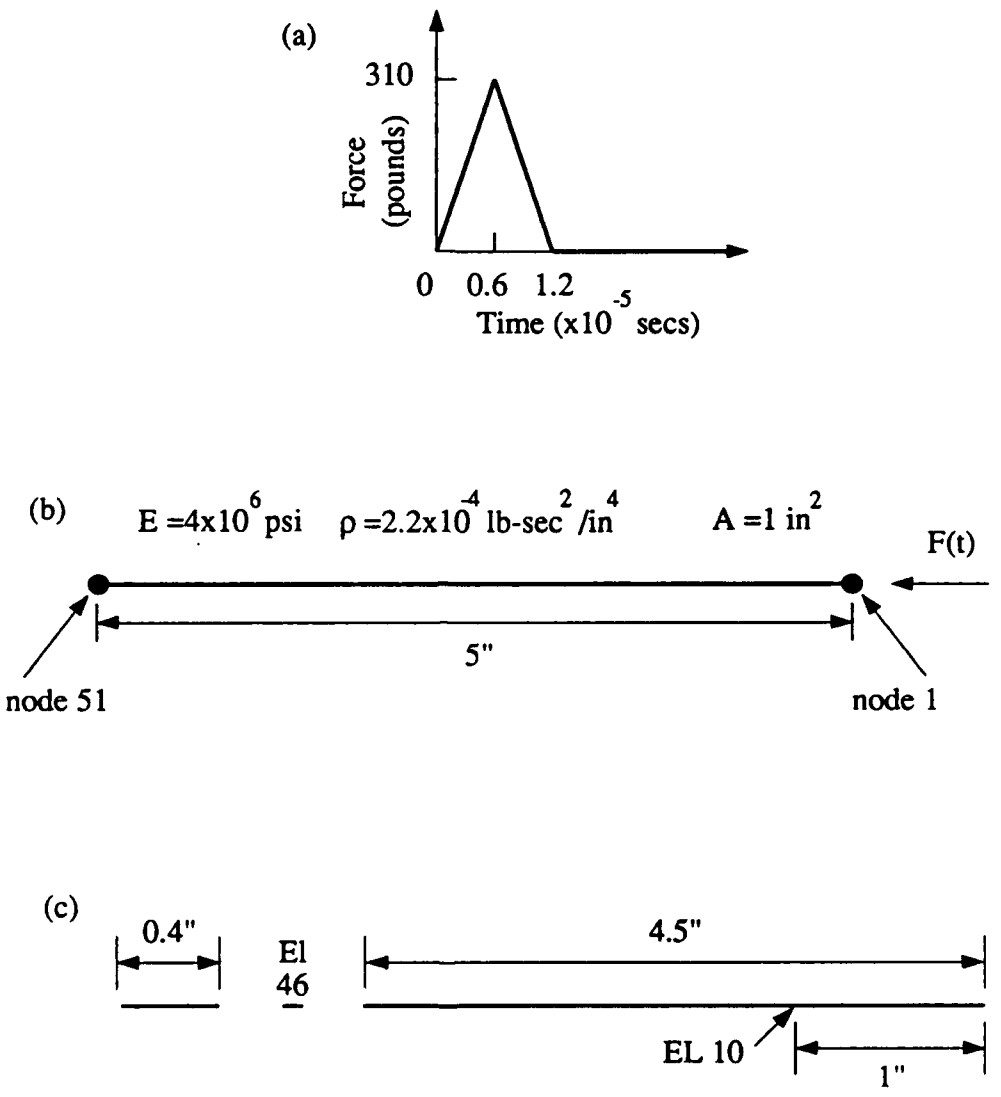

Figure 3.15 Problem 3.3 (a) force history, (b) initial geometry, and (c) fragmented geometry

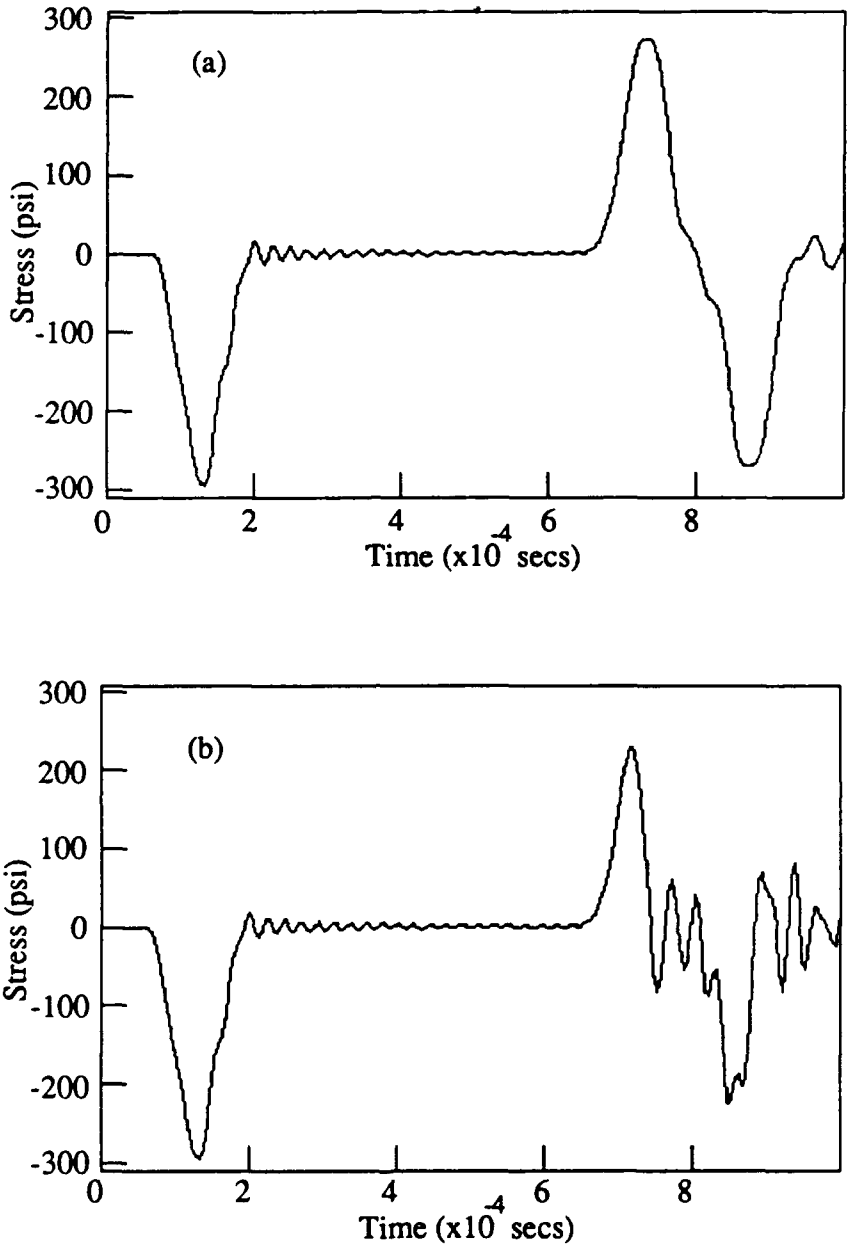

Figure 3.16 Problem 3.3 stress history of element 10 (a) without and (b) with fragmenting permitted

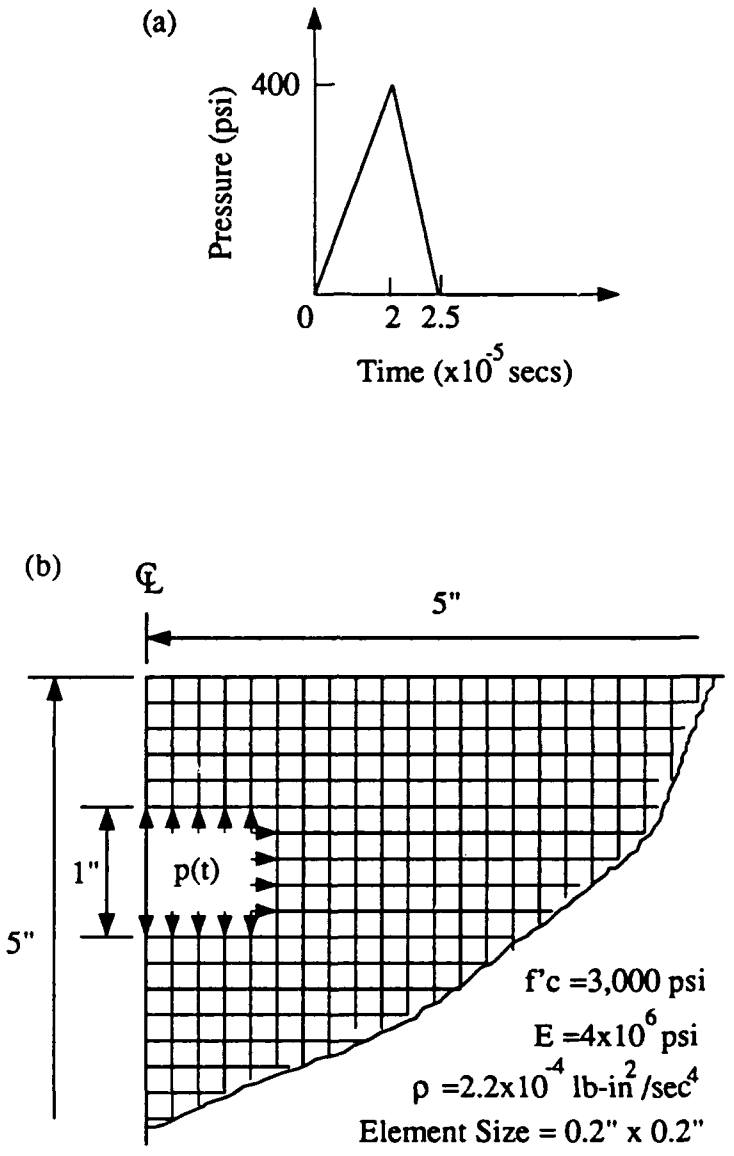

Figure 3.17 Problem 3.4 (a) pressure history and (b) geometry and mesh

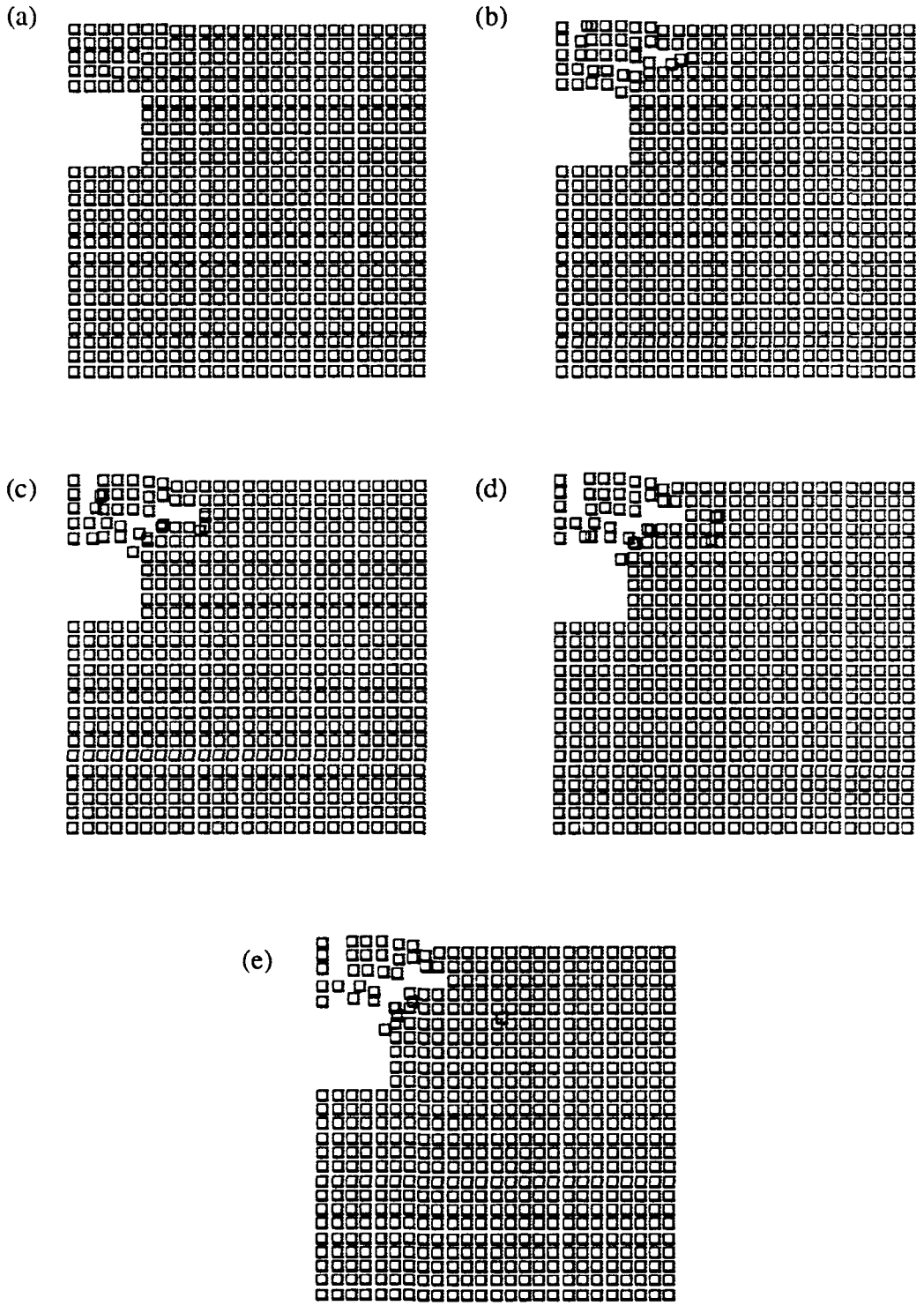

Figure 3.18 Problem 3.4 mesh at (a) .0004, (b) .0008, (c) .0012, (d) .0016, and (e) .002 seconds for elastic-fragment material model

CHAPTER 4 LARGE DEFORMATION FORMULATION

4.1 Introduction

The co-rotational approach like that proposed by Belytschko and Hsieh and detailed in Chapter 2 has been proven effective in transient dynamic problems. As shown in Problem 3.2 of the previous chapter, though, the extremely large deformations encountered in fragmentation cannot be accurately tracked by the traditional co-rotational approach. A different means of calculating internal forces must be developed which is capable of handling problems where the rigid body rotation of an element can be very large, for example in excess of 360° rotation.

A modified co-rotational formulation is proposed which is intended to more accurately handle problems where large rigid body motions are encountered. This approach uses a total formulation similar to that used in Belytschko and Hsieh [14] and combines it with adaptive periodic updating of the mesh geometry. This updating of the geometry allows the formulation to be applied to problems of extremely large rigid body displacements and moderate deformations and still allows the use of small deformation theories for material characterization.

4.2 General formulation

In order to handle problems where the displacements may be extremely large, a modified co-rotational approach is proposed where element geometry is periodically updated for the total deformation formulation. The amount of updating is dependent on the rotation and translation of the elements in the mesh and, thus, adapts to the particular problem. Between one update and the next update, the traditional co-rotational formulation can be used. For each update, the element (or mesh) geometry and the corresponding coordinate systems are changed. A new "base-line" geometry (or material frame) is defined. The process removes the numerical problems associated with large differences in rigid body and deformation magnitudes. The updates also ensure deformations between the updates remain small even though total element deformation may be moderately large. For large element deformation, the use of small strain theory may not remain true if the traditional co-rotational formulation is used. With the updated geometry, small strain assumptions can still be valid.

4.2.1 Kinematics

The updated co-rotational formulation is based on four stages of displacement history. The four stages, shown in Figure 4.1, are: 1) The original geometry, $\underset{\sim}{X}$, at time=0, 2) The current base-line geometry, $\underset{\sim}{x}$, at time=t, 3) The actual deformed geometry, $\underset{\sim}{x}'$, at time=t' and, 4) The convected geometry, $\hat{\underset{\sim}{x}}'$, at the same time as in stage 3. The convected geometry is obtained by an approximated rigid body rotation, $\underset{\sim}{Q}^T$, of the current deformed geometry to the current base-line geometry such that

$d\hat{\underline{x}}' = \underline{Q}^T d\underline{x}'$. Therefore, as:

$$d\underline{x}' = \underline{F}' d\underline{x} \tag{4.1}$$

where $\underline{F}'$ is the deformation gradient from $\underline{x}$ to $\underline{x}'$, $\frac{\partial \underline{x}'}{\partial \underline{x}}$, it follows that:

$$d\hat{\underline{x}}' = \underline{Q}^T \underline{F}' d\underline{x} \tag{4.2}$$

Let

$$\hat{\underline{F}}' = \underline{Q}^T \underline{F}' \tag{4.3}$$

Then,

$$\det|\hat{\underline{F}}'| = \det|\underline{Q}^T| \det|\underline{F}'| \tag{4.4a}$$

$$\det|\underline{Q}^T| = 1 \tag{4.4b}$$

$$\det|\hat{\underline{F}}'| = \det|\underline{F}'| \tag{4.4c}$$

Let

$$2\underline{E}' = \underline{F}^T \underline{F}' - \underline{I} \tag{4.5}$$

where $\underline{E}'$ is the Lagrangian strain tensor from $\underline{x}$ to $\underline{x}'$ and $\underline{I}$ is an identity matrix. Substituting Equation 4.3 into 4.5 gives

$$2\underline{E}' = \hat{\underline{F}}^T \underline{Q}^T \underline{Q}' \hat{\underline{F}}' - \underline{I} \tag{4.6}$$

$$= \hat{\underline{F}}^T \hat{\underline{F}}' - \underline{I} = 2\hat{\underline{E}}' \approx 2\hat{\underline{\varepsilon}}'$$

by using the assumption that the deformation gradient from the updated material frame, $\underline{x}$, to $\underline{x}'$ is small (using a small load increment) even though the strain from the original material frame, $\underline{X}$, to $\underline{x}'$ may not be small where

$$\hat{\underline{\varepsilon}}' = \frac{1}{2}\left[\left[\frac{\partial \hat{\underline{u}}'}{\partial \hat{\underline{x}}'}\right] + \left[\frac{\partial \hat{\underline{u}}'}{\partial \hat{\underline{x}}'}\right]^T\right] \tag{4.7}$$

$$= \frac{1}{2}\left[\left[\frac{\partial \hat{\underline{u}}'}{\partial \underline{x}}\right] + \left[\frac{\partial \hat{\underline{u}}'}{\partial \underline{x}}\right]^T\right]$$

where $\hat{\underline{u}}'$ is the deformation matrix from $\underline{x}$ to $\hat{\underline{x}}'$. Also, the deformation gradient, $\hat{\underline{F}}'$, can be simplified by the following relations:

$$\hat{\underline{F}}' = \underline{Q}^T \underline{F}' \tag{4.8}$$

$$= \underline{Q}^T \underline{R}' \underline{U}'$$

where $\underline{R}'$ and $\underline{U}'$ are the rotation matrix and right stretch matrix obtained by polar decomposition. As $\underline{Q}'$ and $\underline{R}'$ are orthogonal matrices describing approximately the same rotation

$$\underline{I} = \underline{Q}^T \underline{R}' \tag{4.9}$$

In addition,

$$\hat{\underline{F}}' = \underline{U}' \approx \underline{I} \tag{4.10}$$

as small deformation is assumed from $\underline{x}$ to $\underline{x}'$.

For the stress relations, let $\underline{\sigma}'$ be the change in the Cauchy stress from $\underline{x}$ to $\underline{x}'$ and $\underline{S}'$ be the change in the second Piola-Kirchoff stress in the same increment. Then,

$$\underline{\sigma}' = \frac{\rho'}{\rho} \underline{F}' \underline{S}' \underline{F}^T \tag{4.11}$$

where ρ' and ρ are the mass densities at state $\underline{x}'$ and $\underline{x}$ respectively. In terms of the deformation gradient,

$$\underline{\sigma}' = \frac{1}{\det|\hat{\underline{F}}'|} \underline{Q}' \hat{\underline{F}}' \underline{S}' \hat{\underline{F}}^T \underline{Q}^T \tag{4.12}$$

As $\det|\hat{\underline{F}}'| \approx 1$ and $\hat{\underline{F}}' \approx \underline{I}$, it follows that

$$\underline{\sigma}' = \underline{Q}'\underline{S}'\underline{Q}^T \tag{4.13}$$

or

$$\underline{S}' = \underline{Q}^T\underline{\sigma}'\underline{Q}' \tag{4.14}$$

The corresponding change in the Cauchy stress from $\underline{x}$ to $\hat{\underline{x}}'$, $\hat{\underline{\sigma}}'$, is then

$$\hat{\underline{\sigma}}' = \underline{S}' = \underline{Q}^T\underline{\sigma}'\underline{Q}' \tag{4.15}$$

4.2.2 Virtual work

The virtual work equations in the updated approach take on the same initial form as the traditional approach. The differences arise due to the updating of the element geometry and the use of the change in nodal displacements from the current base-line geometry.

The internal virtual work at time $t=t'$ is given as

$$\delta W^{int} = \sum_{i=1}^{\#el} \int_{V_i'} \delta\hat{\underline{\varepsilon}}^T \hat{\underline{\sigma}}\, dV' \tag{4.16}$$

where $\hat{\underline{\sigma}}$ is the element stress and $\delta\hat{\underline{\varepsilon}}$ is the first variation of the element strain which define the response from $\underline{X}$ to $\hat{\underline{x}}'$. The integration is performed over the current volume of the element.

Due to the updating, the strain, $\hat{\underline{\varepsilon}}$, is a combination of the baseline strain (from $\underline{X}$ to $\underline{x}$), $\hat{\underline{\varepsilon}}^b$, and the change in strain from the update (from $\underline{x}$ to $\hat{\underline{x}}'$), $\hat{\underline{\varepsilon}}'$. The stress can be written in the same form

$$\begin{aligned} \hat{\underline{\varepsilon}} &= \hat{\underline{\varepsilon}}^b + \hat{\underline{\varepsilon}}' \\ \hat{\underline{\sigma}} &= \hat{\underline{\sigma}}^b + \hat{\underline{\sigma}}' \end{aligned} \tag{4.17}$$

Taking the first variation of the strain gives

$$\delta(\hat{\underline{\varepsilon}}^{b} + \hat{\underline{\varepsilon}}') = \delta\hat{\underline{\varepsilon}}' \tag{4.18}$$

Substituting Equations 4.17 and 4.18 into Equation 4.16 gives the internal virtual work as

$$\delta W^{int} = \sum_{i=1}^{\#el} \int_{V_i'} \delta\hat{\underline{\varepsilon}}'^{T}(\hat{\underline{\sigma}}^{b} + \hat{\underline{\sigma}}')\, dV' \tag{4.19}$$

The strain, $\hat{\underline{\varepsilon}}'$, is given by the element deformation, $\hat{\underline{u}}'$, and a differential operator, $\hat{\underline{D}}_f$, as

$$\hat{\underline{\varepsilon}}' = \hat{\underline{D}}_f \hat{\underline{u}}' \tag{4.20}$$

For small deformation, $\hat{\underline{D}}_f$ can be written in convected coordinates. The change in nodal displacements in convected coordinates, $\hat{\underline{d}}_i'$, is then used to describe the element deformation by the shape function, $\underline{N}'$, giving

$$\hat{\underline{u}}' = \underline{N}'\hat{\underline{d}}_i' \tag{4.21}$$

The changes in nodal displacements are found using the convected-to-global coordinates rotation matrix, Q', and the change in nodal displacements in the global system, $\underline{d}_i'$,

$$\hat{\underline{d}}_i' = Q^{T}\underline{d}_i' \tag{4.22}$$

Combining Equations 4.20 to 4.22 and taking the first variation give

$$\delta\hat{\underline{\varepsilon}}' = \hat{\underline{B}}' Q^{T}\delta\underline{d}_i' \tag{4.23}$$

where $\hat{\underline{B}}'$ is $\hat{\underline{D}}_f' \underline{N}_i'$. Substituting Equation 4.23 into Equation 4.19 gives the expression for the internal virtual work as

$$\delta W^{int} = (\delta\underline{d}_i')^{T}\sum_{i=1}^{\#el} Q' \int_{V_i'} (\hat{\underline{B}}^{T}\hat{\underline{\sigma}}^{b} + \hat{\underline{B}}^{T}\hat{\underline{\sigma}}')\det|\hat{\underline{F}}'|\, dV' \tag{4.24}$$

with $\hat{\underline{B}}^{T}\hat{\underline{\sigma}}^{b}$ being the baseline internal virtual work and $\hat{\underline{B}}^{T}\hat{\underline{\sigma}}'$ being the change in

internal virtual work from the from the time of the update.

The external virtual work expression remains as described in Chapter 2. That is,

$$\delta W^{ext} = \sum_{i=1}^{\#el} \left[(\delta \underline{d}_i')^T \underline{f}_i^{ext} - (\delta \underline{d}_i')^T \underline{m}_i \ddot{\underline{d}}_i \right] \tag{4.25}$$

Using Equations 4.24 and 4.25 and letting

$$\underline{f}_{ibl}^{int} = Q' \int_{V_i} \hat{\underline{B}}^T \hat{\underline{\sigma}}^b \det |\hat{\underline{F}}'| \, dV \tag{4.26}$$

and

$$\Delta \underline{f}_i^{int} = Q' \int_{V_i} \hat{\underline{B}}^T \hat{\underline{\sigma}}' \det |\hat{\underline{F}}'| \, dV \tag{4.27}$$

give

$$\sum_{i=1}^{\#el} (\delta \underline{d}_i')^T \left[\underline{m}_i \ddot{\underline{d}}_i + \underline{f}_{ibl}^{int} + \Delta \underline{f}_i^{int} - \underline{f}_i^{ext} \right] = 0 \tag{4.28}$$

As the virtual displacement is assumed to be arbitrary, the bracketed quantity after assemblage must identically be equal to zero. Therefore, assemblage of the system gives

$$\underline{M} \ddot{\underline{d}} + \underline{F}^{int} + \Delta \underline{F}^{int} - \underline{F}^{ext} = \underline{0} \tag{4.29}$$

To find the quantity of interest, $\ddot{\underline{d}}$, Equation 4.29 is rearranged to give

$$\ddot{\underline{d}} = \underline{M}^{-1} (\underline{F}^{ext} - \underline{F}^{int} - \Delta \underline{F}^{int}) \tag{4.30}$$

The use of a lumped mass matrix reduces the process of inversion to a simple reciprocal of each diagonal term.

4.3 Formulation implementation

The implementation of the updated co-rotational approach in a computer code requires calculation of the change in the internal nodal forces and a modified time

integration scheme due to the use of the change in displacements from the previous update. The implementation is illustrated by using an existing co-rotational coordinate code LADDAS [75] (Large Displacement Dynamic Analysis of Space Frames). The original LADDAS is designed as a 3-D frame element code using explicit time integration and the traditional co-rotational approach.

4.3.1 Planar-frame element internal forces

As detailed above, the internal forces consist of the change in internal forces and the base-line internal forces. The calculation of both is shown. The changes in internal forces, $\Delta \underline{F}^{int}$, are evaluated based on the changes in displacements, $\Delta \underline{d}$. A simple moment-curvature relationship is derived for a frame element which is superposed by an axial force-displacement relationship. x This relationship is based on the same assumptions used for the internal force calculations in the traditional co-rotational approach detailed in Chapter 2.

The use of direct stiffness calculation for the moment-curvature relationship eliminates the need for assuming shape functions and calculating strains (or deformation gradients) as shown in the general formulations. However, the basic concept of updated material frame (or base-line frame geometry) can be more adequately demonstrated without involving complicated matrix or tensor operations.

The moment-curvature relationship used for small total deformation of an element is based on the geometry shown in Figure 4.2. The two relevant geometries are the base-line geometry with nodal coordinates x_i^{bl} and y_i^{bl}, end rotations θ_{iz}, and length l,

and the current geometry defined by the change in displacements and rotations u_i', v_i', and ϕ_{iz}. The rigid-body rotation between the two geometries is now defined by the cross product relation

$$\psi_z = \sin^{-1}\left[\left| \underset{\sim}{e}_{bl} \times \underset{\sim}{e}' \right|\right] \tag{4.31}$$

where $\underset{\sim}{e}_{bl}$ is the base-line unit vector and $\underset{\sim}{e}'$, is the current unit vector. Using the convected coordinates to separate out the rigid body displacements gives the current geometry as $\hat{\phi}_{1z}$, $\hat{\phi}_{2z}$, and l' shown in Figure 4.3. The element internal forces are a combination of the base-line forces, $\underset{\sim}{f}_i^{bl}$, which are stored from the latest update and the change in forces, $\Delta\underset{\sim}{f}_i$. Letting $\alpha_{iz} = \hat{\phi}_{iz} - \theta_{iz}$ (i=1,2) and assuming a linear elastic simple beam theory and all the end slopes due to deformation being small, the changes in forces are

$$\Delta m_{1z} = \frac{2EI_z}{l'}(2\alpha_{1z} + \alpha_{2z}) \tag{4.32a}$$

$$\Delta m_{2z} = \frac{2EI_z}{l'}(\alpha_{1z} + 2\alpha_{2z}) \tag{4.32b}$$

$$\Delta f_{1x} = \frac{EA}{l}(l - l') \tag{4.32c}$$

The other three remaining incremental force components are found by setting the element into static equilibrium which gives

$$\Delta f_{1y} = \frac{(\Delta m_{1z} + \Delta m_{2z})}{l'} \tag{4.33a}$$

$$\Delta f_{2y} = -\Delta f_{1y} \tag{4.33b}$$

$$\Delta f_{2x} = -\Delta f_{1x} \tag{4.33c}$$

The incremental internal forces are then transformed to the global system for assemblage using the same relationship as shown in the traditional co-rotational

approach

$$\Delta \underset{\sim}{F}^{int} = \underset{\sim}{T}_d^T \Delta \underset{\sim}{f}^{int} \tag{4.34}$$

with $\underset{\sim}{T}_d$ being the transformation defined by

$$\underset{\sim}{F}^{int} = \underset{\sim}{T}_d^T \underset{\sim}{f}^{int} \tag{4.35}$$

where $\underset{\sim}{T}_d$ is the transformation matrix between the current convected coordinates to the global coordinates.

The base-line forces for each element must be treated for the rotation of the element after the update. These forces may be thought of as "residual forces" which remain fixed in magnitude and direction relative to the element while the element rotates. Figure 4.4 shows the element at the moment of the update with the new base-line forces shown. As this element rotates and translates to its new position after the update, these forces rotate with it as shown in Figure 4.5. These forces must be rotated back to global coordinates using the rigid-body rotation angle, θ_z, which was calculated in order to determine the change in internal forces. This relation is

$$\underset{\sim}{f}_{ibl}^{int} = Q' \, \hat{\underset{\sim}{f}}_{ibl}^{int} \tag{4.36}$$

where

$$Q' = \begin{bmatrix} \cos(\theta_{iz}) & \sin(\theta_{iz}) \\ -\sin(\theta_{iz}) & \cos(\theta_{iz}) \end{bmatrix} \tag{4.37}$$

for a planar problem.

4.3.2 Plane-stress/strain element internal forces

The updated approach for the plane stress/strain element used in the current research is a similar to the approach used for the frame element. This is possible as the

element uses linear-elastic material properties allowing superposition.

The change in internal forces are calculated using the change in displacements, Δu_i, and Δv_i, and the updated nodal coordinates in the same equations as shown in Chapter 2. The (approximate) rigid body rotation, θ', is calculated as

$$\theta' = \arctan\left[\frac{y_4\Delta v_2 - y_2\Delta v_4 + x_4\Delta u_2 - x_2\Delta u_4}{4A + y_4\Delta u_2 - y_2\Delta u_4 - x_4\Delta v_2 + x_2\Delta v_4}\right] \tag{4.38}$$

The change in deformation displacements, Δu^{def} and Δv^{def}, are then given by using θ'

$$\begin{Bmatrix}\Delta u_i^{def}\\ \Delta v_i^{def}\end{Bmatrix} = \underline{a} \begin{Bmatrix}\Delta u_i\\ \Delta v_i\end{Bmatrix} + (\underline{a}' - \underline{I})\begin{Bmatrix}x_i\\ y_i\end{Bmatrix} \quad (i=2,3,4) \tag{4.39}$$

with all displacements and coordinates being relative to node 1, $\underline{I}$ being the identity matrix, and $\underline{a}'$ given by

$$\underline{a}' = \begin{bmatrix}\cos\theta' & \sin\theta'\\ -\sin\theta' & \cos\theta'\end{bmatrix} \tag{4.40}$$

These changes in displacements are then used to find the change in internal forces for the element using the same relationship as in Chapter 2.

$$\Delta\underline{f}_e^{int} = \underline{k}_e\, \Delta\underline{d}_e^{def} \tag{4.41}$$

where $\Delta\underline{d}_e^{def}$ are the change in deformation displacements given by Equation 4.39 and $\underline{k}_e$ is the element stiffness matrix for a standard 4-node isoparametric planar element given in Chapter 2. The values in the stiffness matrix are now calculated with the updated geometry in place of the original geometry.

The element forces given in Equation 4.41 are in the convected coordinates. The transformation to global coordinate forces, $\Delta\underline{f}_{egl}^{int}$, is accomplished using the $\underline{a}'$ matrix

defined in Equation 4.40 giving

$$\Delta \underset{\sim}{f}_{egl}^{int} = \underset{\sim}{A}^T \Delta \underset{\sim}{f}_{e}^{int} \tag{4.42}$$

with $\underset{\sim}{A}^T$ defined by

$$\underset{\sim}{A}^T = \begin{bmatrix} \underset{\sim}{a}^T & 0 & 0 & 0 \\ 0 & \underset{\sim}{a}^T & 0 & 0 \\ 0 & 0 & \underset{\sim}{a}^T & 0 \\ 0 & 0 & 0 & \underset{\sim}{a}^T \end{bmatrix} \tag{4.43}$$

The base-line forces must also be updated at each time step to reflect any rigid-body rotation in the element. This is accomplished using the $\underset{\sim}{a}'$ matrix from Equation 4.40 and the relationship used for the planer-frame element in Equation 4.36.

4.3.3 Axisymmetric element internal forces

The non-linear material model used in the axisymmetric solid element dictates a different method be used for the calculation of the internal forces. Superposition of change in internal force and base-line force is not acceptable. Instead, the assumption of small deformations between updates allows the use of a linear kinematic relationship throughout the problem and the superposition of strain is possible. Therefore, the change in displacements, $\Delta \underset{\sim}{d}_e$, are used to calculate the change in strain, $\Delta \underset{\sim}{\varepsilon}$, using the same type of relationship as used in the total formulation for the axisymmetric element

$$\Delta \underset{\sim}{\varepsilon} = \underset{\sim}{B}\, \Delta \underset{\sim}{d}_e \tag{4.44}$$

where $\underset{\sim}{B}$ is the matrix of shape function derivatives for the 4-node isoparametric element using the current geometry.

Even though the co-rotational approach is not used in the axisymmetric element

formulation, the angle of rigid-body rotation between the base-line and current geometries, θ' of Equation 4.38, must still be calculated. This is due to the need to update the base-line strain for the rotation of the element between updates. The base-line strain is transformed from the local coordinates to the global coordinates using a standard second-order tensor transformation

$$\underline{\varepsilon}^{gl} = a'_{ik} a'_{jl} \underline{\varepsilon}^{local}_{ij} \quad (i,j=1,2,3) \tag{4.45}$$

where a'_{ij} are the components of the transformation matrix defined in Equation 4.40.

4.4 Time integration

For the updated approach, the incremental displacement, Δd_t, is computed instead of the total displacement, d_t. The explicit algorithm should be slightly modified to give the total displacement at time $t+\Delta t$

$$d_{t+\Delta t} = d' + \Delta d_{t+\Delta t} \tag{4.46}$$

where d' is the base-line displacement from the previous geometry update. For each time increment, Δt, the displacement changes from Δd_t to $\Delta d_{t+\Delta t}$ and

$$\Delta d_{t+\Delta t} = \Delta t^2 \left[\frac{(F^{ext} - F^{int}_{bl} - \Delta F^{int})}{M} \right] + 2\Delta d_t - \Delta d_{t-\Delta t} \tag{4.47}$$

where F^{int}_{bl} is the internal force at the base-line. When the incremental displacement from the latest update reaches a tolerance limit, the base-line state is updated. The nodal coordinates, x^{bl} and y^{bl}, of the baseline state are updated to

$$x^{bl}_{new} = x^{bl} + \Delta d_{xt} \tag{4.48a}$$

$$y^{bl}_{new} = y^{bl} + \Delta d_{yt} \tag{4.48b}$$

and the base-line displacements are updated to

$$d'^{new} = d_t \tag{4.49}$$

The baseline internal forces, F_{bl}^{int}, are updated at the element level by adding ΔF^{int}. The time integration should then be "restarted" to allow for the updating of the nodal coordinates. The new starting values for Equation 4.47 are

$$\Delta d_{t-\Delta t} = 0 \tag{4.50a}$$

$$\Delta d_t = \Delta d_{t+\Delta t} - \Delta d_t \tag{4.50b}$$

The new base-line velocity and acceleration are

$$\dot{d} = \frac{(\Delta d_{t+\Delta t} - \Delta d_{t-\Delta t})}{2\Delta t} \tag{4.51}$$

and

$$\ddot{d} = \frac{(\Delta d_{t-\Delta t} - 2\Delta d_t + \Delta d_{t+\Delta t})}{\Delta t^2} \tag{4.52}$$

Without going through rigorous studies, the time increment limits originally derived for the traditional approach seem applicable for the present updated algorithm and can be approximated by

$$\Delta t \leq \frac{2}{\omega^{max}} \tag{4.53}$$

where ω^{max} is the maximum frequency of the element given for the axial mode

$$\omega^{max} = \frac{2}{l}\left[\frac{E}{\rho}\right]^{\frac{1}{2}} \tag{4.54}$$

or the bending mode

$$\omega^{max} = n^2\pi^2\left[\frac{EI}{\rho A l^4}\right]^{\frac{1}{2}} \tag{4.55}$$

where

A= Cross–sectional Area

I= Second Moment of Inertia About Axis of Vibration

E= Young's Modulus l= Element Length

ρ= Mass Density n= 1.2

4.5 Numerical results

A simple frame code, LADDAS, has been modified to accommodate the updated geometry. A series of example problems is shown in order to compare the modified code's capabilities to those of the traditional co-rotational approach as well as an Updated Lagrangian formulation.

Problem 4.1 is a beam fixed at both ends subjected to a rectangular pulse loading of 10 kips applied at the center of the span. Symmetry is used in modeling the beam with 10 elements each being 12 inches long. The modulus of elasticity, E, is 3×10^7 pounds/in^2 and the mass density, ρ, is 4.567×10^{-3} pounds–sec^2/in^4. The second moment of inertia about the z-axis, I_z, is 100 in^4 and the cross sectional area, A, is 21.9 in^2 (These section and material properties will be used for Example problems 2 through 4 also). The beam geometry and load history are shown in Figure 4.6 The time history of the mid-span displacement in Figure 4.7 is shown along with the same time history calculated using the original LADDAS code. The results from the two codes match closely indicating the modified code does not lose accuracy in smaller deflection problems.

Problem 4.2 is an undamped cantilever beam subjected to a ramp loading at the tip

shown in Figure 4.8. The loading causes an extremely large deflection of the beam. The tip displacement time history in Figure 4.9 shows the traditional co-rotational approach adopted in the LADDAS code does not yield a stable solution whereas the modified approach does.

Problem 4.3 considers a quasi-static problem. The solution is obtained by attenuating the transient response with the introduction of artificial damping for each load (or time) increment. The artificial damping is denoted as $\alpha=\frac{C}{M}$ where C and M are from the equation of motion $M\ddot{x} + C\dot{x} + Kx = F^{ext}$. For this problem through trial and error, α is set as 120 sec^{-1}. In this problem, a cantilever beam is subjected to an end moment time history, M(t), as shown in Figure 4.10. The two plateaus are arbitrarily selected such that $M(t_{p1}) = 2\pi EI/l$ should deform the beam into a complete circle and $M(t_{p2}) = 4\pi EI/l$ should cause the beam to wrap around itself another time. The traditional co-rotational algorithm was not able to handle the extremely large rotations encountered in this problem but as seen in Figure 4.11, the modified code shows very close agreement to the expected solutions.

Problems 4.4 and 4.5 are similar to the problems considered in Bathe, et al [9]. They are intended to show the modified algorithm in comparison to Total and Updated Lagrangian formulations. The original problems were used as examples of the ability of the then newly developed code NONSAP to handle the geometric non-linearities encountered in large deflection problems and that Total and Updated Lagrangian formulations yield the same results.

Problem 4.4 is a quasi-static solution of a uniformly loaded cantilever beam as shown in Figure 4.12. The modulus of elasticity is 1.2×10^4 psi, Poisson's ratio is 0.2, and the mass density is 1×10^{-6} lbs–sec^2/in^4. The mesh is made up of 4-node isoparametric elements in the modified algorithm, and 8-node isoparametric elements in the Updated Lagrangian formulation. Tip deflections using both formulations are shown for 5 different loadings in Figure 4.13.

Problem 4.5 considers transient response of the same problem as Problem 4.4 with no damping and the loading as shown in Figure 4.14. The time step for the modified algorithm using central difference explicit time integration is 2×10^{-6} seconds and for the Total Lagrangian formulation using Newmark time integration (δ=0.50 and α=0.25) is 4.55×10^{-5} seconds. The Total Lagrangian algorithm also introduces equilibrium iterations which are not used in the modified code. The results from both codes are shown in Figure 4.15 for comparison.

One of the critical questions in the development of a large deformation algorithm for a continuum is the variation of material parameters due to geometrical changes. As a preliminary comparison, the variation is ignored herein, which leads to some discrepancies in the comparison. Constant values of elastic moduli and mass density were used in all the algorithms. For thin-walled structures, such as a cantilever beam, subjected to large displacement, the discrepancies are expected to be small. This is shown in Figures 4.13 and 4.15.

Problem 4.7 is an example of a structure undergoing extremely large displacement and deformation throughout its load history. The load history and structure geometry

are shown in Figure 4.16. Figure 4.17 shows the deformed configurations at 0.03 second time intervals.

Problem 4.8 is Problem 3.2 reaccomplished using the updated formulation to show the need for the modified method. Figure 4.18 shows the traces of the fragmented element end-nodes for both the traditional and updated approaches. The updated approach is capable of tracking elements through over 720° of rotation with the elements not suffering the large distortions found in the traditional code. Figures 4.19 and 4.20 show the deformed configurations for both formulations at 0.1 second intervals.

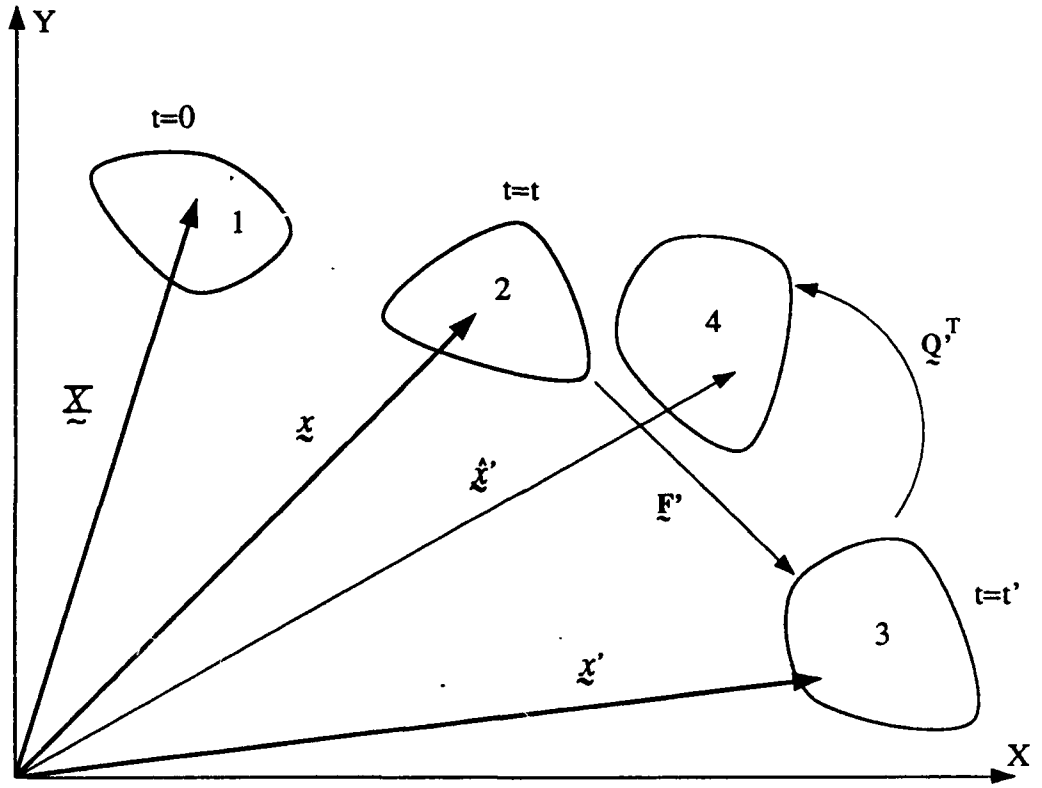

Figure 4.1 Stages of deformation in updated geometry formulation

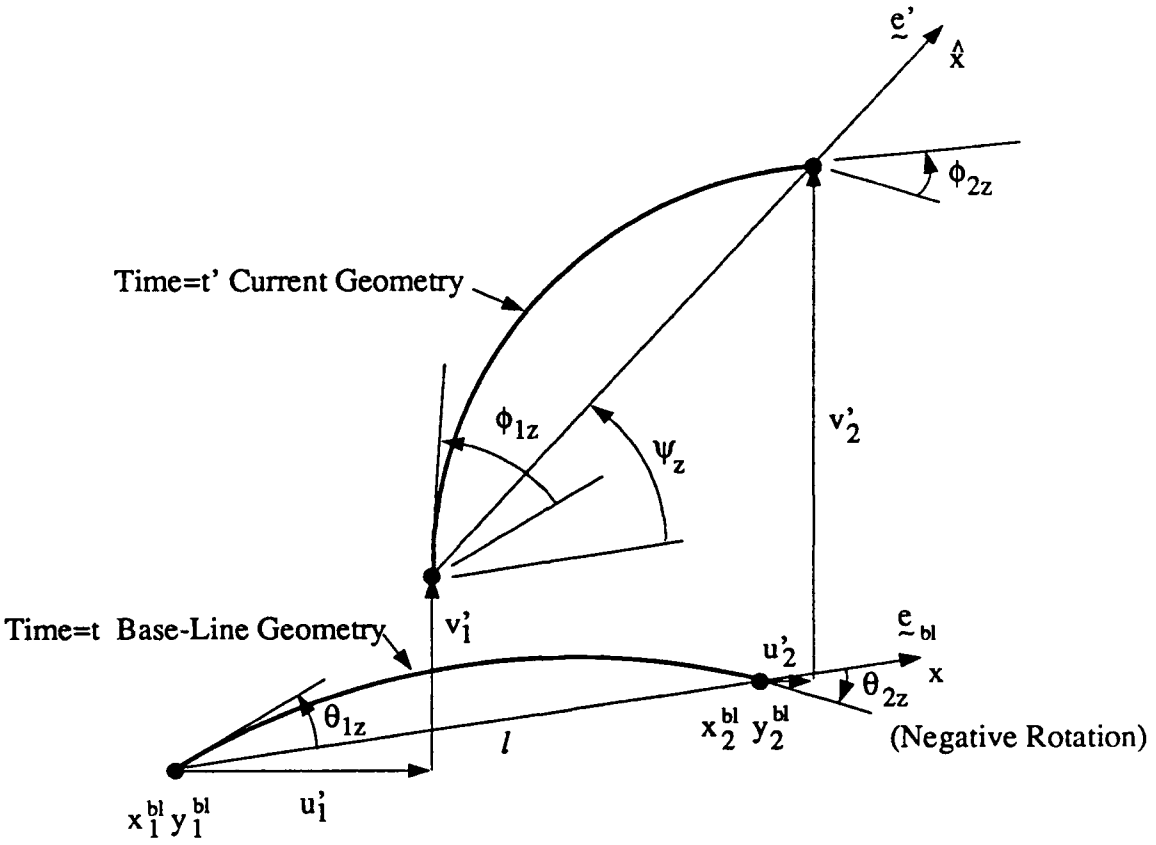

Figure 4.2 Base-line and current geometries

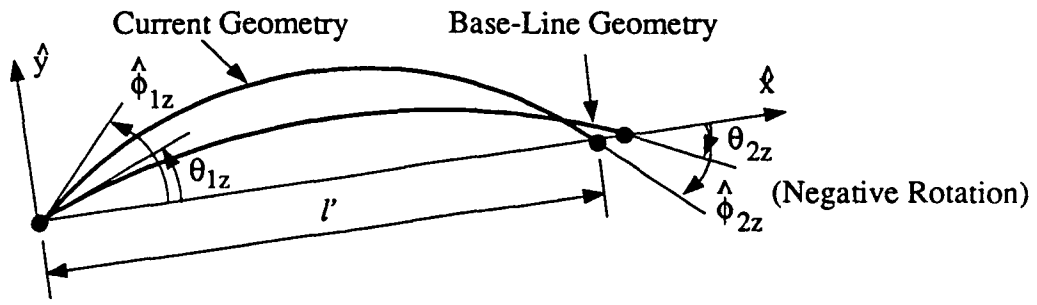

Figure 4.3 Base-line and current geometries with rigid body motion removed

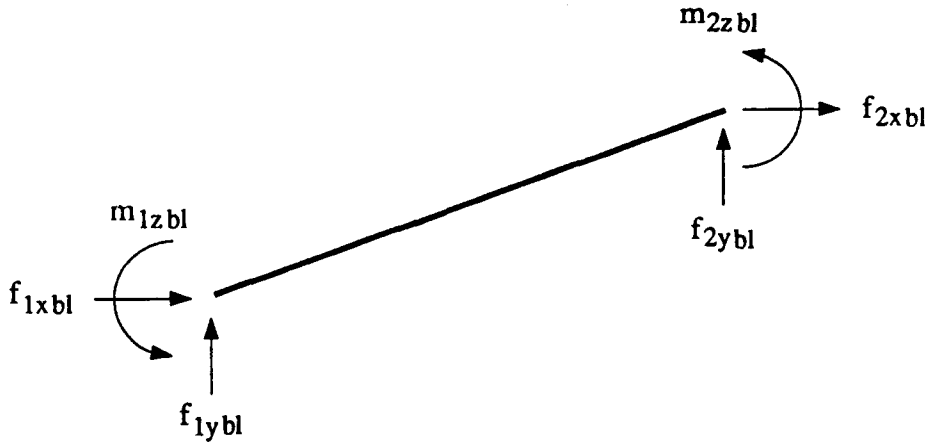

Figure 4.4 Element base-line forces

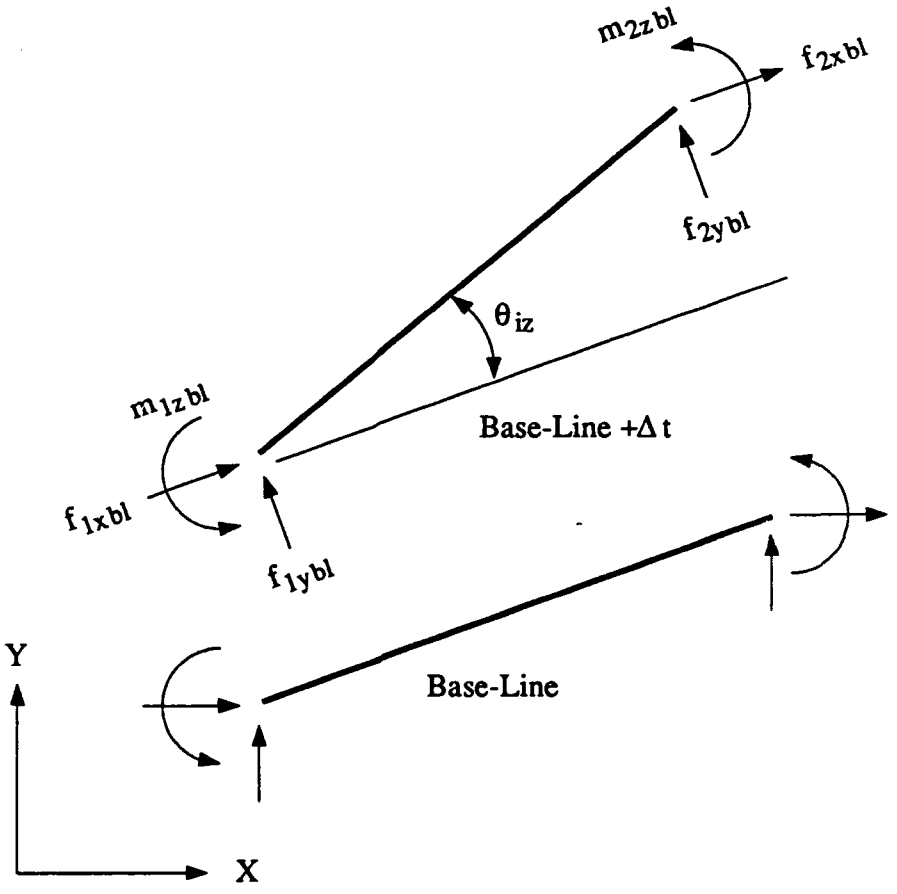

Figure 4.5 Base-line internal forcesΔt after update

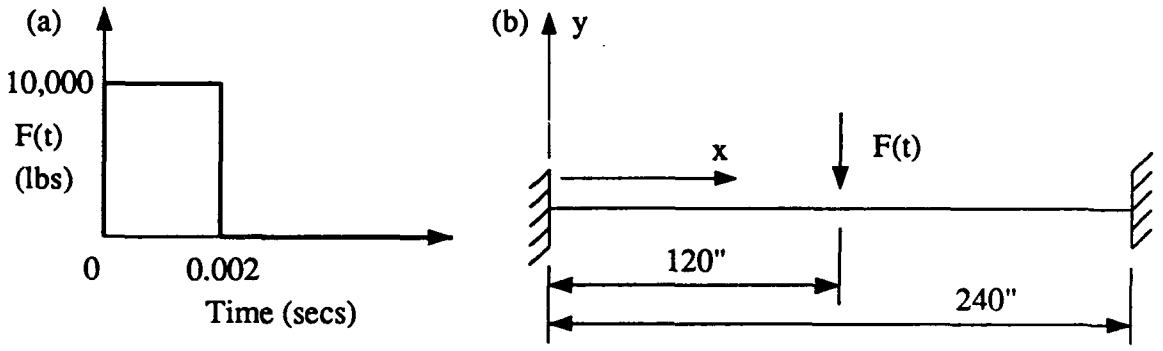

Figure 4.6 Problem 4.1 (a) load history and (b) geometry

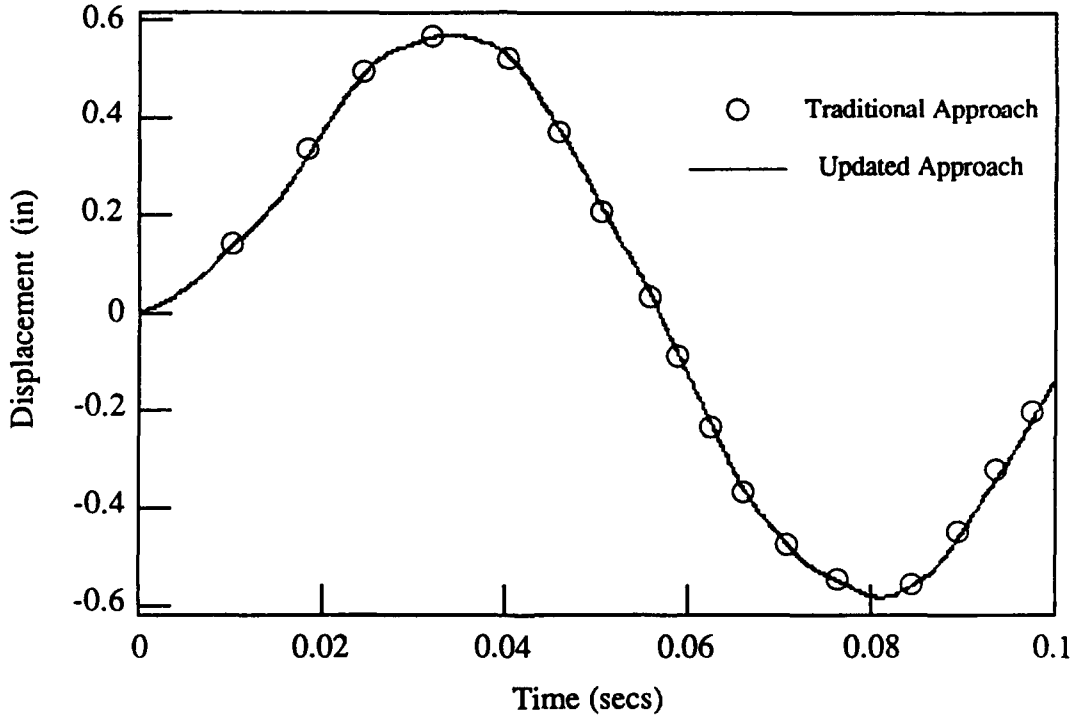

Figure 4.7 Problem 4.1 mid-span displacement history

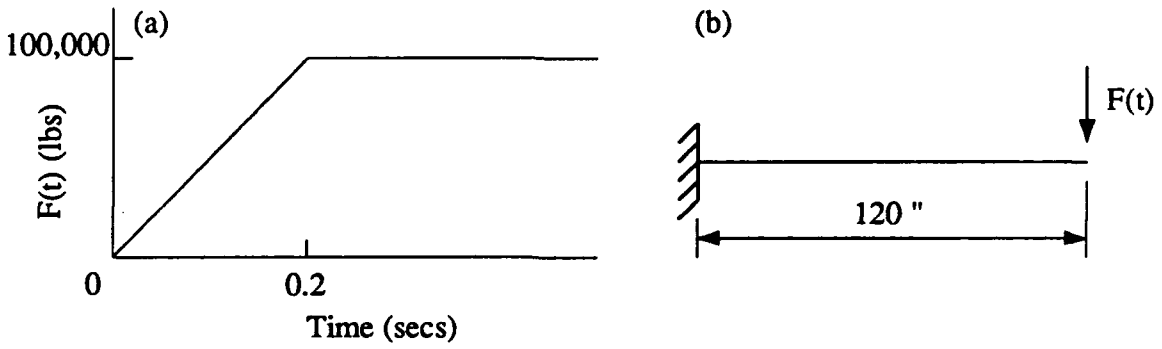

Figure 4.8 Problem 4.2 (a) load history and (b) geometry

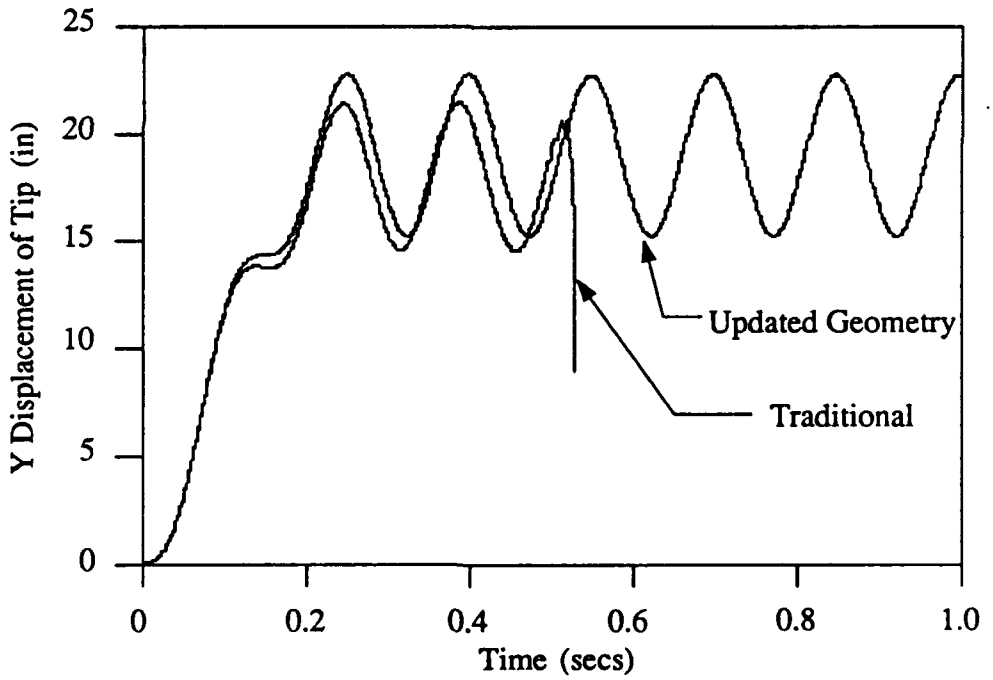

Figure 4.9 Problem 4.2 tip deflection showing comparison of traditional and updated approaches

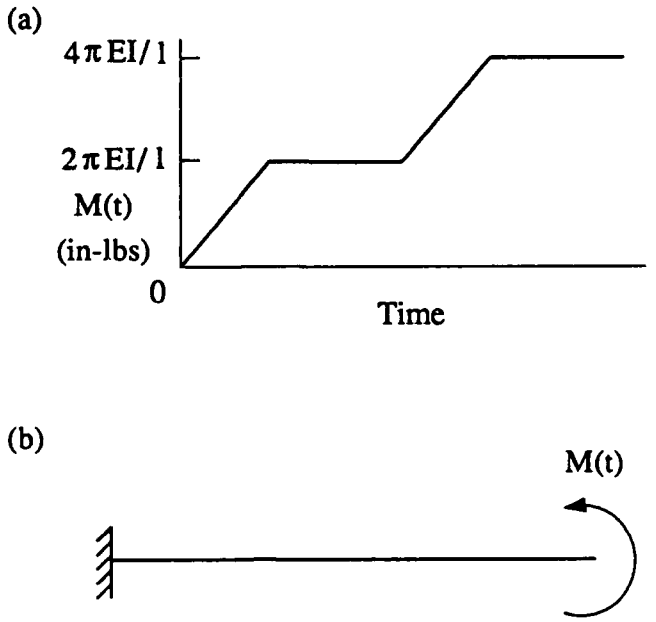

Figure 4.10 Problem 4.3 (a) load history and (b) geometry

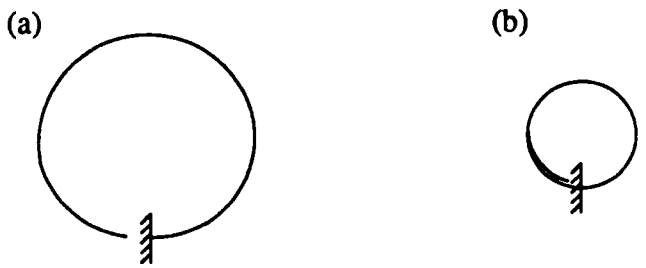

Figure 4.11 Problem 4.3 deformed configurations at (a) M=2πEI/l and (b) M=4πEI/l

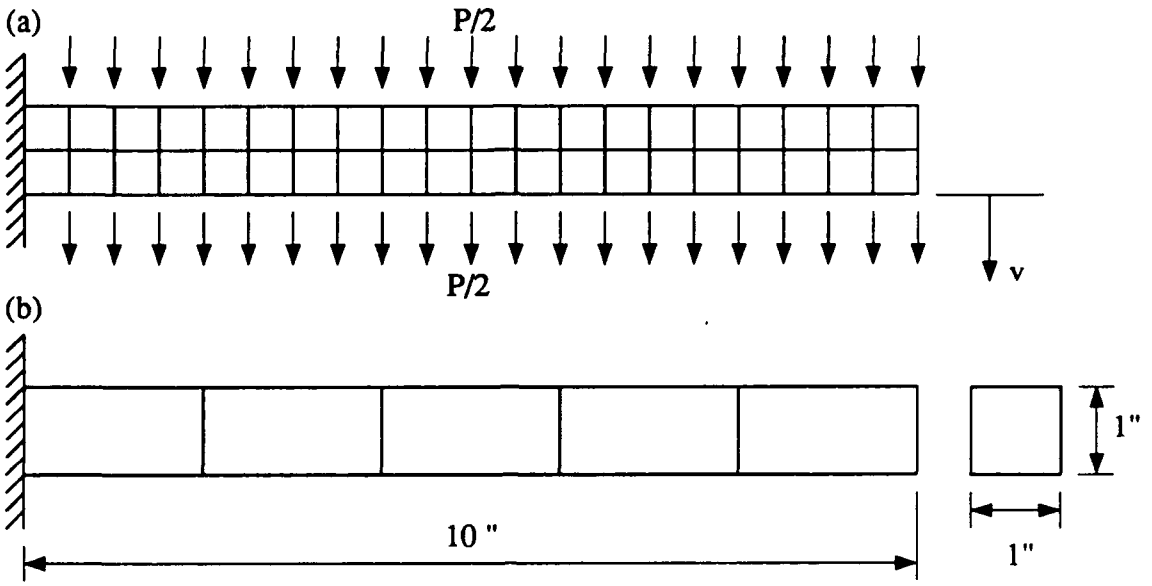

Figure 4.12 Problem 4.4 (a) 4-node element mesh showing loading and (b) 8-node element mesh showing geometry

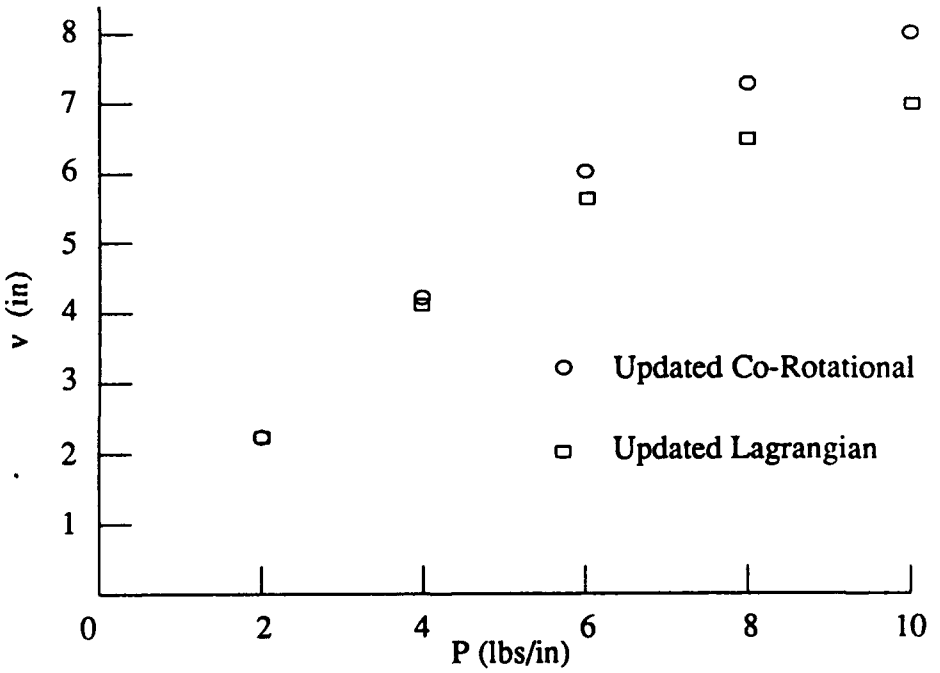

Figure 4.13 Problem 4.4 tip deflection versus load for updated lagrangian and updated co-rotational formulations

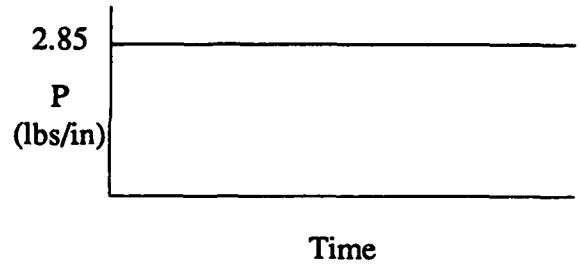

Figure 4.14 Problem 4.5 load history

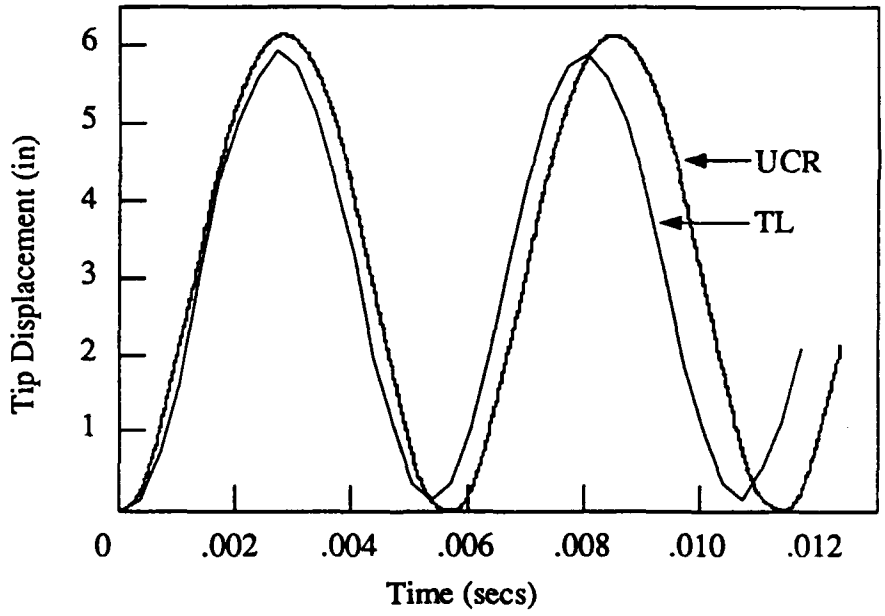

Figure 4.15 Problem 4.5 tip displacement history for updated lagrangian and updated co-rotational formulations

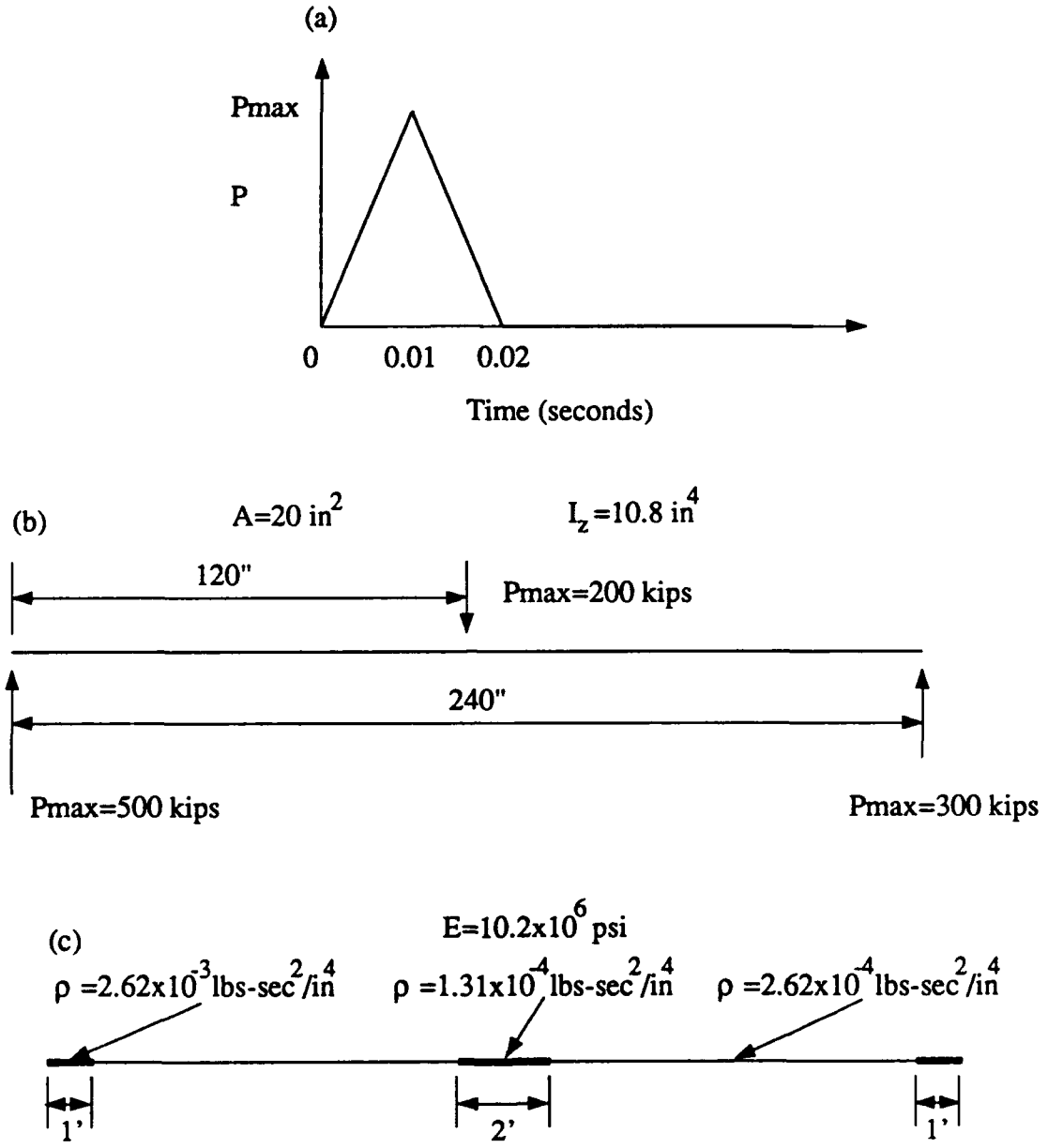

Figure 4.16 Problem 4.6 (a) force histories, (b) structure geometry, section properties, and loadings, and (c) material properties

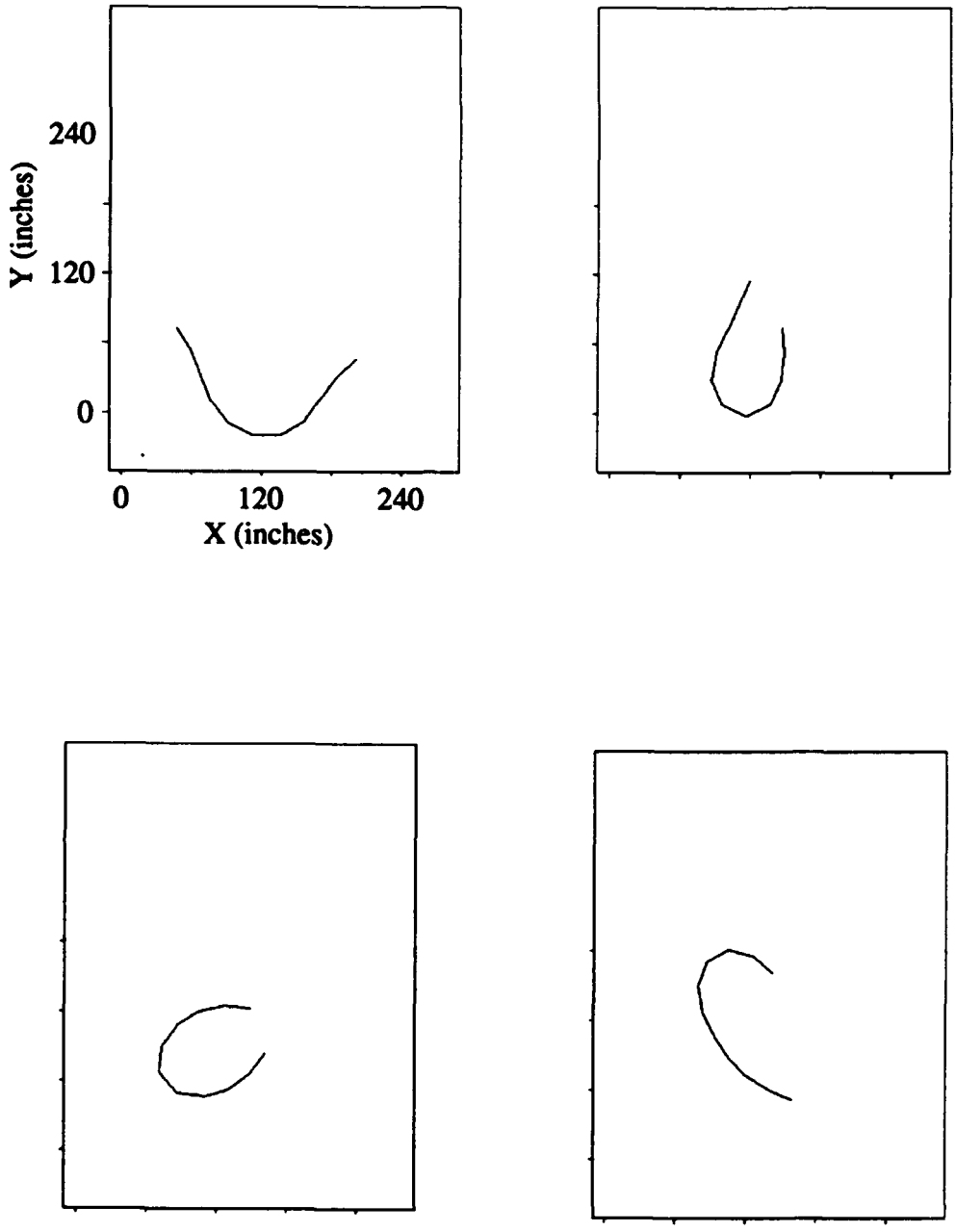

Figure 4.17 Problem 4.6 deformed configuration at 0.03, 0.06, 0.09, 0.12, 0.15, 0.18, 0.21, 0.24, 0.27, and 0.30 seconds

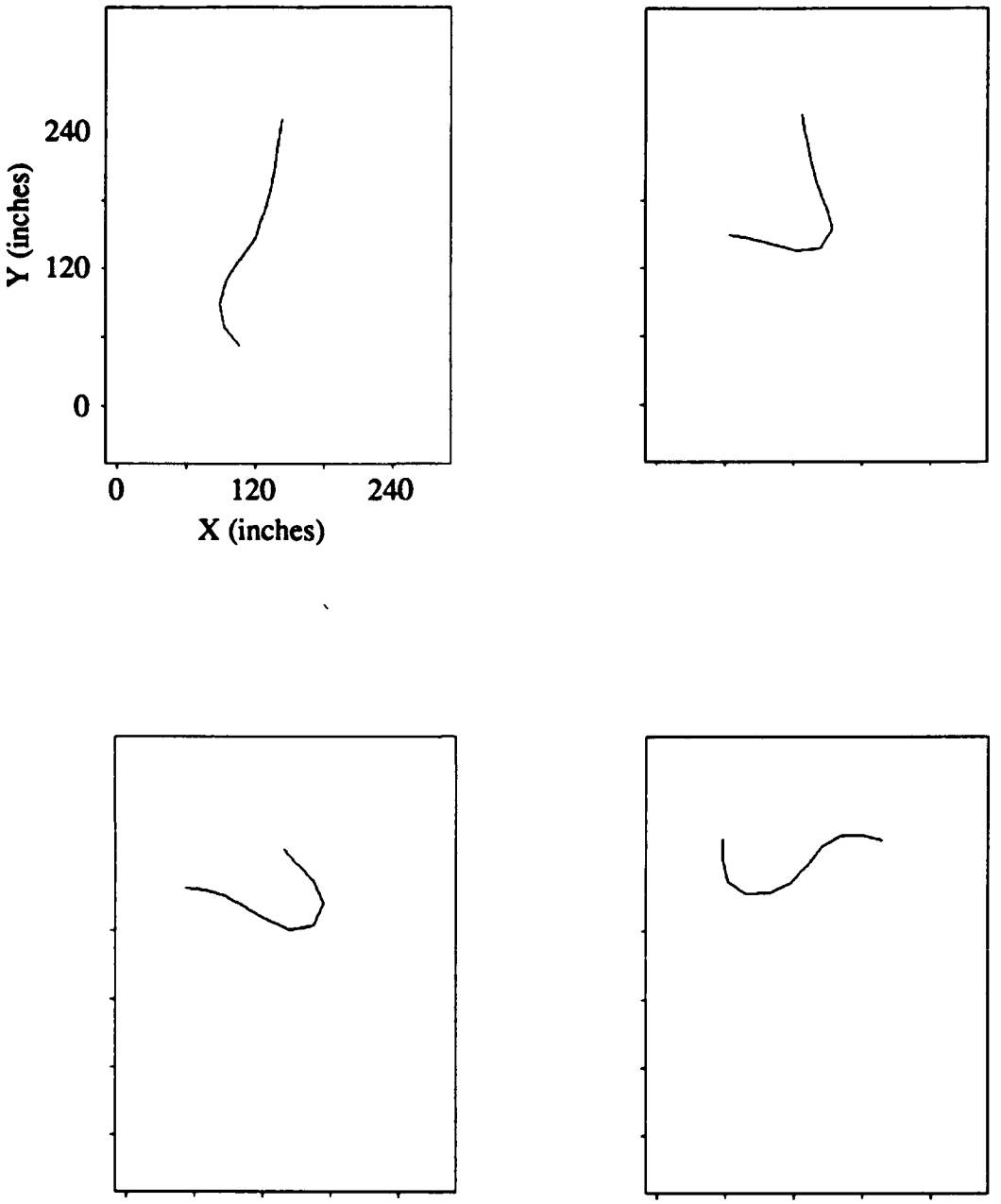

Figure 4.17, continued

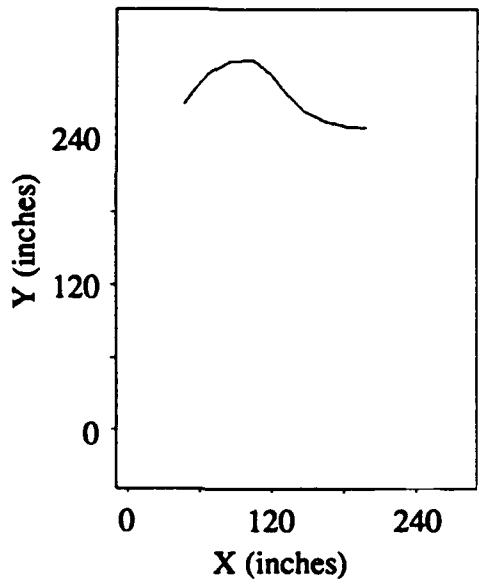

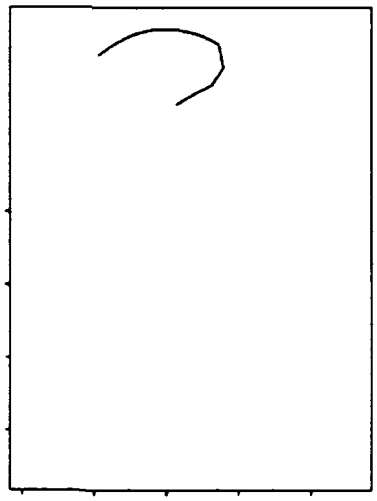

Figure 4.17, continued

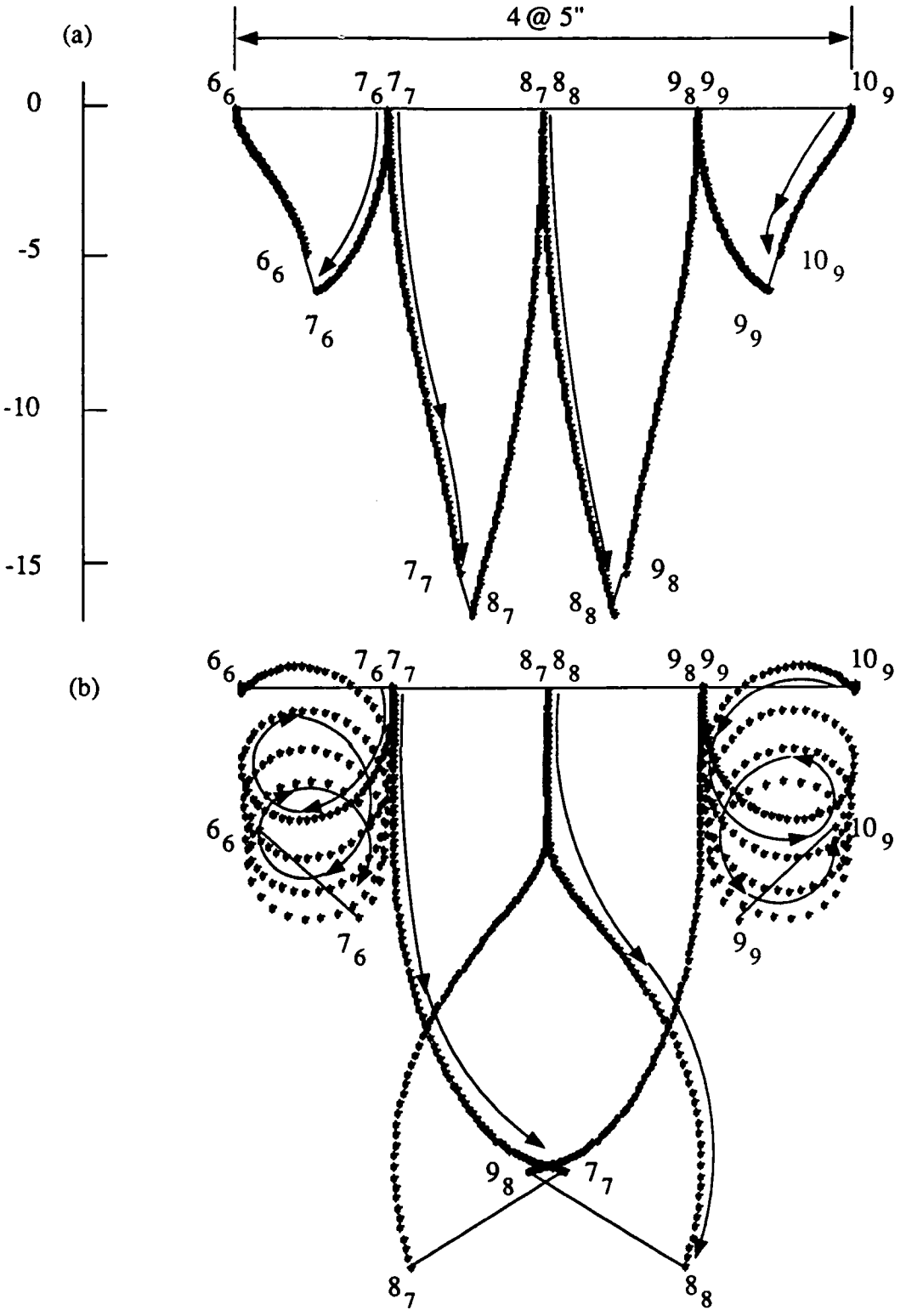

Figure 4.18 Displacement trace of fragments from Problem 3.2 for (a) traditional co-rotational and (b) updated formulations

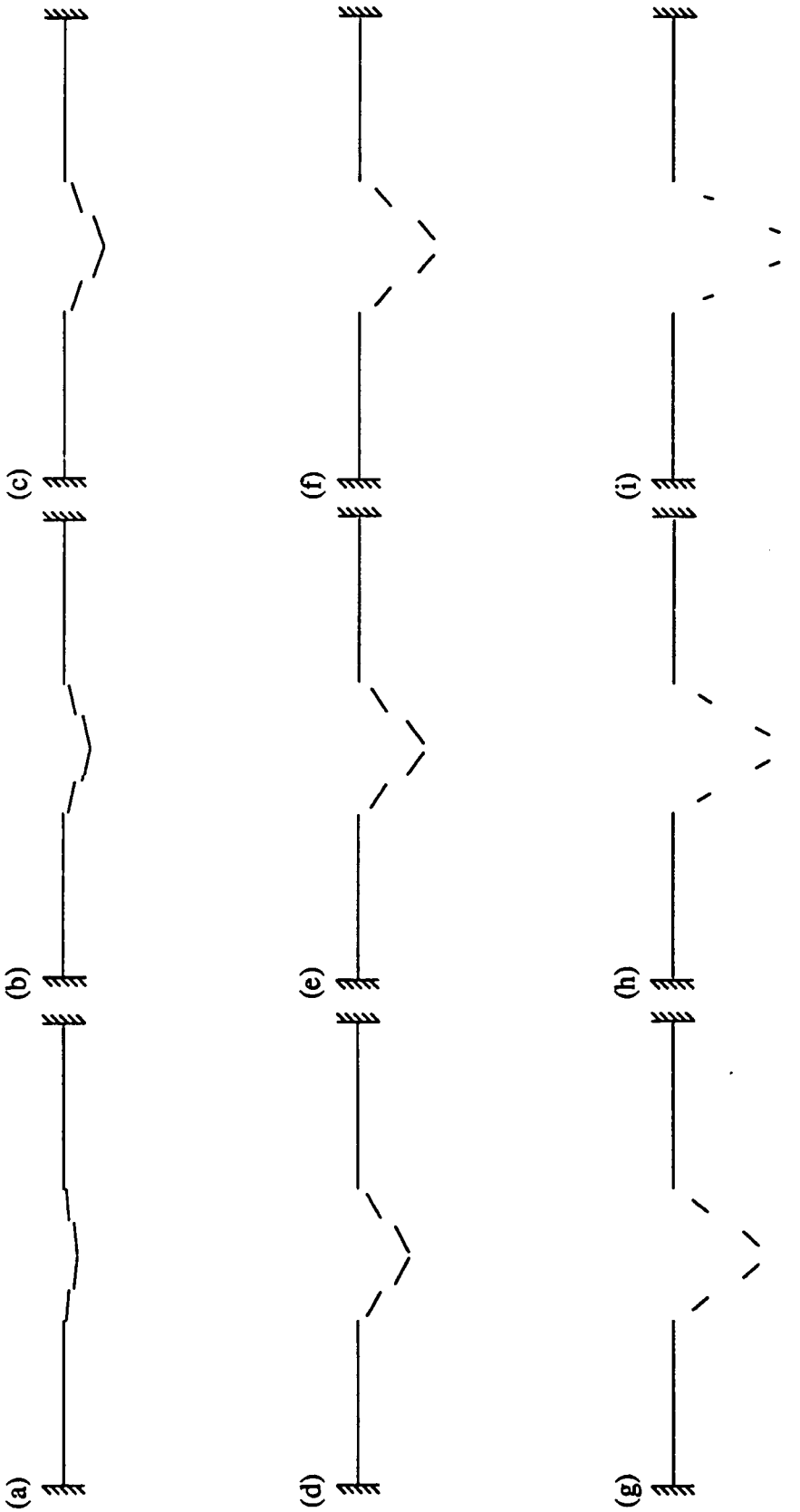

Figure 4.19 Displaced configuration of Problem 3.2 using the traditional co-rotational formulation at (a) 0.1, (b) 0.2, (c) 0.3, (d) 0.4, (e) 0.5, (f) 0.6, (g) 0.7, (h) 0.8, and (i) 0.9 seconds

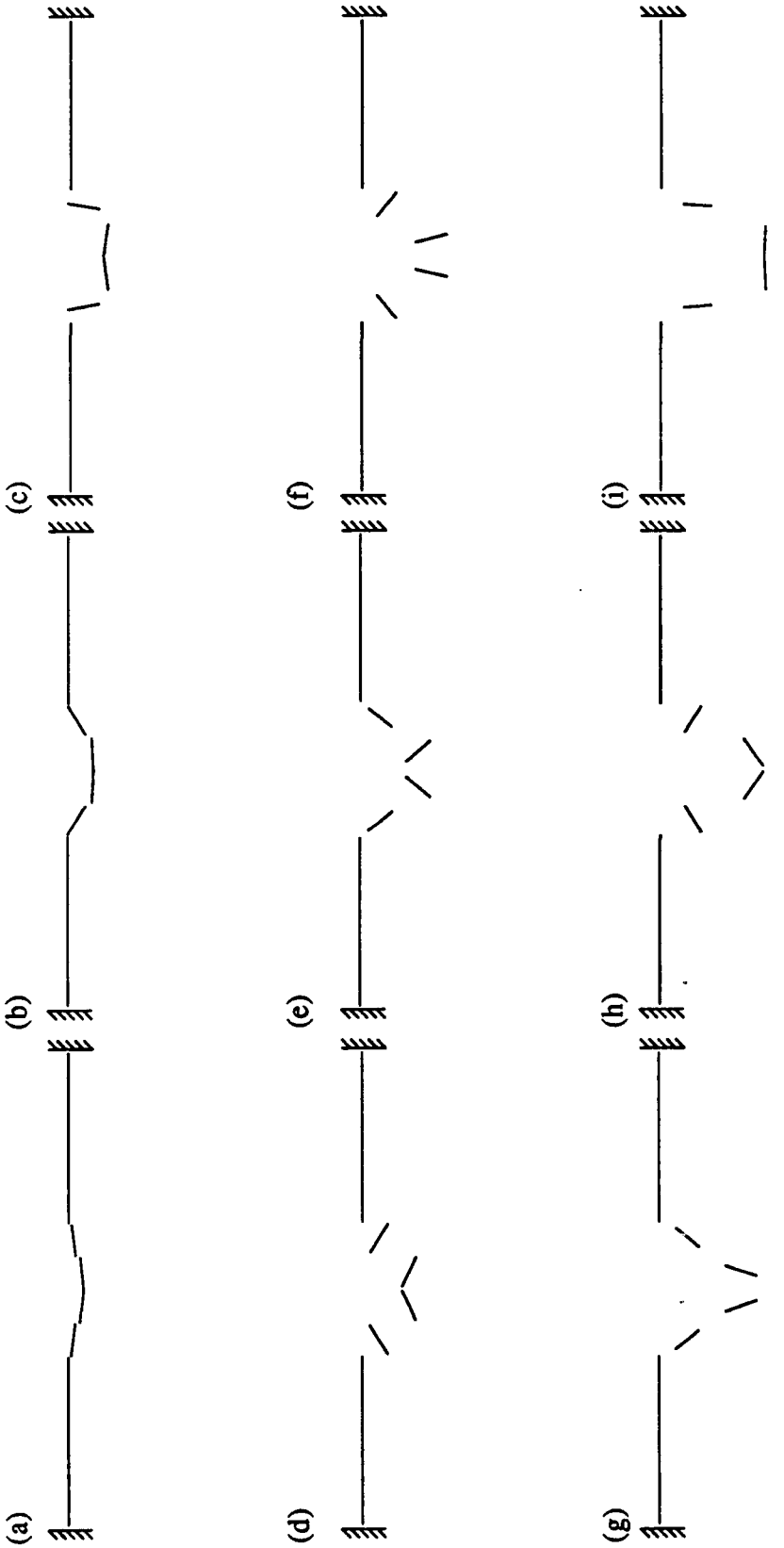

Figure 4.20 Displaced configuration of problem 3.2 using the updated geometry formulation at (a) 0.1, (b) 0.2, (c) 0.3, (d) 0.4, (e) 0.5, (f) 0.6, (g) 0.7, (h) 0.8, and (i) 0.9 seconds

CHAPTER 5 PROJECTILE IMPACT ON CONCRETE TARGETS

5.1 Introduction

The finite element codes developed earlier in this research are extended for the analysis of ballistic impact of non-deformable (rigid) projectiles on concrete targets. A range of impact velocities from below the sub-ordnance range to the lower limits of the ordnance region are studied. As the main emphasis of this research is directed to the ordnance range of impact, a majority of the examples involve impact velocities above 300 m/s.

For a better simulation analysis, it is necessary to introduce modifications into the finite element code to more closely model the phenomena present in the problem of impact. These modifications include:

- Elastic-plastic-fragment concrete material model

- Algorithm for contact and sliding surfaces

- Inter-element collision of fragmented target elements

5.2 Concrete material model

Incorporation of a concrete material model based on experimental data into the

finite element code is required if prediction of concrete impact behavior is expected. The material model chosen for the current study is a plasticity-based model proposed by Hsieh, Ting, and Chen [33] with the experimentally determined constants altered to account for strain rate effects. The plasticity model is chosen due to its close comparison to experimental data for uniaxial and multiaxial stress states and due to its ease of implementation in a finite element program.

The Hsieh-Ting-Chen model is based in classical formulations which are modified to represent the pre-failure incremental stress-strain behavior of plain concrete. The model uses a scaled down version of the failure surface to determine the initial yield surface before which, linear elastic behavior is assumed. Post-yield response is defined by assumed hardening and flow rules. A four-parameter failure surface determines at what stress states cracks are initiated in the concrete continuum. The state of stress at failure is then used to calculate the mode of failure and determines the corresponding post-failure response.

5.2.1 Failure criterion

As the initial yield surface used in the Hsieh-Ting-Chen four-parameter concrete model is of the same shape as the failure surface, the failure surface will first be described. The failure criterion for the model uses the stress invariants I_1 and J_2 defined as

$$I_1 = \sigma_1 + \sigma_2 + \sigma_3$$

$$J_2 = \frac{1}{6}[(\sigma_1-\sigma_2)^2 + (\sigma_2-\sigma_3)^2 + (\sigma_3-\sigma_1)^2]$$

(σ_i, i=1,2,3 are the principal stresses), the maximum principal stress, σ_1, the uniaxial compressive strength, σ_c', and four constants. The failure surface is described by the equation

$$A\frac{J_2}{\sigma_c'^2} + B\frac{\sqrt{J_2}}{\sigma_c'} + C\frac{\sigma_1}{\sigma_c'} + D\frac{I_1}{\sigma_c'} - 1 = 0 \qquad (5.1)$$

The constants A, B, C, and D are calculated based on experimental data for four stress-states at failure. The stress-states used to calibrate the constants are: 1) Uniaxial compression ($\sigma_1 = \sigma_2 = 0$, $\sigma_3 = -\sigma_c'$), 2) Uniaxial tension ($\sigma_1 = \sigma_t'$, $\sigma_2 = \sigma_3 = 0$), 3) Bi-axial compression ($\sigma_1 = 0$, $\sigma_2 = \sigma_3 = -\sigma_{bc}'$), and 4) Confined compression ($\sigma_1 = \sigma_2 = -\sigma_{pc}'$, $\sigma_3 = -\sigma_{cc}'$). A schematic representation of the failure surface is shown in Figure 5.1

5.2.2 Inelastic behavior

The initial yield surface and subsequent loading functions in the plasticity model are of the same shape as the failure surface. Therefore, they are described by Equation 5.1 with a hardening parameter τ substituted in the equation for σ_c'. τ is defined as a percentage of σ_c' with an initial value assumed between 0.25 and 0.35 x σ_c' for static analyses [56]. The use of the failure surface shape for loading functions ensures these surfaces are compatible at failure.

The size of the loading function for the material model is defined by an isotropic

hardening parameter τ which is an experimentally determined function of the effective plastic strain, $\varepsilon_p = \int\sqrt{d\varepsilon_{ij}^p d\varepsilon_{ij}^p}$ ($d\varepsilon_{ij}^p$ is the plastic strain increment). A mixed hardening rule is used with the loading function translation defined by its kinematic hardening parameter α_{ij}.

The value of τ is determined by an experimental relationship between τ and ε_p given as

$$d\tau = M\,H\,d\varepsilon_p$$

with M being the fraction of isotropic hardening (chosen as 0.2 from [84]) and H being the experimentally determined slope of the τ–ε_p curve in a uniaxial test. Labbane [56] uses a regression analysis of experimental data to calculate H as

$$H = \frac{\delta\tau}{\delta\varepsilon} = 1988\,\sigma_c'\,e^{-2650\varepsilon_p} \tag{5.3}$$

The rate of translation of the loading function, $d\alpha_{ij}$, in the kinematic hardening assumes the Ziegler hardening rule to give [56 from 95]

$$d\alpha_{ij} = \frac{H}{\tau}(1-M)\,d\varepsilon^p\bar{\sigma}_{ij} \tag{5.4}$$

with $\bar{\sigma}_{ij} = \sigma_{ij} - \alpha_{ij}$.

The hardening parameters and the loading function are used to formulate an incremental stress-strain relationship

$$d\sigma_{ij} = C_{ijkl}'\,d\varepsilon_{kl} \tag{5.5}$$

The term C_{ijkl}' is a tangential stiffness matrix which is a combination of the initial elastic modulus, C_{ijkl}, and a term based on the loading function and hardening parameters giving

$$C'_{ijkl} = C_{ijkl} - \frac{C_{ijmn}C_{klrs}G_{mnrs}}{C_{mnrs}G_{mnrs} + \frac{H}{\tau}(1-M)\frac{\partial F}{\partial \sigma_{rs}}\bar{\sigma}_{rs} - HM\frac{\partial F}{\partial \tau}G_{mnmn}} \tag{5.6}$$

where the term $G_{mnrs} = \frac{\partial F}{\partial \sigma_{mn}}\frac{\partial F}{\partial \sigma_{rs}}$.

5.2.3 Effect of strain rate on concrete behavior

Increased strain rates found in the dynamic loading (shock, impact, etc.) of concrete structures affect both concrete strength and stress-strain behavior. The experimental data available concerning the rate effect in the concrete response is mainly for quasi-static loadings at low strain rates. Due to increased difficulty of testing and other reasons, there are considerably fewer results available for concrete subjected to higher strain rate loading conditions.

A majority of the dynamic test results for concrete have been obtained from uniaxial test conditions [28,39,50,52,81,83]. From these tests, two important general conclusions can be drawn. The first is concrete strength increases under all loading conditions (uniaxial and multiaxial) with increasing strain rate. The second is a decrease in non-linear stress-strain behavior prior to the peak stress with increasing strain rate. The increase in strength at higher strain rates is more sensitive in tensile conditions than compressive conditions [83]. A plot detailing this behavior is taken from [83] and shown in Figure 5.2. Experimental data has shown compressive strengths as high as 170% of the static strength at $\dot{\varepsilon} = 200$/sec. Tensile tests have shown increases of over 350% at a strain rate of 7/sec [52].

Kormeling [50] stated the main contributor to the rate dependency of concrete behavior is the cement paste due to the relative stability of the various bonds. Using this as justification to apply results of cement paste tests directly to concrete behavior allows assumptions to be made. Jawed [39] showed through experimental data cement paste strength increases with increasing strain rate at an approximately linear rate until a limit state is reached ($\dot{\varepsilon} = 250$/sec for these particular tests). After this point, the strength remains constant for any increase in rate.

Kuennen, et al. [52] showed a different trend at the lower strain rate range. They stated the strength-vs-strain rate curves for concrete describe a bi-linear pattern with only moderate increases in strength below a critical strain rate (60/sec for compression and 5/sec for tension) with a more rapid increase after this point. These tests, unfortunately, do not achieve strain rates as high as Jawed, et al [39]; and, thus, it is not possible to see if their results also show the leveling off of strength beyond the $\dot{\varepsilon} = 250$/sec range. It is also not possible to determine whether tension reaches the constant region more quickly than the 250/sec range of compression as would be indicated from the difference in critical point rates in the Kuennen, et al [52] tested.

The uniaxial testing of concrete at increased rates of strain has also shown the strain-hardening behavior differs from the static response. Tests [41,82,83] have shown the secant modulus prior to failure has increased with increased strain rate. Suaris and Shah [83] attribute this increase to a decrease in pre-peak micro-cracking. They also state the increase in strain rate does not affect the initial tangent modulus of the concrete.

The tests of biaxial loading behavior of concrete [2,65] show general trends of increase in strengths and increase in secant modulus which are consistent with the uniaxial tests. Ahmad and Shah [2] state the strain rate dependency of the secant modulus in unconfined and confined tests to be so comparable they propose using an empirical equation based on uniaxial data for confined concrete.

5.2.4 Model modifications for strain rate

The experimental data available on the behavior of concrete to different modes of loading allow certain assumptions to be made for treating concrete at increased strain rates. These assumptions are:

1) At strain rates achieved in ordnance velocity impact ($\dot{\varepsilon} > 1000$/sec), failure strengths under both uniaxial and multi-axial conditions may be treated as constants.

2) Due to the difference in sensitivity to strain rate between tension and compression, the tensile strength may be increased by 2 or 3 times the static strength whereas the compressive strength may only increase by a factor of 1.5 or 2. This results in the ration of σ_c' to σ_t' changing from approximately 10 for static cases to 6 or 7 for ordnance velocities.

3) The decrease in the non-linear stress-strain response allows concrete to be treated as a linear-elastic material well beyond the 25% to 30% of the compressive failure strength limit of static curves.

These assumptions allow the use of the Hsieh-Ting-Chen plasticity material model

modified for the strain rate induced behavior.

As stated previously, the four constants can be determined from four failure states (uniaxial tension, uniaxial compression, equal biaxial compression, and confined biaxial compression). The test results are represented as a multiple of the uniaxial compressive strength, σ_c'. For standard static use, Labbane [56] assumes the failure states as

$$\sigma_t' = 0.10\sigma_c' \quad \sigma_{bc}' = 1.15\sigma_c' \quad \sigma_{pc}' = 0.8\sigma_c' \quad \sigma_{cc}' = 4.2\sigma_c'$$

which gives the constants as

$$A = 2.0108 \quad B = 0.9714 \quad C = 9.1412 \quad D = 0.2312$$

For application in the dynamic analyses, the uniaxial tensile strength ratio is changed to reflect the different reaction of tensile and compressive strength to increased strain rates. With σ_t' now given as

$$\sigma_t' = 0.1429\,\sigma_c' \quad (\sigma_c'/\sigma_t' = 7)$$

the constants are changed to

$$A = 1.0215 \quad B = 1.4566 \quad C = 5.9289 \quad D = 0.18151$$

Table 5.1 shows how the change of the compressive strength to tensile strength ratio affects failure stresses for three stress states (σ_1 = tensile, σ_2 = 0, σ_3 = −2000psi, σ_1 = 0, σ_2 = compressive, σ_3 = −2000psi, and $\sigma_1 = \sigma_2$ = tensile, σ_3 = −2000psi)

5.2.5 Post-failure region

The third region of behavior is failure defined by Equation 5.1. Once the failure surface is reached, the modifications needed to simulate the local failure are based on the mode of failure. This mode is determined using the state of stress at failure to

calculate a crushing coefficient, α, given by

$$\alpha = -\frac{I_1}{(2\sqrt{3J_2}\cos\theta)} \tag{5.7}$$

for

$$|\theta| = \left| \frac{1}{3}\cos^{-1}\left[\frac{3\sqrt{3}}{2} \frac{J_3}{J_2^{3/2}} \right] \right| \leq 60^\circ$$

Using the criteria of σ_1 being tensile for cracking and ε_1 (maximum principal strain) being compressive for crushing, limits of the modes become: 1) $\alpha < 1$ for pure cracking, 2) $\alpha > (1+\nu)/(1-2\nu)$ for pure crushing, and 3) mixed crushing and cracking between these two values. Using $\nu=0.2$ for concrete puts the limits at <1 for pure cracking and >2 for pure crushing [76].

5.2.5.1 Pure cracking

When pure cracking is detected, the maximum principal stress direction is determined from the existing state of stress. If this direction corresponds to the tangential direction of the axisymmetric element, the constitutive relations are modified to plane stress conditions. If this direction is in the plane of symmetry, the direction is compared to the current element geometry. The node closest to the integration point where failure occurs is released from adjacent elements in the direction of the principal stress. This is the mode of failure which employs the nodal fragmentation algorithm presented in Chapter 3.

No modification of material properties is enforced if pure cracking is detected. If

the element node experiences failure stresses in following time steps, the crushing coefficient at that time step dictates property modifications as outlined in the two following sections.

5.2.5.2 Pure crushing

When the crushing coefficient, α, is greater than 2, the element node is determined to fail by pure crushing. Pure crushing dictates the material behaves as a granular material. One method of treating crushed material is to assume the material strength in all directions ceases to exist and the material is perfectly deformable [84,92]. This is acceptable in reinforced concrete analysis as the residual concrete strength would be relatively insignificant as compared to the reinforcing steel strength. This assumption is not as acceptable in problems where local behavior is dominant as plain concrete is the material being loaded.

Chen and Yamaguchi [22] state zero strength is the lower limit on the actual behavior and perfect plasticity is the upper limit. In order to fall somewhere between these two values, the material properties in the code are modified. The elastic modulus and shear modulus are set at 10% of their uncrushed values. The value of 10% is arbitrary and meant only to model loss of the majority of the strength.

The other modification for a crushed element node is to ensure no tension is allowed in the state of stress at the point of failure. This is done by calculating the principal stresses, σ_1, σ_2, and σ_3, at the integration point for all time steps subsequent to the crushing. If any of the principal stresses are tensile, they are set to zero and the state of

stress is recalculated based on the modifications.

5.2.5.3 Mixed cracking and crushing

The third mode of failure is found in the region between pure cracking and pure crushing and can be considered a combination of the two. The post-failure behavior for this mode is modeled by altering the calculated stress for each subsequent time step. The stress is reduced in proportion to the amount of crushing in the failure as determined by the crushing coefficient, α. Thus, the reduction factor, f_r, is found by

$$f_r = 0.9\,(2.0 - \alpha) + 0.1 \tag{5.8}$$

If α at a subsequent time step is found to exceed 2, the element node is assumed to have crushed completely and is treated the same as if pure crushing were the initial form of failure. In the same manner, if α becomes less than 1, the element node is released in the direction of maximum principal stress.

5.2.5.4 Biaxial state of stresses

As stated previously, if the element is determined to have exceeded the failure criterion in pure cracking and the tangential stress is the maximum principal stress, the element stress-strain relations are modified as a plane state of stresses. This dictates a change be made in the calculation of the crushing coefficient, α [56].

The radial stress in the element may only be compressive. Therefore, if a tensile stress is calculated, the tangential stress is set to zero. In order to determine the type of failure for this stress condition, the original definition of α is investigated. For pure

cracking to occur, the maximum principal stress, σ_1, must be tensile. For pure crushing to occur, the maximum principal strain, ε_1, must be compressive. Using the biaxial stress state of σ_x, σ_y, and τ_{xy}, the coefficient α becomes

$$\alpha = -\frac{\sigma_x + \sigma_y}{\sqrt{(\sigma_x - \sigma_y)^2 + 4\,\tau_{xy}^2}}$$

with the failure mode of cracking defined as

$$\alpha < 1$$

the mode of pure crushing as

$$\alpha > \frac{1+\nu}{1-\nu} = 1.5 \text{ for } \nu = 0.2$$

and the mixed mode as

$$1 \le \alpha \le \frac{1+\nu}{1-\nu}$$

5.2.5.5 Element removal

The study of impact using finite elements brings with it the possibility of extremely large deformation in the mesh. If an element is allowed to deform too much, numerical problems may appear. To avoid such an occurrence, two checks are imposed on the elements. The first such check is to ensure the Jacobian calculated at the gauss integration points being positive. If it is negative or zero, the element is assumed to be compressed beyond acceptable limits and is removed from the internal force calculation loop but the nodal masses remain. If the element sides become extended beyond a limit (greated than two times their original length is arbitrarily chosen in the current computer codes) the element is also removed from the internal force calculation. This

usually occurs in a crushed element which cannot sustain tensile stress and at a later point in the history, is subjected to tensile forces.

5.3 Contact and sliding surfaces

The algorithm used to numerically treat the contact and sliding surfaces inherent in the penetration of the projectile into the target mesh is based on the "master element-slave node" concept introduced by Belytschko and Liu [16]. This concept designates some of the elements in the mesh as master elements. Nodes from the remaining elements are designated slave nodes. Each of these nodes' positions is checked to determine if the node has penetrated any of the master elements' boundaries. If the slave node has penetrated a boundary, the node is moved back to the element boundary and the resulting change in momentum is transferred to the nodes of the corresponding master element. For this study, the projectile element is the master element with the target nodes being the slave nodes.

The projectiles used in the examples consist of one of two shapes shown in Figure 5.3. These shapes are used for simplicity in computing the projectile boundaries necessary in determining penetration. The projectile is assumed to be rigid for computational simplicity. The use of a rigid projectile is also meant to model non-deformable projectile impact necessary in developing all three modes of failure in the concrete target.

Penetration is determined by first calculating the current position of the projectile boundaries using initial coordinates and current displacements of the four projectile

nodes. The position of each target node is then calculated in the same manner. If a target node is found to be within the projectile, the displacement components of the target node are modified to move the node back onto the projectile boundary as shown in Figures 5.4 and 5.5. This change in position is then translated into a force applied to the penetrator by calculating the change in momentum of the target node. This gives the penetrator force, F_p, as

$$F_p = m_{tn} \times \Delta d_{tn}/\Delta t^2$$

with m_{tn} and Δd_{tn} the target node mass and change in position and Δt the time step size. The force is divided among the projectile nodes in proportion to the projectile nodal masses to ensure rigid body motion of the projectile.

5.4 Inter-element collision

Element fragmentation allows fragments to move independently of previously connected elements. Therefore, fragments could possibly travel through other elements which is not true to the actual phenomenon. To prevent this from occurring, an algorithm analogous to the discrete, or distinct, element method used in the analysis of discontinuous media is incorporated into the code.

The inter-element collision algorithm used in the present analyses is simplistic in its application in order to reduce computational effort. Each element is defined as a circle. The diameter of the circle is equal to the original side dimension of the element as shown in Figure 5.6. The center of the circular "pseudo-element" is calculated as the average position of the four corner nodes. The position of the element (termed "target

element") is then compared to the position of all other elements (termed "collider elements") which are not currently connected to the target element.

If the circular region of a collider element is found to be within the circular region of the target element, the inter-penetration distance is calculated as shown in Figure 5.7. This distance is used to calculate a collision force based on an elastic collision. This force is then equally divided between the two elements and distributed among the elements' nodes. The magnitude of the distribution is relative to the nodal mass versus the element mass such that the force creates a rigid body acceleration. The direction of the force is co-linear with the line connecting the centers of the target and collider elements. The direction and the distribution of the forces are shown in Figure 5.8.

5.5 Numerical results

The capability of the fragmentation algorithm and large displacement formulation developed for the analysis of projectile ballistic impact of concrete targets are illustrated in thirteen example solutions. Problem 5.1 involves low velocity impact (sub-ordnance range) with the remaining twelve problems treating higher velocities in the lower end of the ordnance range. The intent of showing Problem 5.1 is to demonstrate the ability of the code to handle the punching shear type failure found in the lower velocity impact. The type of failure particular to the higher velocity impact will then be contrasted to demonstrate the versatility and predictability of the algorithm.

Problem 5.1 considers low-velocity impact using parameters from experiments by Nilsson and Sahlin [67]. The current problem is modified by removing the target's steel

reinforcement to show the failure mode and fragmentation more clearly.

The problem consists of a circular concrete plate with a 1.5 meter radius being impacted by a 0.125 meter radius steel cylinder at 4.8 meters/second. The problem geometry, mesh, material properties, and projectile characteristics are shown in Figure 5.9. The 600 time steps of a constant time increment of $2x10^{-6}$ second give the real time span of the impact as 0.0012 second. The computed failure pattern is shown in Figure 5.10. The deformed mesh is shown at 0.0002, 0.0004, 0.0006, 0.0008, 0.0010, and 0.0012 seconds in Figure 5.11. The crack pattern and meshes show the punching shear type failure common to low-velocity impact of concrete.

The range of damage on the distal face is consistent with that of the Nilsson and Sahlin test specimen. The test specimen shows two major crack rings with the larger being approximately 200 mm in radius and the smaller about 100 mm in radius. The finite element mesh predicts two major failure zones with the larger being approximately 220 mm in radius and the smaller being 150 mm in radius. The problem used 80 cpu minutes on the Purdue ECN Gould NP-1 computer.

The application of the fragmentation algorithm to higher velocity impact of concrete is shown through a series of examples (Problems 5.2 through 5.13). Problem parameters of velocity, projectile shape, elastic limit, and target thickness are varied. The chosen velocities of 12,000 in/sec (305 m/sec), 15,000 in/sec (381 m/sec), and 18,000 in/sec (457 m/sec) are intended to show problems at the low end of the ordnance velocity region. Two of the examples also incorporate the inter-element collision algorithm to show how this affects results.

Problems 5.2 through 5.13 all use meshes similar to those shown in Figure 5.12. The element size used for all the problems is 0.1x0.1 inches with the chosen time step being $1x10^{-8}$ seconds. The elastic modulus of concrete is assumed to be $4.4x10^{6}$ psi with a Poisson's ratio of 0.2. The value of σ_c' is 6,000 psi and the mass density is $2.2x10^{-4}$ lbs–sec^2/in^4. A compilation of individual initial problem parameters is shown in Table 5.2.

Whereas the sub-ordnance impact of Problem 5.1 showed damage on the impact face to be limited to the approximate dimensions of the projectile, all ordnance velocity problems show damage zones from three to greater than 10 times the projectile diameter. Figures 5.13 through 5.18 show the extent of damage resulting from the ordnance velocity impact in Problems 5.2 through 5.7. Figures 5.19 through 5.30 show deformed meshes for Problems 5.2 through 5.13 with Table 5.2 listing final parameters for all the ordnance velocity results.

The figures of the deformed meshes are created by calculating the mid-point of each element in an arbitrarily determined "damage zone." For these problems the damage zone is between 3 and 3.5 inches from the axis of symmetry. The mid-point is then plotted as a square approximately the same size as an undeformed element. If an element is determined to have a zero or negative jacobian or if an element has become distorted (see Chapter 5), the particular element is no longer plotted.

The numerical results from problems not using inter-element collisions show damage consistent with that expected from high-velocity impact of concrete. The major damage besides that caused by direct contact with the projectile spirals away

from the projectile in the same manner as seen by Maurer and Rinehart [63] and Bauer and Calder [11].

The deformed meshes for Problems 5.10 and 5.11 show the addition of the inter-element collision algorithm creates a much greater damage zone than when not using collision. The results from Problem 5.10 show the pronounced crater and ejecta common to impact at these velocities. The results from Problem 5.11 show an immense amount of damage to the mesh suggesting a larger target radius would have been preferable for the problem. It also suggests the inter-element collision algorithm should be studied and tested to a greater extent. The code used in the present research required approximately four times the cpu time when using the collision algorithm as opposed to not using it (approximately 1900 cpu minutes on the Ardent Titan for Problem 5.11 and approximately 500 minutes for Problem 5.7).

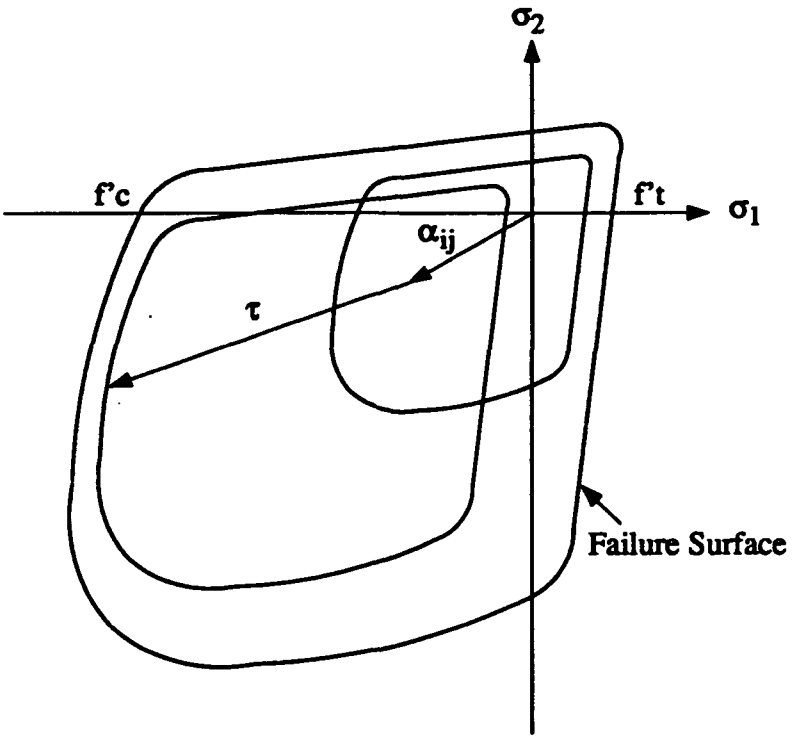

Figure 5.1 Schematic representation of H-T-C 4-parameter concrete material model in the biaxial stress plane from Labbane (1991)

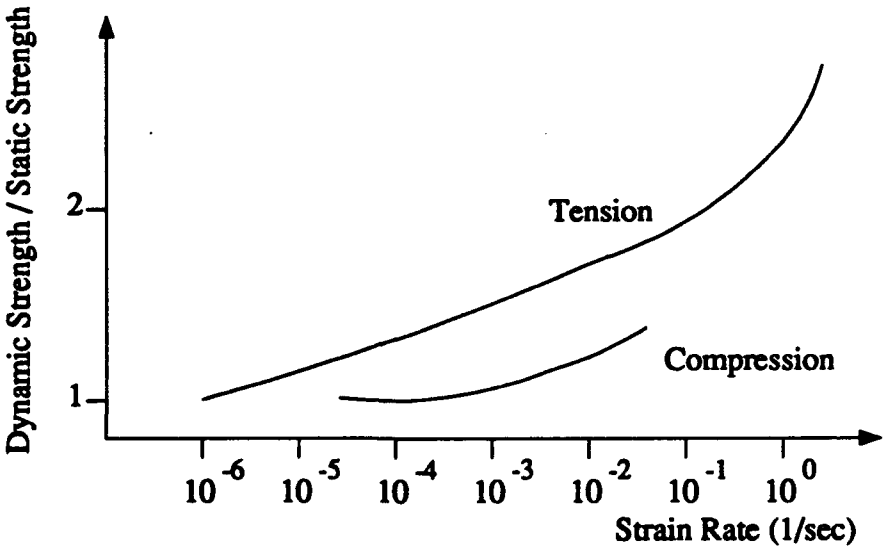

Figure 5.2 Comparison of strain-rate sensitivity in tension and compression from Suaris and Shah (1983)

Table 5.1 Failure stress change with change in f'c/f't ratio using Hsieh-Ting-Chen 4-parameter failure criterion

Stress state			Failure stress	
			f'c/f't=10	f'c/f't=7
σ_1 =tensile	σ_2 =0psi	σ_3 =-2000psi	σ_1 =143psi	σ_1 =180psi
σ_1 = σ_2 (tensile)		σ_3 =-2000psi	σ_1 =132psi	σ_1 =161psi
σ_1 (tensile) =- σ_2 (compressive)		σ_3 =-2000psi	σ_1 =155psi	σ_1 =200psi

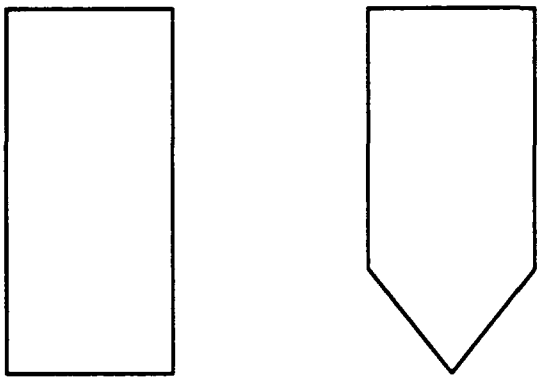

Figure 5.3 Options for projectile shape

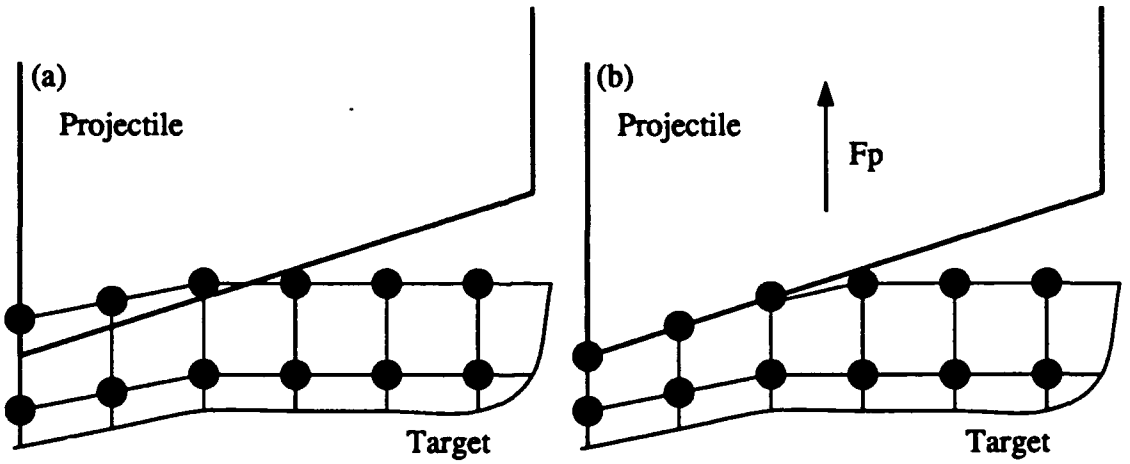

Figure 5.4 Projectile and target (a) before and (b) after penetration algorithm

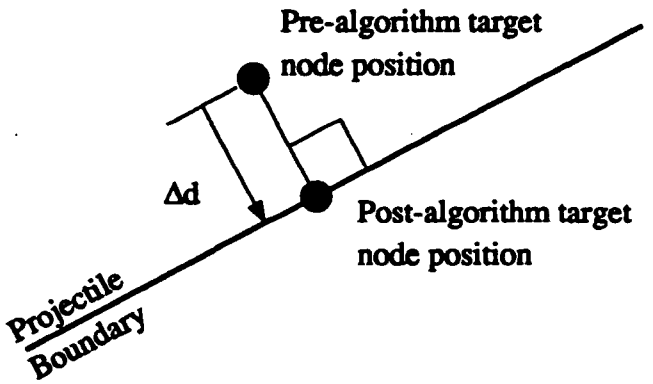

Figure 5.5 Pre-and-post-algorithm target node position due to projectile penetration

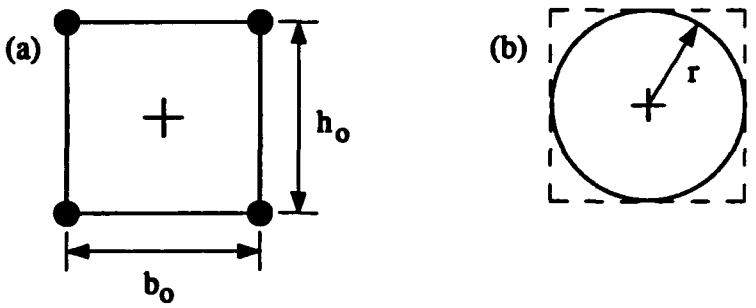

Figure 5.6 (a) Element geometry used to calculate size of pseudo-element and (b) resulting pseudo-element

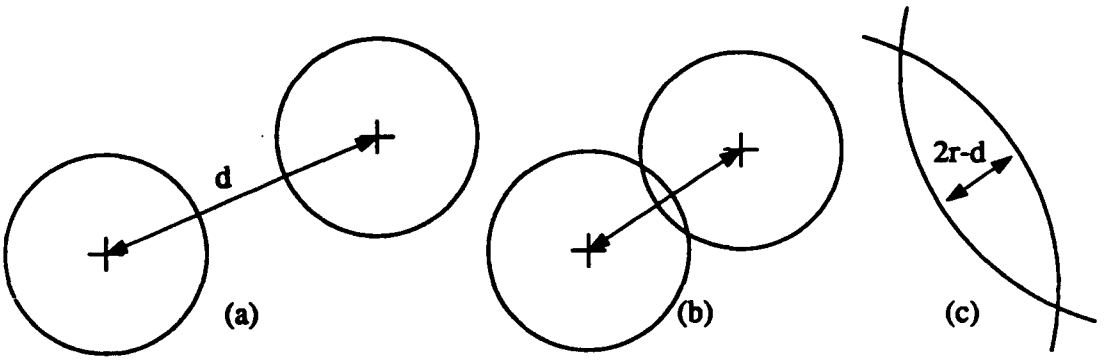

Figure 5.7 Two elements (a) before collision, (b) after collision and (c) enlargement of collision zone

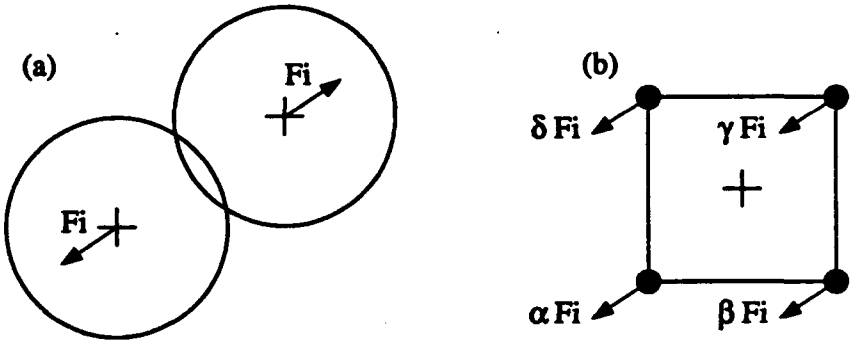

Figure 5.8 Pseudo-forces resulting from collision shown (a) on colliding elements and (b) distributed among nodes of one element involved

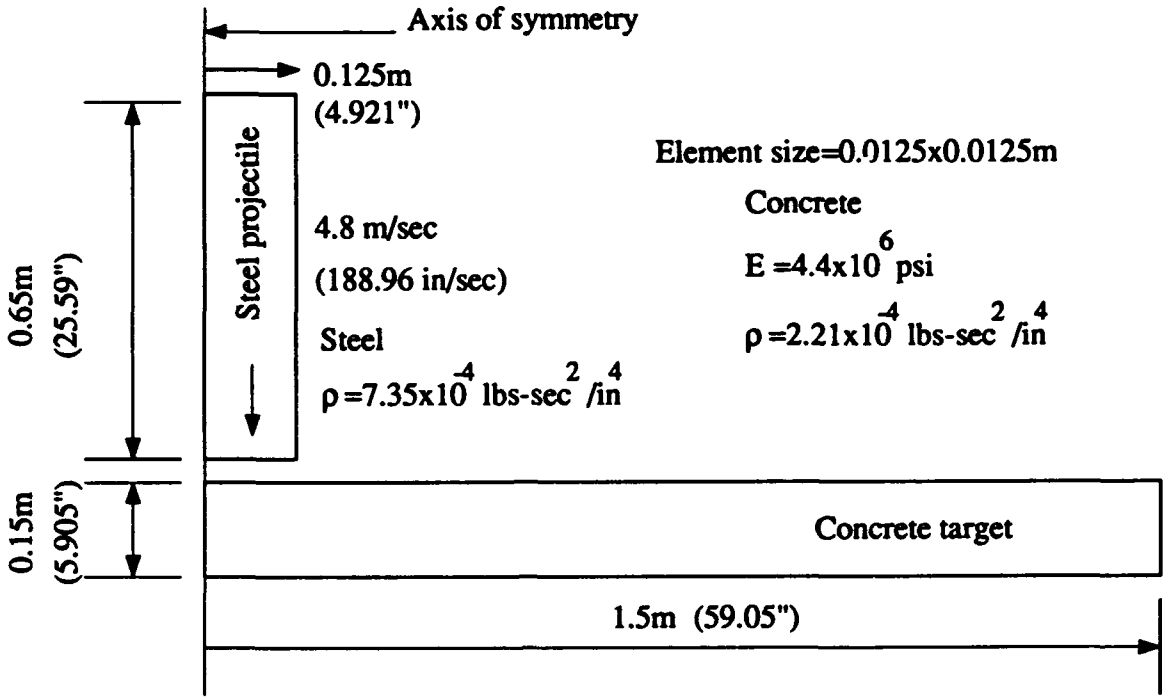

Figure 5.9 Problem 5.1 low-velocity impact geometry, material properties and initial conditions

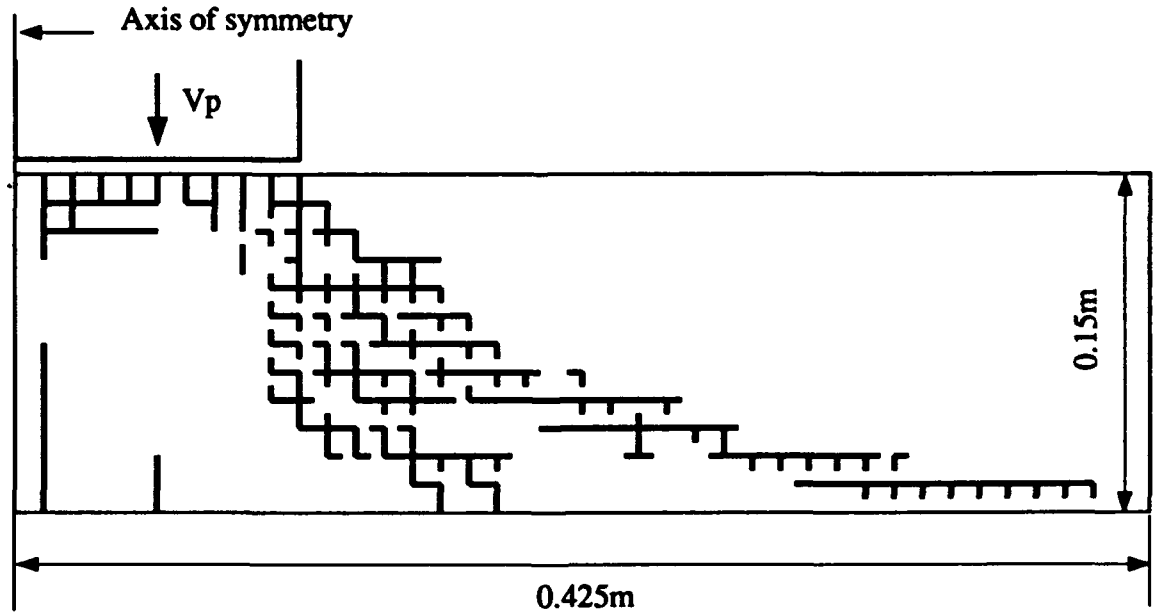

Figure 5.10 Problem 5.1 failure pattern after 0.0012 seconds

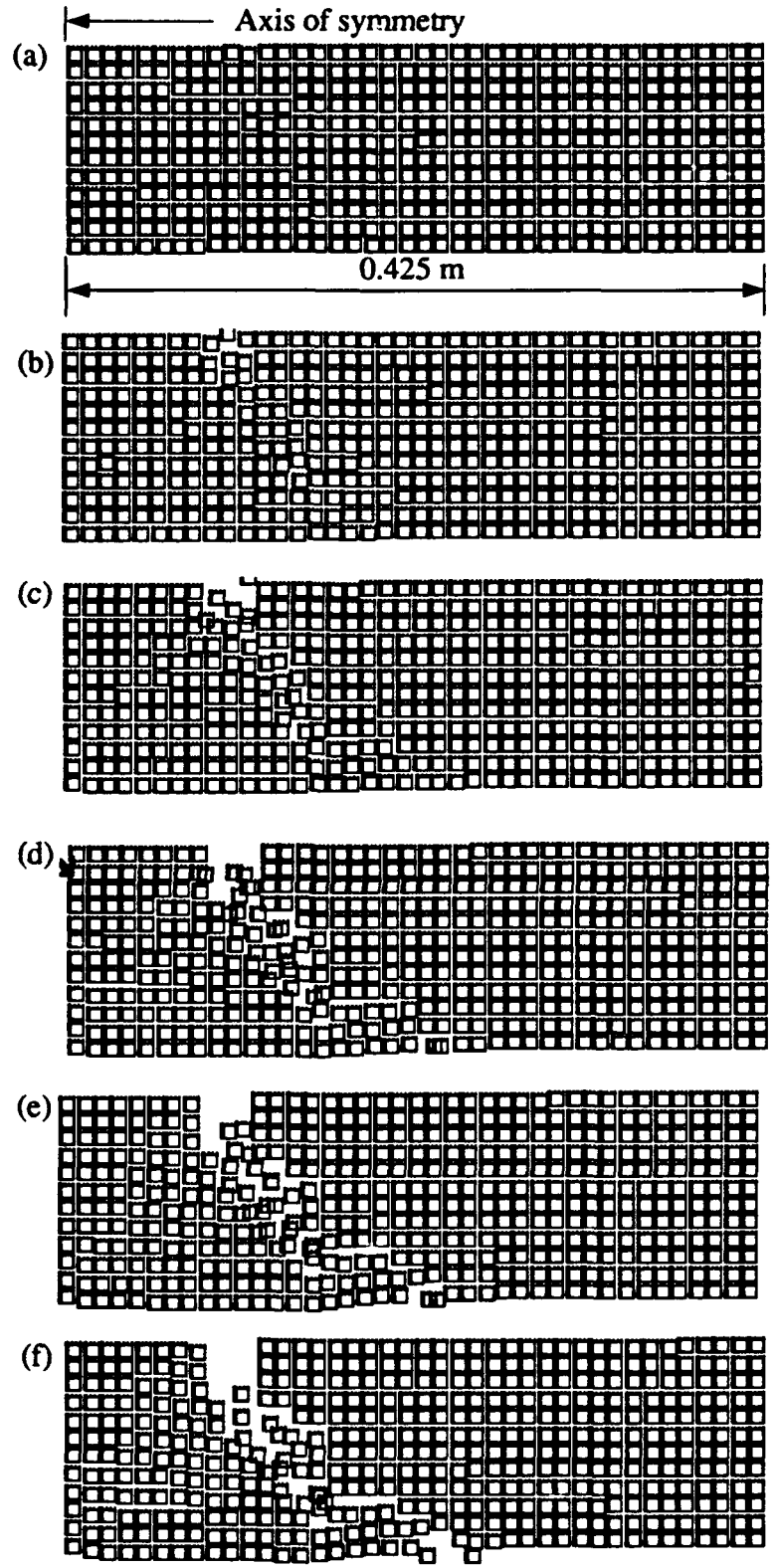

Figure 5.11 Problem 5.1 low-velocity impact of concrete plate at (a) 0.0002, (b) 0.0004, (c) 0.0006, (d) 0.0008, (e) 0.0010, and (f) 0.0012 seconds

Table 5.2 Initial parameters for Problems 5.2 through 5.13

Problem	Projectile Velocity (in/sec)	Projectile Geometry	Target Thickness (in)	Target Radius (in)	Target Material Elastic Limit (xf'c)	Inter-element Collisions?
5.2	12,000	Flat	2	5	0.6	No
5.3	12,000	Angled	2	5	0.6	No
5.4	15,000	Flat	2	5	0.6	No
5.5	15,000	Angled	2	5	0.6	No
5.6	18,000	Flat	2	5	0.6	No
5.7	18,000	Angled	2	5	0.6	No
5.8	18,000	Flat	2	5	0.8	No
5.9	18,000	Angled	2	5	0.8	No
5.10	18,000	Flat	2	5	0.8	Yes
5.11	18,000	Angled	2	5	0.6	Yes
5.12	18,000	Flat	3	6	0.6	No
5.13	18,000	Angled	3	6	0.6	No

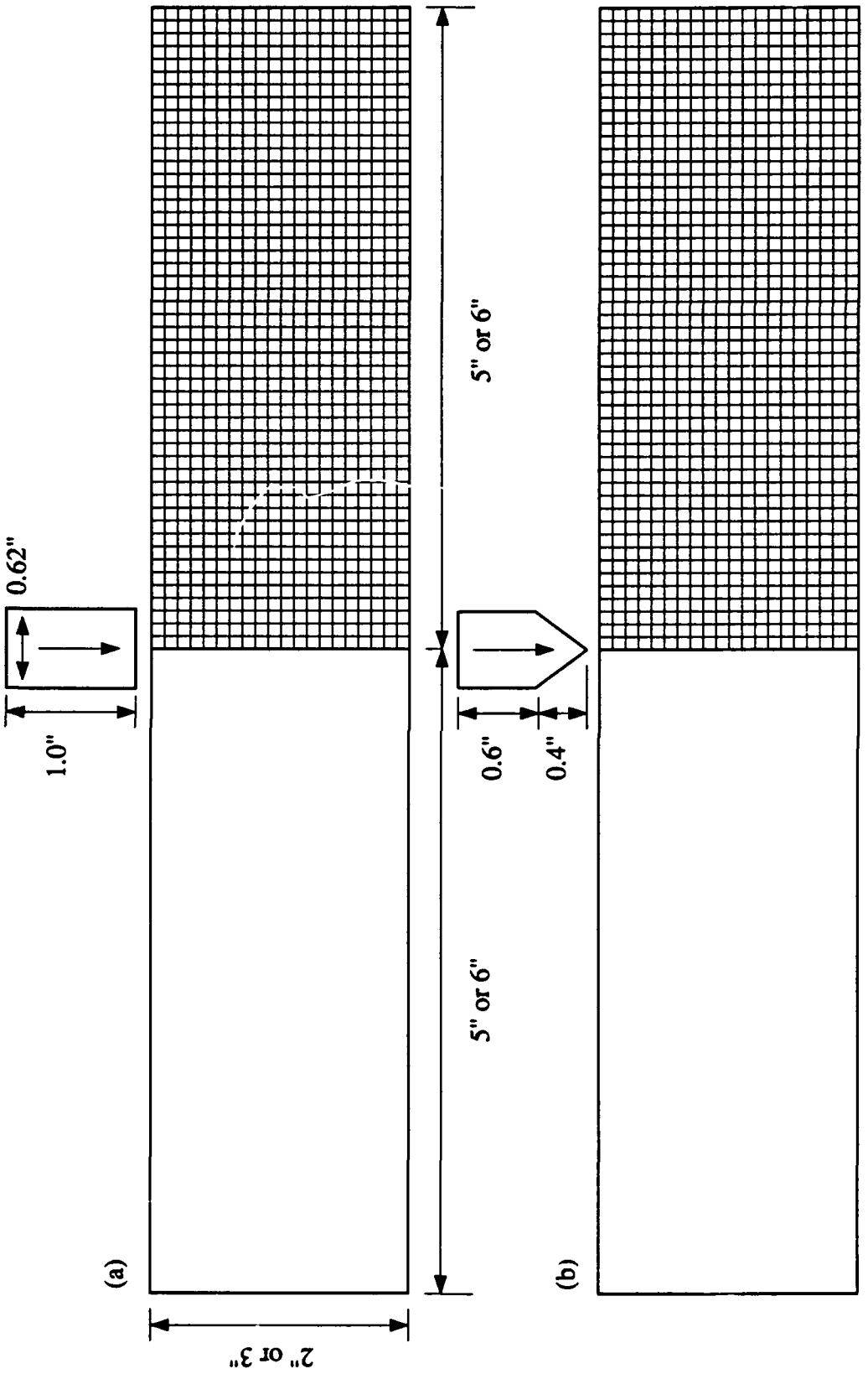

Figure 5.12 General problem geometry, mesh, and projectile configuration for Problems 5.2 through 5.13 with (a) flat projectile and (b) angled projectile

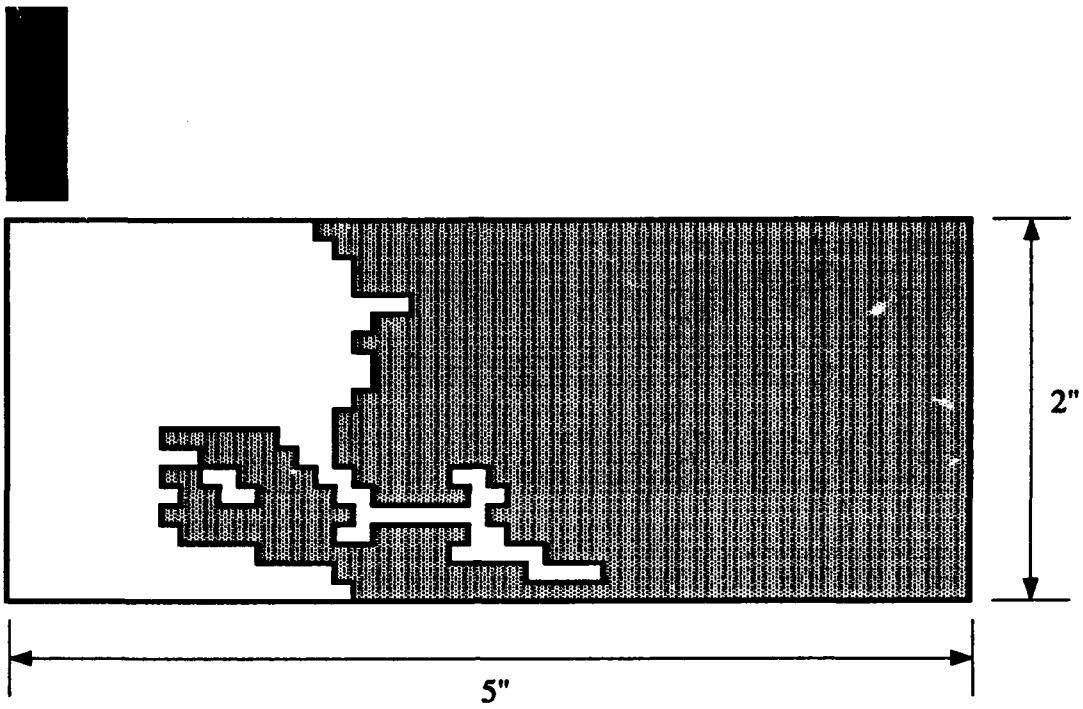

Figure 5.13 Final undamaged target configuration for Problem 5.2

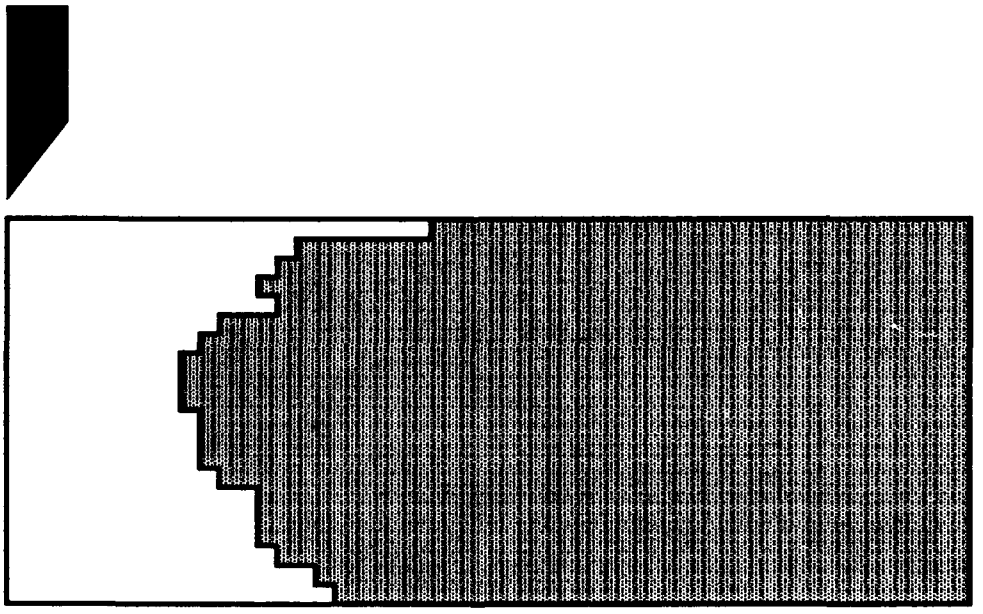

Figure 5.14 Final undamaged target configuration for Problem 5.3

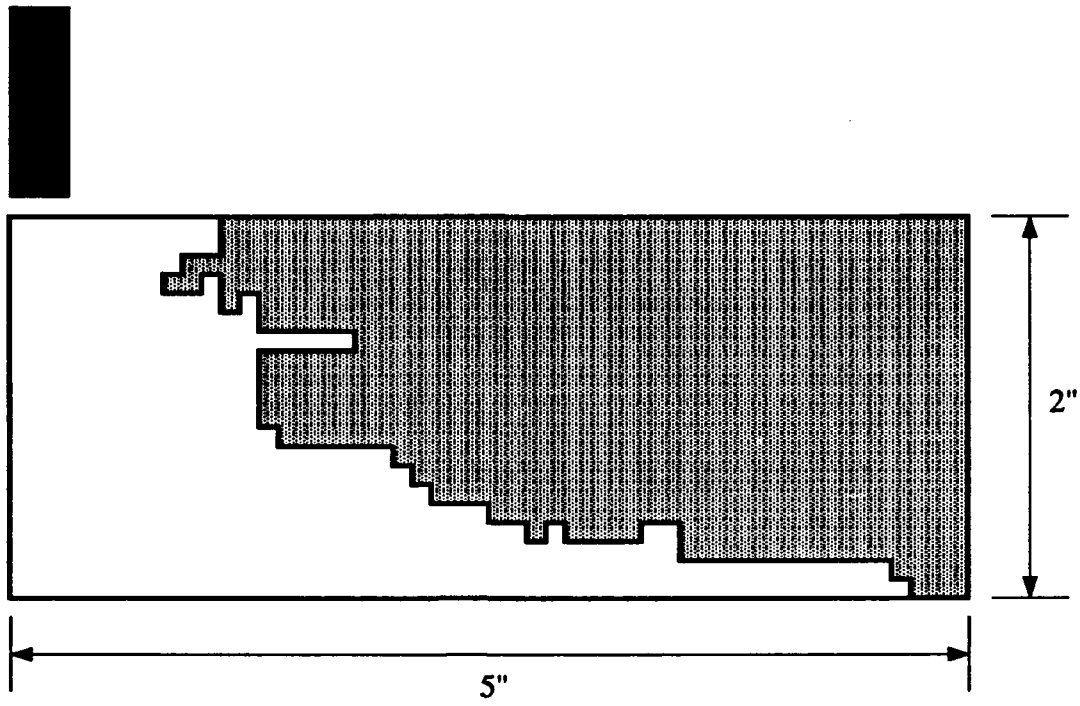

Figure 5.15 Final undamaged target configuration for Problem 5.4

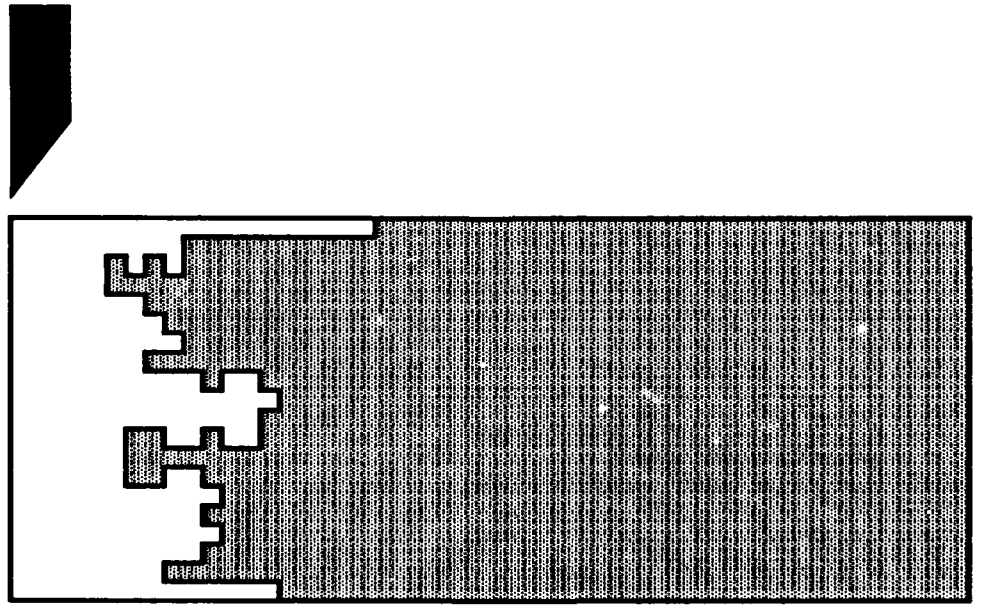

Figure 5.16 Final undamaged target configuration for Problem 5.5

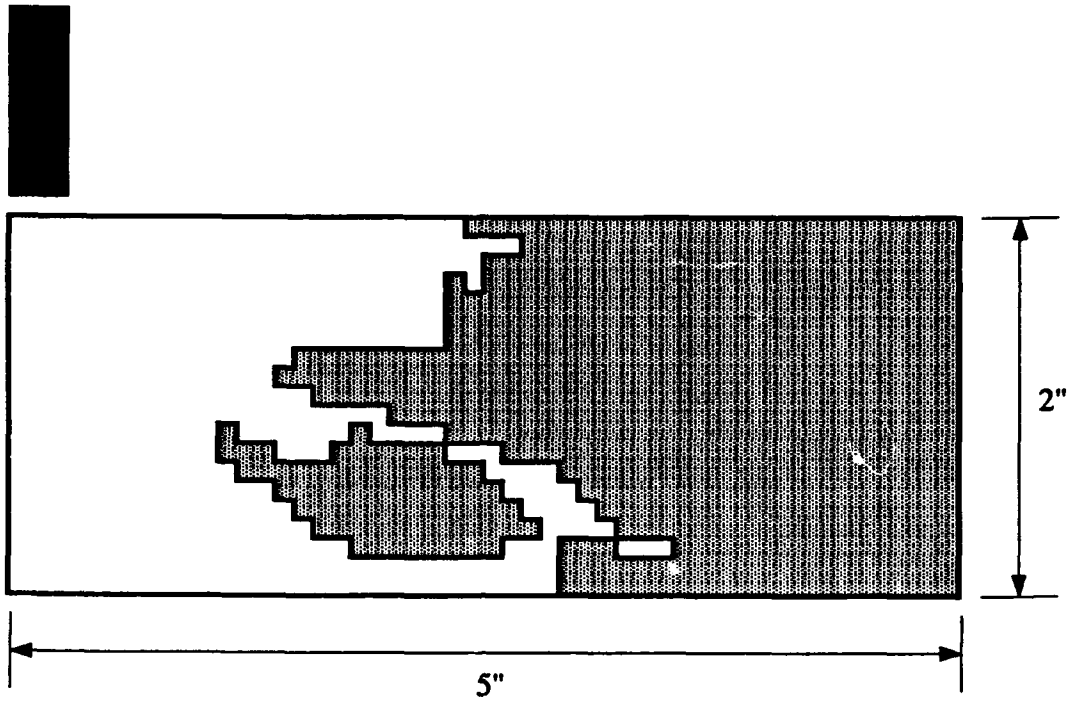

Figure 5.17 Final undamaged target configuration for Problem 5.6

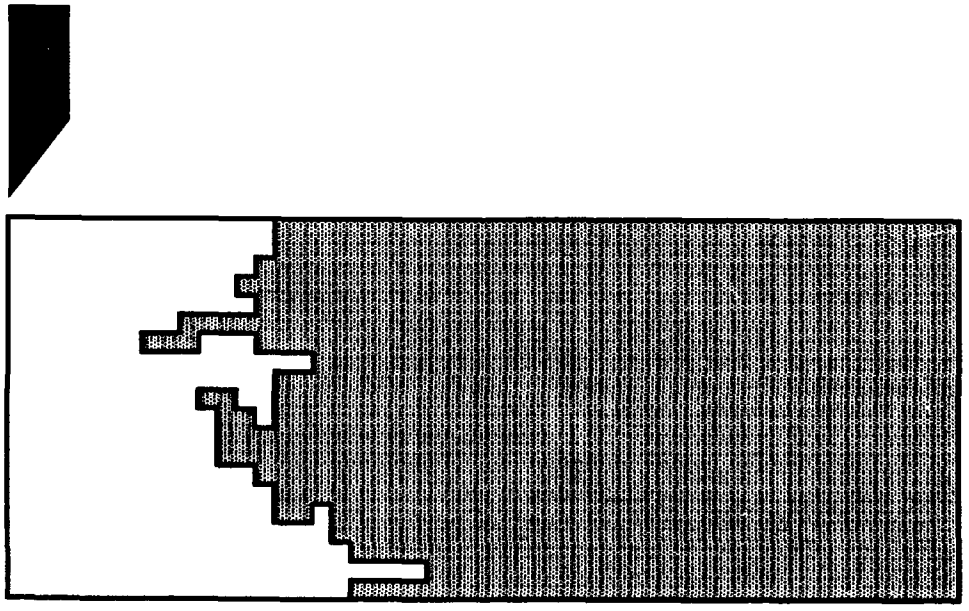

Figure 5.18 Final undamaged target configuration for Problem 5.7

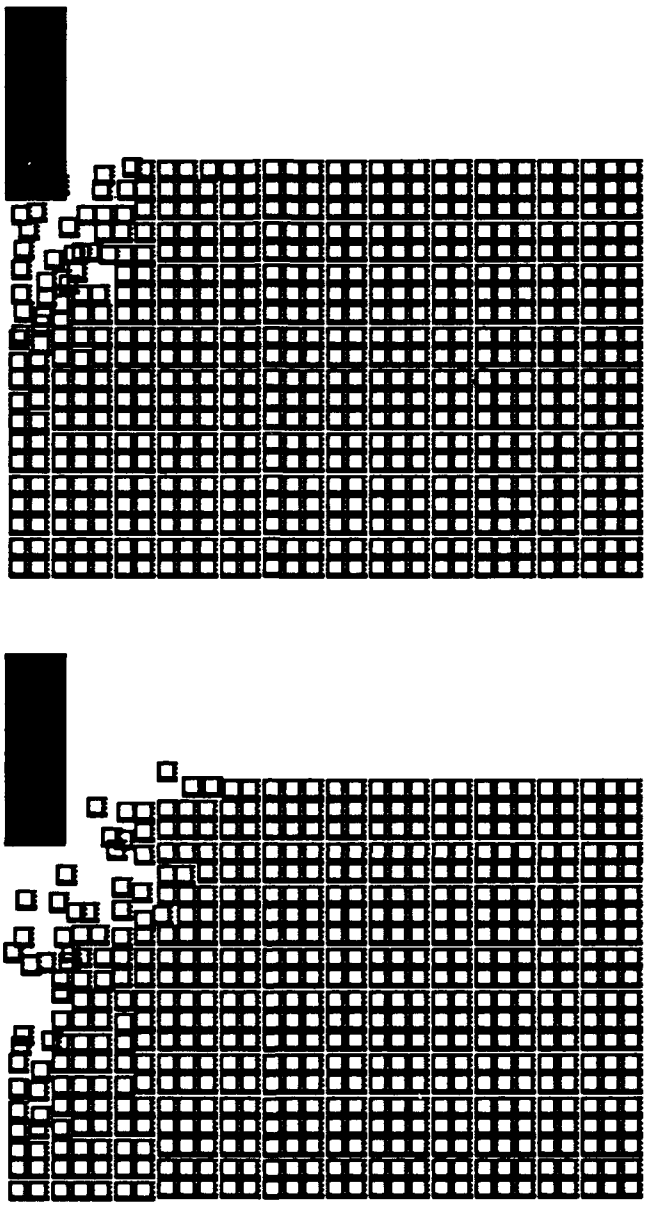

Figure 5.19 Deformed mesh for Problem 5.2 at 0.2×10^{-4}, 0.4×10^{-4}, 0.6×10^{-4}, and 0.8×10^{-4} seconds

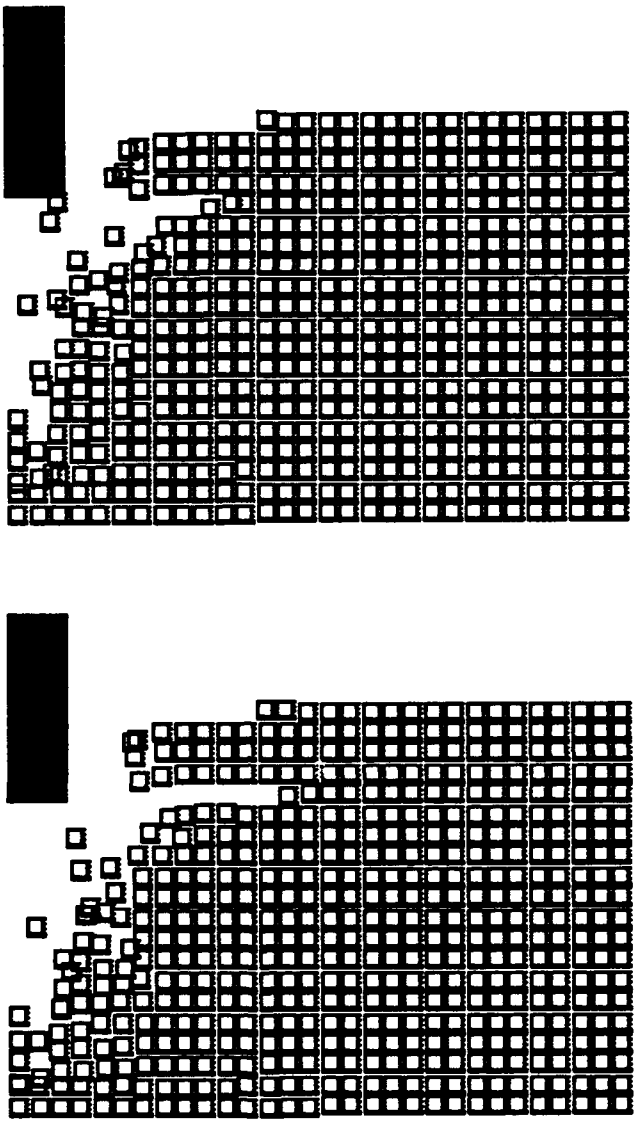

Figure 5.19, continued

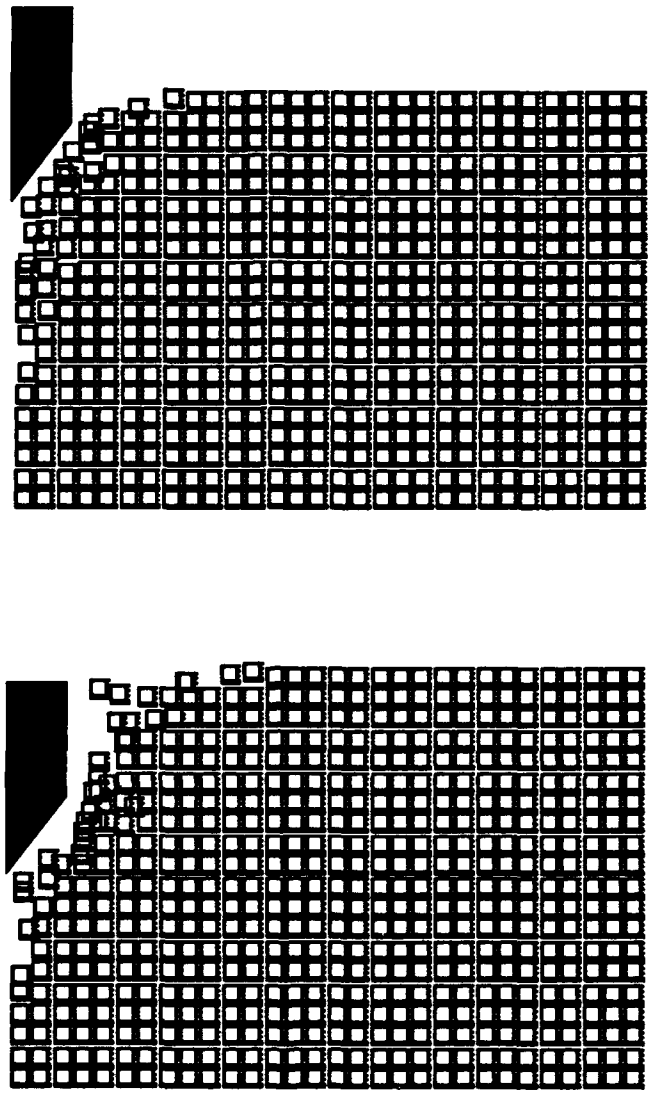

Figure 5.20 Deformed mesh for Problem 5.3 at 0.5×10^{-4}, 1×10^{-4}, 1.5×10^{-4}, 2×10^{-4}, and 2.4×10^{-4} seconds

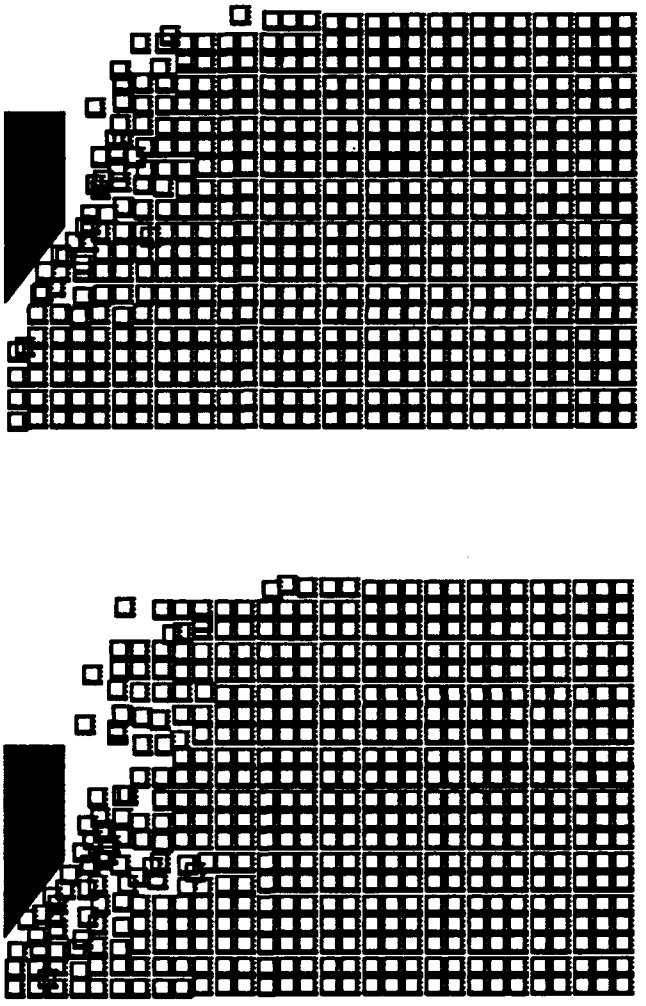

Figure 5.20, continued

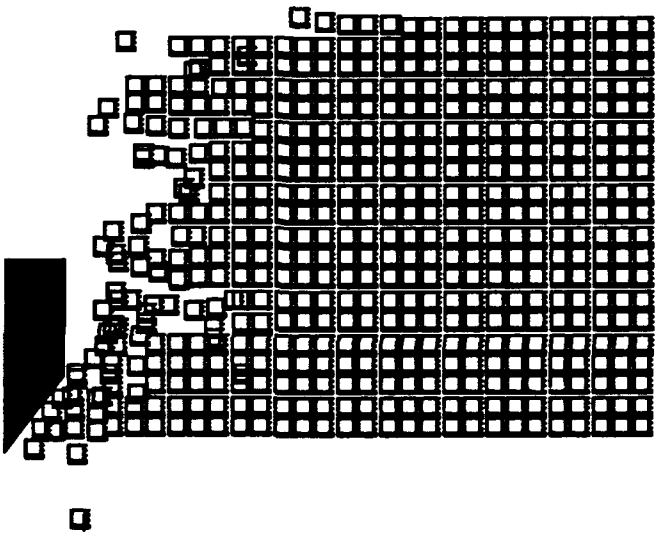

Figure 5.20, continued

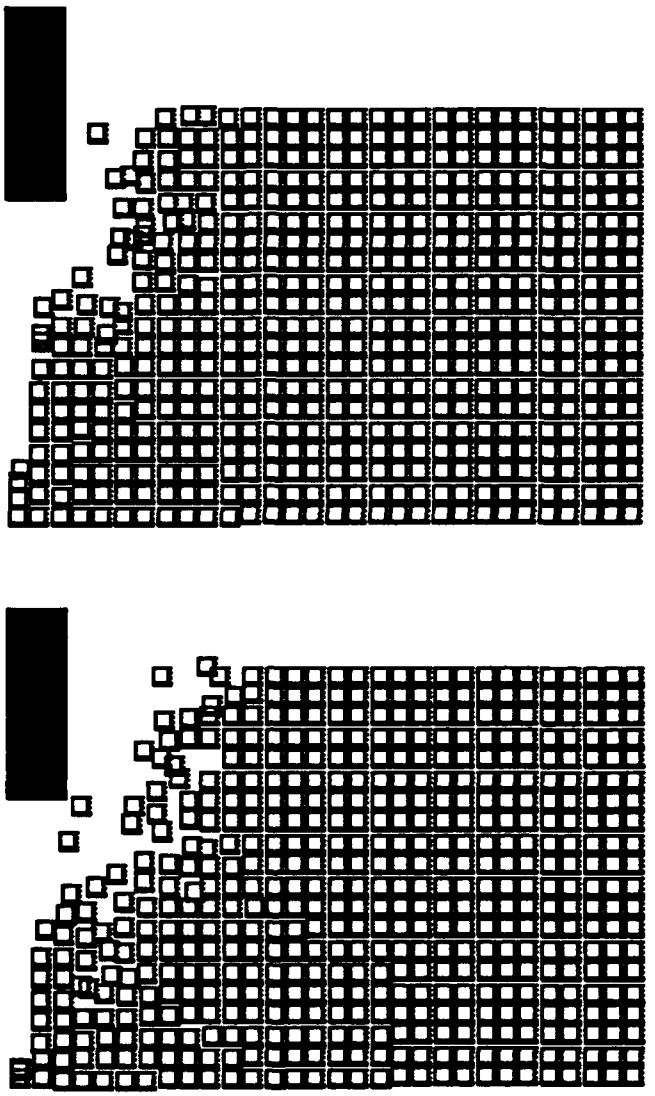

Figure 5.21 Deformed mesh for Problem 5.4 at 0.5×10^{-4}, 1×10^{-4}, 1.5×10^{-4}, 2×10^{-4}, 2.5×10^{-4}, and 3×10^{-4} seconds

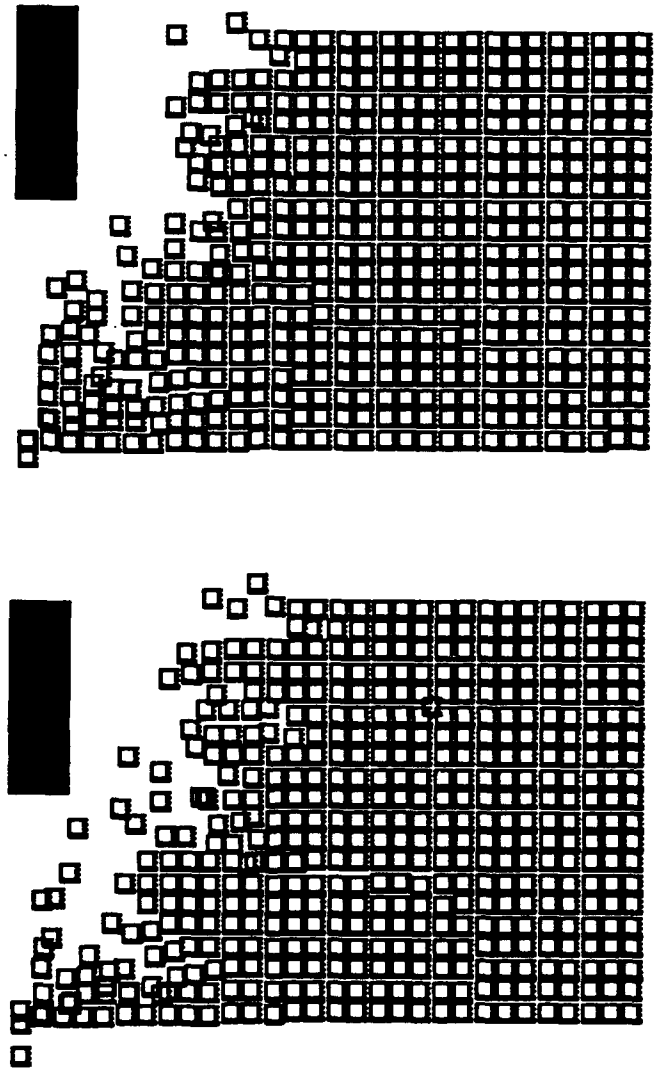

Figure 5.21, continued

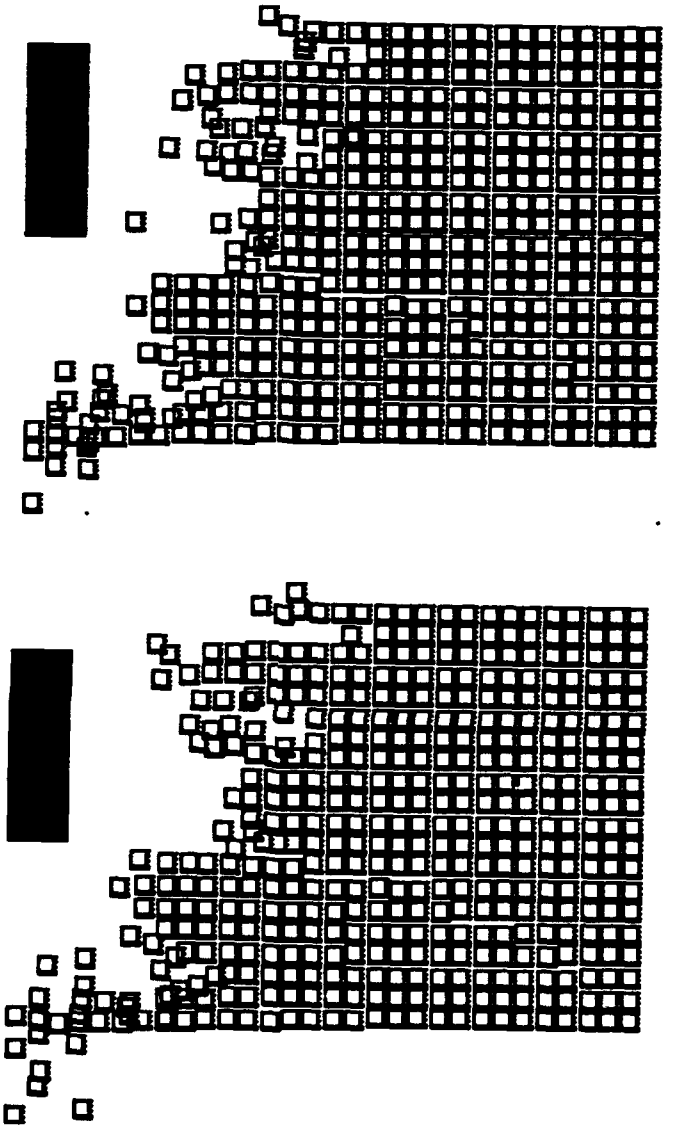

Figure 5.21, continued

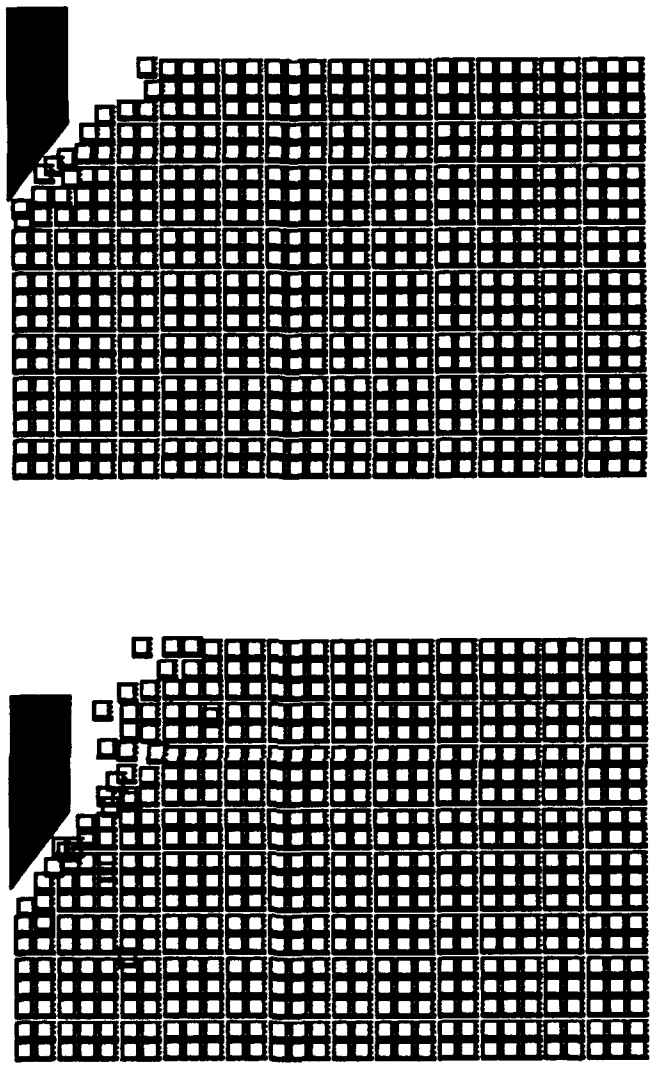

Figure 5.22 Deformed mesh for Problem 5.5 at 0.5×10^{-4}, 1×10^{-4}, 1.5×10^{-4}, and 2×10^{-4} seconds

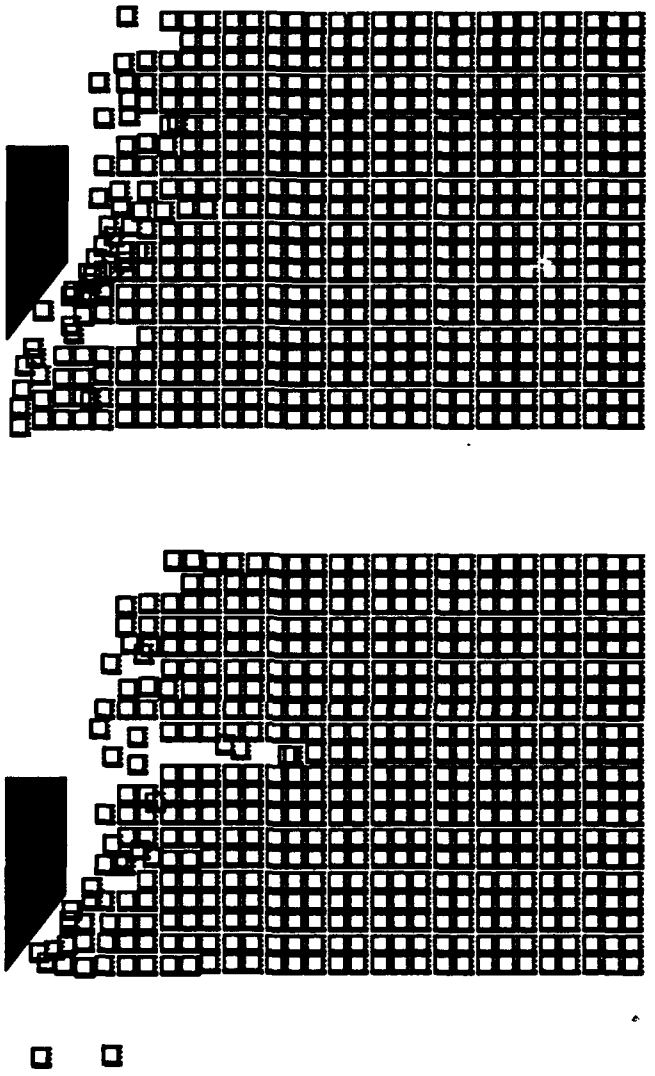

Figure 5.22, continued

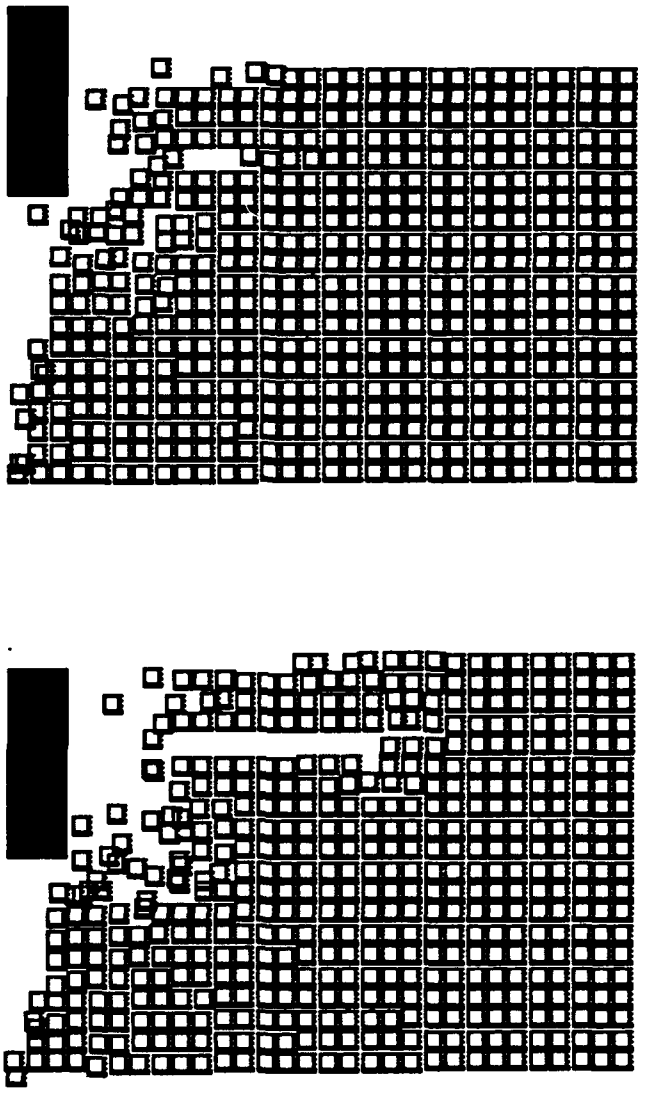

Figure 5.23 Deformed mesh for Problem 5.6 at 0.5×10^{-4}, 1×10^{-4}, 1.5×10^{-4}, 2×10^{-4}, 2.5×10^{-4}, and 2.6×10^{-4} seconds

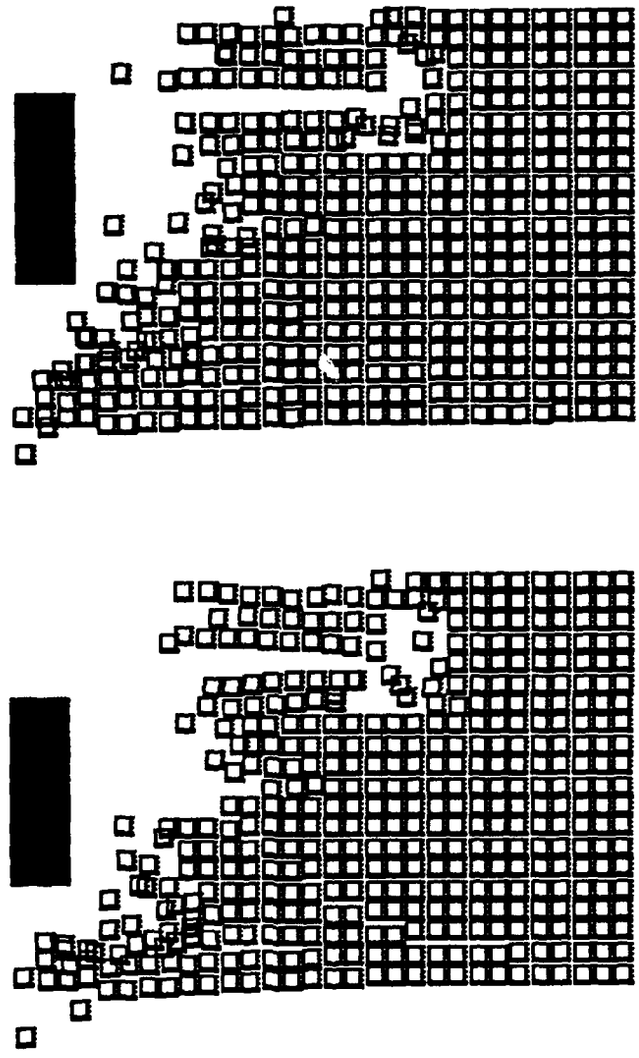

Figure 5.23, continued

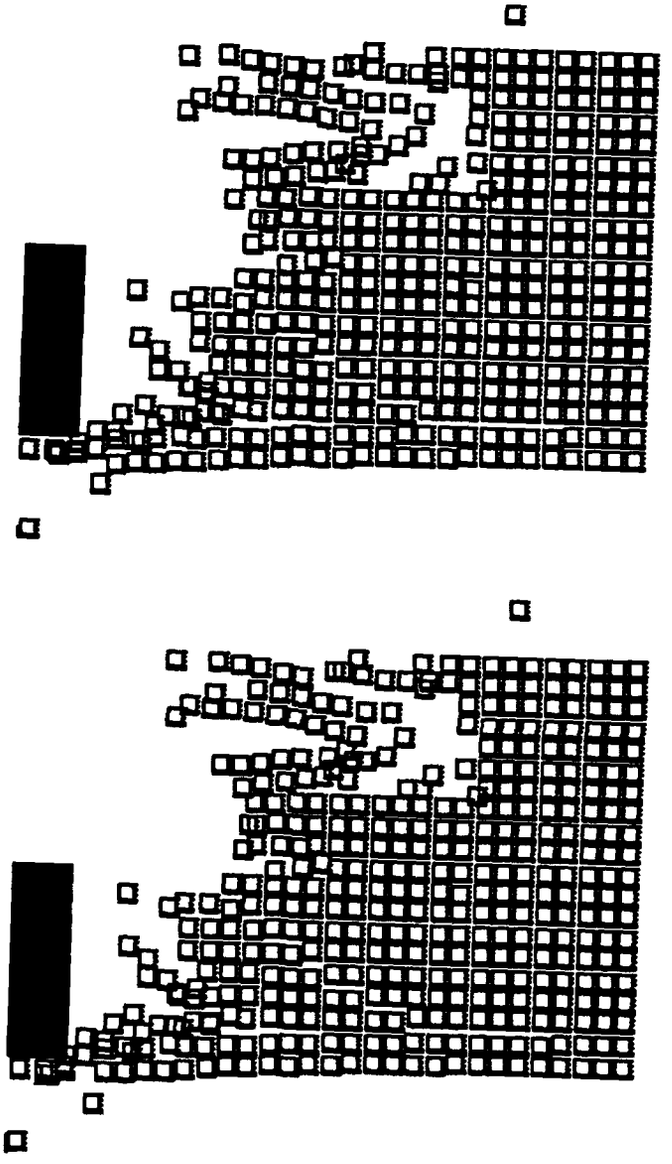

Figrure 5.23, continued

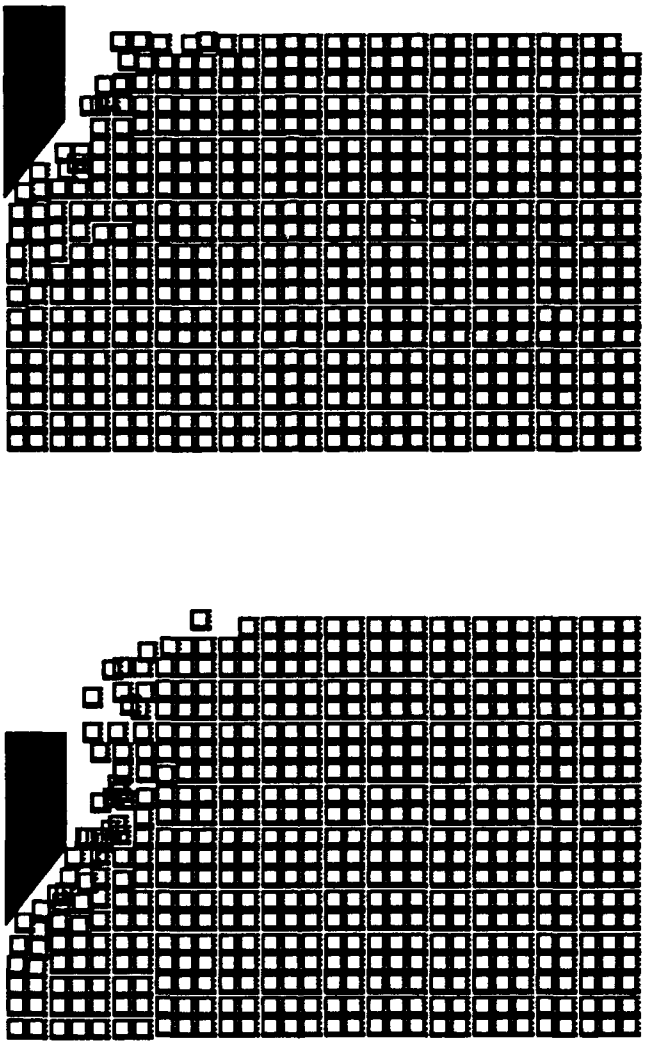

Figure 5.24 Deformed mesh for Problem 5.7 at 0.5×10^{-4}, 1×10^{-4}, 1.5×10^{-4}, and 1.6×10^{-4} seconds

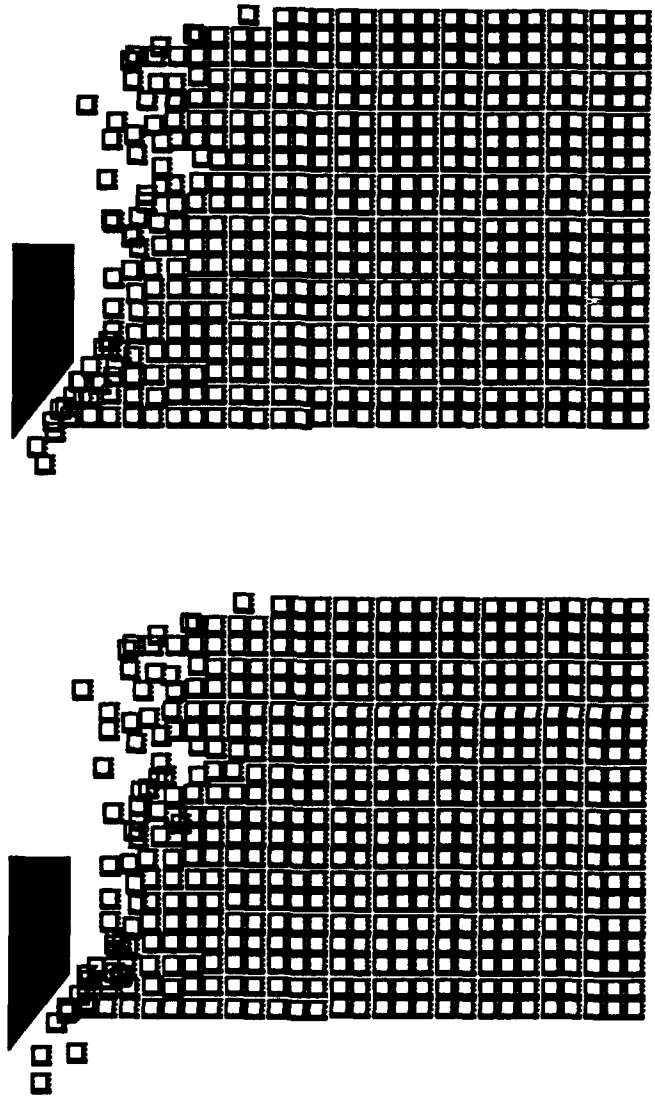

Figure 5.24, continued

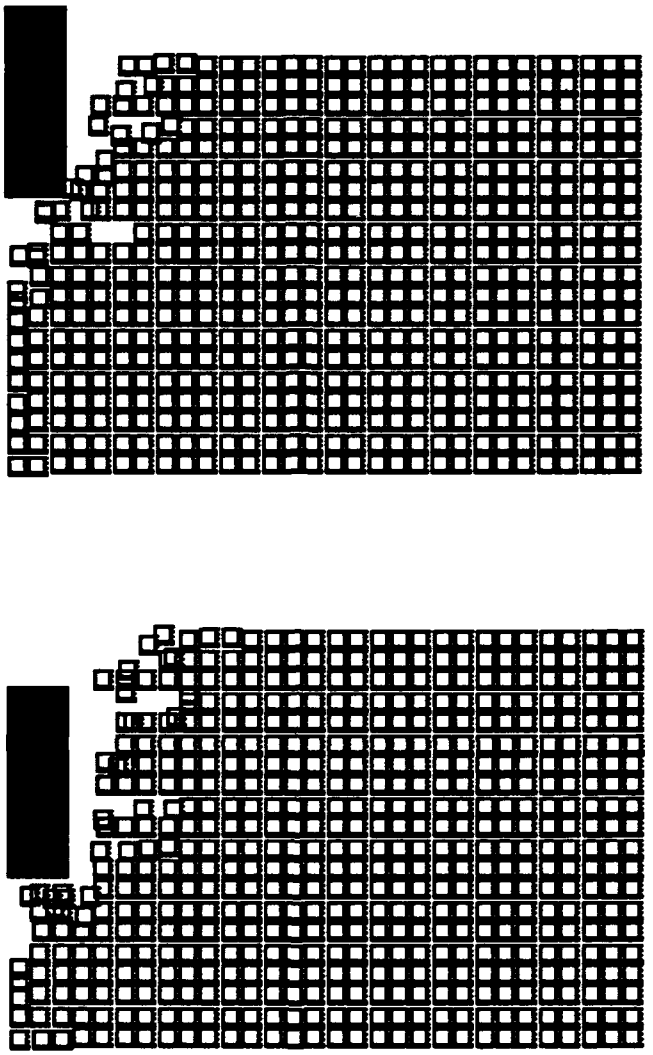

Figure 5.25 Deformed mesh for Problem 5.8 at 0.5×10^{-4}, 1×10^{-4}, 1.5×10^{-4}, and 2×10^{-4} seconds

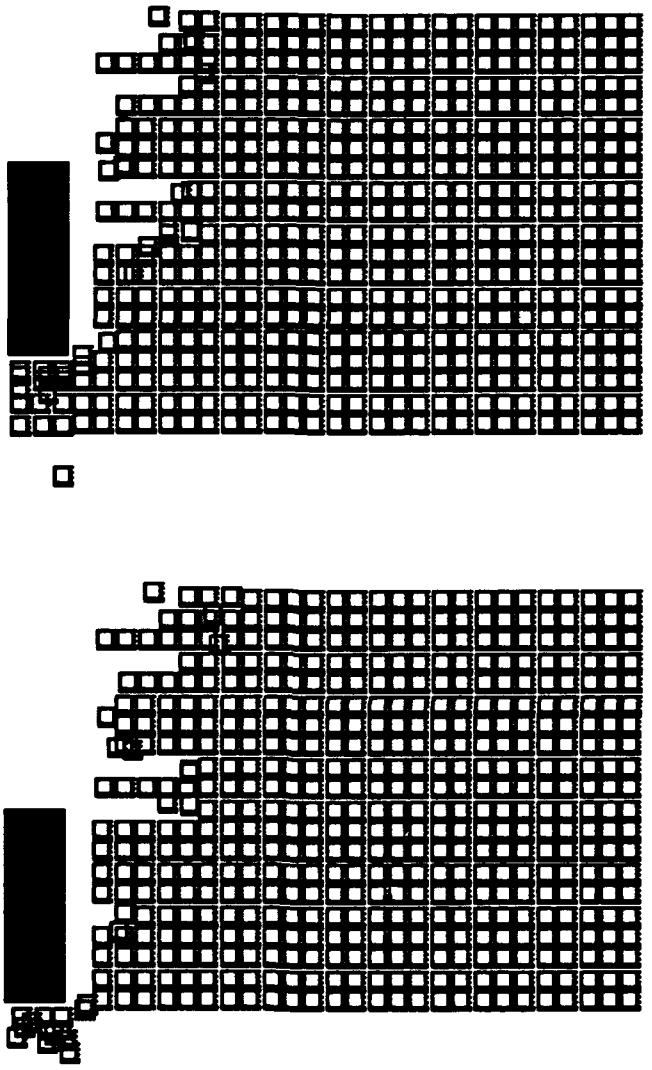

Figure 5.25, continued

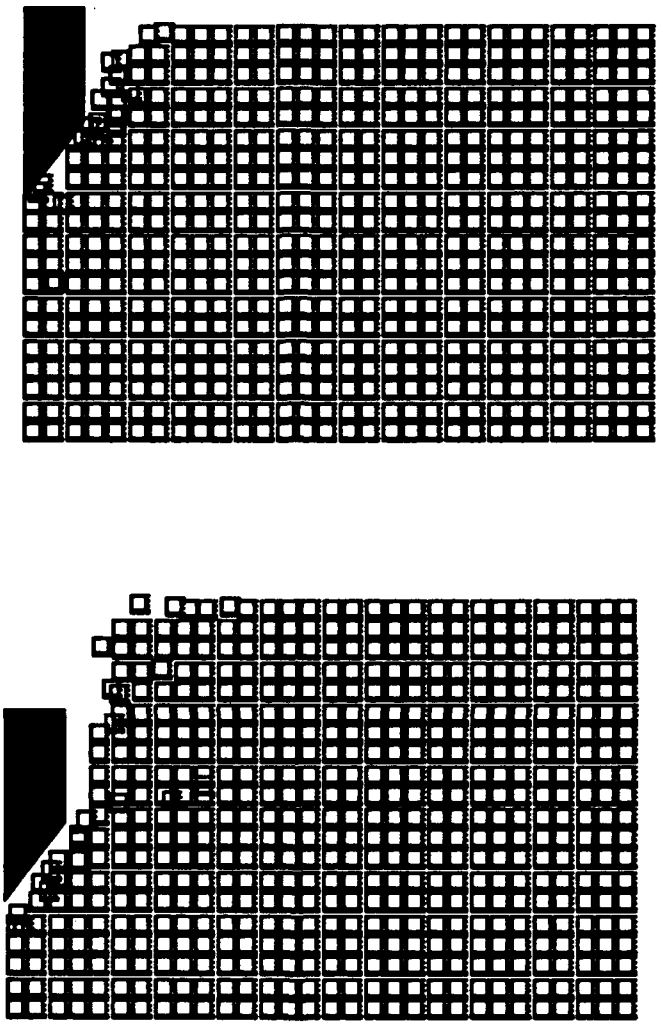

Figure 5.26 Deformed mesh for Problem 5.9 at 0.5×10^{-4}, 1×10^{-4}, and 1.5×10^{-4} seconds

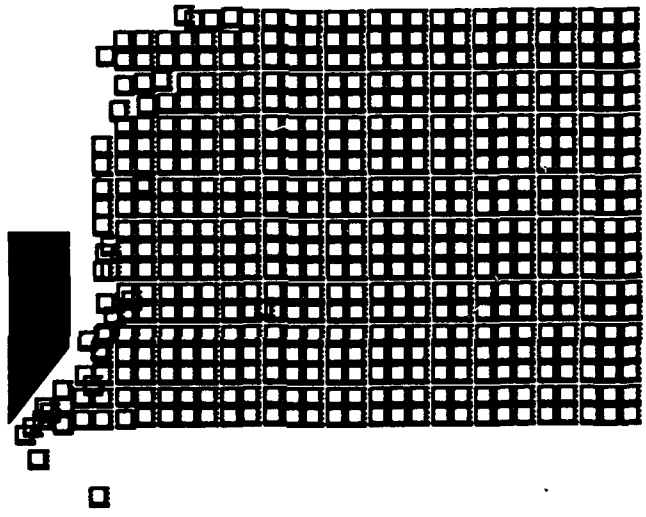

Figure 5.26, continued

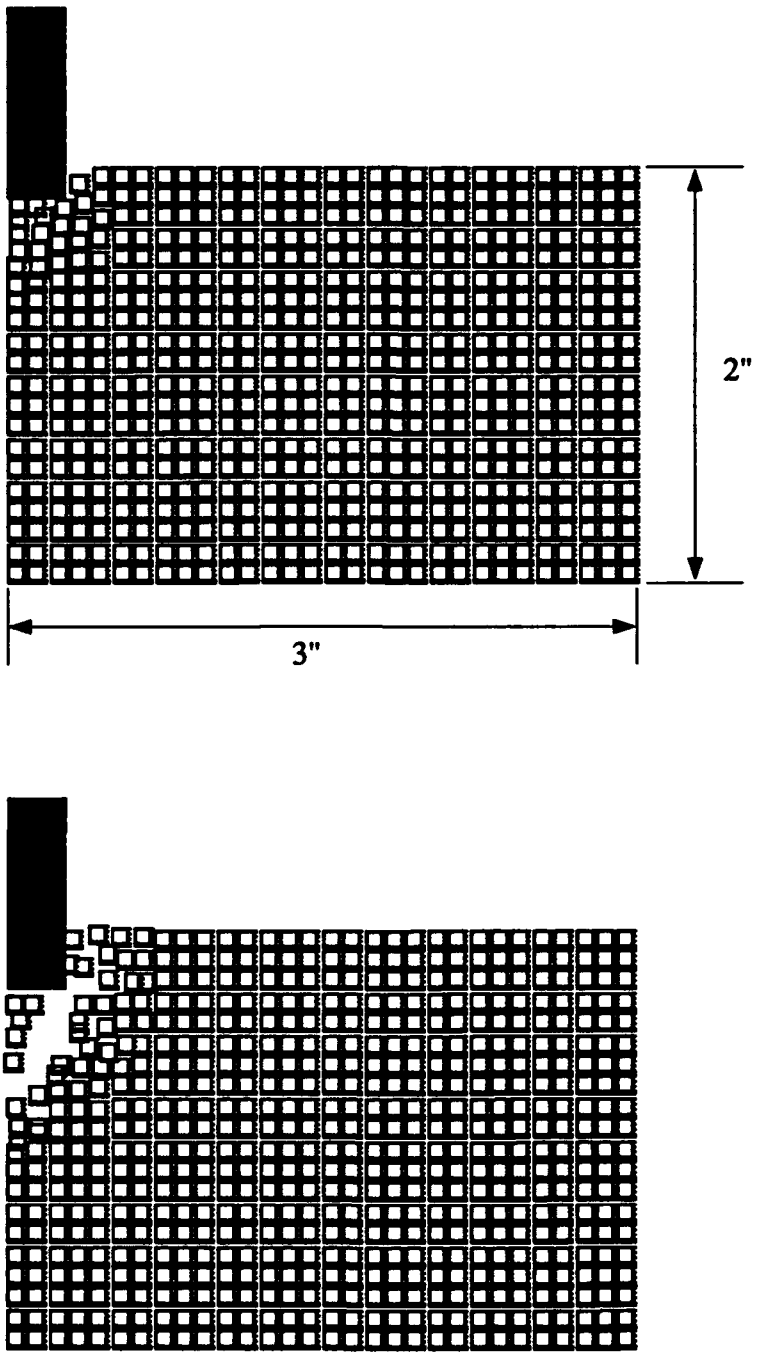

Figure 5.27 Deformed mesh for Problem 5.10 at $1x10^{-5}$, $2x10^{-5}$, $3x10^{-5}$, $4x10^{-5}$, and $5x10^{-5}$ seconds

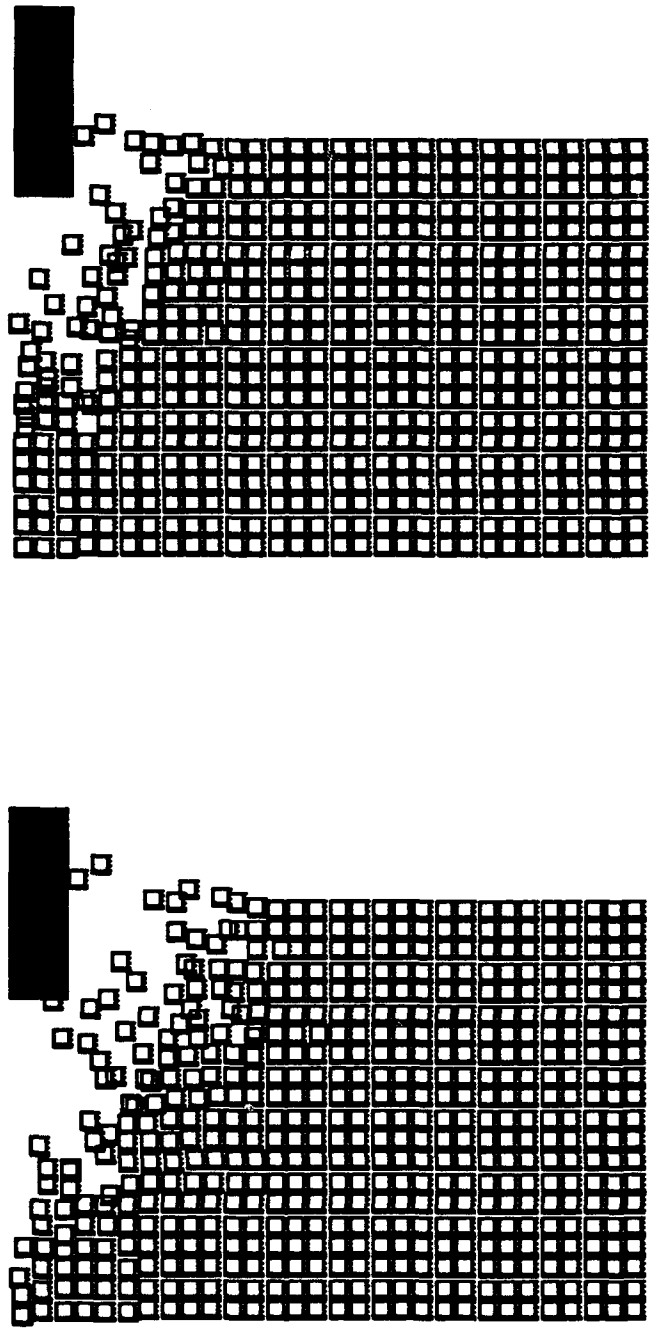

Figure 5.27, continued

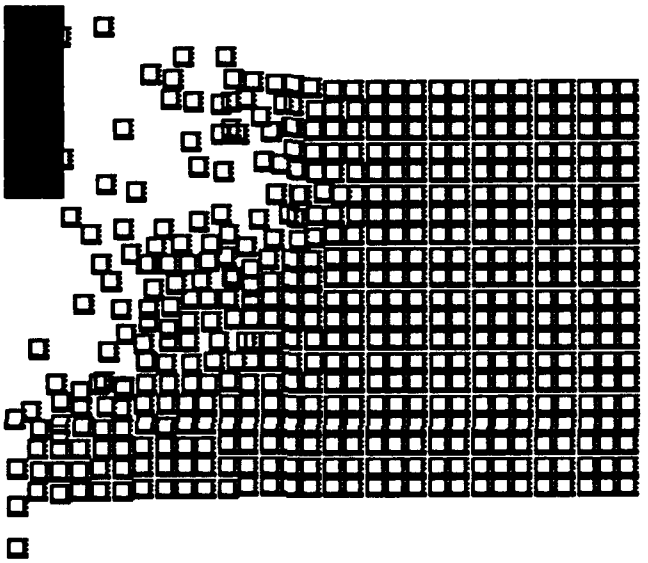

Figure 5.27, continued

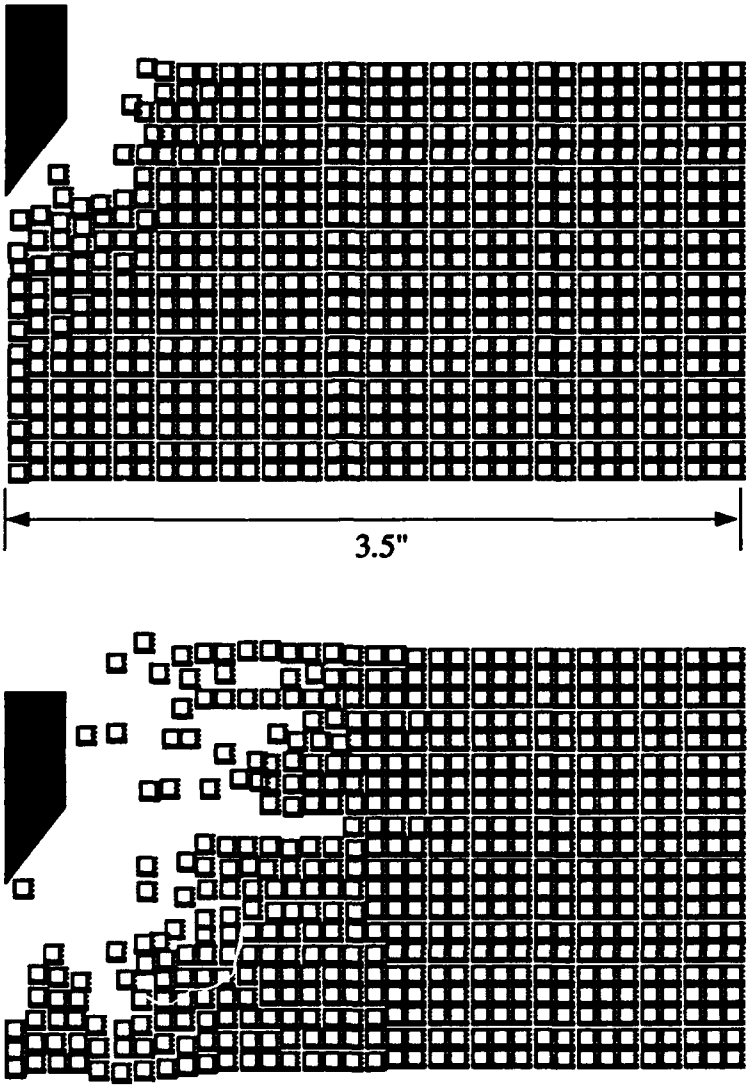

Figure 5.28 Deformed mesh for Problem 5.11 at 0.5×10^{-4}, 1×10^{-4}, 1.5×10^{-4}, and 2×10^{-4} seconds

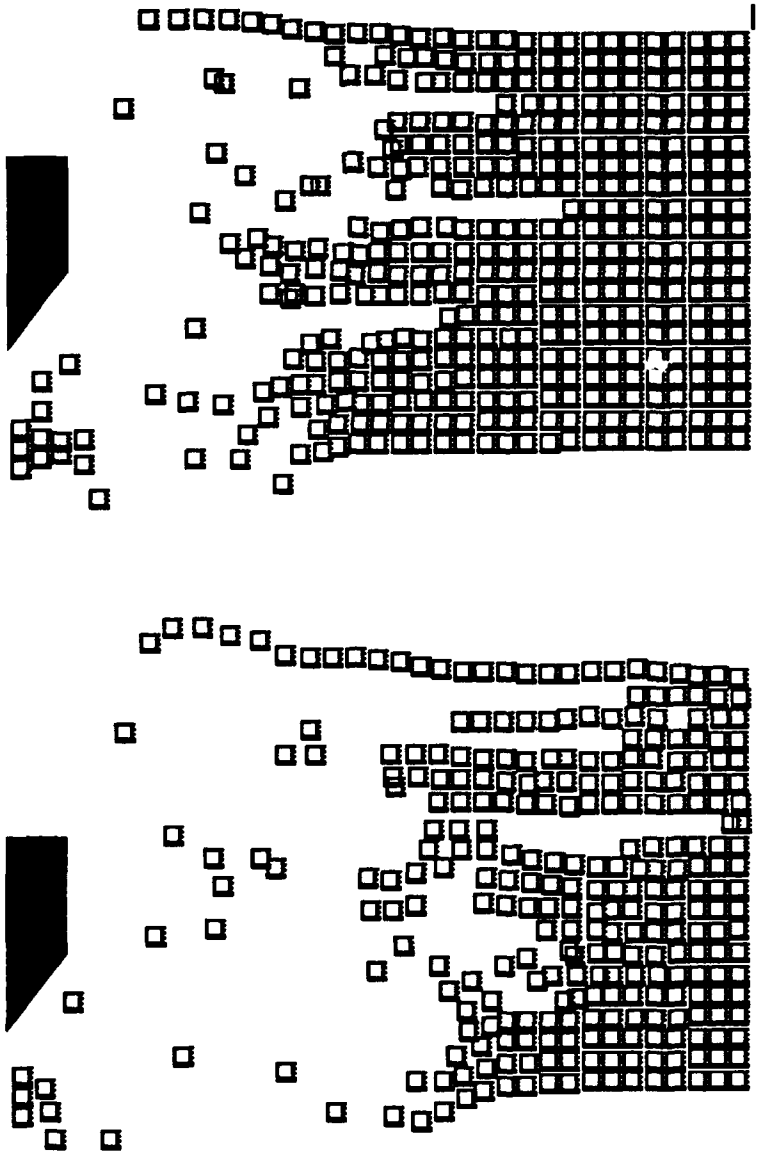

Figure 5.28, continued

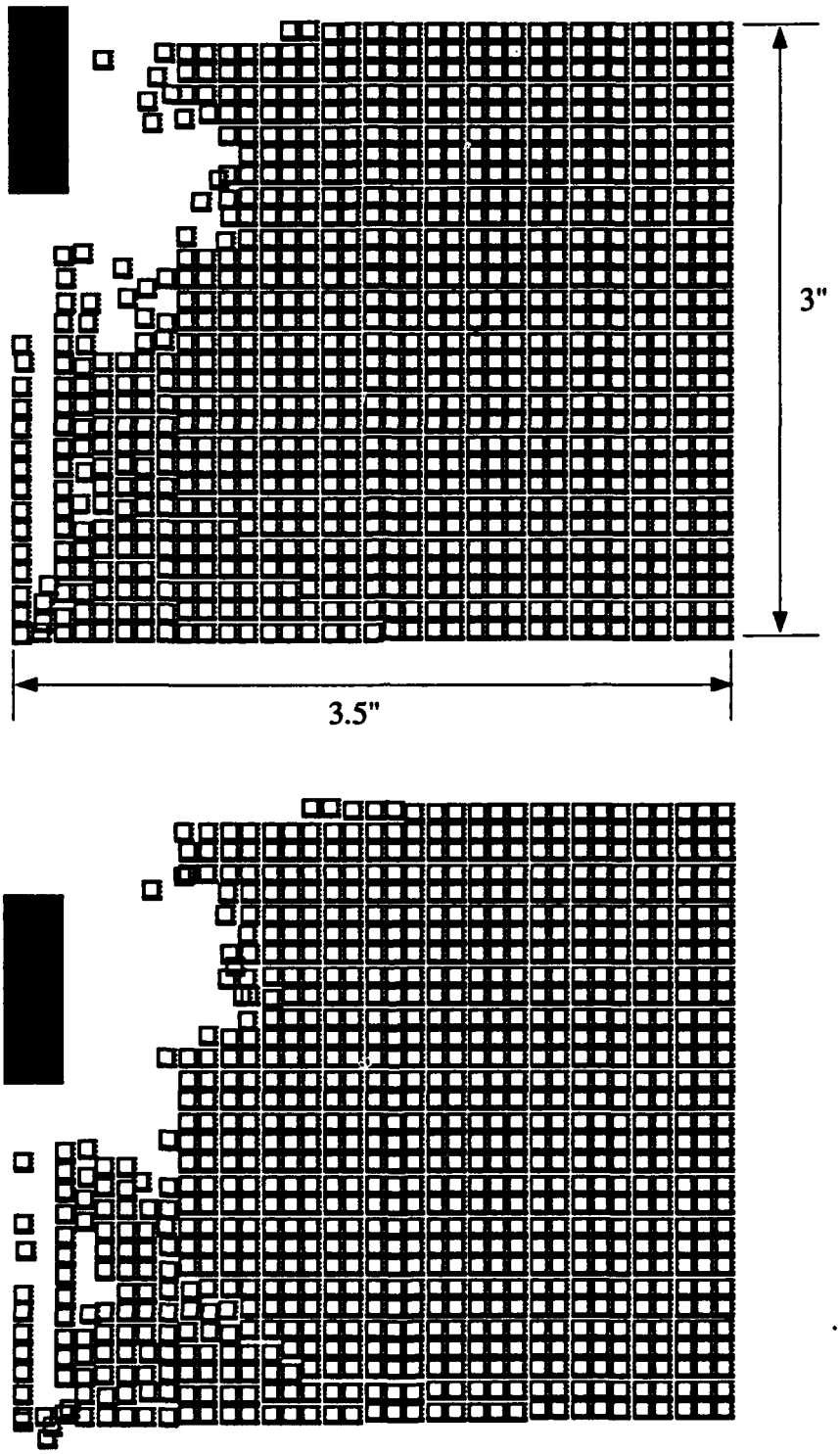

Figure 5.29 Deformed mesh for Problem 5.12 at $1x10^{-4}$, $2x10^{-4}$, $3x10^{-4}$, and $3.9x10^{-4}$ seconds

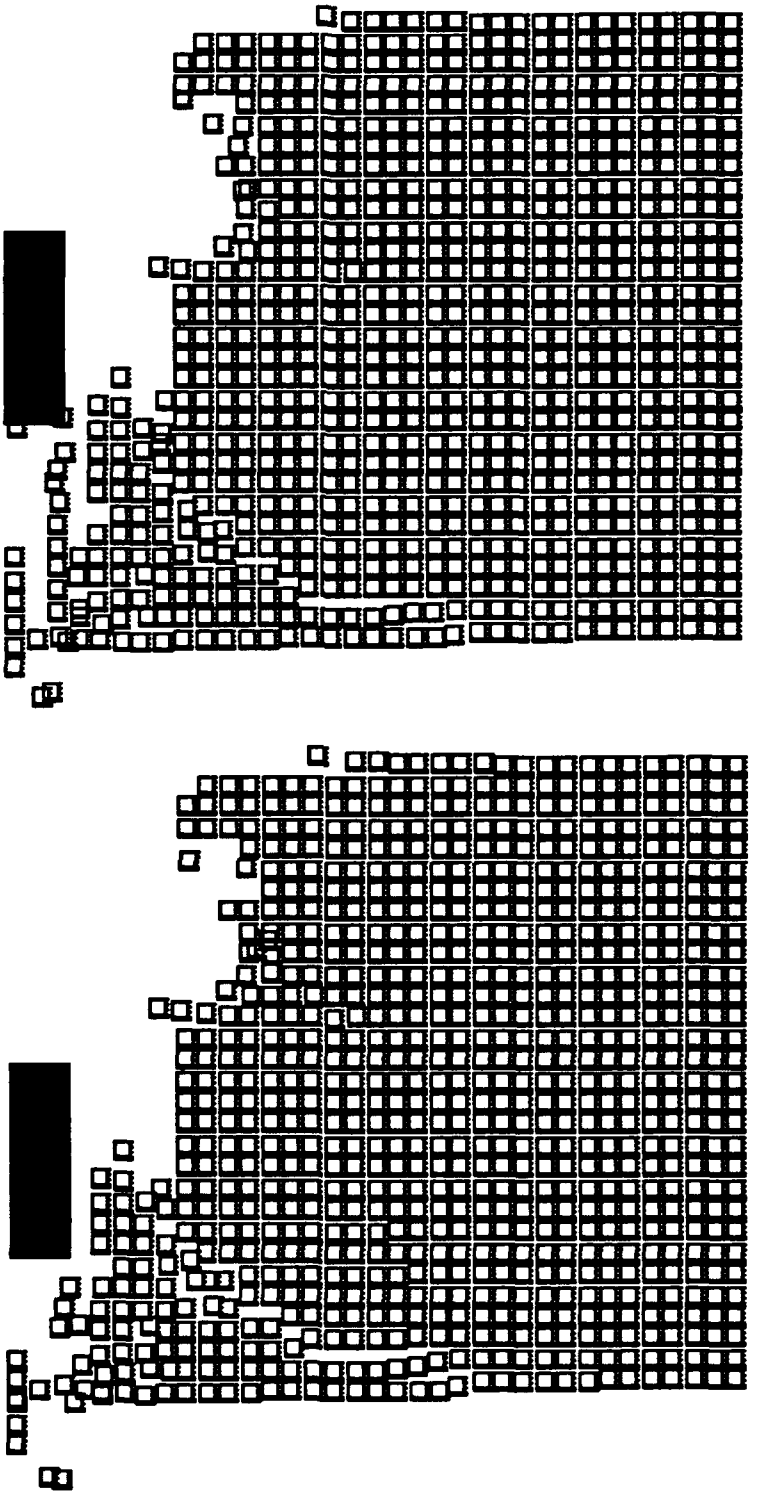

Figure 5.29, continued

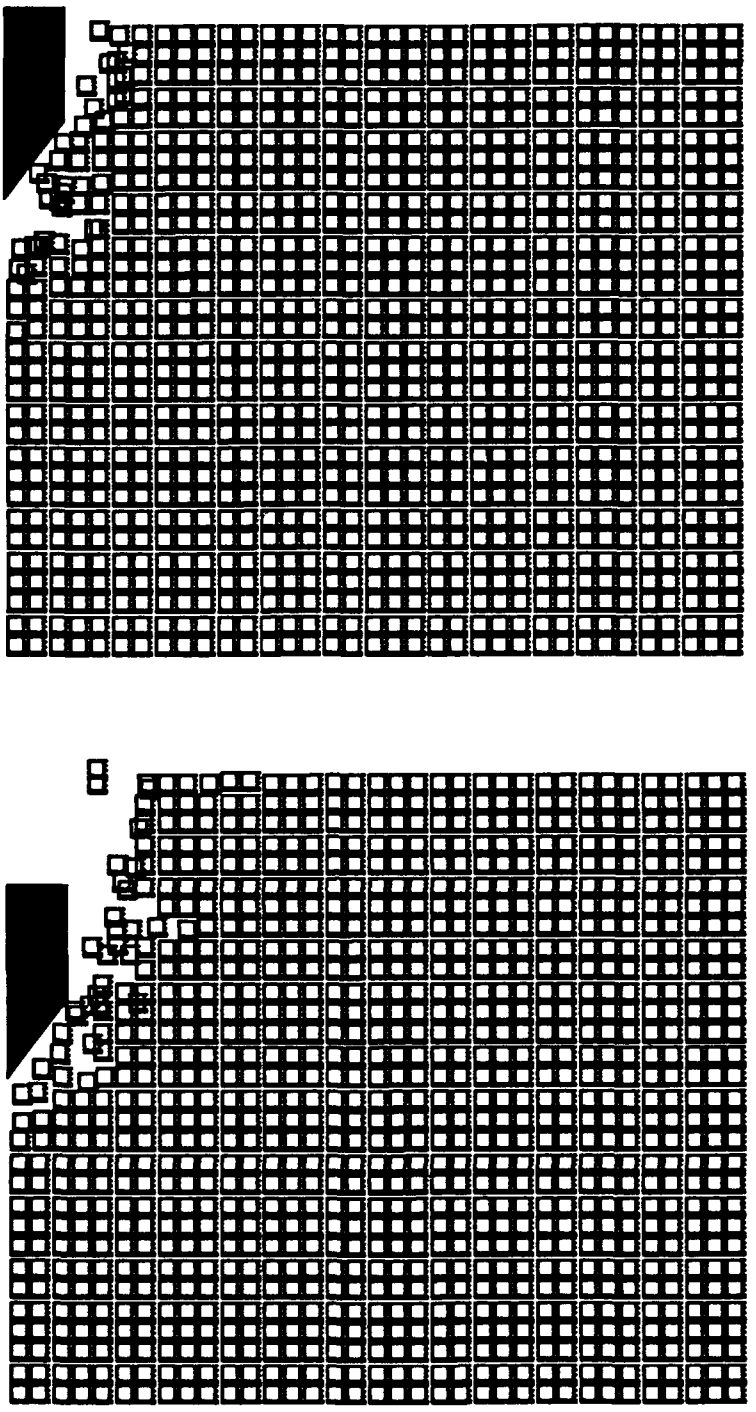

Figure 5.30 Deformed mesh for Problem 5.13 at 0.5×10^{-4}, 1×10^{-4}, 1.5×10^{-4}, 2×10^{-4}, and 2.5×10^{-4} seconds

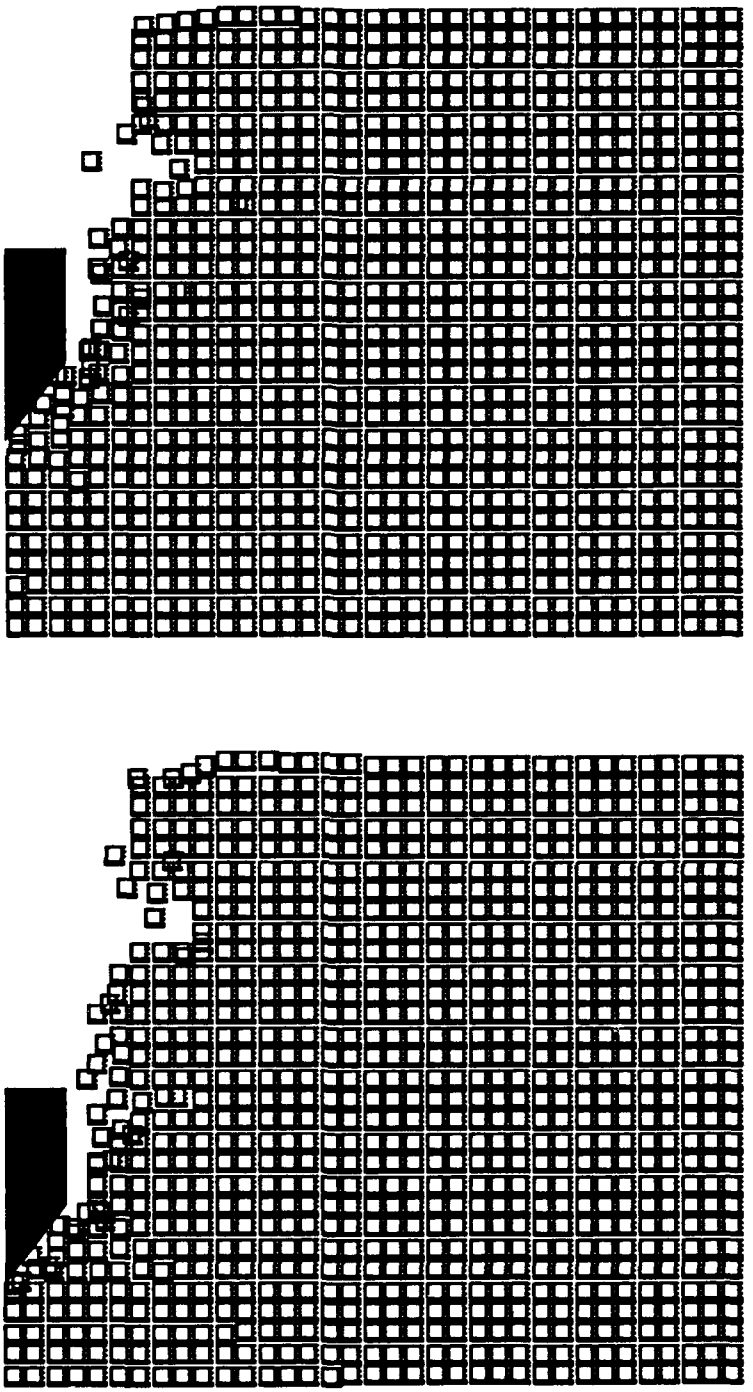

Figure 5.30, continued

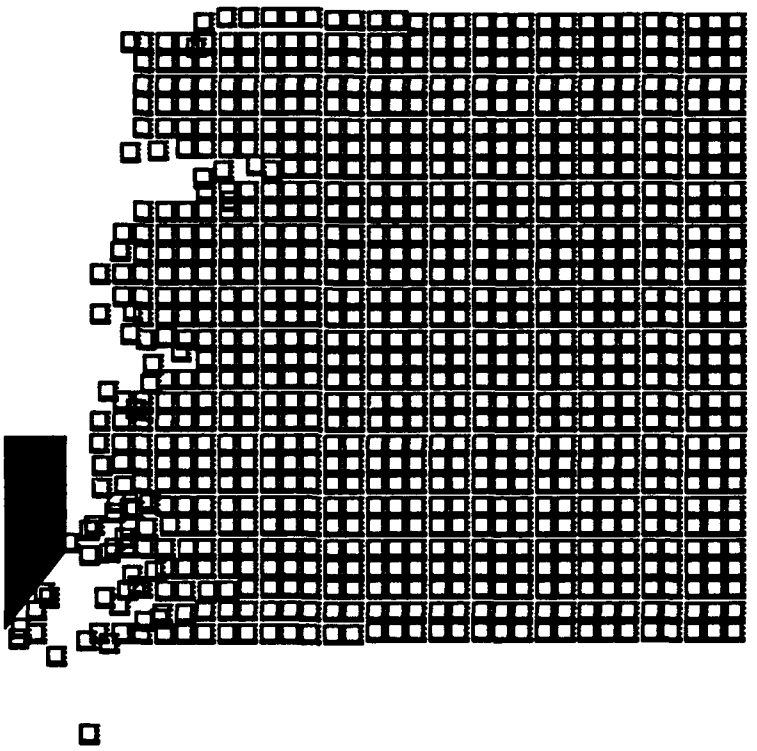

Figure 5.30, continued

Table 5.3 Final parameters for Problems 5.2 through 5.13

Problem	Final Projectile Velocity (in/sec)	Max. Penetration Depth (in)	Time of Max. Penetration (sec)
5.2	Rebound	0.501	0.791×10^{-4}
5.3	6,299	Complete (2 in)	0.242×10^{-3}
5.4	1,757	1.24	0.350×10^{-3}
5.5	6,408	Complete (2 in)	0.200×10^{-3}
5.6	5,394	Complete (2 in)	0.260×10^{-3}
5.7	10,973	Complete (2 in)	0.141×10^{-3}
5.8	6,246	Complete (2 in)	0.203×10^{-3}
5.9	10,384	Complete (2 in)	0.146×10^{-3}
5.10	7,617	0.632	0.529×10^{-4}
5.11	3,594	Complete (2 in)	0.224×10^{-3}
5.12	4,398	2.45	0.400×10^{-3}
5.13	7,370	Complete (3 in)	0.259×10^{-3}

CHAPTER 6 CONCLUSIONS AND RECOMMENDATIONS

6.1 Conclusions

The solution of ordnance velocity impact of concrete targets is still in its infancy. The solution technique which has been developed most extensively is the empirical approach which is also the least flexible. Numerical analysis using the finite element method is much more flexible but not as widely used due to limitations in its ability to accurately represent physical phenomena involved in the impact process. Numerical simulations such as the distinct element method are able to recreate some of these processes but do not model the initial structure well due to the method's inherent discrete body representation of a system. This method of modeling the initial structure restricts numerical simulations to recreating known failure patterns and from predicting patterns and behavior.

A fragmentation algorithm is presented which has the ability to create new free surfaces in a mesh and completely fragment pieces from the structure. The incorporation of the algorithm into the finite element method allows the study of failure propagation while retaining the ability of the finite element method to accurately calculate distribution and redistribution of stresses throughout the structure. This algorithm, thus, brings the computational methods of numerical analysis and numerical simulation closer together and allows a much wider range of problems to be treated.

The algorithm is shown to be well suited to the specific problem of ordnance velocity impact. A series of example problems shows the ability of the algorithm to create new surfaces and entirely separate fragments. The large zones of damage caused by fragmentation at the impact and distal faces common to concrete impact are modeled by the technique.

The high velocity impact problems indicate a possible characteristic of complete penetration caused by a non-deformable projectile. In the literature, it is commonly reasoned that the distal face spalling in concrete impact problems is caused by a reflection of the tensile wave [8,98] The numerical results of Problems 5.2 through 5.12 do not show failure states of stresses in the fragmented elements at the distal face which would indicate tensile stresses due to a reflected compressive stress wave; and, thus, do not support this interpretation for non-deformable projectile impact.

A non-deformable projectile which completely penetrates the target does create a strong compressive wave which is the incident wave in wave-induced spalling. It does not, though, provide a zero stress or greatly reduced compressive stress wave which is required to allow a net-tensile stress on reflection. (A deformable projectile impact allows a relief wave when it is stopped.) Projectile acceleration data from the numerical results show no significant reduction in projectile forces needed to allow the formation of a relief wave. The assumption that the spalling is not caused by a reflected tensile wave is also supported by experiments of Forrestal [25] into dry porous rock which show that the magnitude of the projectile's acceleration steadily increases during initial cratering with the highest accelerations found at the point of tunnel creation.

Since test data do not support the assumption that a stress wave reflection causes distal face damage, the question remains: what does cause this damage which is considerably wider than the projectile diameter? The numerical results suggest that it is caused by the same spiral shear stresses which cause the impact face cratering. The failure patterns from the examples show the damage to progress at the approximate dilatational wave speed in the shear spiral pattern. The shear spirals with larger radii are directed more to the distal face of the target. Therefore, only those with the smaller radii possess sufficient energy to reach the impact face. The spirals which are medium in size curve downward toward the distal face but then curve back toward the impact face; they do not contain enough energy to reach that face. The largest of the spirals curve downward and reach the distal face before they curve away from it. These are the spirals which cause the distal face damage and create a larger damage zone than found at the impact face. This is supported by the damage patterns observed in the example problems.

Test results show that the damage to the target directly in front of the projectile progresses at the same speed as the shear spirals which create the impact face and distal face damage. This would indicate the tunneling failure is initially caused by the largest of the spirals which travel in almost a straight line from impact face to distal face. These spirals fracture the target material in front of the projectile with the actual tunnel being formed by the projectile pushing the fragmented concrete out of the projectile's path. This suggests all modes of failure in concrete impact (cratering, tunneling, and spalling) are caused primarily by the shear spirals.

6.2 Recommendations

1. The greatest hindrance in any analysis of impact is the lack of reliable and conclusive experimental test data on material properties. Before prediction of concrete impact behavior can be verified, more data must be obtained for both pre-failure and post-failure behaviors. A material model based on damage accumulation theory, as opposed to classical plasticity, may be helpful in damping out excessive crack propagation found along the impact and distal faces.

2. One possible disadvantage of the current fragmentation algorithm is its inability to allow cracking to progress in any direction. Current numerical results do show the failure pattern to follow expected paths even when the path is not a straight line. Automatic mesh refinement techniques may help further. The development of an adaptive element or re-meshing the problem during the event may be necessary for predicting more complex failure propagation.

3. The inter-element collision algorithm used in the current code is extremely crude. A more refined algorithm should be studied and implemented into the code to achieve more accurate results.

4. The extreme CPU requirements (500 to over 2000 minutes on the Ardent Titan which is approximately 75 times faster than the DEC VAX-11/780) dictate the need for faster computational ability in order to develop the analysis further.

5. Integration of graphics capability into the program could enhance usefulness and also facilitate future development of the algorithm.

LIST OF REFERENCES

LIST OF REFERENCES

1. ACI Committee 318, "Building code requirements for reinforced concrete (ACI 318-89)," American Concrete Institute, Detroit, 1989
2. Ahmad, S., and Shah, S.P., "Behavior of hoop confined concrete under high strain rates", *ACI J.*, 1985, pp 634-647
3. Air Force Flight Dynamics Lab, Technical Report JTCG/AS-74-D-002, Wright-Patterson Air Force Base, Ohio, 1976
4. Anderson, C.E. and Bodner, S.R., "Ballistic impact: The status of analytical and numerical modeling", *Int. J. Impact Eng.*, vol.7, 1988, pp 9-35
5. Argyris, J.H., Kelsey, S., and Kaneel, H., *Matrix Methods for Structural Analysis - A Precis of Recent Developments*, MacMillan Co., New York, 1964
6. Awerbuch, J.R. and Bodner, S.R., "Analysis of the mechanics of perforation of projectiles in metallic plates", *Int. J. Solids Structs.*, vol.10, 1974, pp 671-684
7. Babosa, R. and Ghaboussi, J., "Discrete finite element method," *J. Geotech. Eng.*, ASCE, Accepted for publication, 1990
8. Backman, M.E. and Goldsmith, W., "The mechanics of penetration of projectiles into targets", *Int. J. Engng. Sci.*, vol.16, 1978, pp1-99
9. Bathe, K.J., Ramm, E., and Wilson, E.L., "Finite element formulations for large deformation dynamic analysis," *Int. J. Num. Meth. Eng.*, vol.9, 1975
10. Bathe, K.J., *Finite Element Procedures in Engineering Analysis*, Prentice-Hall, Englewood Cliffs, NJ, 1982
11. Bauer, A. and Calder, P.N., "Projectile penetration in rock", *Proceedings of the 5th Canadian Rock Symposium*, The Canadian Advisory Committee on Rock Mechanics, 1969, pg 157-169
12. Bazant, Z.P. and Oh, B.H., "Strain-rate in rapid triaxial loading of concrete", *Proceedings, ASCE*, 108(EM5), 1982, pp 764-782
13. Belytschko, T., "Nonlinear analysis and numerical stability," *Shock and Vibration Computer Programs: Reviews and Summaries*, W. Pilkey and B. Pilkey (eds), Naval Research Laboratory, Washington, D.C., 1975

14. Belytschko, T. and Hsieh, B.J., "Non-linear transient finite element analysis with convected coordinates," *Int. J. Num. Meth. Eng.*, vol.17, 1973

15. Belytschko, T. and Schwer, M.J., "Large displacement, transient analysis of space frames," *Int. J. Num. Meth. Eng.*, vol.11, 1977

16. Belytschko, T. and Liu, W.K., "Computational methods for impact and penetration", *Impact*, Balkema, 1988, pp 151-164

17. Blazynski, *Materials at High Strain Rates*, Elsevier Applied Science, NRC/Nat'l Acad. Sciences, 1987

18. Bodner, S.R., "Modeling ballistic perforation", *Structural Impact and Crashworthiness: Volume 1*, Elsevier, 1984, Chapter 4

19. Brown, S.J., "Energy release protection for pressurized systems. Part II. Review of studies into impact/terminal ballistics", *Applied Mechanics Reviews*, vol.39, 1986, pp 177-201

20. Chen, W.F., *Plasticity in Reinforced Concrete*, McGraw-Hill, 1982

21. Chen, W.F. and Han, D.J., *Plasticity for Structural Engineers*, Springer-Verlag, 1988

22. Chen, W.F., and Yamaguchi, E., "On constitutive modeling of concrete materials," *Finite Element Analysis of Reinforced Concrete Structures*, Proceedings of the seminar sponsored by the Japan Society for the Promotion of Science and the U.S. National Science Foundation, edited by C. Meyer and H. Okamura ASCE, 1985, pp 48-71

23. Dubois, J.J., Chedmail, J.F., and Bianchini, J.C., "Numerical analysis of impact penetration problems for nuclear reactor safety", *Transactions of the 4th SMiRT*, vol.J., 1977, paper 7/1

24. Forrestal, M.J., "Closed form solutions for forces on conical-nosed penetrators into geological targets with constant shear strength", *Mech. of Mat'ls*, vol.1, 1982, pp 285-295

25. Forrestal, M.J., "Penetration into dry porous rock", *Int. J. Solids and Structures*, 22, 1986, pp 1485-1500

26. Fu, C.C., "On the stability of explicit methods for numerical integration of the equations of matrices in finite elements," *Int. J. Num. Meth. Eng.*, vol.4, 1972

27. Gelman, M.D., Nelson, R.B., and Ito, Y.M., "Impact of AP projectile into array of large caliber boulders," *Technical Report SL-87-30*, U.S. Army Engineer Waterways Experiment Station, Nov. 1987

28. Glinicki, M.A., "Effect of the loading-rate on the tensile strength of concrete", *Cement Based Composites: Strain Rate Effects on Fracture*, Materials Research Society, vol.64, 1985, pp87-92

29. Halder, A., "Energy-balanced approach to evaluate local effects of impact of non-deformable missiles on concrete structures", *Transactions of the 8th SMiRT*, vol.J., 1985, paper 6/3

30. Hallquist, J.O., *Theoretical Manual for DYNA3D*, Lawrence Livermore Laboratory Report No. UCID-19401, University of California, 1982

31. Heider, N., "3D-finite element impact simulation on concrete structures", *Computational Techniques for Contact, Impact, Penetration and Perforation of Solids*, ASME, AMD vol.103, 1989, pp 359-372

32. Heuze, F., et. al., "Models for rock mass dynamics", *Mechanics Computing in 1990's and Beyond*, ASCE, Conf. Proc. vol. 2, 1991, pp 1169-73

33. Hsieh, S.S, Ting, E.C., and Chen, W.F., " A plastic-fracture model for concrete," *Int. J. Solids and Structures*, vol.18, No.3, 1982

34. Hughes, J.R., *The Finite Element Method*, Prentice-Hall, Englewood Cliffs, NJ, 1987

35. Ipson, T.W., Recht, R.F., and Schmelling, W.A., Rpt NWC TP 5607, Naval Weapons Center, China Lake, California, 1973

36. Isenberg, J., Mufti, A.A., Schonbrich, W.C., and Meyer, C., "Dynamic analysis," *State-of-the-art Report on Finite Element Analysis of Reinforced Concrete*, Chap. 7, ASCE, 1982

37. Isenberg, J., and Levine, H.S., "Analysis of reinforced concrete under shock loading," pp 444-464

38. Iura, M., and Atluri, S.N., "Dynamic analysis of finitely stretched and rotated 3-D space-curved beams," *Proc. Int. Conf. Comp. Eng. Sci.*, S.N. Atluri and G. Yagawa (eds), Springer-Verlag, Berlin, 1988

39. Jawed, I., Childs, G., Ritter, A., and Winzer, S., "High-strain-rate behavior of hydrated cement pastes," *Cement and Concrete Research*, vol. 17; 1987, pp 433-440

40. John, R., and Shah, S.P., "Constitutive modeling of concrete under impact loading", *Impact*, Balkema, 1988, pp 37-65

41. John, R., and Shah, S.P., "Fracture of concrete subjected to impact loading," *Cement, Concrete, and Aggregates*, CCAGDP, vol. 8, No. 1, Summer 1986, pp 24-32

42. Johnson, G.R., Stryk, R.A., and Nixon, M.E., "Two and three dimensional computational approaches for steel projectiles impacting concrete targets", *Impact*, Balkema, 1988, pp 233-250

43. Kabo, J.M., "Fragmentation of rock under dynamic loads", *Rock Mechanics*, vol.9, 1977, pp213-243

44. Kennedy, J.M., Belytschko, T., and Schoeberle, D.F., *STRAW - A Nonlinear Fluid-Structural and Thermomechanical Finite Element Program*, ANL/RAS 85-8, Argonne National Laboratory, Argonne, Illinois, 1985

45. Kennedy, R.P., "A review of procedures for the analysis and design of concrete structures to resist missile impact effects", *Nuc. Eng. and Design*, vol.37, 1976, pp 183-203

46. Key, S.W., "Finite element procedure for the large deformation dynamic response of axisymmetric solids," *J. Comp. Meth. Applied Mech. Eng.*, vol.4, 1974

47. Key, S.W., "Improvements in transient dynamic time integration with application to spent nuclear fuel shipping cask impact analyses," *Finite Element Methods for Nonlinear Problems*, P.G. Bergan, K.J. Bathe, and W. Wunderlich (eds), Springer-Verlag, Berlin, 1986

48. Kimsey, K.D., "Calculation of penetration", *Theoretical Foundations for Large-scale Computations for Non-linear Material Behavior*, Mechanics of Elastic Solids 6, 1983, pp 165-176

49. Klezpaczko, J.R., "Fracture initiation under impact", *Int. J. Impact Eng.*, vol.3, 1985, pp 191-210

50. Kormeling, H.A., "The rate theory and the impact tensile behavior of plain concrete," *Fracture Toughness and Fracture Energy of Concrete*, F.H. Wittman ed., Elsevier Science Publishers, Amsterdam, 1986, pp 467-477

51. Krieg, R.D., and Key, S.W., "Transient shock response by numerical time integration," *Int. J. Num. Meth. Eng.*, vol.7, 1973

52. Kuennen, S.T., Ross, C.A., and Tedesco, J.W., "Compression and tensile strength analysis of concrete at high strain rates," *Structures Congress '91 Compact Papers*, ASCE, 9th Structures Congress, Indianapolis, IN, 1991, pp 283-286

53. Kulak, R.F., "Three-dimensional contact/impact methodology", *Impact*, Balkema, 1988, pp 183-200

54. Kumano, A. and Goldsmith, W., "Impact response of rocks to metallic strikers", *Response of Geologic Materials to Blast Loading and Impact*, ASME, AMD vol.16, 1985, pg 149-174

55. Labbane, M., Ting, E.C., and Sutton, C.D., "Evaluation of plasticity-based models for concrete," *School of Civil Engineering, Report CE-STR-91-18*, Purdue University, 1991

56. Labbane, M., "Computational failure analysis of reinforced concrete plate assemblages," Ph.D. Dissertation, Purdue University, W. Lafayette, IN, May, 1991

57. Levy, N. and Goldsmith, W., "Normal impact and perforation of thin plates by hemispherically tipped projectiles", *Int. J. Impact Eng.*, vol.2, 1984, pp 209-229

58. Longscope, D.B., "Closed form approximations for forces on conical penetrators into dry porous rock", *J. Applied Mechanics*, vol.18, 1981, pp 971-972

59. Luk, V.K. and Forrestal, M.J., "Penetration into semi-infinite reinforced concrete with spherical & ogival nose projectiles", *Int. J. Impact Eng.*, vol.6, 1987, pg 291-301

60. Marchertas, A.H., and Belytschko, T., "Non-linear finite-element formulation for transient analysis of three-dimensional thin structures" , *Argonne National Laboratory Report ANL-8104*, Argonne, Illinois, 1974

61. Mattiasson, K., "On the Co-rotational finite element formulation for large deformation problems", Chalmers University of Technology Department of Structural Mechanics, Publication 83:1, Goeteborg, 1983

62. Maurel, P., Lacoste, J.M., Hoffmann, A., and Jamet, P., "Three Dimensional Dynamic Analysis of a Thick Reinforced Concrete Slab Subjected to the Impact of a Projectile", *Transactions of the 8th SMiRT*, vol.J., 1985, paper 6/1

63. Maurer, W.C. and Rinehart, J.S., "Impact crater formation in rock", *J. Appl. Phys.*, vol.31, No.7, 1960

64. Mindness, S., Banthia, N.P., et. al., "Crack development in cementious materials under impact loading", *Cement Based Composites: Strain Rate Effects on Fracture*, Materials Research Society, vol.64, 1985

65. Mlakar, P.F., Vitaya-Udom, K.P., and Cole, R.A., "Dynamic tensile-compressive behavior of concrete," *ACI Journal*, Jul-Aug 1985, pp484-491

66. Nash, P.T., Zabel, P.H., and Wenzel, A.B., "Penetration studies into concrete and granite," *Response of Geologic Materials to Blast Loading and Impact*, ASME, AMD vol.16, 1985, pp 175-181

67. Nilsson, L. and Sahlin, S., "Impact of a steel rod on a reinforced concrete slab," *Dynamic Modeling of Concrete Structures*, ACI, SP-73, 1982, pp 165-187

68. Nygard, M.K., and Bergan, P.G., "Advances in treating large rotations for non-linear problems," *State-of-the-art Surveys on Computational Mechanics*, A.K. Noor and J.T. Oden (eds), ASME, 1989

69. Oden, J.T., and Key, S.W., "Analysis of static nonlinear response by explicit time integration," *Int. J. Num. Meth.*, vol.7, 1973

70. Oh, B.H., "Behavior of concrete under dynamic loads," *ACI Material Journal*, 84(1), 1987, pp 8-13

71. Palomby, C., and Strange, W.J., "Blunt missile perforation of thin plates by discing", *Int. J Impact Eng.*, vol.7, 1988, pp 85-100

72. Park, K.C., "Evaluating time integration methods for nonlinear dynamic analysis," *Finite Element Analysis of Transient Nonlinear Behavior*, T. Belytschko, et al. (eds), AMD 14, New York, ASME, 1975

73. Ravid and Bodner, S.R., "Dynamic perforation of visco-plastic plates by rigid projectiles", *Int. J. Engng. Sci.*, 21, 1983, pp 577-591

74. Reinhardt, H.W., "Strain rate effects on the tensile strength of concrete as predicted by thermodynamic and fracture mechanics models", *Cement Based Composites: Strain Rate Effects on Fracture*, Materials Research Society, vol.64, 1985, pp1-14

75. Saha, N.K., and Ting, E.C., *Large Displacement Dynamic Analysis of Space Frames*, CE-STR-83-5, School of Civil Eng., Purdue Univ., West Lafayette, IN. 1983

76. Saha, N.K., "Plasticity-based modeling and analysis of concrete structures," Ph.D Dissertation, Purdue University, W. Lafayette, IN, Dec, 1983

77. Seely, F.B., *Resistance of Materials*, J. Wiley & Sons, New York, 1947, pp304-327

78. Shah, S.P., and John, R., "Rate sensitivity of Mode I and Mode II fracture of concrete", *Cement Based Composites: Strain Rate Effects on Fracture*, Materials Research Society, vol.64, 1985

79. Shi, Gen-hua,"Discontinuous Deformation Analysis: A New Numerical Model for the Statics and Dynamics of Block Systems", PhD Dissertation, Univ. of Calif., Berkeley, August, 1988

80. Sliter, G.E., "Assessment of empirical concrete impact formulas", *Journal of the Structural Division: ASCE*, vol.106, 1980, pp 1023-1045

81. Soroushian, P., Choi, K., and Fu, G., "Tensile strength of concrete at different strain rates," *Material Research Society Symposium Proc.*, Material Research Society, 1986, pp 87-92

82. Suaris, W., and Shah, S.P., "Constitutive model for dynamic loading of concrete," *Journal of Structural Engineering*, ASCE, vol. 111, No. 3, March 1985, pp 563-575

83. Suaris, W., and Shah, S.P.,"Properties of concrete subjected to impact", *J. Struct. Eng.*, ASCE, 109(7), 1983, pp 1727-1741

84. Ting, E.C., and Yenner, M., "Numerical plastic-fracture models for concrete," *School of Civil Engineering, Report CE-STR-84-8*, Purdue University, 1984

85. Tokeda, "Strain rate effects on concrete and reinforcement, and their contribution to structures", *Cement Based Composites: Strain Rate Effects on Fracture*, Materials Research Society, vol.64, 1985

86. U.S. Army Ballistic Research Laboratories, *A Penetration Equations Handbook*, Joint Technical Coordination Group, Aberdeen Proving Ground, Maryland, 1966

87. Uchida, T., Subota, H., and Yamada, T., "Experimental investigations on reinforced concrete slabs subjected to impact loading," *Trans. of the 8th Int. Conf. on SMiRT*, vol. J, 1985, pp173-201

88. Weaver, W., and Johnston, P.R., *Structural Dynamics by Finite Elements*, Prentice-Hall, Englewood Cliffs, N.J., 1987

89. Woodward, R.L., "A structural model for thin plate perforation by normal impact of blunt projectiles", *Int. J. Impact Eng.*, vol.6, 1987 , pp 129-140

90. Wright, T.W. and Frank, K., "Approaches to penetration problems", *Impact*, Balkema, 1988, pp85-104

91. Yankelevsky, D.Z., "Analysis of impact and penetration into geomaterials using engineering models", *Impact*, Balkema, 1988, pp 67-83

92. Yenner, M., Chompooming, K., and Jiang, Z., "Plasticity and endochronic based constitutive models for concrete," *Constitutive Modeling for Engineering Materials with Applications*, D. Hsi and T.J. Kozik, eds., ASME, Winter Annual Meeting, Nov-Dec 1988, Chicago, IL

93. Young, W.C., *Roark's Formulas for Stress & Strain*, Mcgraw-Hill, New York, 1989

94. Yuan, "Plate perforation by deformable projectiles - A plastic wave theory", *Int. J. Impact Eng.*, vol.1, 1983, pp 393-412

95. Ziegler, H., "A modification of Prager's hardening rule," *Quarterly of Applied Mathematics*, 1959, pp 55-65

96. Zienkiewicz, O.C. and Taylor, R.L., *The Finite Element Method, Volume 1*, McGraw-Hill, New York, 1989

97. Zukas, J.A., Jonas, G.H., Kimsey, K.D., Misey, J.J., and Sherrick, T.M., "Three-dimensional impact solutions: Resources and results", *Computer Analysis of Large Scale Structures*, ASME, AMD vol.49, 1981, pp 35-68

98. Zukas, J.A., *Impact Dynamics*, J. Wiley & Sons, New York, 1982

VITA

VITA

Darren L. Rice was born 8 November 1962 in Streator, Illinois. He graduated from Purdue University with a Bachelor of Science in Civil Engineering and received his commission in the United States Air Force in May 1984. In 1988, after serving two assignments at base-level civil engineering positions, he received an assignment to return to graduate studies through the Air Force Institute of Technology Civilian Institute program. He received his Master of Science in Civil Engineering from Purdue University in December 1989 and continued on at that time to pursue the degree of Doctor of Philosophy.